

TRW

13-5

AD A 048471

D D C  
RECEIVED  
DEC 30 1977  
RECEIVED

DUPLICATE COPY

TRW

DEFENSE AND SPACE SYSTEMS GROUP

One Space Park • Redondo Beach, California 90278

14 TRW-23906-7114-RU-00

**ABRES FLIGHT TEST EVALUATION OF RV ACCURACY**

14 V1 30 E 11

[Redacted]

1974 SEPTEMBER

12 228 p1

DDC  
RECEIVED  
DEC 30 1977  
REGISTERED  
F

Prepared for  
Headquarters  
Space and Missile Systems Organization  
Air Force Systems Command  
Los Angeles, California

15  
Change Order No. P00001  
Contract No. F04701-73-C-0020  
CDRL No. A023

18 SAMSO CDRL A023

Prepared by

354 545



One Space Park  
Redondo Beach, California 90278

**DISTRIBUTION STATEMENT A**  
Approved for public release;  
Distribution Unlimited



## ABSTRACT

Current emphasis on improved weapon system accuracy improvement may eventually require the development and flight test evaluation of an RV designed for minimum reentry dispersion. This report documents the flight test measurement requirements necessary to verify the reentry system accuracy performance including climatology, ballistic coefficient and lift effects for a minimum dispersion reentry vehicle. The study was performed parametrically for a reentry vehicle configuration with ballistic coefficients ranging from 1500 to 4000 psf over a range of reentry angles from 15 to 40 degrees. The study develops a reentry error budget which defines the magnitude of expected errors, and the most sensitive altitude regions. The results are used to establish measurement requirements including the types of measurements that must be made, the altitude region and the accuracies of the measurements. The capabilities of off-board and on-board instrumentation to meet the measurement requirements are examined including an extensive error analysis using the metric trackers in the Kwajalein terminal area. Different methods of post-flight data processing are reviewed.

CONTENTS

NOMENCLATURE.....	xiii
1. INTRODUCTION.....	1-1
1.1 Background.....	1-1
1.2 Study Objective.....	1-2
1.3 Study Organization.....	1-3
2. SUMMARY.....	2-1
2.1 Reentry Error Budget Study.....	2-1
2.2 Reentry Error Measurement Study.....	2-4
3. REENTRY ERROR BUDGET.....	3-1
3.1 Introduction.....	3-1
3.2 Climatology Dispersions.....	3-2
3.3 Ballistic Coefficient Dispersions.....	3-27
3.4 Lift Dispersions.....	3-44
3.5 Total Reentry Accuracy.....	3-72
4. FLIGHT TEST MEASUREMENT REQUIREMENTS.....	4-1
4.1 Introduction.....	4-1
4.2 General Measurement Requirement.....	4-2
4.3 Total Reentry Miss Measurement.....	4-13
4.4 Drag Deceleration Measurements.....	4-14
4.5 Climatology Measurements.....	4-16
4.6 Lift Measurements.....	4-22
4.7 Special Instrumentation Requirements.....	4-33
4.8 Summary.....	4-35
5. REENTRY METRIC TRACKING ANALYSIS.....	5-1
5.1 Introduction.....	5-1
5.2 Error Analysis Technique.....	5-2

## CONTENTS (Continued)

5.3	Trajectory Parameters.....	5-9
5.4	Tracker Characteristics.....	5-13
5.5	Error Analysis: Current Versus Predicted Sensor Errors	5-19
5.6	Error Analysis: Effect of Different Trackers.....	5-27
5.7	Error Analysis: Effect of Survey Accuracy.....	5-35
5.8	Error Analysis: Effect of High Altitude Lift.....	5-37
5.9	Error Analysis: Effect of Ballistic Coefficient and Reentry Angle.....	5-37
5.10	Error Analysis: Effect of Target Location.....	5-43
6.	ON-BOARD INSTRUMENTATION STUDIES.....	6-1
6.1	Introduction.....	6-1
6.2	Axial Acceleration Measurements.....	6-1
6.3	Lift Measurements.....	6-4
7.	REENTRY DATA ANALYSIS TECHNIQUES.....	7-1
7.1	Introduction.....	7-1
7.2	Single Point in Time Analysis of Off-Board Data.....	7-1
7.3	Multiple Point in Time Analysis of Off-Board Data....	7-2
7.4	Multiple Point in Time Analysis of Off-Board and On-Board Data.....	7-5
8.	REFERENCES.....	8-1
APPENDICES		
A	DESCRIPTION OF THE VEHICLE'S AERODYNAMIC COEFFICIENTS AND TRAJECTORIES.....	A-1
B	INFLUENCE COEFFICIENTS.....	B-1

TABLES

3.1	Summary of Reentry Error Categories, Significant Determining Parameters, and Applicable Figure Numbers . . . . .	3-73
3.2	Reentry Error Budget Summary. . . . .	3-79
5.1	Metric Tracker Performance Characteristics. . . . .	5-15

## ILLUSTRATIONS

Figure No.

3.1	Downrange Density Influence Coefficient, ( $W/C_D A = 1500$ PSF) . . . . .	3-4
3.2	Downrange Density Influence Coefficient, ( $W/C_D A = 2000$ PSF) . . . . .	3-5
3.3	Downrange Density Influence Coefficient, ( $W/C_D A = 3000$ PSF) . . . . .	3-6
3.4	Downrange Density Influence Coefficient, ( $W/C_D A = 4000$ PSF) . . . . .	3-7
3.5	Time Density Influence Coefficient, ( $W/C_D A = 1500$ PSF) . . . . .	3-8
3.6	Time Density Influence Coefficient, ( $W/C_D A = 2000$ PSF) . . . . .	3-9
3.7	Time Density Influence Coefficient, ( $W/C_D A = 3000$ PSF) . . . . .	3-10
3.8	Time Density Influence Coefficient, ( $W/C_D A = 4000$ PSF) . . . . .	3-11
3.9	Kwajalein Density Variations . . . . .	3-13
3.10	Downrange Impact Dispersions Due to Kwajalein Annual Density Variations. . . . .	3-14
3.11	Axial Trajectory Impact Dispersions Due to Kwajalein Annual Density Variations . . . . .	3-15
3.12	Downrange Impact Dispersions and Biases Due to Kwajalein Monthly Density Variations ( $W/C_D A = 2000$ PSF, $\gamma_{RE} = 20$ DEG) . . . . .	3-16

ILLUSTRATIONS (Continued)

<u>Figure No.</u>		
3.13	Downrange/Crossrange Wind Influence Coefficient, ( $W/C_D A = 1500$ PSF) . . . . .	3-19
3.14	Downrange/Crossrange Wind Influence Coefficient, ( $W/C_D A = 2000$ PSF) . . . . .	3-20
3.15	Downrange/Crossrange Wind Influence Coefficient, ( $W/C_D A = 3000$ PSF) . . . . .	3-21
3.16	Downrange/Crossrange Wind Influence Coefficient, ( $W/C_D A = 4000$ PSF) . . . . .	3-22
3.17	North - South Wind Variations for Kwajalein . . . . .	3-23
3.18	East - West Wind Variations for Kwajalein . . . . .	3-24
3.19	Downrange Impact Dispersions due to Kwajalein Annual Wind Variations. . . . .	3-25
3.20	Crossrange Impact Dispersions due to Kwajalein Annual Wind Variations. . . . .	3-26
3.21	Impact Dispersions Due to Kwajalein Annual Seasonal Wind Variations ( $W/C_D A = 2000$ PSF, $\gamma_{RE} = 20$ Deg) . . . . .	3-28
3.22	Impact Biases Due to Seasonal Wind Variations ( $W/C_D A = 2000$ PSF, $\gamma_{RE} = 20$ Deg). . . . .	3-29
3.23	Downrange Impact Dispersions Due to Ablation Uncertainties . . . . .	3-33
3.24	Axial Trajectory Dispersions At Impact Due to Ablation Uncertainties. . . . .	3-34

## ILLUSTRATIONS Continued)

<u>Figure No.</u>		
3.25	Ratio of Drag Coefficient Components to Total Drag Coefficient . . . . .	3-37
3.26	Weighted and Total Drag Coefficient Uncertainties . . . . .	3-39
3.27	Downrange Impact Dispersion Due to 2.5 Percent Drag Variation. . . . .	3-40
3.28	Axial Impact Dispersion Due to 2.5 Percent Drag Variation. . . . .	3-41
3.29	Uprange Impact Displacement Due to Angle-of-Attack Induced Drag Effects. . . . .	3-43
3.30	Downrange Impact Dispersions Due to Ballistic Coefficient Variations. . . . .	3-45
3.31	Trajectory Coordinate System. . . . .	3-46
3.32	Trajectory Displacements Due to Initial Angle-of-Attack . . . . .	3-49
3.33	Trajectory Displacements Due to Initial Angle-of-Attack . . . . .	3-50
3.34	Trajectory Displacements Due to Initial Angle-of-Attack . . . . .	3-51
3.35	Trajectory Displacements Due to Initial Angle-of-Attack . . . . .	3-52
3.36	Roll Resonance Altitude for Various Roll Rates . . . . .	3-59
3.37	Typical Angle-of-Attack and Windward Meridian History During Reentry . . . . .	3-61
3.38	Effect of Step Change in Trim Angle on Impact Displacement for Two RPS Spin Rate . . . . .	3-63

ILLUSTRATIONS (Continued)

<u>Figure No.</u>		
3.39	Trajectory Coordinate Comparison for Roll Trim Simulations . . . . .	3-65
3.40	Trajectory Coordinate Comparison for Roll Trim Simulations . . . . .	3-66
3.41	Trajectory Coordinate Comparison for Roll Trim Simulations . . . . .	3-67
3.42	Trajectory Coordinate Comparison for Roll Trim Simulations . . . . .	3-68
3.43	Trajectory Coordinate Comparison for Typical Flight Test . . . . .	3-70
3.44	Reentry Error Budget for Kwajalein Target Area . . . . .	3-80
3.45	Variation of Reentry CEP with Ballistic Coefficient and Trim Angle. . . . .	3-81
4.1	Impact Measurement Requirements for Reentry Contributors. . . . .	4-9
4.2	Deceleration Measurement Accuracy Requirements Per 100 Feet of Allowable Reentry CEP . . . . .	4-17
4.3	Density Measurement Accuracy Requirement Per 100 Feet of Allowable Reentry CEP and Current Capabilities. . . . .	4-19
4.4	Wind Measurement Accuracy Requirements Per 100 Feet of Allowable Reentry CEP and Current Capabilities. . . . .	4-21
4.5	Lateral Acceleration Measurement Requirements in Trajectory Coordinates Per 100 Feet of Allowable Reentry CEP . . . . .	4-27

## ILLUSTRATIONS (Continued)

Figure No.

4.6	Position Measurement Requirements for Lift Effects Per 100 Feet of Required Reentry CEP Accuracy . . . . .	4-31
5.1	Input/Output for RETAP and SMAP Programs . . . . .	5-6
5.2	KMR Primary Targets and Instrumentation Sites. . . . .	5-11
5.3	Effect of Reentry Angle on Range - Altitude Relationship . . . . .	5-12
5.4	Trajectory Position Uncertainties (XYZ) for Nominal Error Analysis . . . . .	5-21
5.5	Trajectory Position Uncertainties (Downrange and Crossrange) for Nominal Error Analysis . . . . .	5-22
5.6	Trajectory Velocity Uncertainties for Nominal Error Analysis . . . . .	5-24
5.7	Trajectory Deceleration Uncertainties for Nominal Error Analysis . . . . .	5-26
5.8	Trajectory Position Uncertainties Using Different RADOT Combinations . . . . .	5-28
5.9	Trajectory Deceleration Uncertainties Using Different RADOT Combinations . . . . .	5-29
5.10	Trajectory Position Uncertainties Using Different Radar and RADOT Combinations . . . . .	5-31
5.11	Trajectory Position Uncertainties Using TRADEX in Lieu of ALCOR. . . . .	5-32
5.12	Trajectory Position Uncertainties Using Shipboard Radar . . . . .	5-34
5.13	Trajectory Deceleration Uncertainties Using Doppler Measurement. . . . .	5-36

ILLUSTRATIONS (Continued)

<u>Figure No.</u>		
5.14	Effect of Relative Survey Accuracy on Position Accuracy . . . . .	5-38
5.15	Effect of High Altitude Lift on Position Accuracy . . . . .	5-39
5.16	Effect of Ballistic Coefficient and Reentry Angle on Position Accuracy . . . . .	5-41
5.17	Effect of Ballistic Coefficient and Reentry Angle on Deceleration Accuracy . . . . .	5-42
5.18	Effect of Target Location on Position Accuracy . . . . .	5-44
5.19	Effect of Target Location on Deceleration Accuracy . . . . .	5-45
6.1	Comparison of Drag Deceleration Measurement Requirements Per 100 Feet of Allowable CEP With Bell Aerospace Accelerometer. . . . .	6-5
6.2	Vehicle Fixed Lateral Acceleration Measurement Requirements Per 100 Feet of Allowable CEP . . . . .	6-9
6.3	Vehicle Orientation Measurement Requirements Per 100 Feet of Allowable CEP. . . . .	6-10
A.1	Ballistic Coefficient Histories. . . . .	A-2
A.2	Altitude Histories . . . . .	A-4
A.3	Velocity Histories . . . . .	A-5
A.4	Deceleration Histories . . . . .	A-6
A.5	Dynamic Pressure Histories . . . . .	A-7
A.6	Mach Number Histories. . . . .	A-8

NOMENCLATURE

<u>SYMBOL</u>	<u>DEFINITION</u>	<u>UNITS</u>
A	Characteristic reference area	ft <sup>2</sup>
A	Partial error matrix, $\frac{\partial f}{\partial X}$	
A <sub>D</sub>	Drag deceleration	ft/sec <sup>2</sup>
A <sub>i</sub>	Input acceleration	ft/sec <sup>2</sup>
A <sub>T</sub>	Lateral acceleration	ft/sec <sup>2</sup>
A <sub>X</sub> , A <sub>Y</sub> , A <sub>Z</sub>	Acceleration along trajectory X, Y, Z axes	ft/sec <sup>2</sup>
a <sub>x</sub> , a <sub>y</sub> , a <sub>z</sub>	Acceleration along vehicle x, y, z axes	ft/sec <sup>2</sup>
B	Partial error matrix, $\frac{\partial f}{\partial Z}$	
C <sub>L</sub>	Lift coefficient	
C <sub>m</sub>	Pitching moment coefficient	
C <sub>m<sub>α</sub></sub>	Moment coefficient derivative $\frac{\partial C_m}{\partial \alpha}$	1/degree
C <sub>m<sub>θ</sub></sub>	Pitch damping coefficient	sec
C <sub>N</sub>	Normal force coefficient	
C <sub>N<sub>α</sub></sub>	Normal force coefficient derivative, $\frac{\partial C_N}{\partial \alpha}$	1/degree
CEP	Circular error probability	ft

NOMENCLATURE (Continued)

<u>SYMBOL</u>	<u>DEFINITION</u>	<u>UNITS</u>
d	Vehicle diameter	ft
$f_N$	Natural pitching frequency	1/second
g	Gravitational constant	ft/sec <sup>2</sup>
H, h	Altitude	ft
$H_m$	Maximum measurement altitude	ft
$I'$	$\frac{I_y}{qAd}$	sec <sup>2</sup>
$I_{DR}^W, I_{CR}^W$	Downrange and crossrange wind influence coefficients	ft/fps/ft
$I_T^W$	Time wind influence coefficient	sec/fps/ft
$I_{DR}^\beta$	Downrange ballistic coefficient influence coefficient	ft%/ft
$I_T^\beta$	Time ballistic coefficient influence coefficient	sec%/ft
$I_{DR}^\rho$	Downrange density influence coefficient	ft%/ft
$I_T^\rho$	Time density influence coefficient	sec%/ft
$I_x, I_y, I_z$	Moments of inertia about vehicle x, y, z axes	slug-ft <sup>2</sup>
$K_0, K_1, K_2, K_3$	Accelerometer error coefficients	
M	Covariance of random noise $[E\{nn^T}]$	
$M_\infty$	Mach number	

## NOMENCLATURE (Continued)

<u>SYMBOL</u>	<u>DEFINITION</u>	<u>UNITS</u>
m	Vehicle mass	slugs
m'	$\frac{mv}{qA}$	sec
n	Vector of unbiased random noise	
p	Vehicle roll rate	1/sec, deg/sec
q	Dynamic pressure	lbs/ft <sup>2</sup>
R	Trajectory displacement at impact	ft
R (h, $\hat{h}$ )	Correlation coefficient between altitudes h and $\hat{h}$	
U, V, W	Trajectory coordinate system (up, down, cross)	
v	Vehicle velocity	ft/sec
W	Vehicle weight	lbs
W	Measurement weighting factor	
W <sup>-1</sup>	Covariance of noise	
X	Vehicle state vector	
X, Y, Z	Trajectory coordinate system	
x, y, z	Vehicle fixed coordinate system	
Y	Vector of sensor measurements	
Z	Vector of systematic errors	
$\alpha$	Angle-of-attack	deg
$\beta$	Ballistic coefficient, $W/C_D A$	lbs/ft <sup>2</sup>

## NOMENCLATURE (Continued)

<u>SYMBOL</u>	<u>DEFINITION</u>	<u>UNITS</u>
$\gamma$	Reentry angle	deg
$\theta$	Vehicle relative orientation	deg
$\theta_c$	Vehicle half coning angle	deg
$\rho$	Density	slug/ft <sup>3</sup>
$\Sigma$	Covariance	
$\sigma$	Standard deviation	
$\omega_0$	Vehicle's basic oscillation frequency	1/sec
$\Delta\omega$	Component of total pitch frequency resulting from roll	1/sec

Subscripts And Superscripts

Acc	Accuracy
A	Actual
a	Ablated
C	Contributors
$C_D$	Drag coefficient
CR	Crossrange
DR	Downrange
EW	East - West
e	Estimated
F	Final

## NOMENCLATURE (Continued)

<u>SYMBOL</u>	<u>DEFINITION</u>
I	Instantaneous
L	Lift
m	Mass
m	Measurement
NS	North - South
o	Initial
pos	Position
pp	Pierce point
RE	Reentry condition
Res	Resonance
S	Ballistic simulation
sc	Scoring
T	Total
u	Unaccountable
w	Wind
X	Contribution to impact miss
$\beta$	Ballistic coefficient
$\rho$	Density
%	Percent error

## 1.0 INTRODUCTION

### 1.1 BACKGROUND

The weapon system accuracy of a ballistic missile system depends on the accuracy of (1) geodetic and geophysical (G&G) targeting constants, (2) the guidance and control (G&C) system, (3) the RV separation system, and (4) RV reentry dispersions. Historically, the most significant constraints to accuracy improvements have been G&G and G&C errors, while RV separation system errors and reentry dispersions have not been significant in comparison. The emphasis was therefore logically devoted to improvements in earth surveys and gravity models, and development of more accurate guidance systems, resulting in continued weapon system accuracy improvements. The recently developed Advance Inertial Reference Sphere (AIRS), if implemented as a guidance system, for example, is expected to significantly improve the G&C accuracy. If present forecasts of this accuracy are realized, it will be necessary to improve the RV accuracy in order to obtain an acceptable ratio of RV to guidance system contribution to total miss. Obviously, further improvements in weapon system accuracy must include increased emphasis on the reentry system and the endoatmospheric reentry dispersions.

Many study programs aimed at improved RV performance (not all are accuracy oriented) are currently in existence. Those concentrating on a better understanding and reduction of reentry dispersions include remote weather forecasting (RWF), nosetip material testing, ablation-shape change correlations, and studies of RV dynamic behavior including the roll trim phenomenon associated with small high ballistic coefficient vehicles. Based on successful completion of these technology studies it is anticipated that it will be possible to develop a significantly more accurate reentry system. Development and verification of a high accuracy reentry system will require a test program with stringent range instrumentation accuracy requirements to adequately measure and isolate

the various contributors to reentry dispersions. To adequately quantify the sensor measurement requirements it is necessary to enumerate and quantify the expected dispersion mechanisms for a reentry vehicle designed to meet high accuracy objectives. The analytic techniques necessary to model RV dispersion mechanisms and to specify the measurement requirements in terms of typical sensor system specifications have been developed. It only remains to apply these techniques to determine the instrumentation requirements and the extent to which current and future capabilities meet these requirements.

## 1.2 STUDY OBJECTIVE

Developing an RV error budget and error model, and from this developing measurement requirements, is the primary task of this study. Specifically, the objective of this report is to determine the flight test measurement requirements necessary for the evaluation of an ABRES reentry vehicle designed to meet improved accuracy objectives. This includes the following areas of study:

1. Determination of the contributors to reentry dispersion for an RV designed to meet high accuracy objectives;
2. Identification of the means of accurately measuring the dispersion mechanisms;
3. Identification of the major sources of measurement error and their effect on accurately isolating dispersion mechanisms.

The class of reentry vehicles considered was restricted to ballistic, spin stabilized, medium to high ballistic coefficient configurations ( $W/C_D A = 1500$  to  $4000$  psf) designed for use at reentry angles of 15 to 40 degrees.

Results of the study should enable optimization of the following requirements:

- Trajectory - sensor requirements
- On-board sensor requirements
- Sensor calibration requirements
- Required modification to current metric tracking sensors
- Multiple sensor data processing requirements

The Kwajalein target area complex was used as an instrumentation configuration baseline to provide a guideline in modeling sensor accuracy performance.

### 1.3 STUDY ORGANIZATION

Section 2 contains a summary of the study and the major conclusions. A reentry error budget including climatology, ballistic coefficient and lift induced dispersions is developed in Section 3. This budget and the relationship between parameter uncertainties and impact dispersions provided the basis for the flight test measurement requirements established in Section 4.

Section 5 examines the current and predicted capabilities of off-board metric sensors to meet the measurement requirements. This includes studies to determine the accuracy associated with different sensor combinations, target areas, and reentry angles. Section 6 develops on-board instrumentation measurement requirements based on Section 3 studies and reviews different on-board instrumentation systems that might be used to achieve these measurement requirements.

Section 7 reviews the data processing techniques currently used for analyzing metric tracking and on-board data. Potential improvements in post-flight evaluation techniques are recommended.

## 2.0 SUMMARY

This section summarizes the major findings and conclusions of the study. The analysis was conducted in two parts: (1) reentry error budget study, and (2) a reentry error measurement study.

### 2.1 REENTRY ERROR BUDGET STUDY

Reentry dispersion contributors are classically grouped into three major classifications as shown below:

#### 1. Climatology

- Density
- Winds

#### 2. Ballistic Coefficient

- Mass loss
- Drag coefficient (zero angle-of-attack)
- Drag coefficient (angle-of-attack induced)

#### 3. Lift

- Initial angle-of-attack
- Roll resonance (high and low altitude)
- Boundary layer transition
- Roll Trim

Estimates were made of the impact dispersions resulting from variations of the above contributors over a range of ballistic coefficients (1500 psf to 4000 psf) and reentry angles (15 degrees to 40 degrees).

#### 2.1.1 Climatology

Climatology dispersions result from variations of winds and density about some mean value. Of the two effects, winds is the larger and affects both downrange and crossrange dispersions, but induces a negligible effect along the trajectory. These characteristics makes it possible to decouple wind effects from deceleration but not from lift.

Wind variations were found to have a negligible effect on the trajectory above 90 KFT, with the greatest effect between 10 KFT and 30 KFT.

Density variations affect only the deceleration of the vehicle along the trajectory resulting primarily in time-of-flight dispersions. Some second order effects do occur in the downrange direction due to trajectory bending caused by differences in the velocity profile. Little downrange effect was found above 100 KFT, although displacements along the trajectory are experienced at higher altitudes. The trajectory is most sensitive to density variations between 20 KFT and 50 KFT altitude.

### 2.1.2 Ballistic Coefficient

Ballistic coefficient variations throughout reentry cause effects which are similar to density effects, appearing primarily as a time-of-flight dispersion with second order effects in the downrange direction. Of the three ballistic coefficient dispersion contributors, the flight-to-flight mass loss variation has the smallest effect. It occurs below 100 KFT where significant heating can occur. It should be noted that only clear weather ablation was considered. The erosion caused by hydrometer impact on a RV experiencing bad weather offers a potential for a significantly increased miss. However, these effects are difficult to quantify even when a specific RV is under consideration.

Drag coefficient effects are the largest ballistic coefficient contributor, resulting from both the 2.5 to 3.0 percent flight-to-flight variation in the zero angle-of-attack component and uncertainties in the vehicle's angle-of-attack induced drag. While the zero angle-of-attack component has a negligible effect on downrange dispersion above 100 KFT to 120 KFT, the angle-of-attack component could conceivably have effects at higher altitude if the angle-of-attack becomes large. Efforts should obviously be made to keep the initial reentry angle-of-attack as low as possible.

### 2.1.3 Lift

Lift induced dispersions are potentially the largest of the reentry errors, resulting in flight-to-flight variations of the trajectory about its otherwise ballistic trajectory. The cause of all these dispersions can be attributed to the angle-of-attack induced lift on the vehicle. However, the mechanisms inducing the angle-of-attack divergence can be categorized into four distinctly different classes. The initial angle-of-attack is introduced at deployment by separation and spin system asymmetries and deployment tipoff rates. Effects of initial angle-of-attack become noticeable below 240 KFT as lateral trajectory displacements. Roll resonance effects occur whenever the vehicle's natural pitching frequency approaches the roll rate. The magnitude of the dispersion is dependent on the dynamic pressure, and hence the altitude at which it occurs. Although this phenomenon can occur twice during reentry, it is assumed that low altitude roll resonance will be avoided in the design of a minimum dispersion reentry vehicle. Asymmetric boundary layer transition along the surface of the vehicle is the third mechanism producing angle-of-attack divergence. This causes asymmetric lift on the vehicle resulting in slight to moderate reentry dispersions. The final lift contributor, and the one commanding the most attention in reentry vehicle design today, is roll trim resulting from asymmetric nosetip ablation. These effects can occur at altitudes from 70 KFT or 80 KFT down to impact, becoming most sensitive to trim angle changes in the 40 KFT altitude region. The analysis performed in this report indicates that trim angles must be limited to less than 0.2 degree if reentry vehicle dispersions are to be minimized.

### 2.1.4 Total Reentry Accuracy

The intent of the reentry error budget study of Chapter 3 was to identify the potential dispersion mechanisms and their relevant altitude regions and magnitudes for the purpose of selecting measurement requirements in subsequent sections. However, when the results are combined, it also

provides reasonable lower limits of ballistic coefficient and reentry angle for a high accuracy reentry vehicle. The results given on Table 3.2 are for a Kwajalein target area and indicate that ballistic coefficients of at least 2000 psf and minimum reentry angles of 20 to 25 degrees are necessary since accuracies below these levels degrade very quickly. Hence, the remainder of the study used 2000 psf and 20 degrees as lower limits for these parameters. Figure 3.44 graphically compares the various reentry errors using these constraints.

## 2.2 REENTRY ERROR MEASUREMENT STUDY

The measurement portion of the study sets forth general flight test measurement requirements and reviews the ability of off-board and on-board instrumentation to achieve these criteria. The parameters that must be measured include (1) total reentry miss, (2) climatology effects on dispersion, (3) vehicle deceleration along the trajectory, and (4) vehicle lift effects.

In developing the measurement requirements, the following criteria were used: (1) each reentry error contributor should be evaluated to an accuracy sufficient to verify the reentry system CEP; (2) measurements throughout reentry must be made to an accuracy sufficient to maintain an adequate identification of the cause of error to the desired fraction of the allocated CEP; and (3) flight test measurements must verify the reentry accuracy at the lowest reentry angle intended for the vehicle even though flight testing may be performed at higher angles.

In establishing the measurement accuracy criteria, it was necessary to specify the correlation between measurement errors at different altitudes. These correlations indicate the degree to which measurement errors at one altitude are correlated with errors at any other altitude. No correlation implies that only uncorrelated, random measurement noise exists at each altitude. At the other extreme, perfect correlation implies that a measurement error at one altitude is completely

correlated with that at another. This would result from a constant measurement bias or systematic error. The particular choice of a correlation coefficient results in significantly different measurement constraints. However, correlation coefficients are not readily available for the various types of reentry measurement instrumentation. This study therefore, made the pessimistic assumption that perfect correlation exists between instrument errors throughout reentry. Although this is admittedly conservative, it is believed to be more representative of actual instrumentation errors than an assumption of no correlation. Due to the general nature of this study, no attempt was made to determine more precise values for the correlation. However, this resulted in measurement accuracy criteria which are probably overly stringent and could probably be relaxed for most instruments. Further study is strongly recommended in this area.

#### 2.2.1 Total Reentry Miss

The total reentry miss can be computed only if measurements are made of the reentry pierce point and impact location. Pierce point measurements must include the vehicle's position and velocity at a point along the trajectory prior to the onset of reentry effects. The lowest possible pierce point altitude is generally 200 KFT to 300 KFT and is limited by lift effects. It was found that total reentry miss measurement accuracies of ten to fifteen feet should be achieved for accurate verification of the total reentry performance per 100 feet of reentry CEP.

Measurement of the vehicle's pierce point can be accomplished through either radar or optical metric measurements of the trajectory. An extensive analysis was performed to determine the capability of the Kwajalein terminal complex to make such measurements. Both current and future metric sensor error models as provided by the range were used. The analysis was performed using an error analysis technique that

correlates successive points in time through the equations of motion. This method offers a significant improvement over the point-by-point technique frequently used.

The error analysis considered the combined effect of various combinations of the following sensors: ALCOR, TRADEX, MPS-36, RADOT, ballistic camera and an instrumentation ship. It was found that current and predicted high altitude position measurement capabilities do not achieve the required accuracies. Downrange and crossrange accuracies at pierce point (300 KFT) of about thirty feet are achievable under optimal tracking conditions. The effect of changes or additions in several sensors was also considered. It was found that position measurement accuracies are significantly affected by the inclusion of optical sensors, high altitude lift, reentry angle and target location. Other parameters, including survey uncertainty and ballistic coefficient were found to have a negligible effect.

Scoring accuracies under five feet are currently achievable and are considered satisfactory for the analysis of reentry vehicle performance. Hence, measurements of the total reentry system miss are limited only by pierce point accuracies.

### 2.2.2 Climatology

Wind and density measurements are necessary not only to determine the climatology reentry error, but also to decorrelate the observed deceleration into ballistic coefficient and density contributions and to decorrelate lateral position errors into wind and lift effects. Wind measurements should be made to an altitude of 90 KFT, with measurement accuracies of one to four feet per second in the 10 KFT to 40 KFT region, depending upon the ballistic coefficient and reentry angle. Density measurements should be made to much higher altitudes - up to 180 KFT - since significant angle-of-attack induced drag variations can be experienced at these altitudes. The required accuracy of density measurements reaches a

maximum at 40 KFT, corresponding with the region of highest sensitivity to deceleration variations. These measurements should be made near the time of reentry and in close proximity of the trajectory.

Climatology measurements are typically achieved using Rawinsonde and Rocketsonde measurements although other methods are available, particularly for wind. A review of the accuracy specifications for these instruments shows that under the perfectly correlated error assumption, winds cannot be measured to the required accuracy and density measurement accuracies meet the measurement requirements only for high ballistic coefficient vehicles at steep reentry angles. Multiple measurements or improved instrument accuracies should therefore be considered.

### 2.2.3 Drag Deceleration

Measurement of the drag deceleration enables ballistic coefficient and density effects to be decorrelated if the density profile is known. These measurements should be performed to the altitude of roll resonance - up to 180 KFT - since angle-of-attack induced drag effects along the trajectory can occur below this altitude. The accuracy measurement requirements are identical to density.

Drag deceleration can be derived using either off-board or on-board measurements. The use of on-board instruments is, of course, the most direct approach and instruments with sufficient accuracy to meet the requirements do exist. The use of off-board measurements, however, is not direct, but rather infers the deceleration by deriving a deceleration history that results in a best fit to the metric position data. It was found that exclusive use of metric off-board data results in sufficiently accurate decelerations for reentry angles exceeding 30 degrees, but only marginal accuracy for shallower reentry angles. Doppler measurements can provide some increase in accuracy below 50 KFT. It is recommended that axial accelerometers be used for making drag measurements.

Ablation and angle-of-attack measurements are required to altitudes of approximately 100 KFT and 180 KFT if the ballistic coefficient is to be separated into its component parts. These can be accomplished through on-board measurements.

#### 2.2.4 Lift

The derivation of lift effects can be accomplished by either off-board metric measurements of the vehicle's lateral displacement from its otherwise ballistic trajectory or on-board measurements of the vehicle's lateral acceleration history. External metric data provide direct measurements of lift effects, and the use of on-board instrumentation directly measures the source of the displacement effects, i.e., angle-of-attack induced lift acceleration.

Metric lateral position measurement accuracies of ten to fifteen feet are required between 50 KFT and 240 KFT, where lift effects tend to dominate the lateral displacements. Below 50 KFT, the accuracy requirement becomes more stringent as wind dispersions become more significant. The metric tracker analysis indicated that these accuracies are currently achievable only below 120 KFT. Hence, high altitude lift effects cannot be adequately measured with off-board measurements above this altitude.

On-board measurements require body-fixed lateral accelerations and vehicle orientations relative to earth fixed coordinates. The accuracies of these measurements are exceedingly stringent at high altitudes, decreasing as the vehicle reenters. The orientation measurement requirement is the most difficult to achieve and would require an inertial platform.

If the vehicle's initial angle-of-attack can be either accurately measured or kept below a few degrees, upper altitude lift effects would be reduced to an insignificant level, and the measurement requirements for evaluating lift effects could be reduced to that altitude region where roll resonance is expected to occur. This would affect both metric and on-board instrumentation accuracy requirements.

### 2.2.5 Data Analysis Techniques

Numerous techniques are currently in existence for processing post-flight data. It is strongly recommended that a minimum variance, multiple point-in-time method be used that correlates the data through the equations of motion rather than using a polynomial smoothing technique. The use of a program that simultaneously regresses on both off-board and on-board data should be considered, although further study of this approach is recommended.

### 3.0 REENTRY ERROR BUDGET

#### 3.1 INTRODUCTION

This section of the study addresses the development of a reentry error budget used subsequently for selecting sensor measurement requirements. The analysis is directed at: (1) identification of the potential dispersion mechanisms, (2) definition of the altitude region where each error source exhibits significant dispersion, and (3) quantification of the error magnitude where possible. Since reentry dispersions are dependent upon both ballistic coefficient and reentry angle, a parametric study was performed for ballistic coefficients ranging from 1500 to 4000 psf, and reentry angles ranging from 15 to 40 degrees.

The reentry dispersion producing mechanisms can be categorized into three major classifications:

- Climatology effects
- Ballistic coefficient errors
- Lift effects

The dispersions resulting from flight-to-flight variations in each of the error mechanisms were estimated. These dispersions were determined in three principle directions: (1) downrange in the plane of the trajectory, (2) crossrange to the trajectory plane, and (3) axially along the trajectory in the direction of the velocity vector. Downrange and crossrange dispersions have an obvious effect on impact accuracy while all three dispersions affect the accuracy of a vehicle targeted to intercept an airborne point. It is stressed, however, that the results of this section are intended for use in selecting reentry measurement requirements and not operational RV design criteria. The dispersions which would be used in an RV design oriented study would tend to be larger due to more severe climatology variations (i.e. Soviet verses Kwajalein) and larger mass property uncertainties. Kwajalein climatology was used

because it is the most likely test area for full scale reentry testing of a high accuracy RV.

### 3.2 CLIMATOLOGY DISPERSIONS

Climatology induced trajectory dispersions result from differences between targeted and test day atmospheric density and winds. These differences affect the position of the RV both along its intended trajectory, and downrange and crossrange of the nominal trajectory. The actual dispersion for a given flight requires knowledge of the test day and targeted climatologies. However, it is possible to bound the expected magnitude of the climatology induced reentry error prior to the flight by examining wind and density statistics based on data acquired at the target area over a period of years. Two types of statistical parameters were examined for this purpose: (1) mean climatology profiles, and (2) variation of the data about this mean. The statistics are based on monthly and seasonal data acquired in the Kwajalein area over several years.

Analysis of the mean profiles is useful since it indicates the expected bias between the mean climatology profile for the particular time of year chosen for the test and the targeted profile used for the particular mission. This bias can of course be eliminated by targeting with seasonal or monthly climatology. Random variations about the mean are the most significant statistic since they indicate the portion of the reentry error which cannot be eliminated in targeting.

#### 3.2.1 Density

Free-stream density variations directly affect the dynamic pressure experienced by a reentry vehicle, causing position errors both along the trajectory and in the downrange direction. A higher than targeted density profile, for example, would result in a late RV arrival at impact, and an uprange, or foreshortened impact. Furthermore, unknown

density variations directly affect the ability to derive the correct ballistic coefficient from flight test deceleration data. The density profile is therefore one of the more important reentry parameters.

Influence Coefficients: Effects of the mean climatology profiles and random variations on the trajectory at impact were determined through the use of density influence coefficients, a convenient method of propagating altitude dependent variations to any desired time or altitude. The downrange miss influence coefficient,  $I_{DR}^P$ , specifies the uprange/downrange position displacement at impact due to a variation in density over a one foot altitude interval. Instead of using the absolute value of density, the variation is measured in terms of the percentage variation from the mean or targeted density. Hence, the units are feet downrange/percent density variation/foot altitude. These coefficients are presented on Figures 3.1 through 3.4 for the ballistic coefficients and reentry angles of interest.

The time miss influence coefficient,  $I_T^P$ , is similar to the downrange coefficient but specifies the time displacement from nominal along the trajectory at impact as a result of a perturbing influence. The units are seconds/percent density variation/foot altitude. These coefficients are presented in Figures 3.5 through 3.8, and may be converted to axial trajectory miss influence coefficients at impact by multiplying  $I_T^P$  by the impact velocity. Axial trajectory dispersions are of particular importance in arming and fuzing systems.

The influence coefficients of Figures 3.1 through 3.8 show that for a given density variation profile the impact dispersion increases with decreasing ballistic coefficient and reentry angle. Furthermore, the sensitivities tend to be relatively small above 100 KFT, becoming most sensitive to density variations between 20 KFT and 50 KFT. The numerical techniques used to determine the effect of biases on the mean density profile and dispersions about this mean are presented in Appendix B.

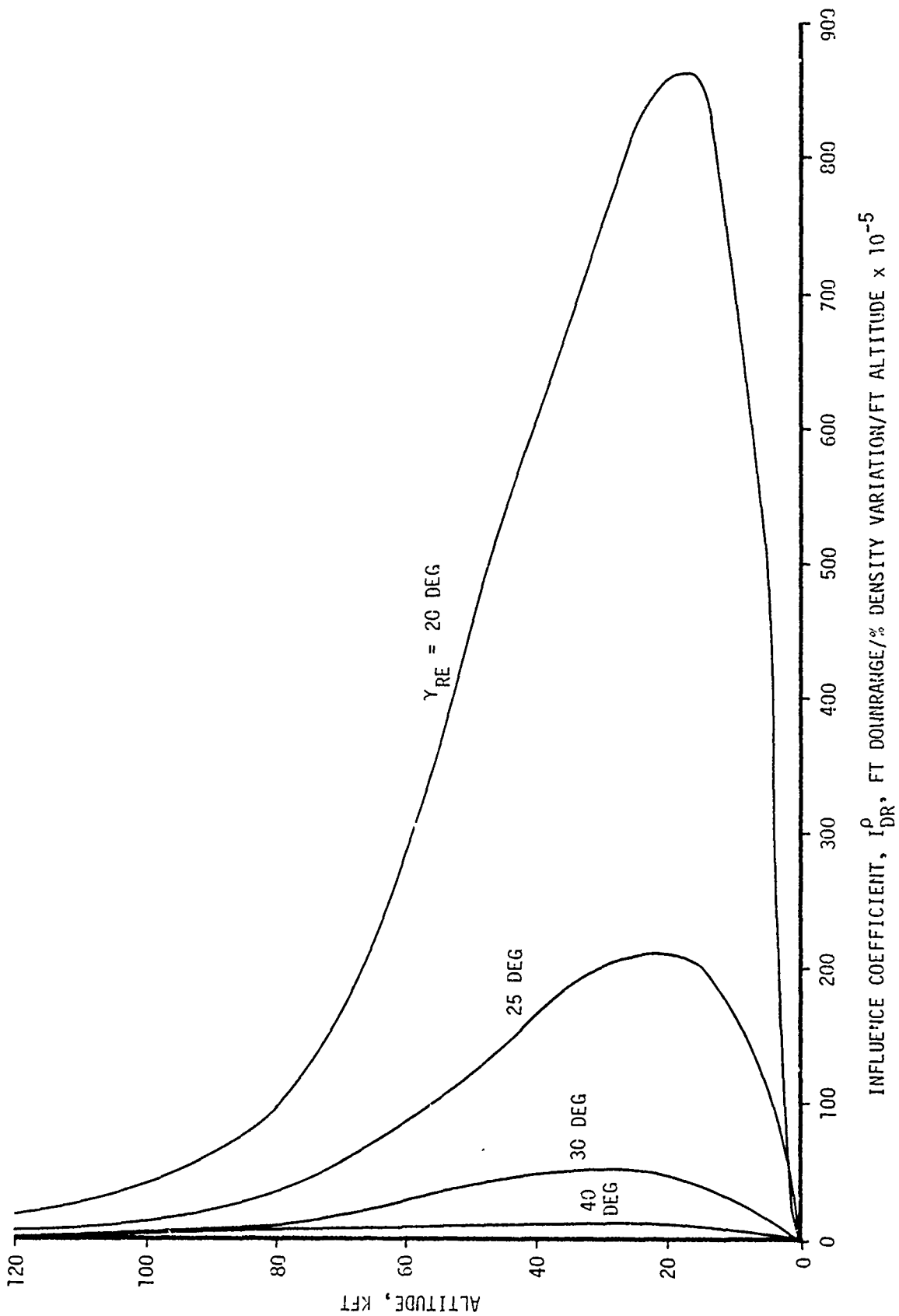


Figure 3.1 Downrange Density Influence Coefficient, ( $W/C_D A = 1500 \text{ PSF}$ )

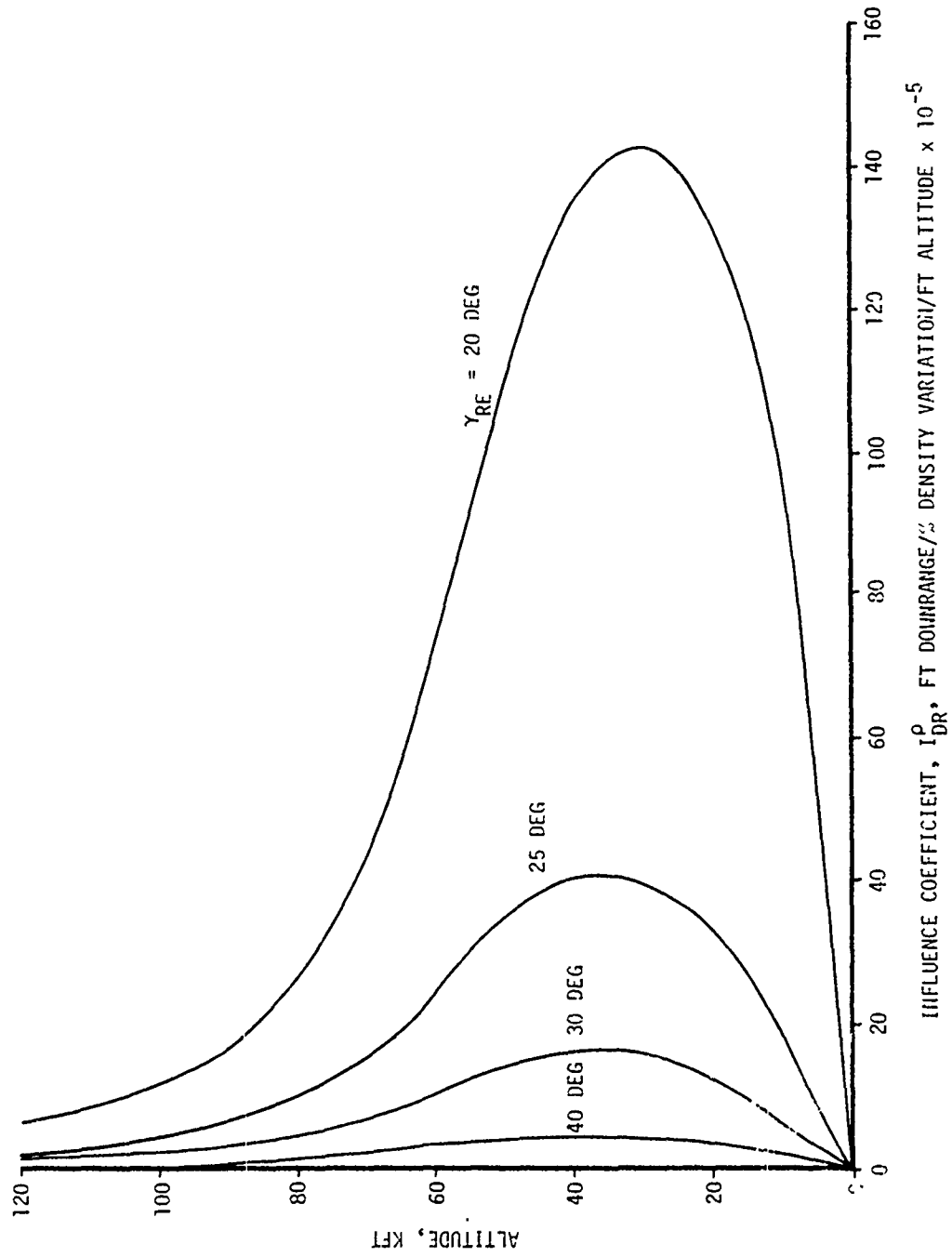


Figure 3.2 Downrange Density Influence Coefficient, ( $W/C_D A = 2000 \text{ PSF}$ )

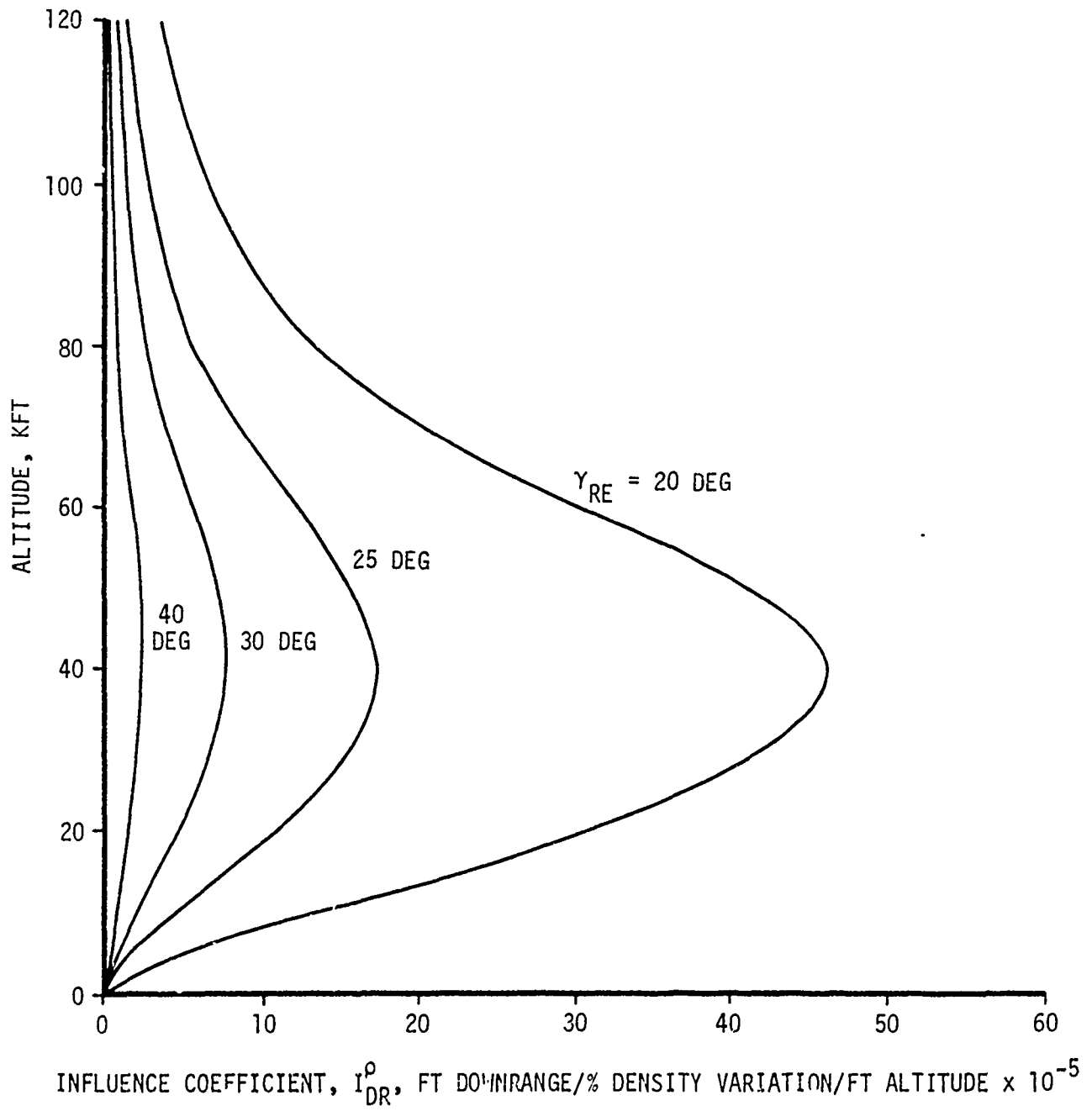


Figure 3.3 Downrange Density Influence Coefficient, ( $W/C_D A = 3000$  PSF)

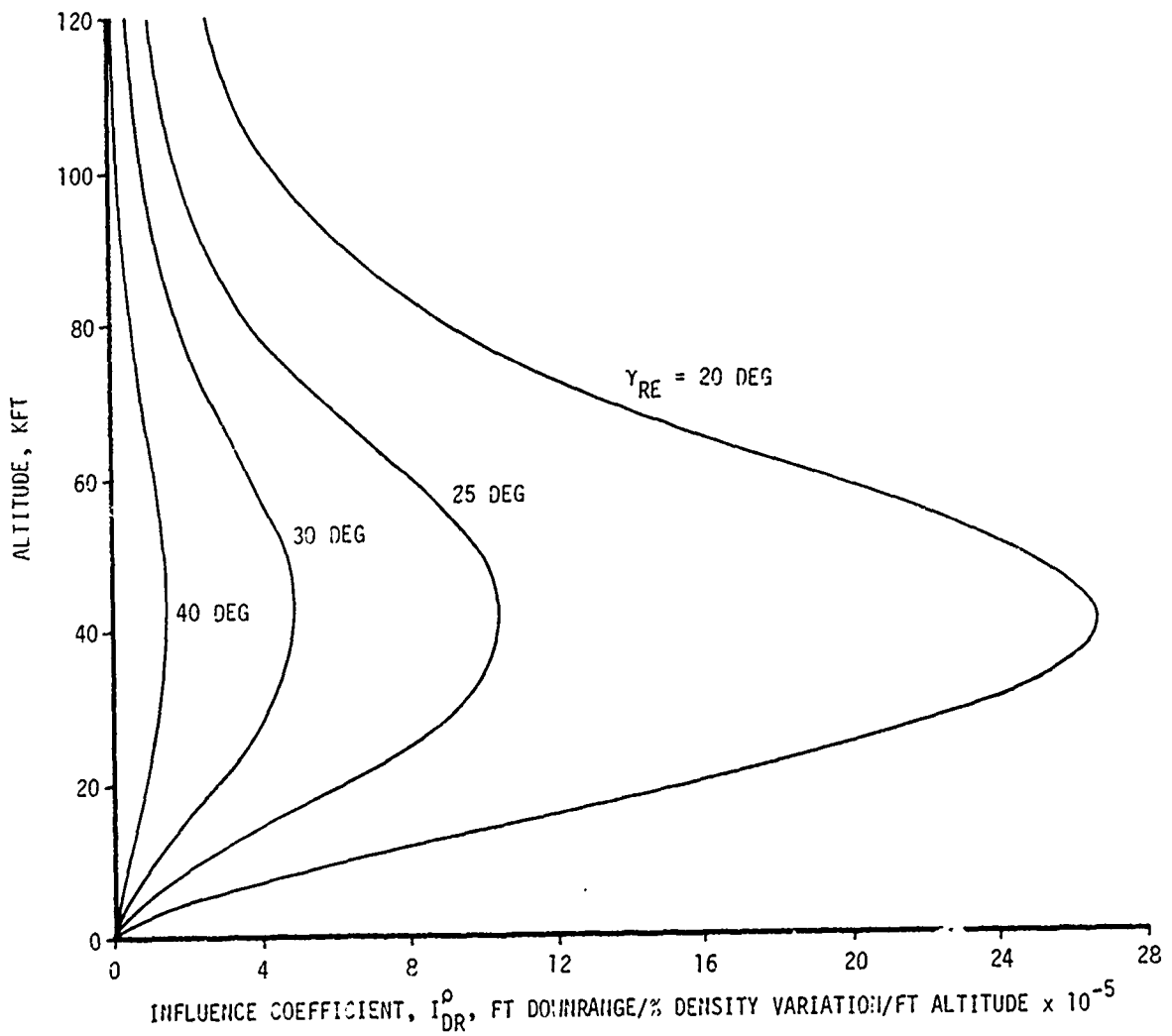


Figure 3.4 Downrange Density Influence Coefficient, ( $W/C_D A = 4000 \text{ PSF}$ )

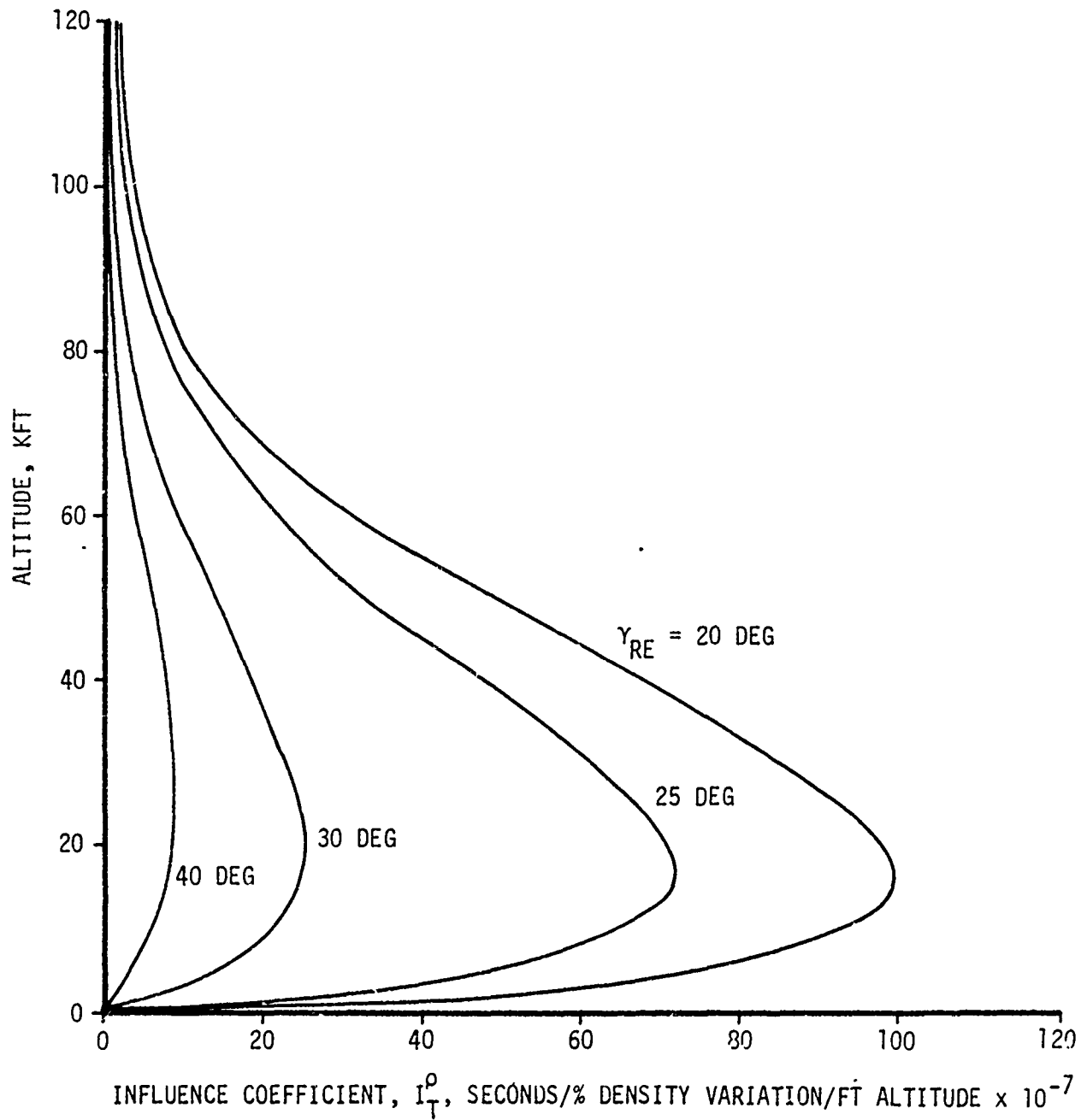


Figure 3.5 Time Density Influence Coefficient, ( $W/C_D A = 1500$  PSF)

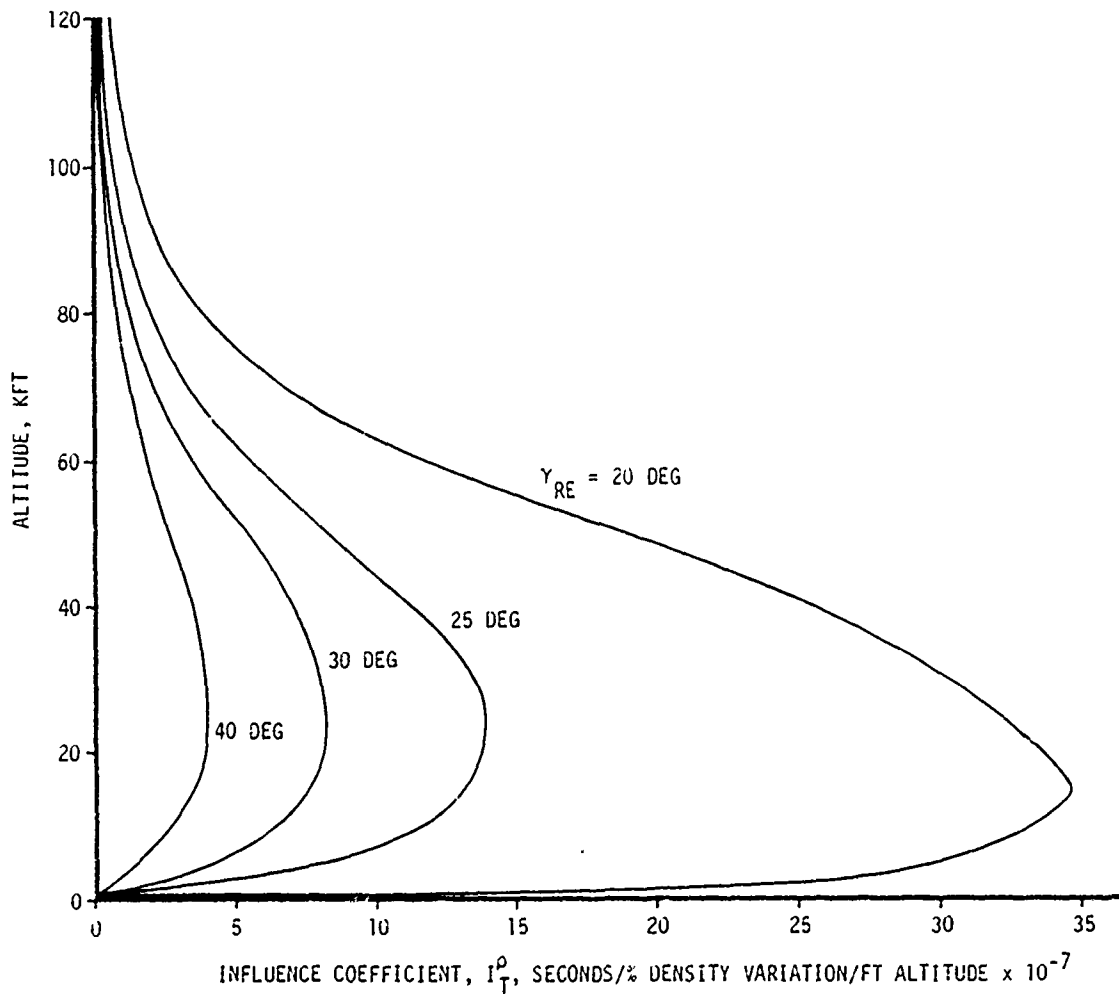


Figure 3.6 Time Density Influence Coefficient, ( $W/C_D A = 2000 \text{ PSF}$ )

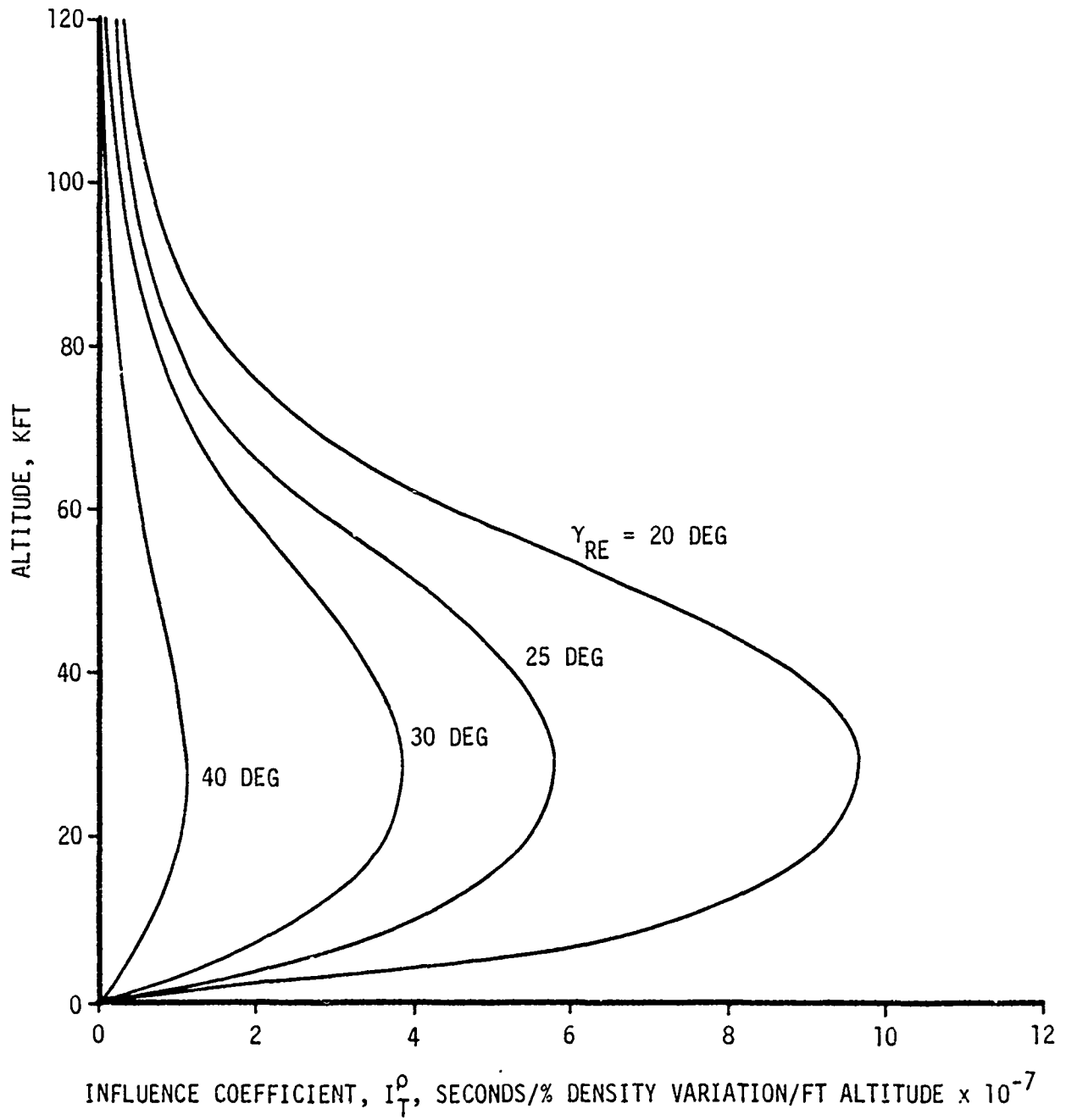


Figure 3.7 Time Density Influence Coefficient, ( $W/C_D A = 3000$  PSF)

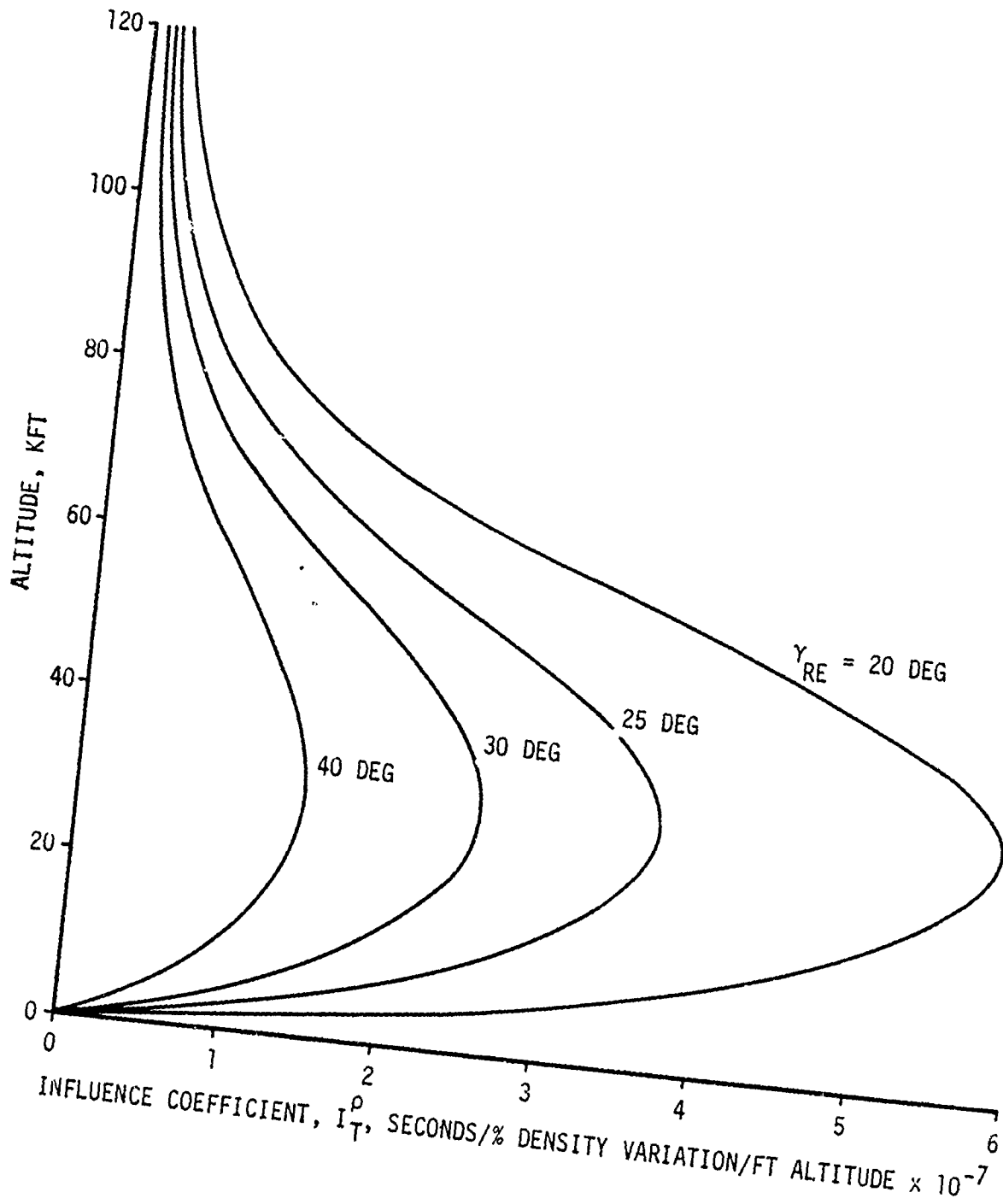


Figure 3.8 Time Density Influence Coefficient, ( $W/C_D A = 4000$  PSF)

Random Density Dispersions: Density variations in the Kwajalein area have been extensively examined in the USAF ETAC studies of References 1 and 2. Statistical data, including means, dispersions, and correlation coefficients, are presented for each month, season, and on an annual basis. Low altitude data (0 to 120 KFT) are based on Rawinsonde readings while high altitude data (120 to 210 KFT) are based on Rocketsonde readings. Figure 3.9 compares the density variations in percent of the mean density as a function of altitude for the annual data with two monthly based variations. Density variations above 210 KFT were assumed constant at 5%, however, variations above 210 KFT have an insignificant effect on reentry dispersions.

The effect of annual density variations on the RV trajectory at impact is presented on Figures 3.10 and 3.11 for downrange and axial trajectory dispersions respectively. The results show the sensitivity of the impact dispersions to the ballistic coefficient and reentry angle, and indicate the importance of climatology on impact dispersions. Since these data are based on Kwajalein rather than Soviet climatology they are not applicable to operational RV design studies. USSR targets experience far more severe density variations, which can result in dispersions over five times as large as those for Kwajalein.

Monthly variations were also computed to determine the month-to-month differences in downrange impact dispersions. Computations were made for the 2000 ballistic coefficient vehicle at a 20 degree reentry angle to accentuate the dispersions. The results are presented on Figure 3.12 and indicate that although more severe density variations do occur in the winter months, the difference in these variations is small and differs no more than six feet from the annual variation. Larger ballistic coefficient vehicles or steeper reentry angles would result in even smaller differences.

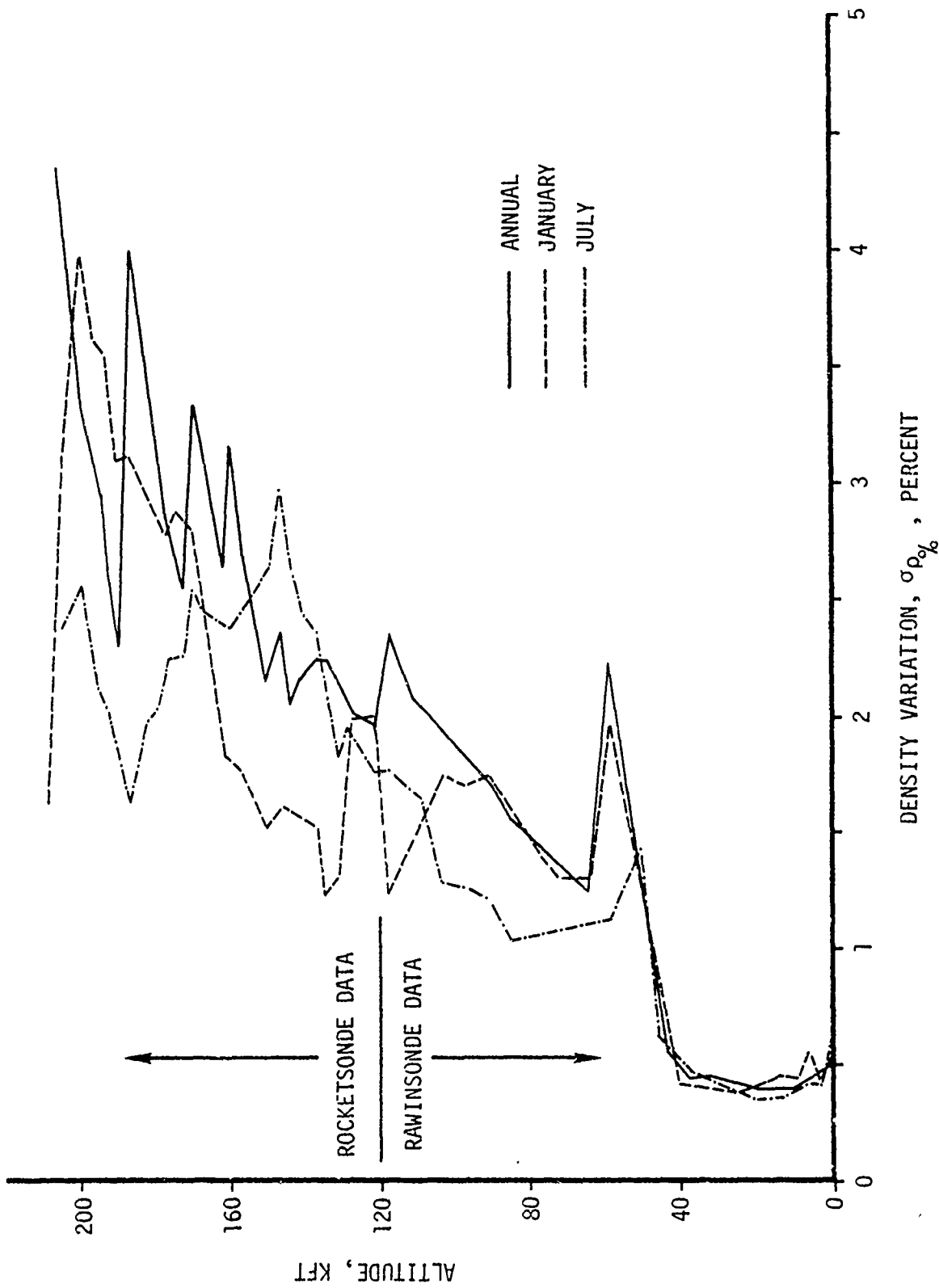


Figure 3.9 Kwajalein Density Variations

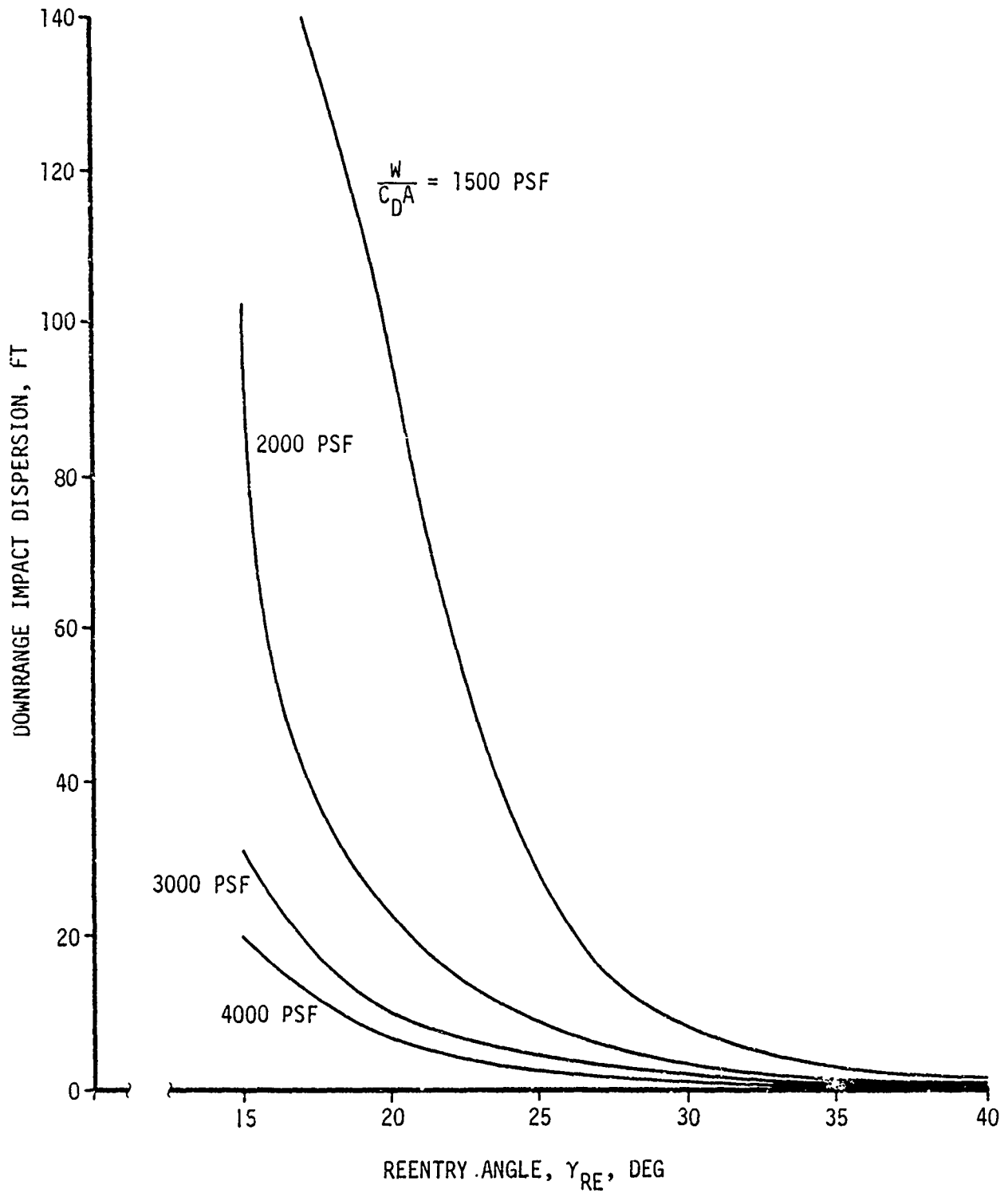


Figure 3.10 Downrange Impact Dispersions Due to Kwajalein Annual Density Variations

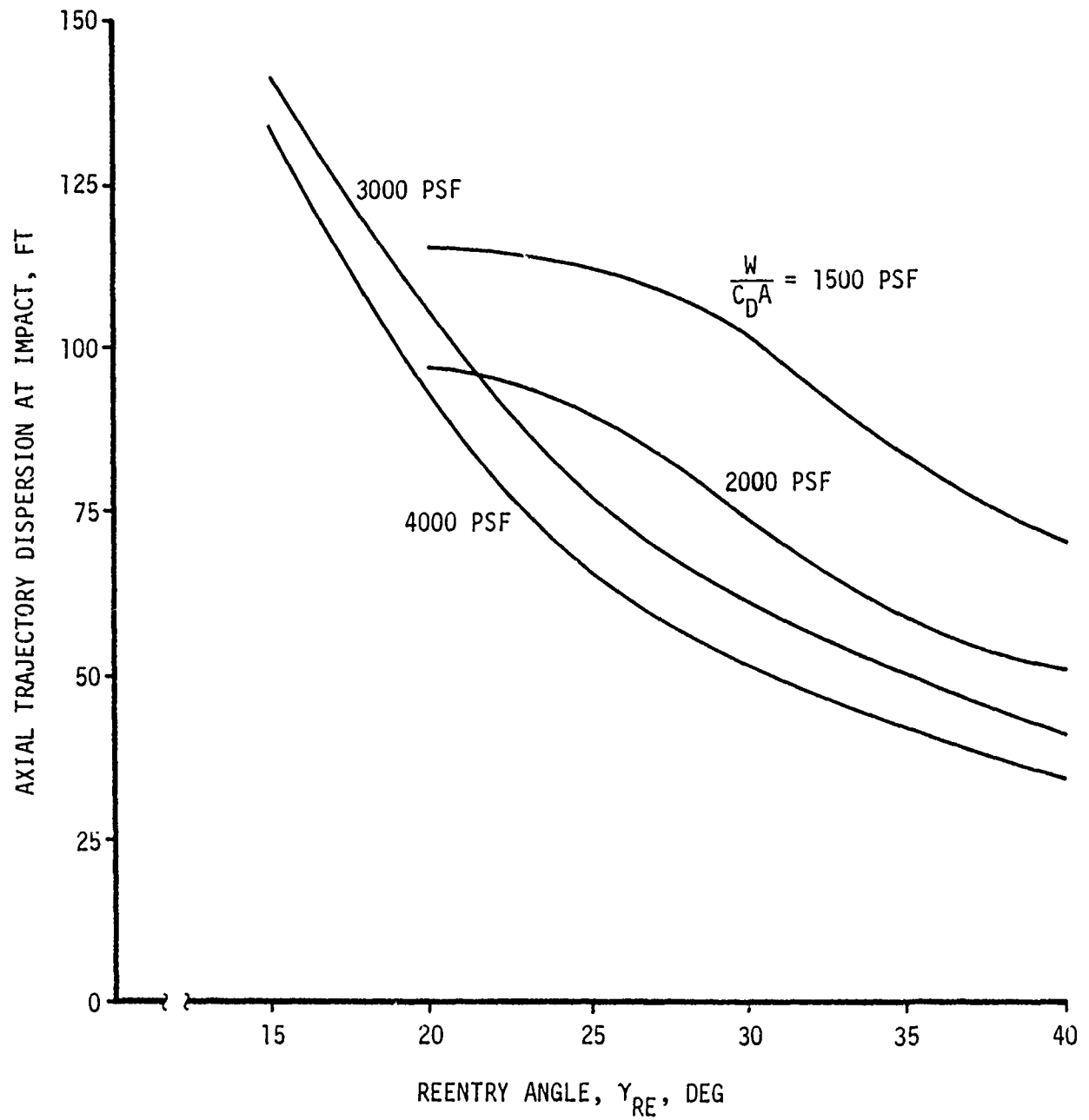


Figure 3.11 Axial Trajectory Impact Dispersions Due to Kwajalein Annual Density Variations

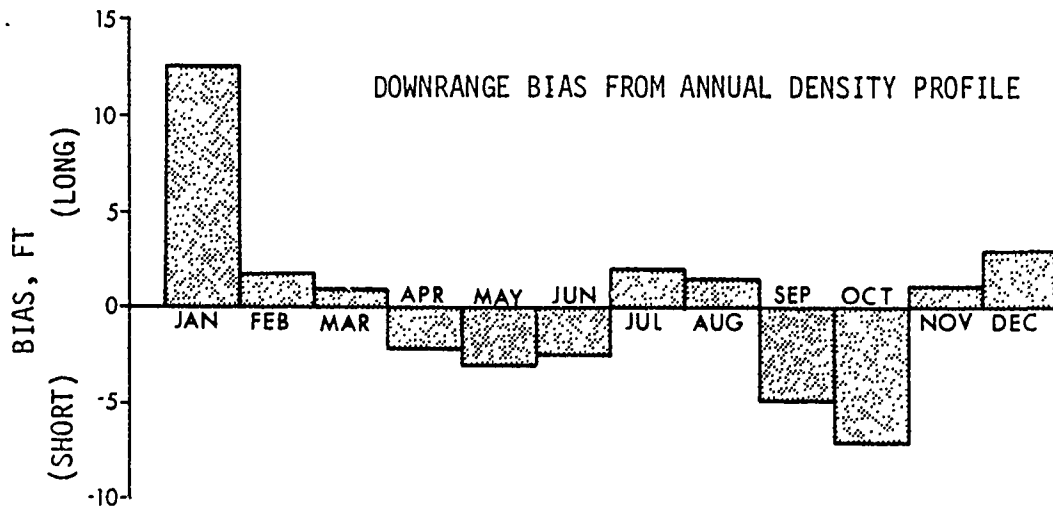
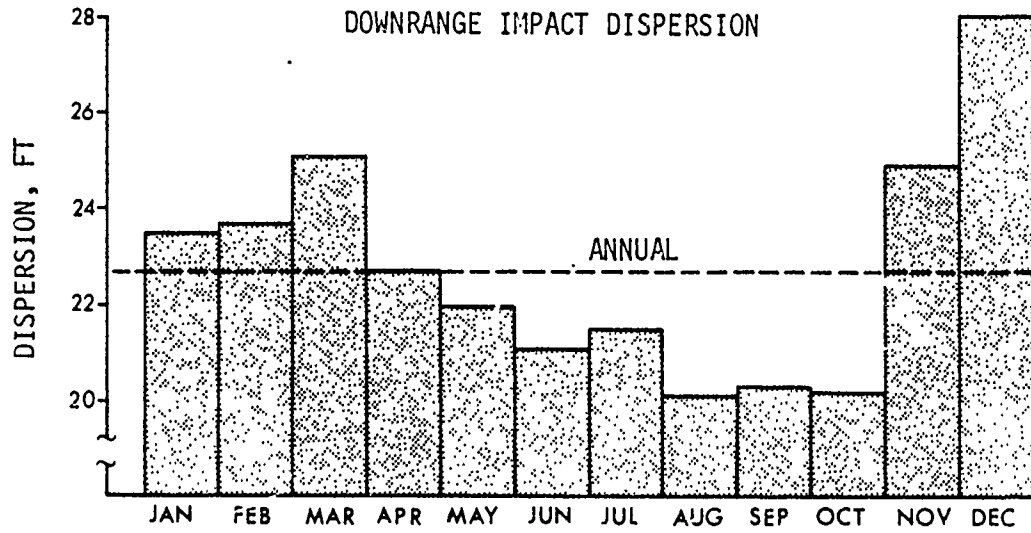


Figure 3.12 Downrange Impact Dispersions and Biases Due to Kwajalein Monthly Density Variations ( $W/C_D A = 2000$  PSF,  $\gamma_{RE} = 20$  DEG)

Mean Density Bias: The monthly and annual density variations used in the previous section are computed about a mean density profile. If the targeted profile differs from this mean a biased impact error can be expected. The interest in the present study, however, is not in determining how much difference exists between the annual mean density profile and the targeted profile since this difference could be biased out by targeting with this annual mean. Rather, it is more pertinent to determine the different impact biases that result using different monthly mean profiles. These biases were again computed for the 2000 ballistic coefficient vehicle at a 20 degree reentry angle and are presented on Figure 3.12. The results indicate that with the exception of January the differences between the monthly biases are not significant when compared with the magnitude of the dispersions. The implication for targeting purposes is that little benefit would be gained in targeting the vehicle on a monthly or seasonal basis into the Kwajalein area.

### 3.2.2 Wind

Wind variations cause position uncertainties primarily downrange and crossrange of the nominal trajectory leaving the axial position relatively unaffected. This section presents impact biases and dispersions resulting from Kwajalein wind statistics.

Influence Coefficients. Influence coefficients for winds were used in a manner analogous to the density study to determine the effects of random and mean wind variations on the trajectory at impact. The downrange and crossrange influence coefficients,  $I_{DR}^W$  and  $I_{CR}^W$ , specify the uprange/downrange and crossrange displacement at impact due to the variation in wind over a one foot altitude interval. The wind variation is measured in terms of the absolute value instead of percent difference as in the density study. Hence, the units are feet/foot per second wind variation/foot altitude. It was found that the coefficients  $I_{DR}^W$  and  $I_{CR}^W$  were

nearly identical, therefore, the coefficients presented on Figures 3.13 through 3.16 are applicable to both downrange and crossrange.

The time influence coefficient,  $I_T^W$ , specifies the axial trajectory displacement in time at impact due to wind variations. The units are seconds/foot per second wind variation/foot altitude and may be converted to an axial trajectory miss influence coefficient by multiplying  $I_T^W$  by the impact velocity. The resulting coefficients were so small as to be negligible in all except the 1500 psf ballistic coefficient case at low reentry angles. Therefore, the coefficients are not presented here and axial trajectory displacements were not computed for wind variations.

The downrange wind influence coefficients of Figures 3.13 through 3.16 are similar in appearance to the density coefficients, increasing with decreasing ballistic coefficients and reentry angle. Maximum sensitivities occur at lower altitudes, in the 20 KFT region. The small coefficients above 90 KFT indicate negligible dispersion due to winds above this altitude.

An important implication of the negligible axial trajectory sensitivity to wind effects is that the trajectory's drag deceleration history may be attributed to ballistic coefficient and density effects but not to wind effects. Wind induced lateral displacements, however, are directly correlated with lift effects.

Random Wind Dispersions. One sigma wind dispersions for the Kwajalein area were obtained from the USAF ETAC studies of Reference 3 for altitudes from 0 to 105 KFT. Annual and seasonal wind dispersions are presented on Figures 3.17 and 3.18 for north-south and east-west directions respectively. Impact dispersions resulting from annual wind variations are presented on Figures 3.19 and 3.20 for the downrange and crossrange directions respectively. A comparison with Figure 3.10 reveals that wind induced dispersions are significantly larger than density dispersions. Again,

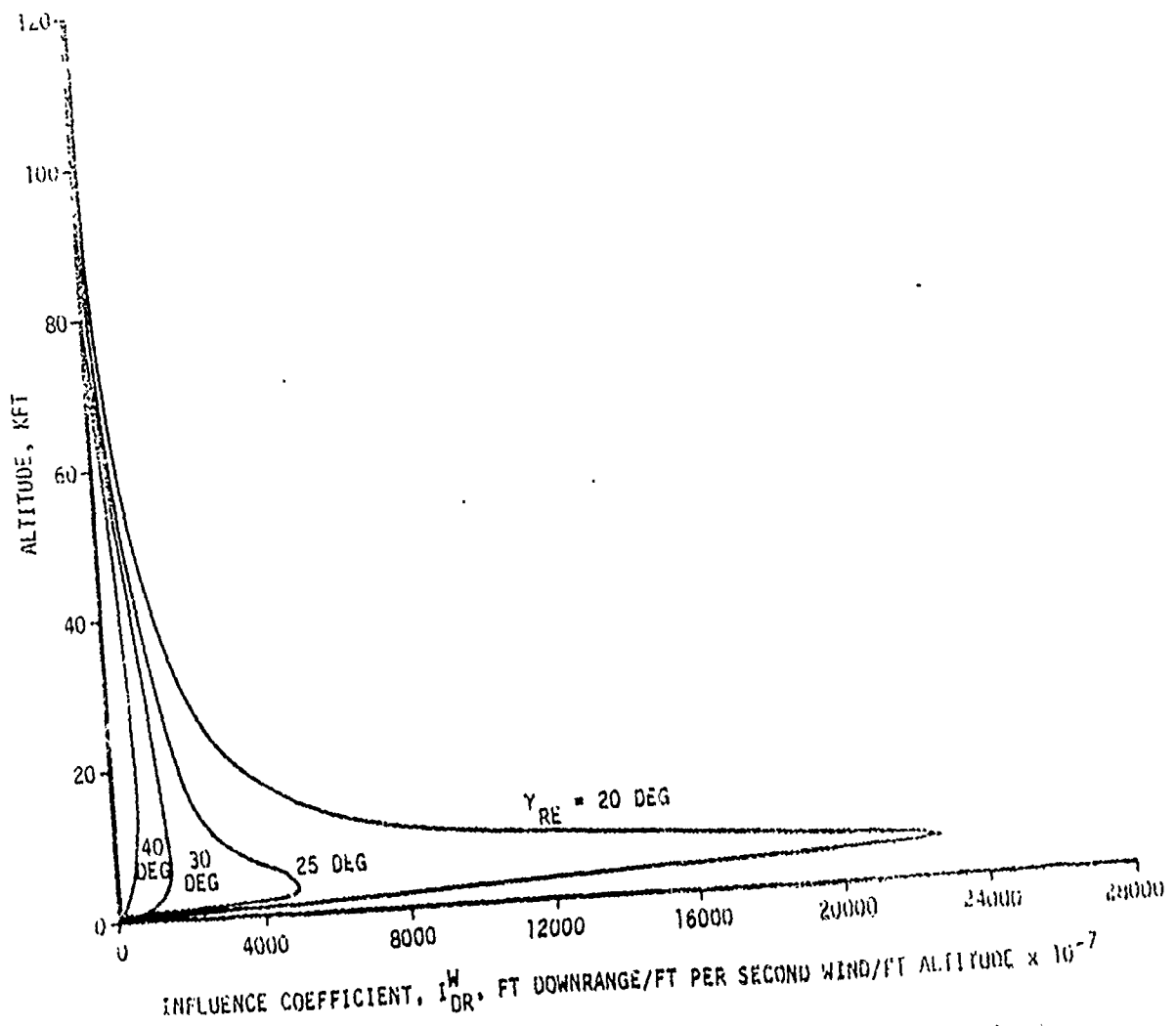


Figure 3.13 Downrange/Crossrange Wind Influence Coefficient,  
( $W/C_D A = 1500$  PSF)

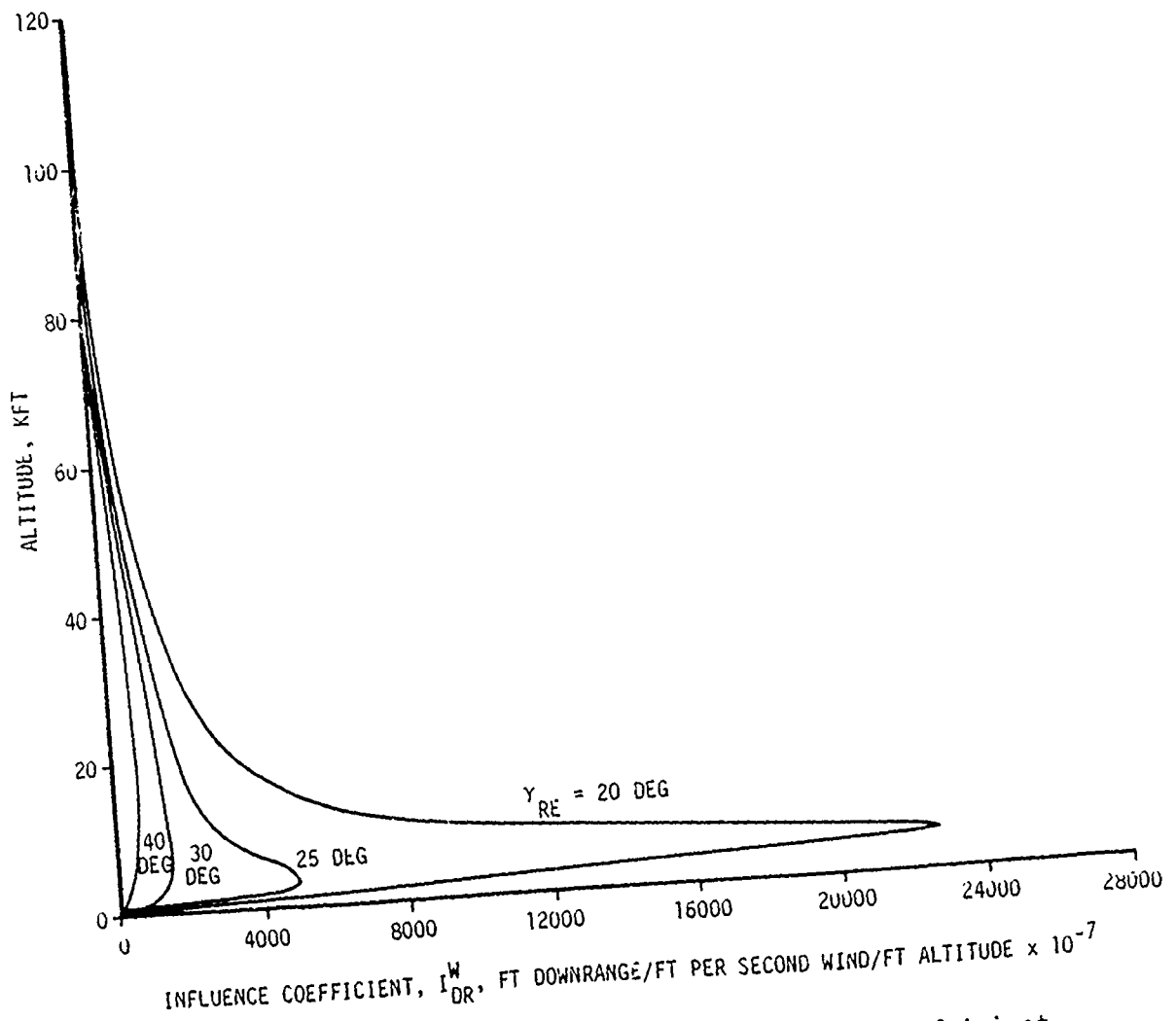


Figure 3.13 Downrange/Crossrange Wind Influence Coefficient,  
( $W/C_D A = 1500$  PSF)

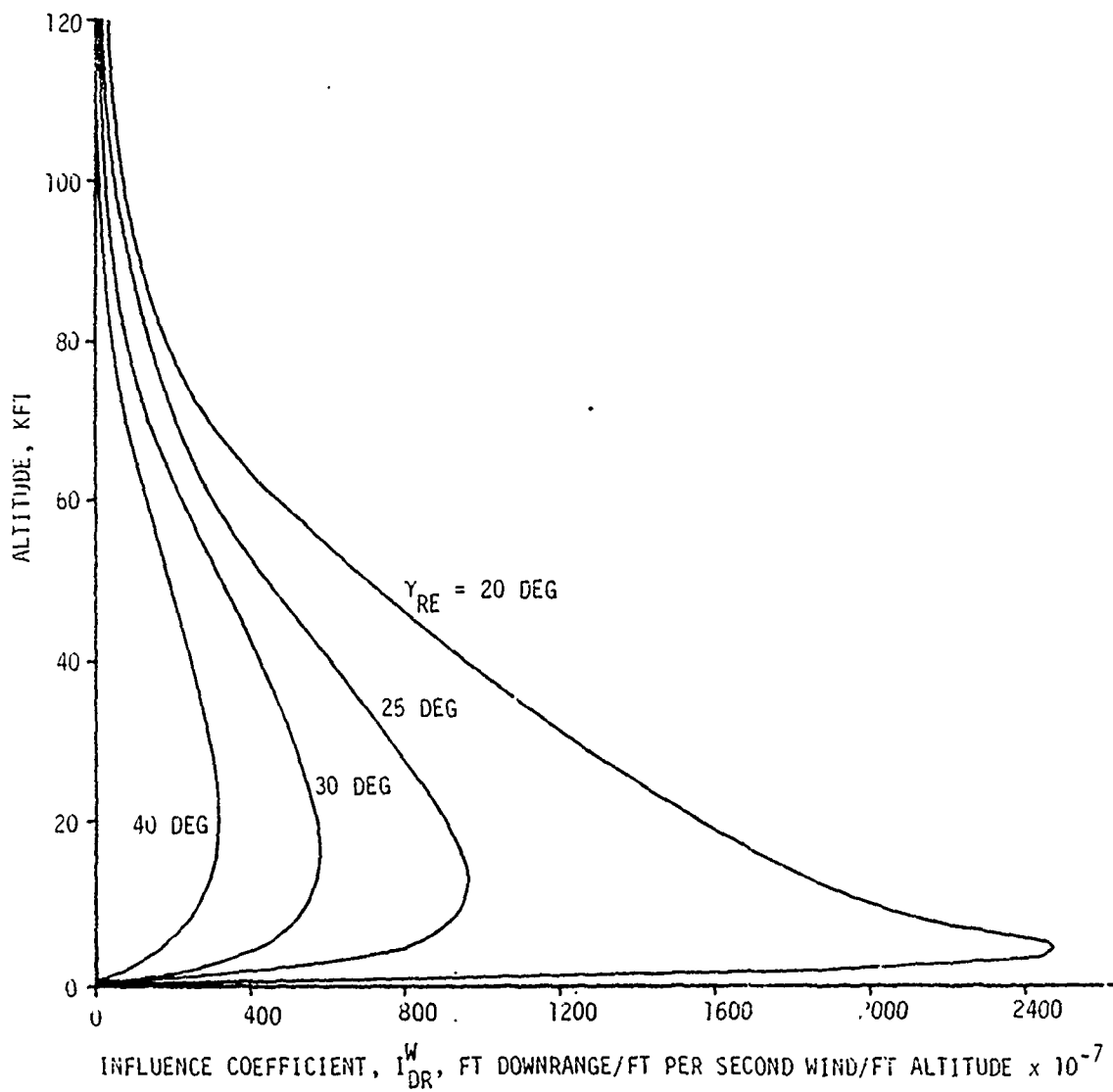


Figure 3.14 Downrange/Crossrange Wind Influence Coefficient,  
( $W/C_D A = 2000$  PSF)

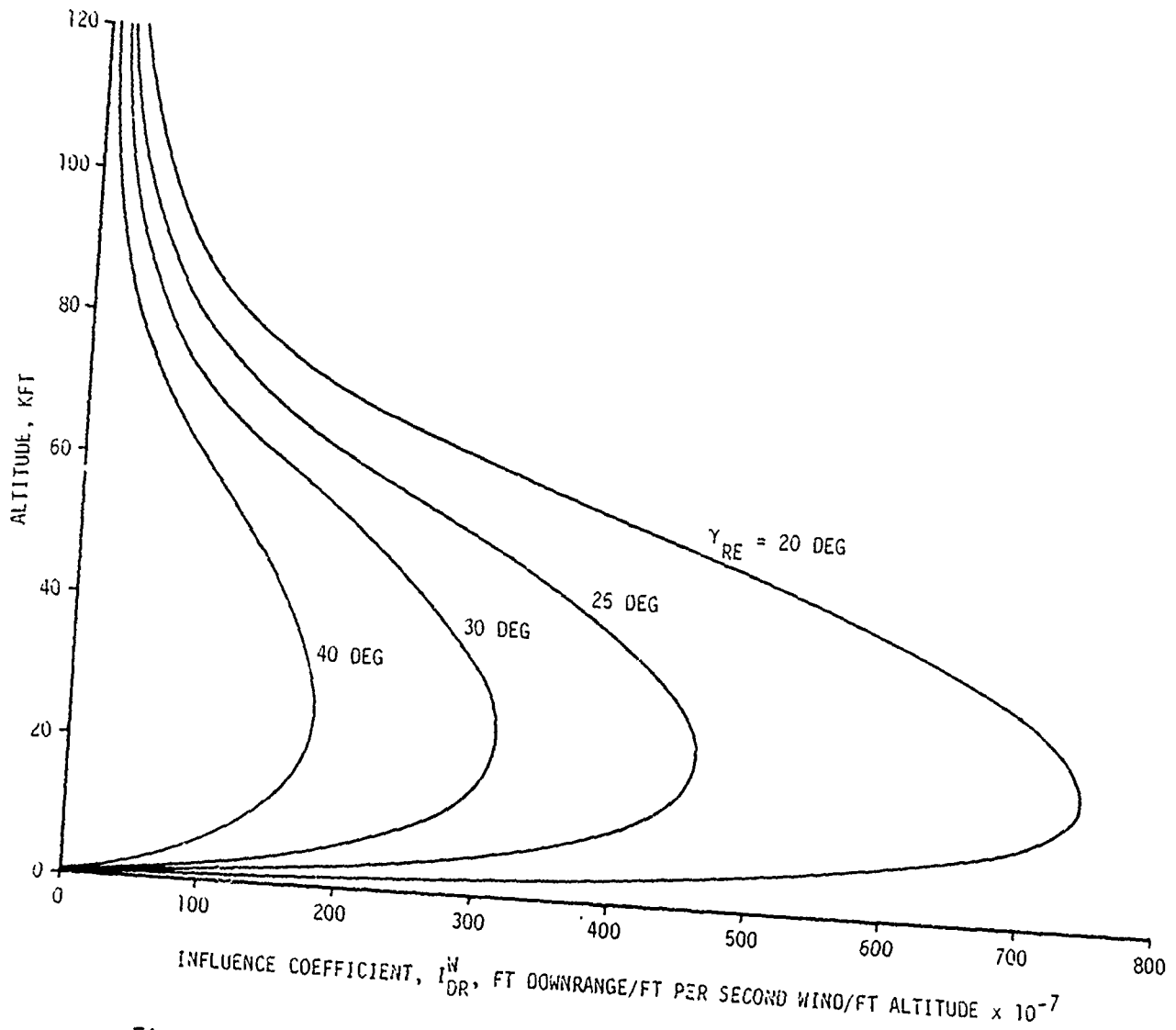


Figure 3.15 Downrange/Crossrange Wind Influence Coefficient,  
( $W/C_D A = 3000$  PSF)

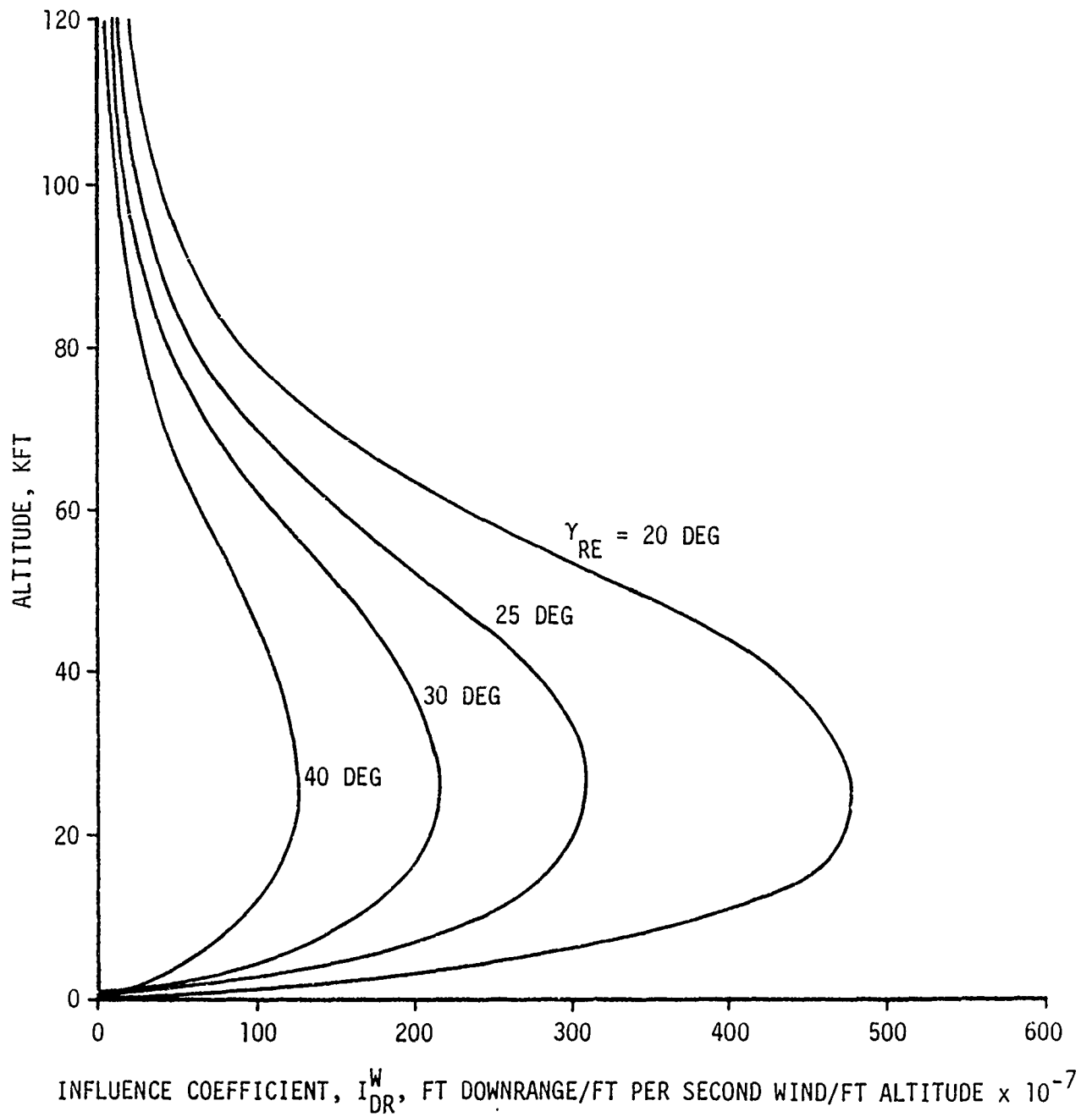


Figure 3.16 Downrange/Crossrange Wind Influence Coefficient,  
( $W/C_D A = 4000$  PSF)

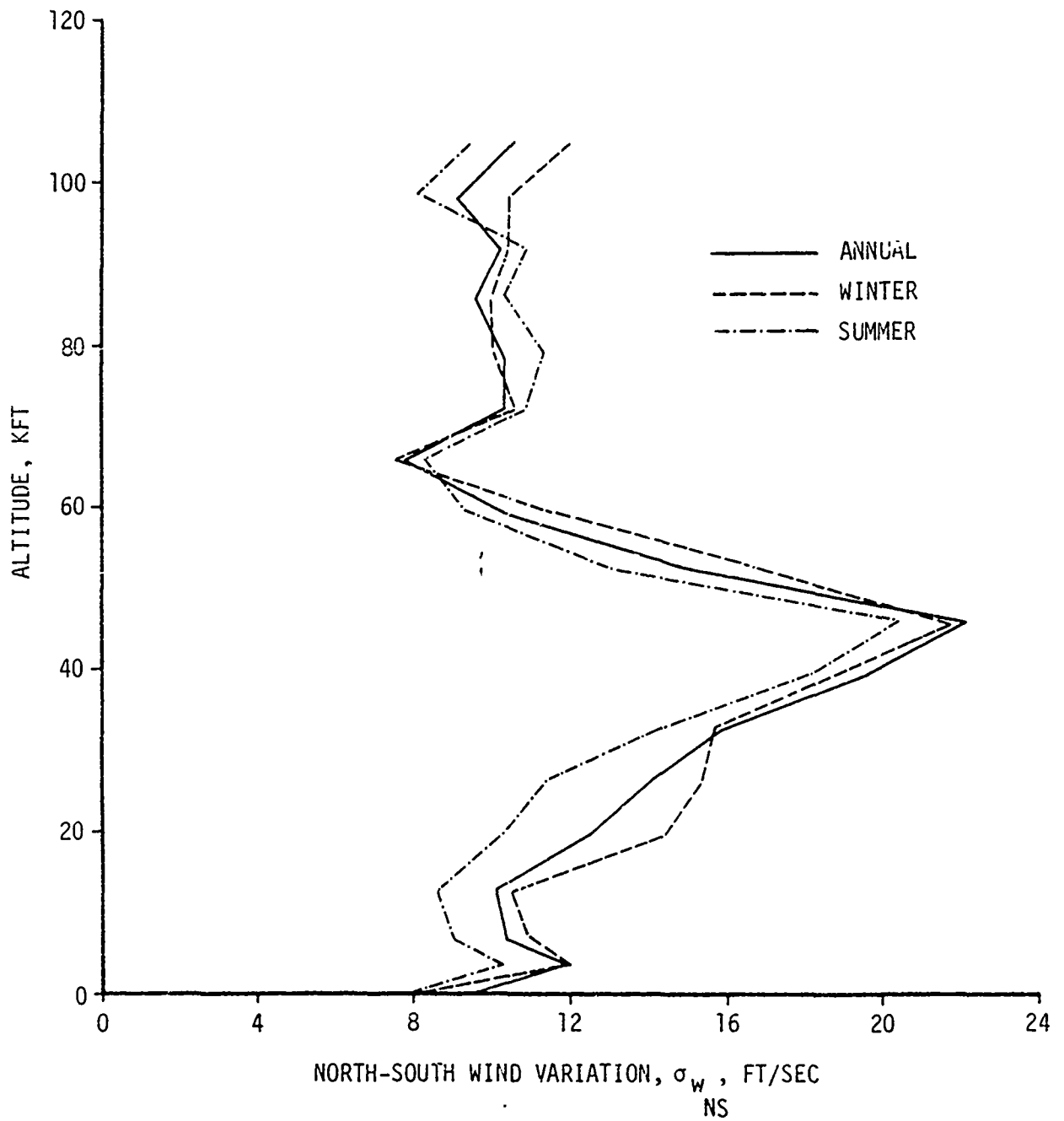
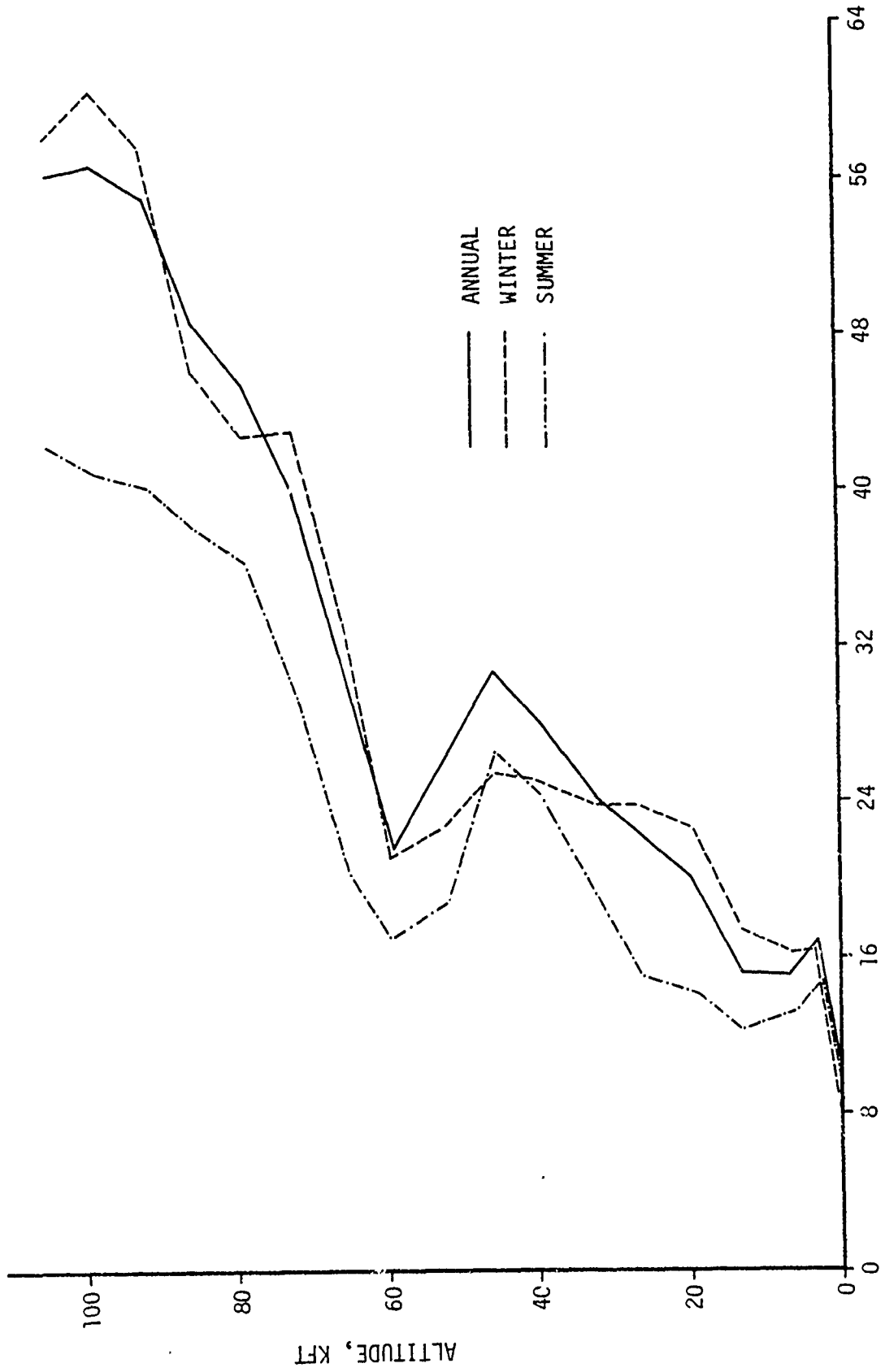


Figure 3.17 North - South Wind Variations for Kwajalein



EAST-WEST WIND VARIATION,  $\sigma_w$ , FT/SEC  
EW

Figure 3.18 East - West Wind Variations for Kwajalein

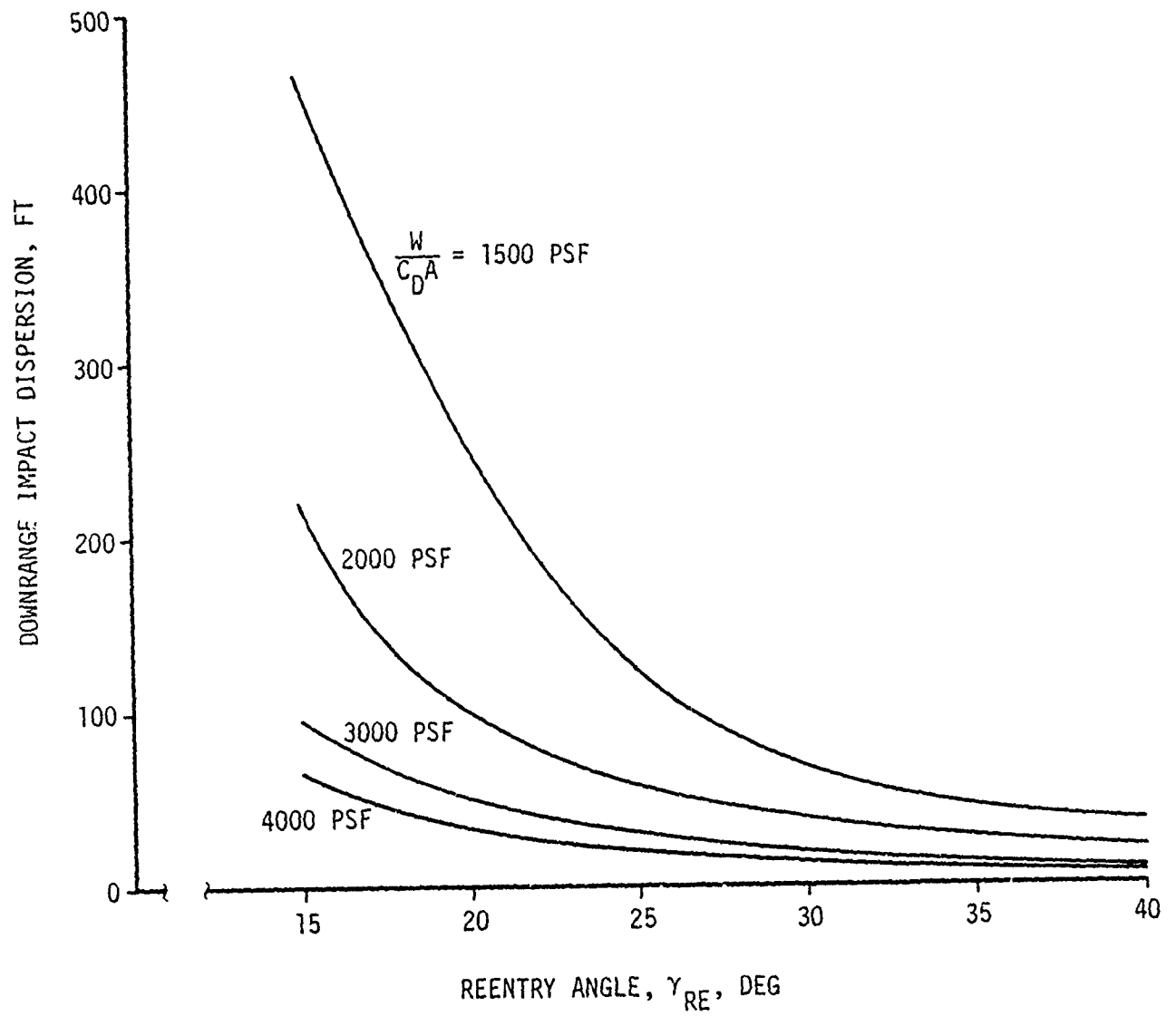


Figure 3.19 Downrange Impact Dispersions Due to Kwajalein Annual Wind Variations

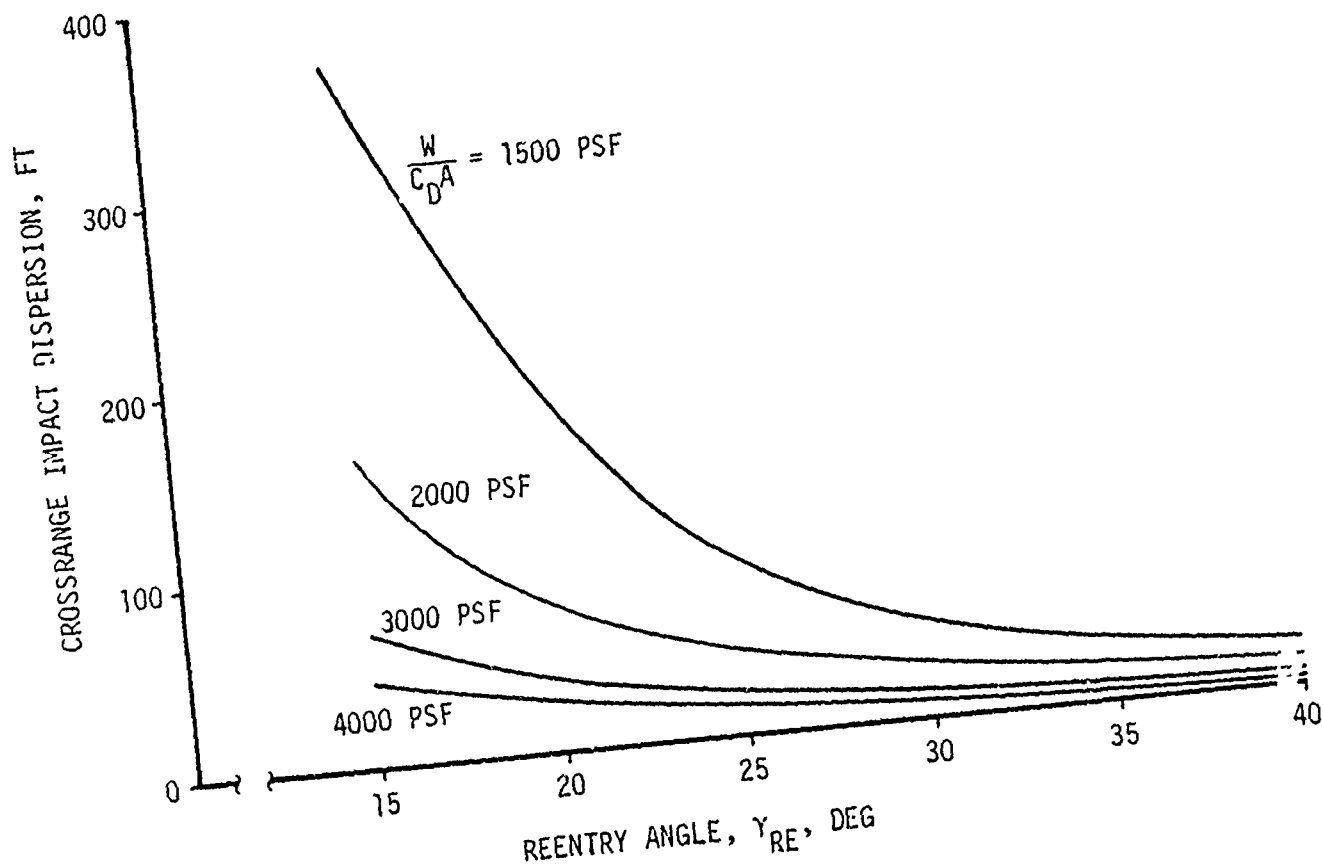


Figure 3.20 Crossrange Impact Dispersions Due to Kwajalein Annual Wind Variations

these parametric charts are not applicable to operational design studies since Soviet and Kwajalein statistics are significantly different.

The impact dispersions resulting from seasonal wind variations are presented on Figure 3.21 for the 2000 ballistic coefficient vehicle at 20 degrees reentry angle. The results indicate little difference in the impact dispersions throughout most of the year, except for summer months, which exhibit a smaller dispersion.

Mean Wind Bias. The difference between the annual mean and targeted wind profile results in a biased impact error. However, as explained in the density study section, it is more useful to determine the variation in means throughout the year rather than the difference between the targeted and annual means, since the latter bias can be removed in targeting. These biases were computed for the 2000 PSF ballistic coefficient vehicle at a reentry angle of 20 degrees, and are presented in Figure 3.22 for both annual and seasonal means. The results show that rather large variations occur in the biases throughout the year, suggesting that some benefit would be gained by targeting with seasonal winds for the Kwajalein area. However, the 20 degree reentry angle tends to accentuate the biases.

### 3.3 BALLISTIC COEFFICIENT DISPERSIONS

The deceleration experienced by a vehicle is directly proportional to the ballistic coefficient. The ballistic coefficient is expressed by the instantaneous vehicle weight divided by its instantaneous drag coefficient and a fixed reference base area ( $\frac{W}{C_D A}$ ). Ballistic coefficient uncertainties, therefore, result from variations in vehicle mass and drag coefficient. Base area uncertainties were excluded since the drag coefficient is generally referenced to a constant base area with any change in base area cross section resulting from ablation appearing as a drag coefficient variation. The ballistic coefficient uncertainty may then be expressed as:

$$\sigma_{\beta\%} = \left[ \sigma_{m\%}^2 + \sigma_{C_D\%}^2 \right]^{1/2}$$

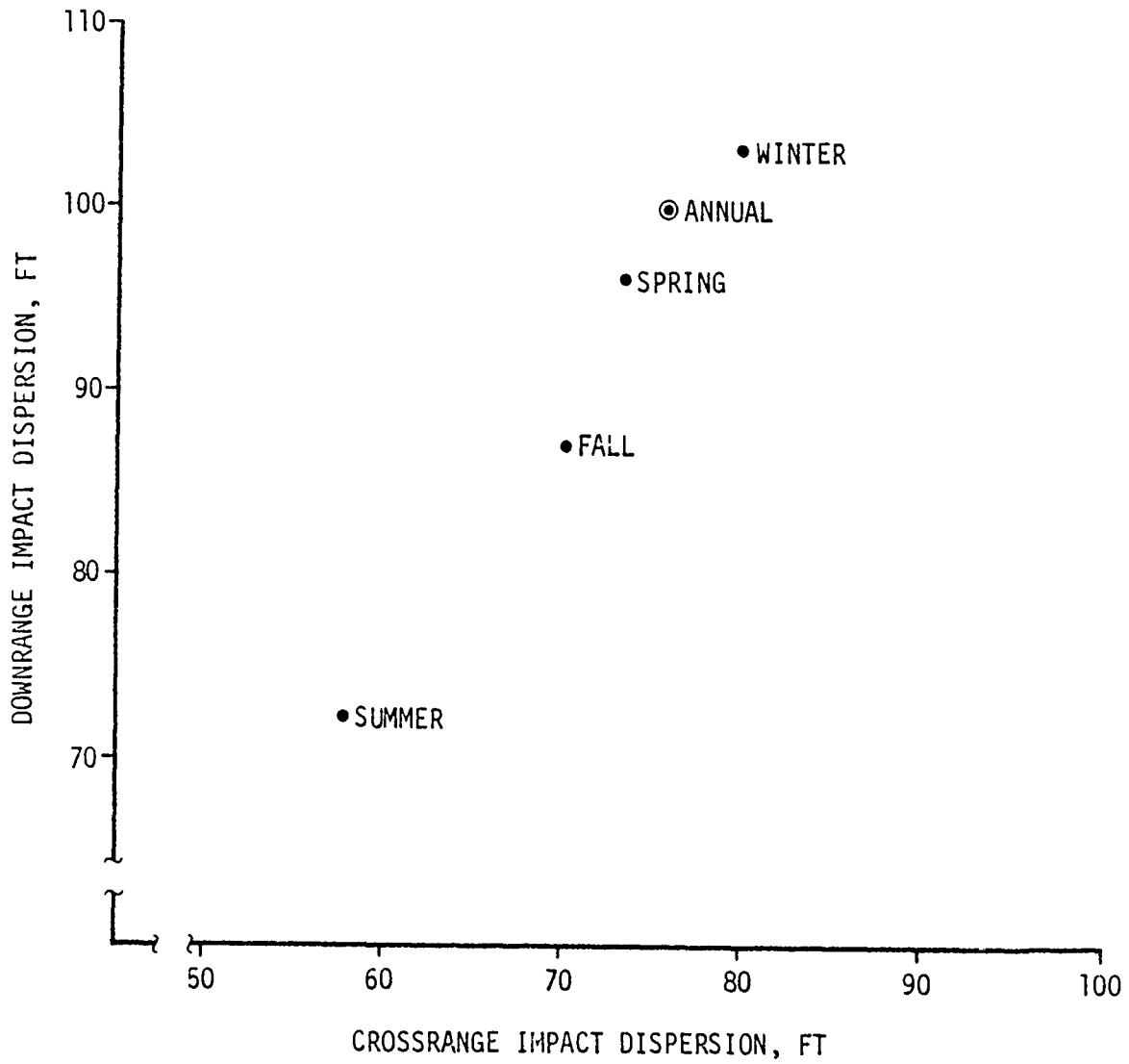


Figure 3.21 Impact Dispersions Due to Kwajalein Annual Seasonal Wind Variations ( $W/C_D A = 2000$  PSF,  $\gamma_{RE} = 20$  Deg)

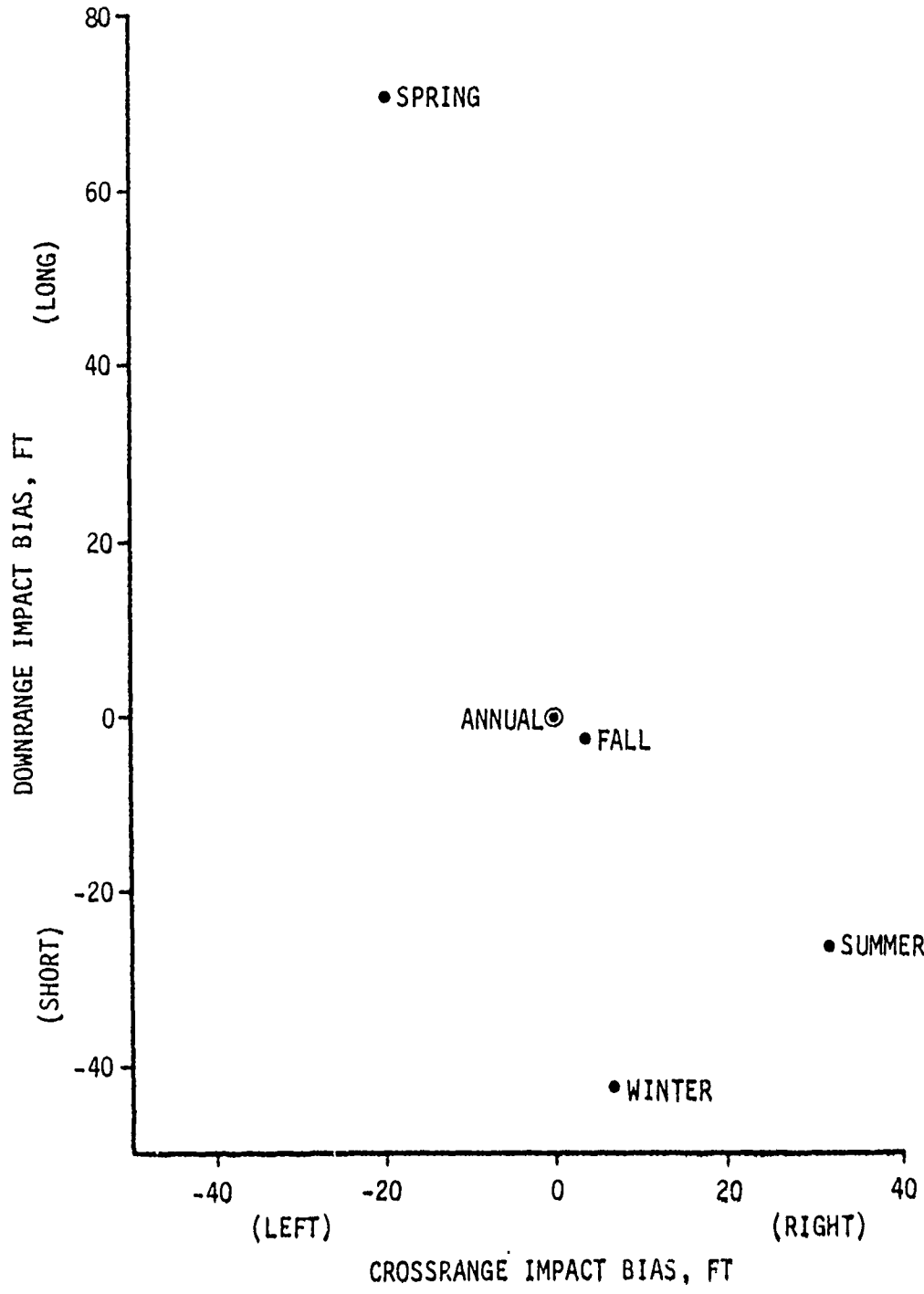


Figure 3.22 Impact Biases Due to Seasonal Wind Variations  
( $W/C_D A = 2000$  PSF,  $\gamma_{RE} = 20$  Deg)

where each uncertainty is expressed as a percent variation in the parameter.

The actual magnitude of each uncertainty for the various parameters is dependent upon specific vehicle dependent characteristics such as geometry, heat shield material, separation system, etc. Since this study is for a hypothetical vehicle, assumptions were made regarding some of the parameters while others were treated parametrically. Considerable data are available for high ballistic coefficient vehicles, and ballistic coefficient variations for these vehicles are believed to be representative of high ballistic coefficient vehicles in general.

This study also makes extensive use of influence coefficients to determine the effects of the various uncertainties. The influence coefficients are essentially identical to those for density presented on Figures 3.1 through 3.8. This similarity is expected since density and ballistic coefficient uncertainties contribute in nearly an identical manner to deceleration uncertainties. The only difference that could be considered in computing ballistic coefficient and density influence coefficients is the use of the hydrostatic pressure equation to propagate density perturbations to the ground. This, however, was found to have a negligible effect. Downrange and axial trajectory displacements may then be determined in an analogous manner to the density uncertainties, replacing  $I_{DR}^{\rho}$  and  $I_T^{\rho}$  by  $I_{DR}^{\beta}$  and  $I_T^{\beta}$  respectively. The units of  $I_{DR}^{\beta}$  are feet downrange/percent error in ballistic coefficient/foot altitude, while the units for  $I_T^{\beta}$  are seconds of time/percent error in ballistic coefficient/foot altitude.

### 3.3.1 Mass Uncertainties

The mass history of the vehicle during reentry is equivalent to the initial mass less the ablated mass:

$$m(h) = m_0 - m_a(h).$$

Hence, the uncertainty in the mass history is composed of variations in both the initial mass and ablated mass loss during reentry:

$$\sigma_m = [\sigma_{m_0}^2 + \sigma_{m_a}^2]^{1/2}$$

Initial Mass: Uncertainties in the initial mass of an operational vehicle arise from manufacturing tolerances in the weight of various components of the reentry vehicle, and any mass ejected from the vehicle prior to reentry, such as propellant for spin stabilizing the vehicle. Typical flight test vehicle mass property variations (mass and moments of inertia), however, exceed those for an operational vehicle since they are assembled one at a time with various test related on-board equipment configurations. For this reason mass properties for flight test vehicles should be measured after the vehicle is fully assembled. This enables discrepancies between the actual and nominal weight used in targeting to be removed as an impact bias, and reduces the initial mass uncertainty to the uncertainty associated with weighing the assembled RV and with estimating the amount of mass ejected from the vehicle prior to reentry. It was assumed in this study that the initial mass uncertainty could be reduced to a negligible magnitude.

Ablation Mass Loss: The ablation mass loss uncertainty is attributable to uncertainties in modeling the vehicle ablation rate history during reentry. The many contributors to this uncertainty include variations in the heat shield properties, vehicle shape history (particularly nosetip shape changes), climatology, and other factors. If the initial mass uncertainty is assumed negligible, the total mass uncertainty is equivalent to the ablated mass loss uncertainty, and the percent mass uncertainty is then given by:

$$\sigma_{m\%} = \frac{m_a}{m} \sigma_{m_{a\%}}$$

The ablative mass loss uncertainty results from uncertainties in both modeling the ablation rate and in flight-to-flight variations of the RV heatshield properties. If  $m$  is expressed as  $m_0 - m_a$ , the resulting

expression becomes:

$$\sigma_{m\%} = \sigma_{m_{a\%}} \frac{m_a/m_0}{1 - m_a/m_0}$$

This form is convenient since  $m_a/m_0$  is altitude dependent while  $\sigma_{m_{a\%}}$  is often specified as a constant. The downrange and axial trajectory impact dispersions can then be determined by using the influence coefficients to numerically integrate  $\sigma_{m\%}$  during reentry as described in Appendix B.

Approximate parametric impact dispersions were derived by assuming that the mass loss ratio during reentry,  $m_a/m_0$ , increases in a linear fashion from 100 KFT to impact. This linear relationship may be expressed as:

$$m_a/m_0 = (1 - h/10^5) (m_a/m_0)_F \quad (h \leq 100 \text{ KFT})$$

After some manipulation and assumptions regarding relative magnitudes of the various terms, the expression becomes:

$$\sigma_{m\%} = \sigma_{m_{a\%}} (1 - h/10^5) (m_a/m_0)_F$$

Since  $\sigma_{m_{a\%}}$  and  $(m_a/m_0)_F$  are constants, the percent uncertainty may be normalized:

$$\sigma_{m\%} / \sigma_{m_{a\%}} / (m_a/m_0)_F = 1 - h/10^5$$

This expression was integrated throughout reentry using the influence coefficient and reentry angles of interest. Correlation coefficients of unity were used between altitude layers, reflecting the high degree of correlation between the mass variation at one altitude with that at another. The dispersion parameters,  $\sigma_{DR} / \sigma_{m_{a\%}} / (m_a/m_0)_F$ , and

$\sigma_A / \sigma_{m_{a\%}} / (m_a/m_0)_F$  are presented as functions of reentry angle on

Figures 3.23 and 3.24 respectively. Hence, knowledge of the final ratio of ablated to initial mass and the mass loss uncertainty in percent enables the dispersion to be determined for any particular vehicle exhibiting the assumed linear mass loss history. Typical values for current vehicles are  $\sigma_{m_{a\%}} = 10\%$  and  $(m_a/m_0)_F = .05$ .

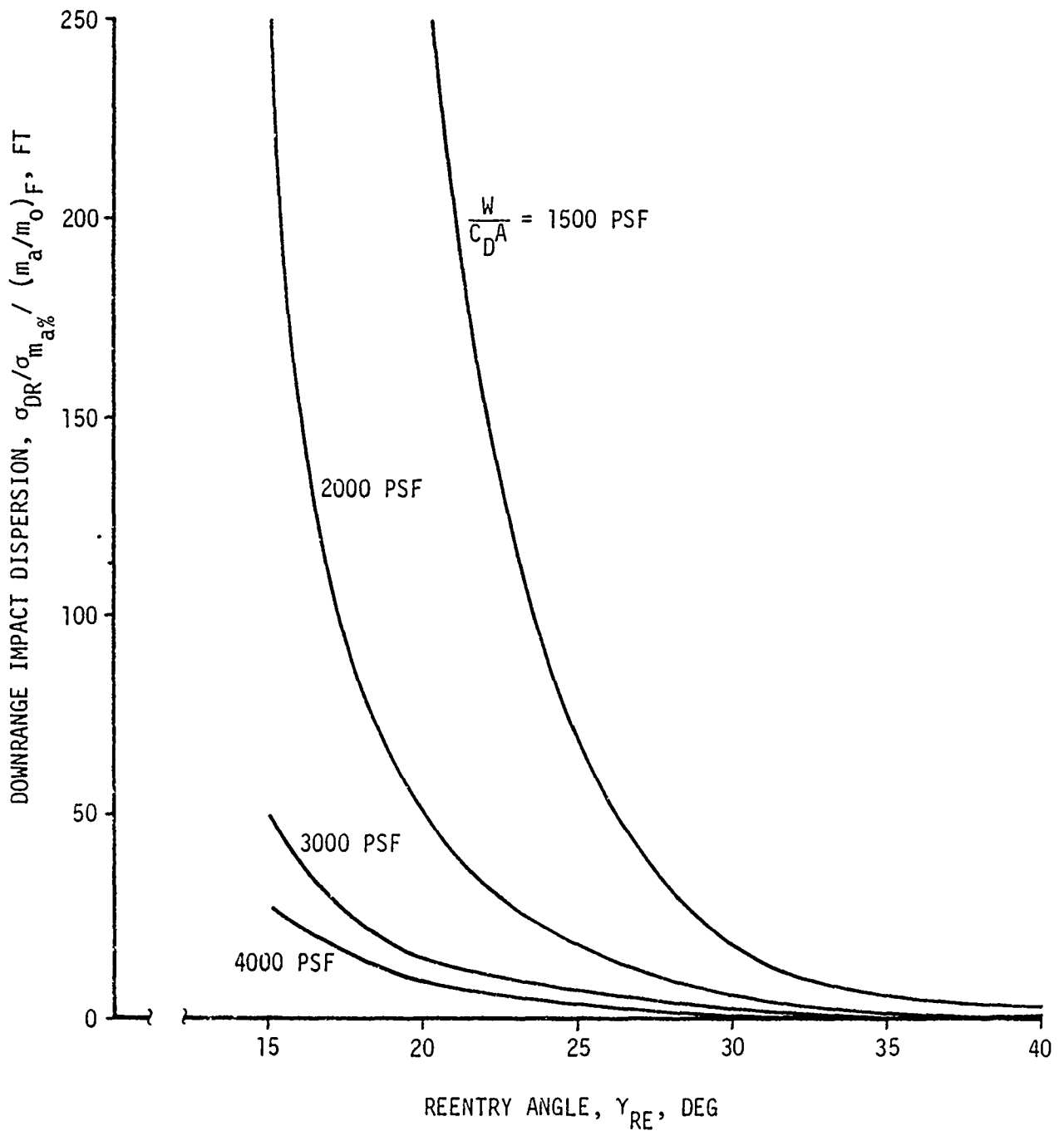


Figure 3.23 Downrange Impact Dispersions Due To Ablation Uncertainties

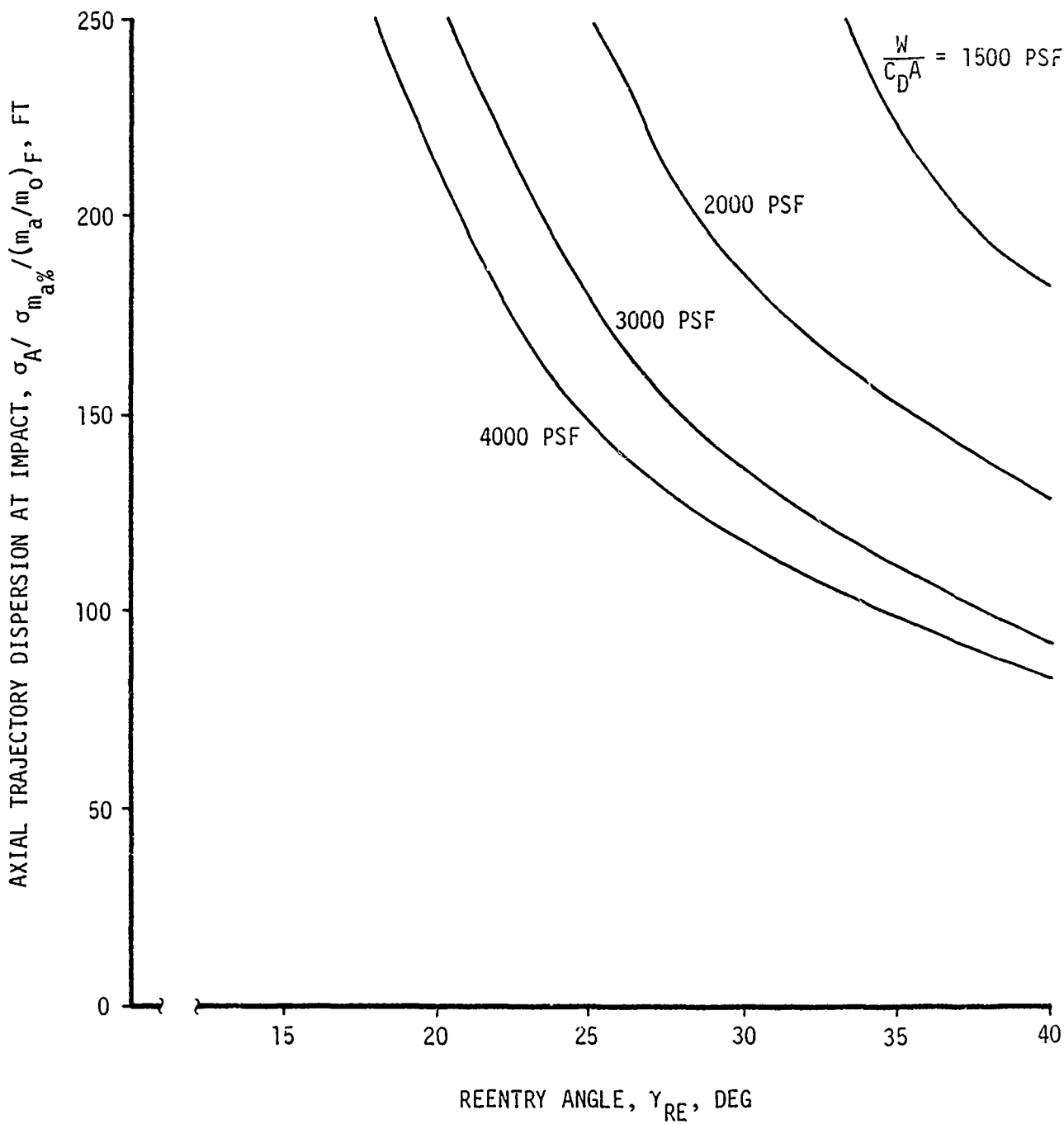


Figure 3.24 Axial Trajectory Dispersions At Impact Due To Ablation Uncertainties

### 3.3.2 Drag Coefficient

Analytical techniques used to predict drag coefficient histories have been well developed through the use of flight and wind tunnel tests to validate theoretical aerodynamic models. To develop an accurate drag history prediction it is necessary to consider the following aerodynamic parameters:

- Inviscid drag
- Viscous drag (laminar and turbulent)
- Base drag
- Nose blunting drag due to nosetip shape change
- Surface roughness drag due to roughened ablator surface
- Angle-of-attack induced drag

A detailed uncertainty analysis would involve an investigation of each component based on design tolerances, test data, etc. for a specific reentry vehicle configuration. A simplified approach which can be applied to reentry vehicles in general is to consider the total drag as having a Mach number dependent drag, altitude dependent drag, and angle-of-attack induced drag. The total drag may then be expressed as the sum:

$$C_D = C_D (M_\infty) + C_D (h) + C_D (\alpha)$$

Drag components which are primarily Mach number dependent include inviscid and base drag, while viscous drag is primarily altitude dependent. Nose bluntness and surface roughness have both Mach number and altitude dependence. Below approximately 150 KFT the viscous drag achieves some Mach number dependence. The angle-of-attack component is often assumed in targeting to be altitude dependent only. The corresponding drag coefficient uncertainty, assuming each component is independent, is given by:

$$\sigma_{C_D} = \left[ \sigma_{C_D}^2 (M_\infty) + \sigma_{C_D}^2 (h) + \sigma_{C_D}^2 (\alpha) \right]^{1/2}$$

Hence, the percent variance associated with the total drag coefficient is equal to a weighted sum of the percent variances of the individual components:

$$\sigma_{C_D\%} = \left\{ \left[ \frac{C_D(M_\infty)}{C_D} \right]^2 \sigma_{C_D\%}^2(M_\infty) + \left[ \frac{C_D(h)}{C_D} \right]^2 \sigma_{C_D\%}^2(h) + \left[ \frac{C_D(\alpha)}{C_D} \right]^2 \sigma_{C_D\%}^2(\alpha) \right\}^{1/2}$$

The ratio of the individual drag coefficient components to the total drag coefficient for the drag model used in the present study are presented on Figure 3.25. These ratios are nearly invariant with ballistic coefficient and reentry angle for those vehicles impacting at supersonic velocities. Figure 3.25 indicates that the altitude dependent drag dominates at high altitudes and the Mach number dependent coefficient dominates below 200 KFT. The angle-of-attack component is based on a five degree reentry angle-of-attack at 300 KFT, damping to near zero by 100 KFT, with a slight divergence after transition (90 KFT).

The uncertainties associated with the predicted drag model are dependent on many factors unique to a particular vehicle, including its basic configuration, heatshield material, ballistic coefficient, etc. The specific values used in this section to make dispersion calculations are based on theoretical and flight test data accumulated on high ballistic RV's and are believed to be fairly representative of this class of vehicle.

Mach Number Dependent Drag: The accuracy of the Mach number dependent drag is nearly constant at high Mach numbers, becoming less certain in the transonic region. Theoretical analyses and flight test data have indicated that typical uncertainties for high ballistic coefficient vehicles are three percent in the supersonic and hypersonic regimes, increasing to five percent in the transonic region. High ballistic coefficient vehicles seldom approach transonic velocities except at very low reentry angles, as evidenced by the Mach number histories presented for the various vehicles in Appendix A. The weighted contribution of the uncertainty,  $(C_D(M_\infty) / C_D) \sigma_{C_D}(M_\infty)$ , based on the drag coefficients ratios in Figure 3.25 is presented on

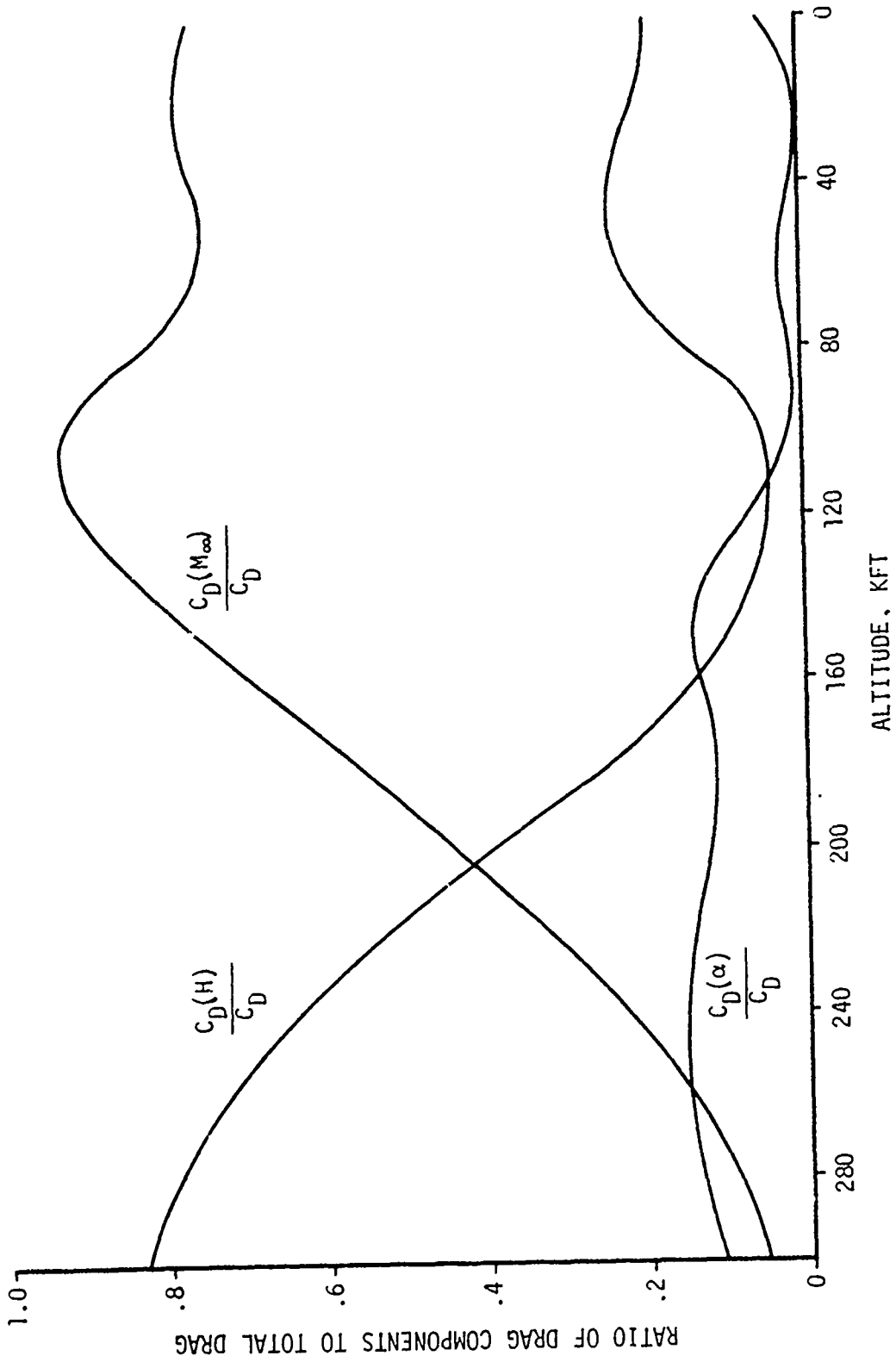


Figure 3.25 Ratio of Drag Coefficient Components to Total Drag Coefficient

Figure 3.26. It is observed to be small at high altitudes, increasing as the vehicle reenters.

Altitude Dependent Drag: The altitude dependent drag uncertainty,  $\sigma_{C_D\%}(h)$ , is generally large at high altitudes, decreasing at lower altitudes. This uncertainty is approximately 10% above 250 KFT, decreasing to 5.0% below that altitude for high ballistic coefficient vehicles. The weighted contribution of this uncertainty,  $(C_D(h)/C_D) \sigma_{C_D\%}(h)$ , is also presented on Figure 3.26.

The combined uncertainty of Mach number and altitude dependent drag is also presented on Figure 3.26. It indicates that below 150 KFT the total drag uncertainty (excluding angle-of-attack) is nearly constant at 2.5 percent. This is believed to be representative of the accuracy with which the drag coefficient can be modeled for a high ballistic coefficient vehicle. Parametric curves are presented on Figures 3.27 and 3.28 representing the downrange and axial trajectory dispersions at impact resulting from a constant 2.5 percent uncertainty in drag. These dispersions were calculated assuming perfect correlation between the drag variations at different altitudes.

Angle-of-Attack Dependent Drag: The vehicle angle-of-attack during reentry induces both lift and drag forces on the vehicle. The aerodynamic mechanisms which produce an angle-of-attack are discussed in the next section on lift effects. In general, the resulting lift effects are more significant to the trajectory dispersion than are the drag effects. Furthermore, angle-of-attack uncertainties are often the smallest drag dispersion contributors. This is true because the contribution of the angle-of-attack uncertainty to the total drag uncertainty is weighted by the factor  $C_D(\alpha)/C_D$ , which is observed to be relatively small as shown in Figure 3.25. The magnitude and time during reentry at which angle-of-attack divergence can occur is vehicle dependent, making it difficult to quantify the dispersions. For these reasons only the initial

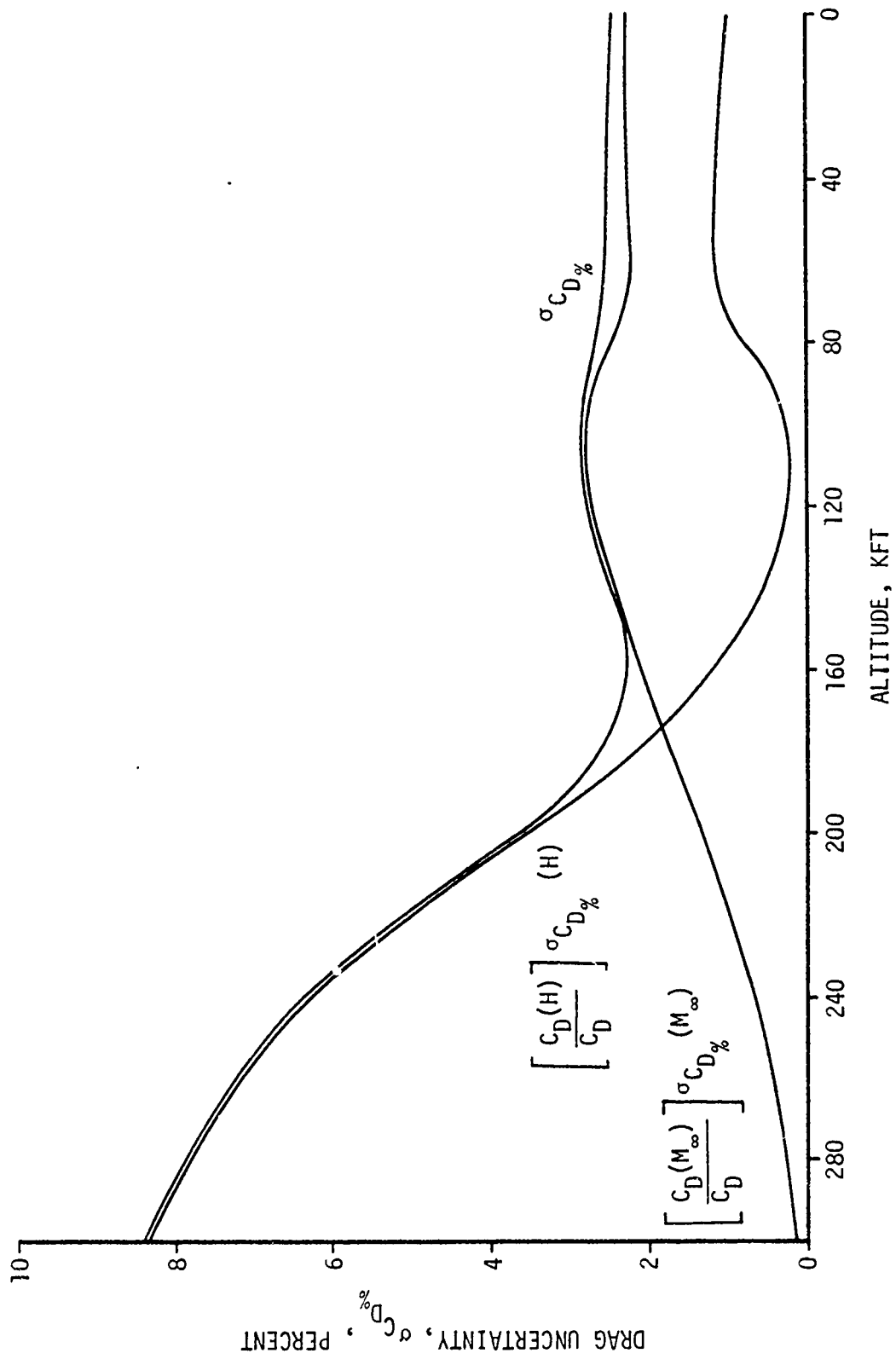


Figure 3.26 Weighted and Total Drag Coefficient Uncertainties

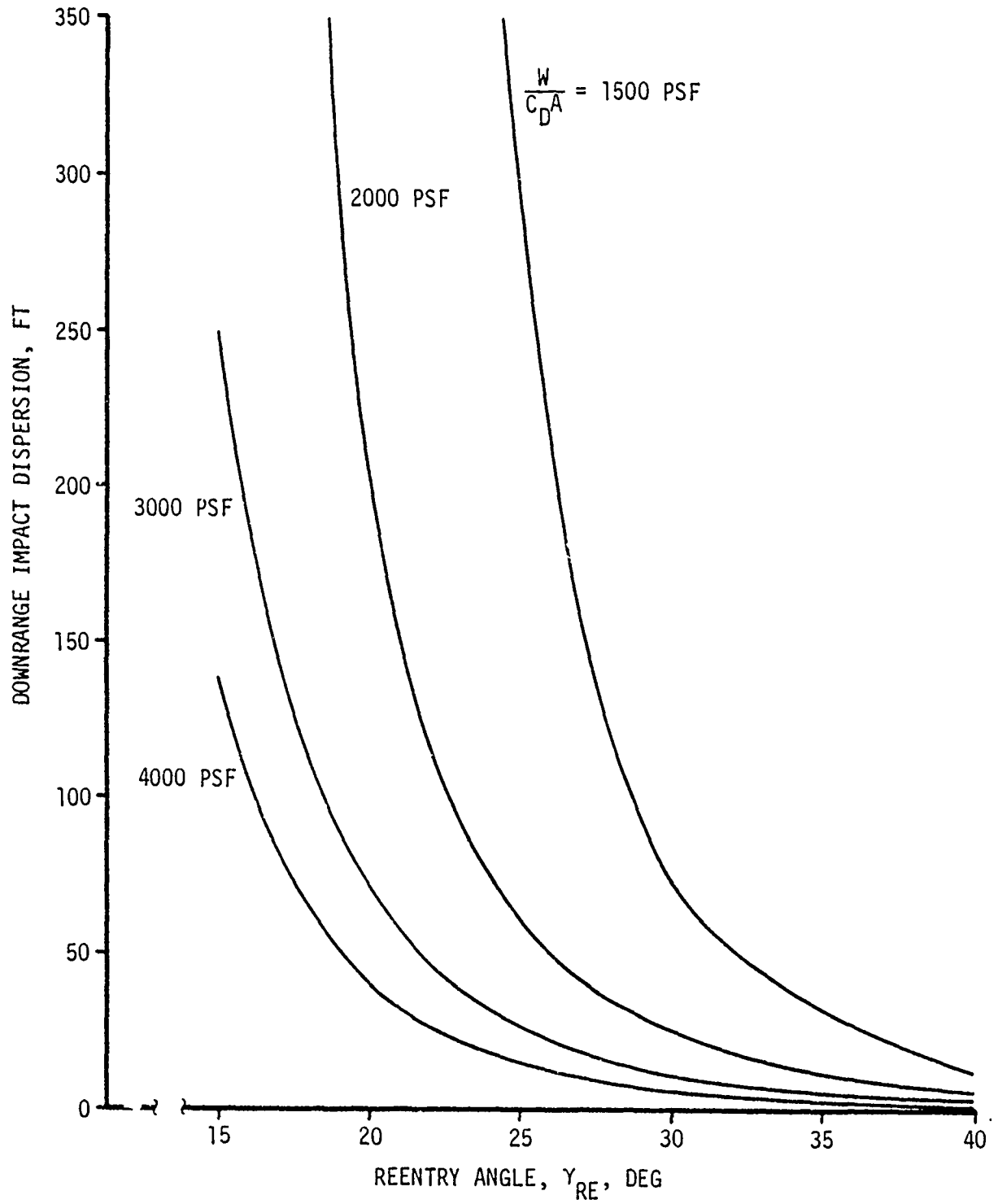


Figure 3.27 Downrange Impact Dispersion Due To 2.5 Percent Drag Variation

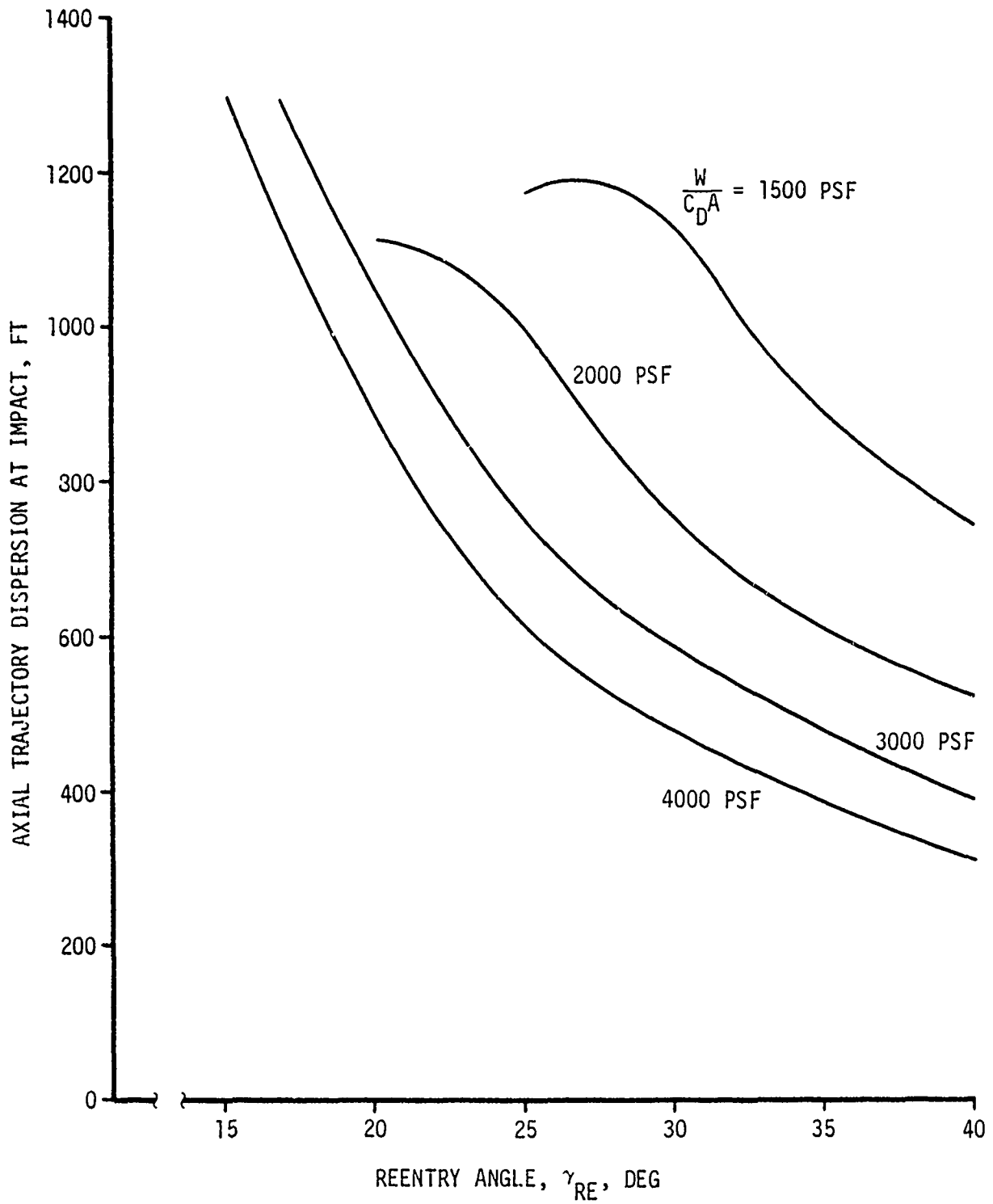


Figure 3.28 Axial Impact Dispersion Due to 2.5 Percent Drag Variation

reentry angle-of-attack uncertainties resulting from RV deployment have been considered in this section.

During RV separation from the booster and spin stabilization there are several error sources which contribute to misalignment of the RV with respect to its desired orientation. This in turn produces an angle-of-attack at reentry. The reentry angle-of-attack produces induced drag and the variability in angle-of-attack results in a variation of total drag about the nominal value based on typical initial angle-of-attack conditions. Any nonzero angle-of-attack, regardless of its orientation, induces additional drag and, in the absence of lift induced effects, causes the RV to impact uprange of its intended target unless some nonzero angle-of-attack was assumed in targeting the RV.

Uprange impact misses resulting from various values of initial angle-of-attack at reentry are presented on Figure 3.29 for various ballistic coefficients and reentry angles. The specific mass properties and aerodynamic coefficients specified in Appendix A were used and thus defined the angle-of-attack convergence. The behavior is believed to be typical of most high ballistic coefficient vehicles. The results should be treated as approximate since certain assumptions were made to preclude lift effects. Additional discussion of this effect is contained in Section 3.4.

Use of Figure 3.29 to predict impact dispersions requires knowledge of both the mean and standard deviation of the angle-of-attack. This is often accomplished by a Monte Carlo analysis of the separation and spin-up sequence to determine the vehicle orientation relative to its velocity vector at reentry. The results of such an analysis yield the mean angle-of-attack and the standard deviation about the mean. It is observed that if the angle-of-attack can be maintained below five degrees, initial angle-of-attack induced drag effects are negligible compared with

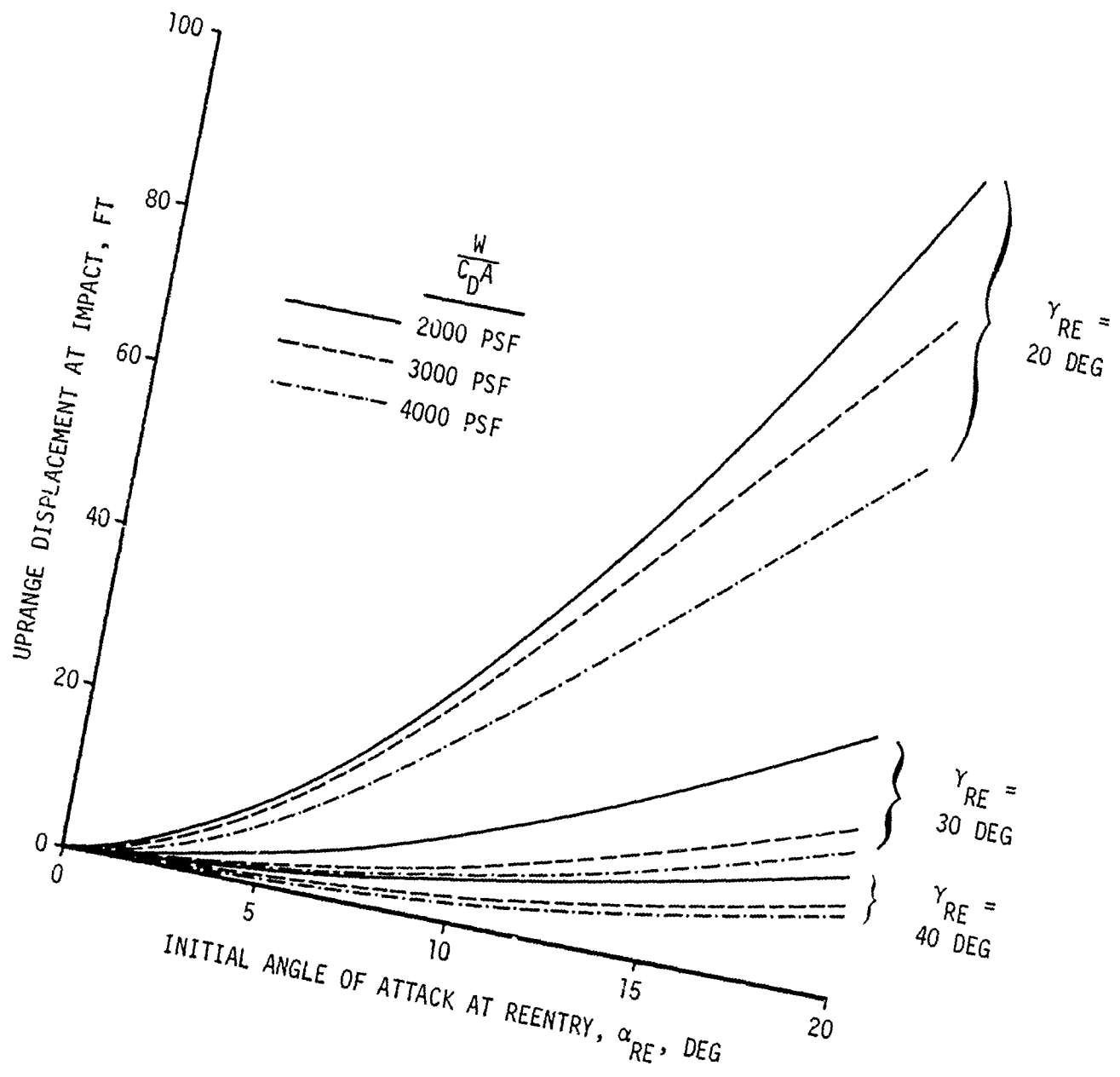


Figure 3.29 Uprange Impact Displacement Due To Angle-of-Attack Induced Drag Effects

Mach number and altitude dependent drag variations. This is believed to be within the tolerance of several deployment systems currently in use.

The combined downrange effect of the various ballistic coefficient uncertainty contributors is presented on Figure 3.30, assuming  $\sigma_{m_a\%} = 10\%$ ,  $(m_a/m_0) = .05$ ,  $\sigma_{C_D\%} = 2.5\%$ , and  $\sigma_{\alpha_0} = 5.0$  degrees. The 2.5% drag uncertainty was found to dominate at all but the lowest reentry angle and ballistic coefficient.

### 3.4 LIFT DISPERSIONS

Lift forces on a reentry vehicle are generally not predictable in targeting a ballistic RV since both the magnitude and direction of the effects are random. Therefore, any net lift will deflect the RV from its nominal non-lifting trajectory, resulting in an impact error. In general, a vehicle will experience instantaneous lift accelerations throughout reentry resulting from its nonzero angle-of-attack. However, for a spinning vehicle the rotation of the vehicle's lift vector about its mean flight path during reentry has the effect of averaging out these lifting forces. Little net lift effect would in fact occur if the angle-of-attack and windward meridian remained constant - or changed very slowly - and the vehicle precessed about its velocity vector. In reality these conditions do not exist and lift effects represent a major contributor to reentry dispersion. At least five lift producing mechanisms exist for high ballistic coefficient vehicles, and include the following in the order in which they occur during reentry:

- Initial angle-of-attack at reentry
- High altitude roll resonance
- Boundary layer transition
- Roll trim
- Low altitude roll resonance

A discussion of these contributors and the results of analytical analyses of each of the above effects are described in this section.

Several of the studies in this section were performed in the non-spinning trajectory coordinate system shown on Figure 3.31. This

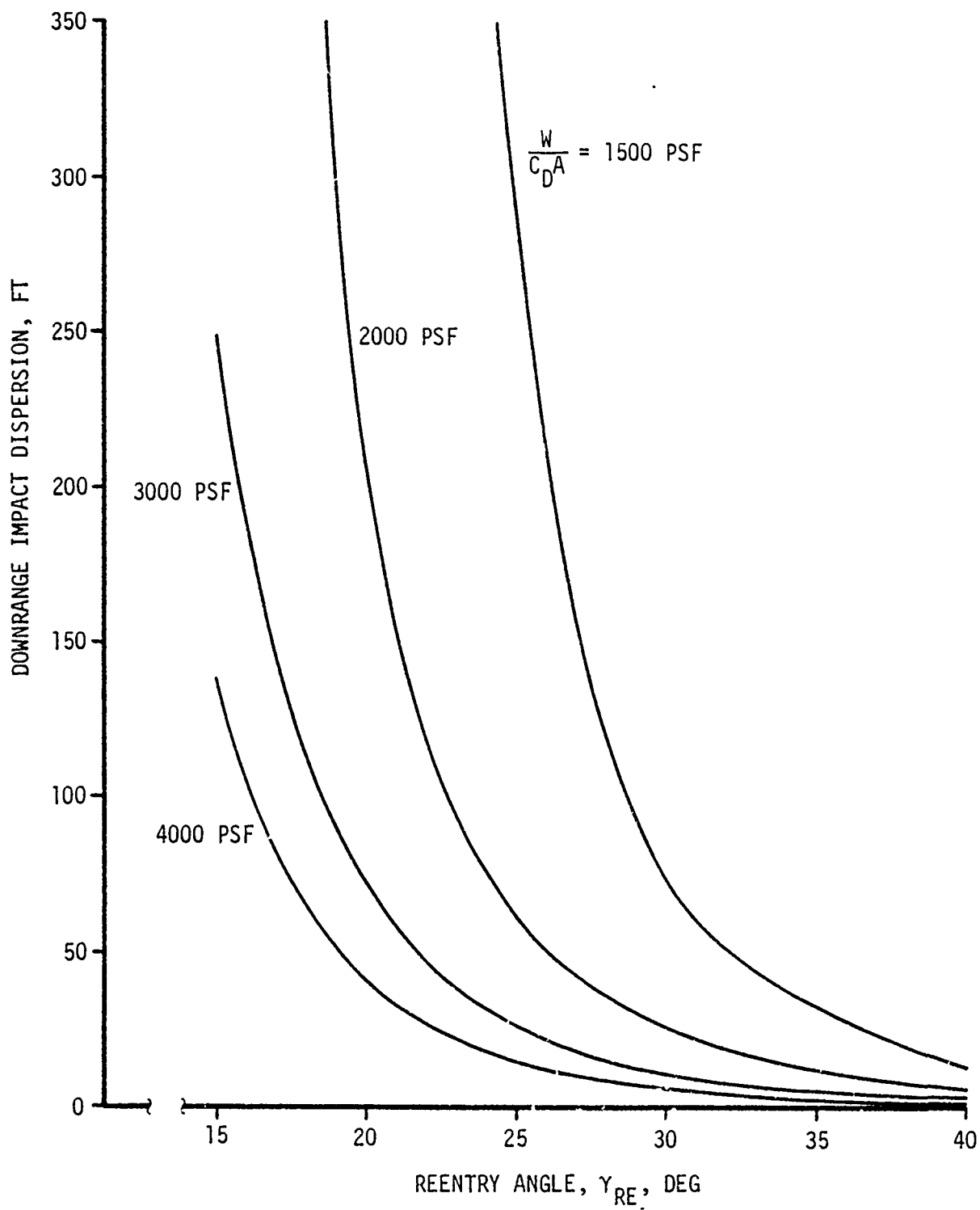


Figure 3.30 Downrange Impact Dispersions Due to Ballistic Coefficient Variations

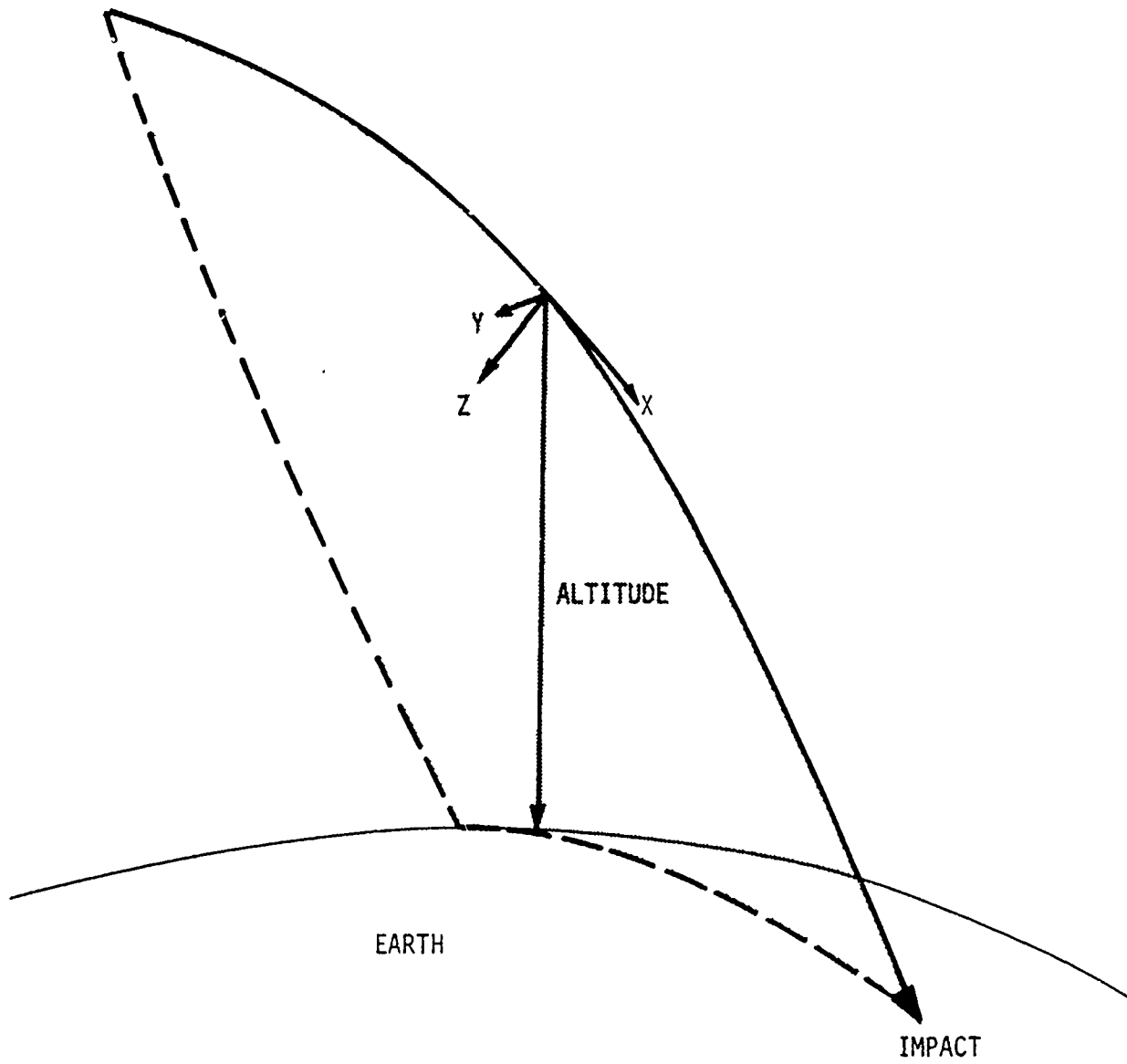


Figure 3.31 Trajectory Coordinate System

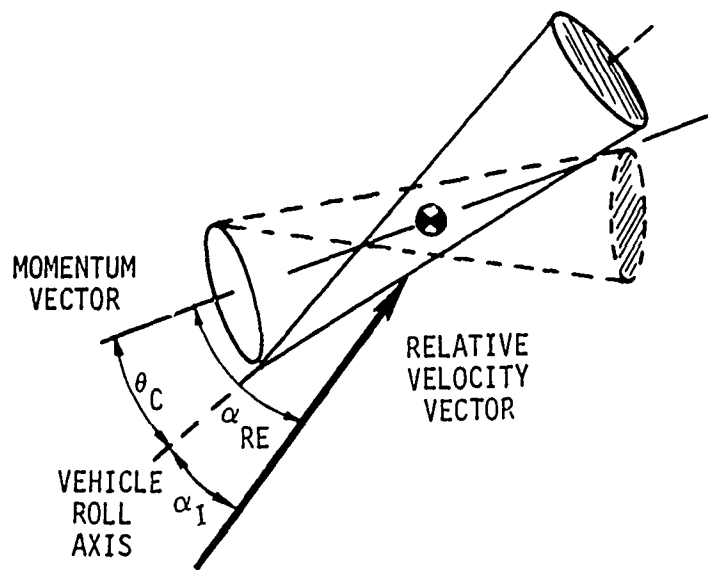
system is a right-handed Cartesian ( $X, Y, Z$ ) system that moves with the vehicle and is fixed at the center of gravity of the vehicle, with the  $X$ -axis directed along the velocity vector. The  $Y$ -axis is perpendicular to the trajectory plane and the  $Z$ -axis is directed toward earth, completing the orthogonal set. This system is particularly convenient for uncoupling lift and drag effects since lift effects will appear as  $Y$  and  $Z$  displacements while  $X$  displacements reflect drag effects. The uncoupling is possible, however, only when negligible bending of the trajectory occurs, typical of high ballistic coefficient vehicles.

### 3.4.1 Initial Angle-of-Attack

The initial angle-of-attack and its effect on drag were described in Section 3.3.2. In that section, it was assumed that the vehicle's angular momentum and velocity vector were coincidental to preclude net lift effects. This situation is, of course, rarely achieved and net lift effects are experienced.

The sketch below illustrates the relationship between the vehicle's roll axis, momentum vector, and velocity vector prior to reentry.

HIGH ALTITUDE VEHICLE CONING MOTION



The angle  $\alpha_{RE}$  refers to the angle between the angular momentum vector and the velocity vector and represents a mean angle-of-attack. The angle  $\theta_C$  refers to the half coning angle between the vehicle roll axis and momentum vector. The instantaneous angle-of-attack,  $\alpha_I$  is the resultant angle between the velocity vector and roll axis and represents the vector sum of  $\alpha_{RE}$  and  $\theta_C$ . It is this angle that causes the instantaneous drag and lift forces. Many factors can contribute to these angles including the accuracy of the guidance and control system, RV deployment mechanism and RV spin stabilization system. A method used to predict the mean and dispersion of  $\alpha_{RE}$  and  $\theta_C$  is a Monte Carlo simulation which was previously discussed in Section 3.3.2 and consists of modeling the event using manufacturing tolerances or design criteria. The resulting mean can be used for targeting the mission and the uncertainty used for determining its contribution to the impact dispersion.

The effect which  $\alpha_{RE}$  and  $\theta_C$  have on the trajectory during reentry and at impact is dependent on those parameters which govern the RV dynamics during reentry including ballistic coefficient, mass properties, aerodynamic coefficients, roll rate, etc. The limited scope of this study precluded studying the effect of all these parameters in extensive detail, however, several trajectory simulations were made varying some of these parameters to determine how and where the lift effects develop, and what effect each parameter has on the trajectory. Typical aerodynamic and mass properties for a high ballistic vehicle were used as given in Appendix A.

The specific parameters that were varied were restricted to the reentry angle, ( $\gamma_{RE}$ ), half coning angle ( $\theta_C$ ), and mean reentry angle-of-attack ( $\alpha_{RE}$ ). Results of the study are contained in Figures 3.32 through 3.35 which present position residuals in a trajectory coordinate system. Each plot compares a six degree of freedom trajectory simulation, initialized with the parameters shown, with a non-lifting point mass simulation. The momentum vector was initialized in an orientation that results primarily in a crossrange (Y) displacement. An orientation could have been chosen to maximize the Z - displacement, but the displacements

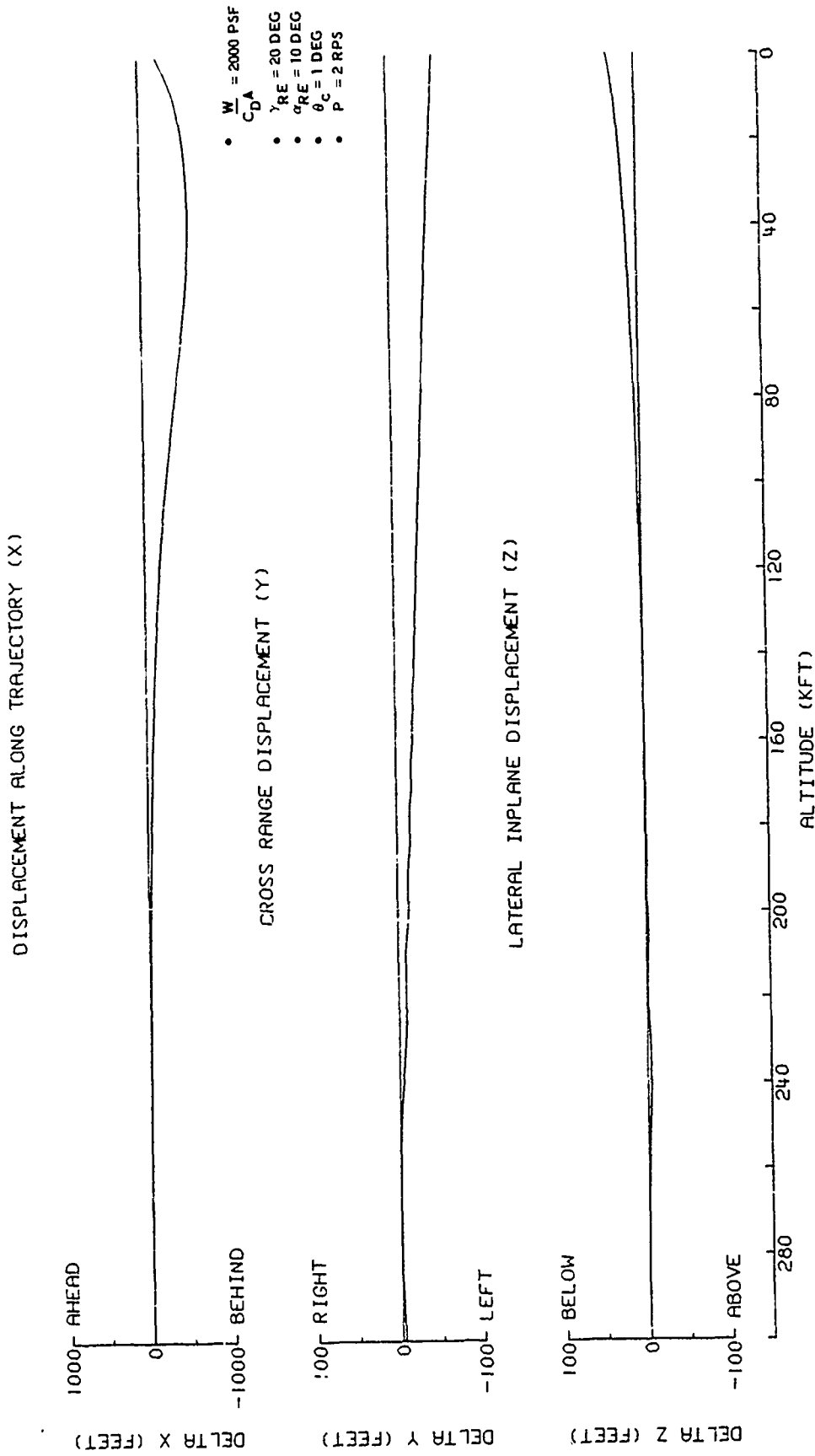


Figure 3.32 Trajectory Displacements Due to Initial Angle-of-Attack

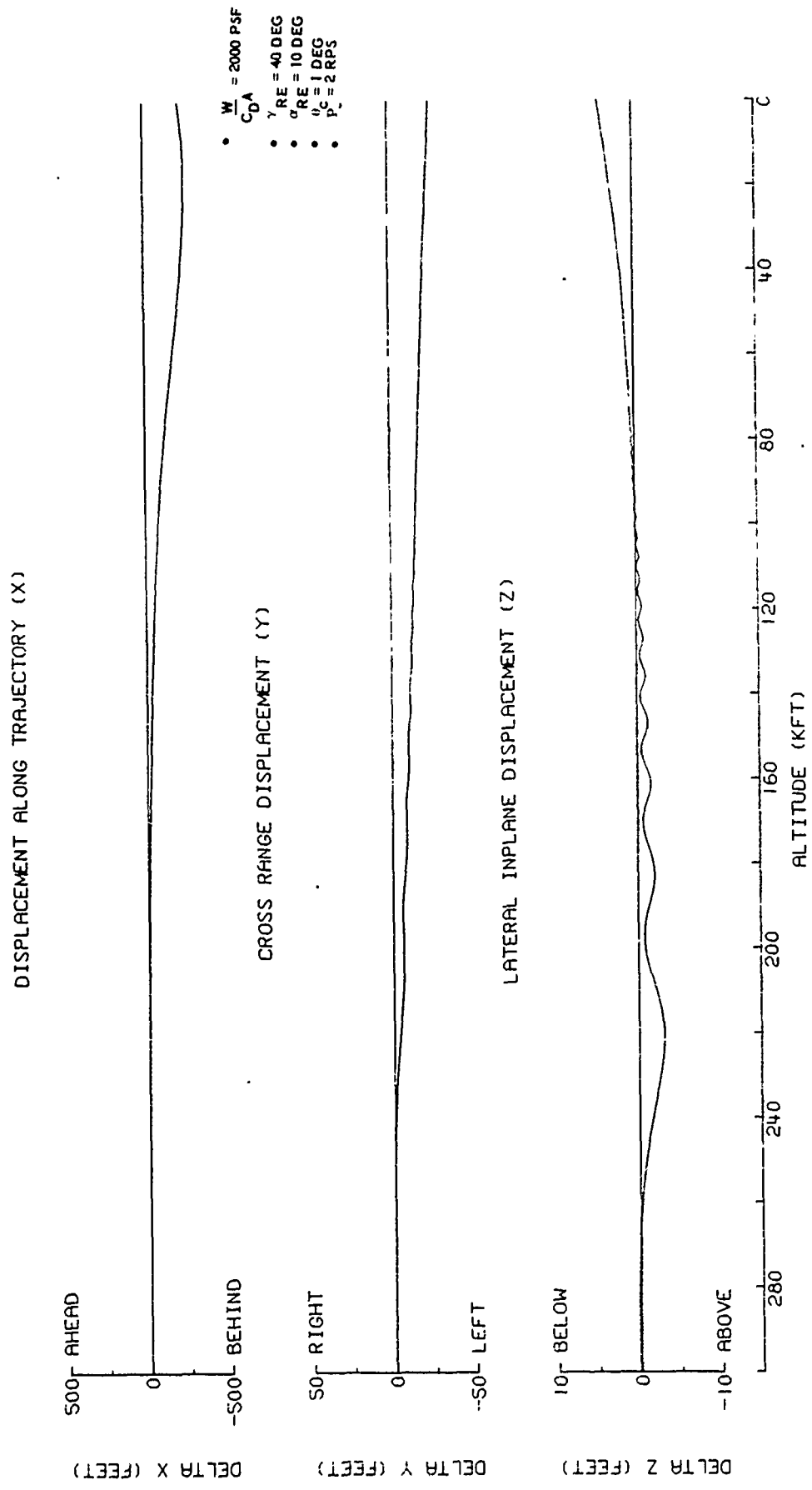


Figure 3.33 Trajectory Displacements Due to Initial Angle-of-Attack

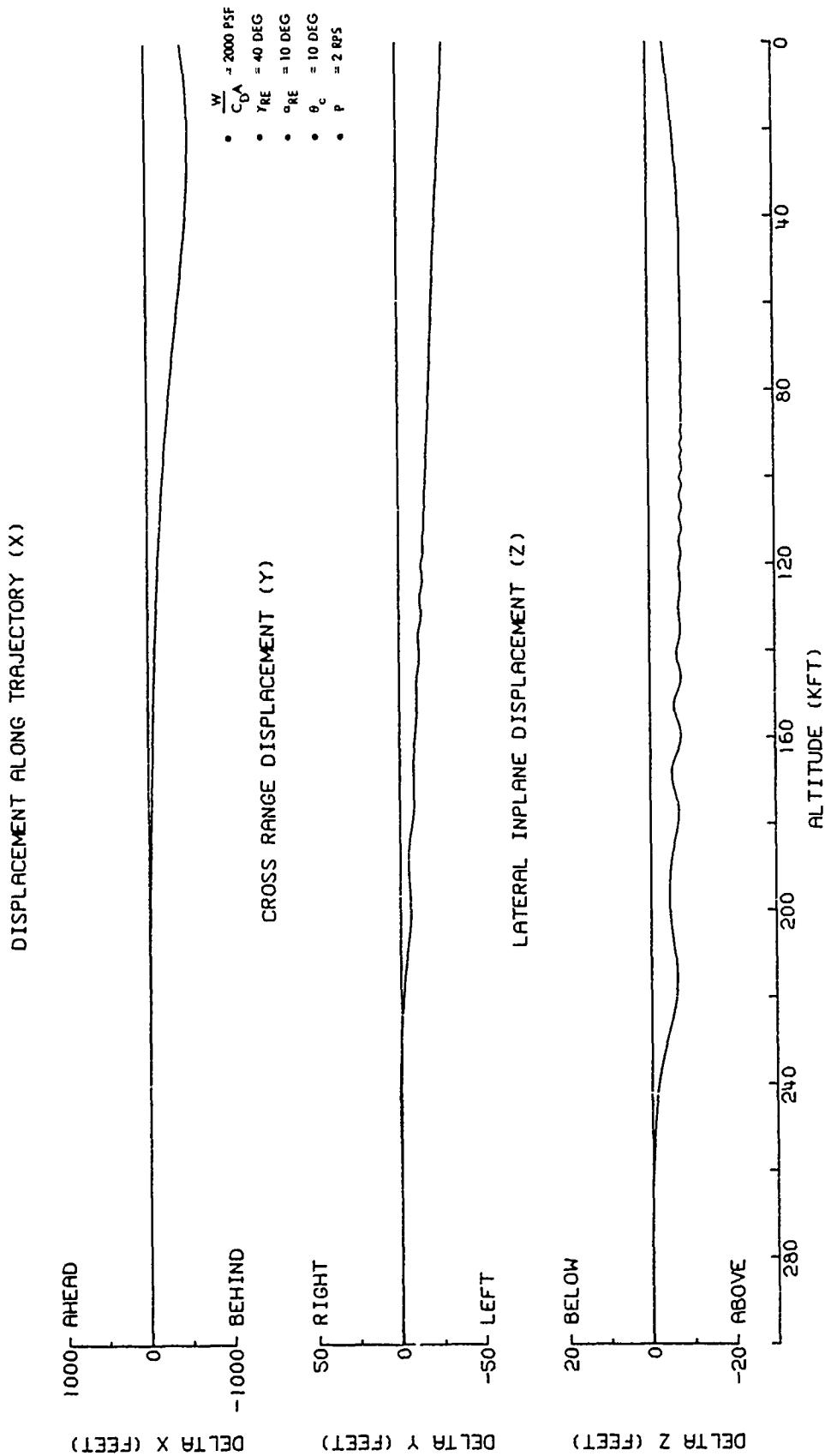


Figure 3.34 Trajectory Displacements Due to Initial Angle-of-Attack

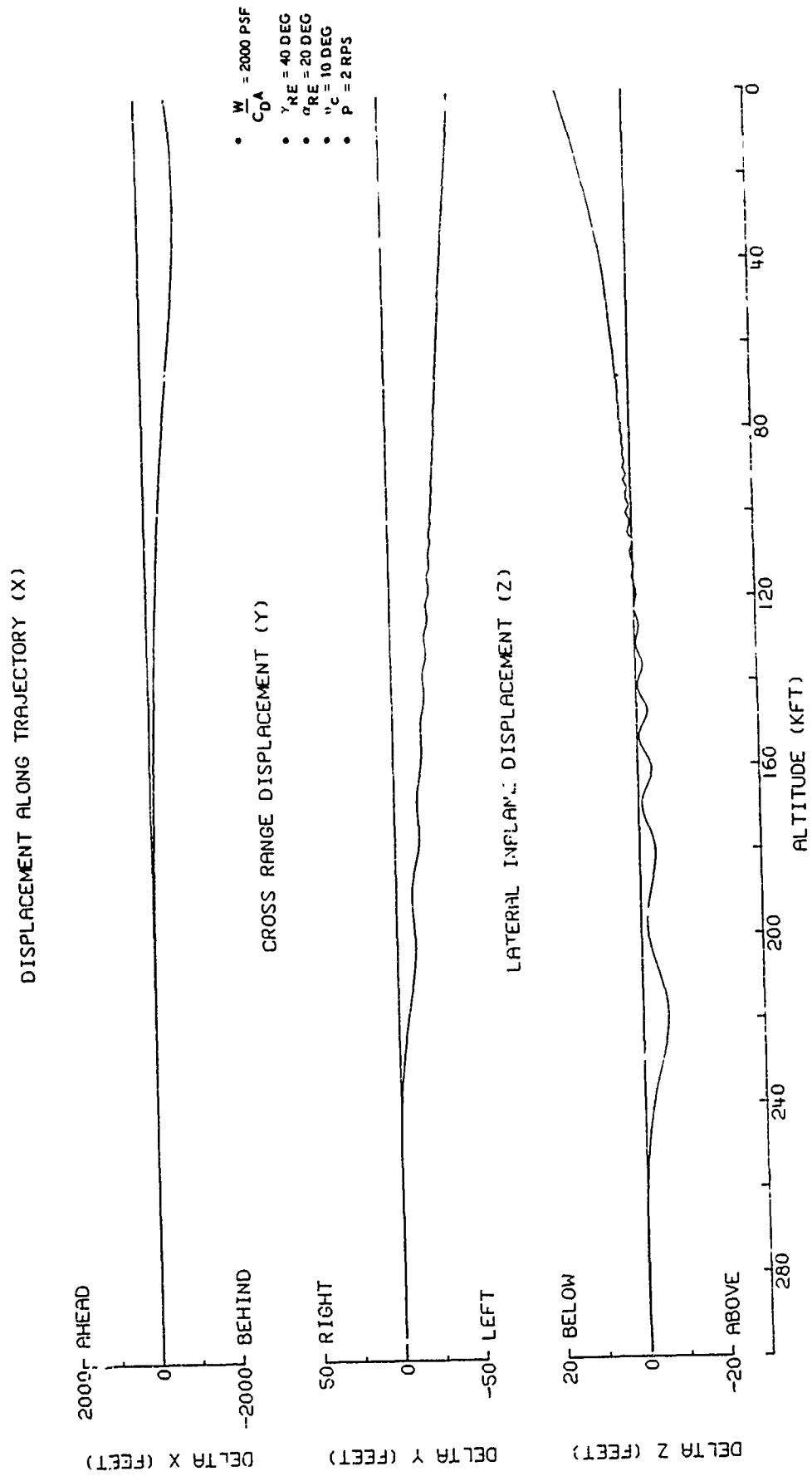


Figure 3.35 Trajectory Displacements Due to Initial Angle-of-Attack

would have been nearly identical to the Y - displacement, except at low altitudes where the trajectory bends and the increased drag due to the angle of attack results in a Z displacement.

The significant conclusions that may be drawn from the Figures are the following:

1. Lift and drag effects resulting from an initial angle-of-attack are evident at a fairly high altitude, with a noticeable deflection of the trajectory occurring near 250 KFT.
2. The reentry angle,  $\gamma_{RE}$ , has a large effect on both lift and drag. The dispersions are inversely proportional to  $\gamma_{RE}$  (Figures 3.32 and 3.33).
3. The half coning angle,  $\theta_c$ , has a small effect on lift, but significant affect on drag (Figures 3.33 and 3.34).
4. The mean angle-of-attack,  $\alpha_{RE}$ , has a significant effect on both lift and drag (Figures 3.34 and 3.35).

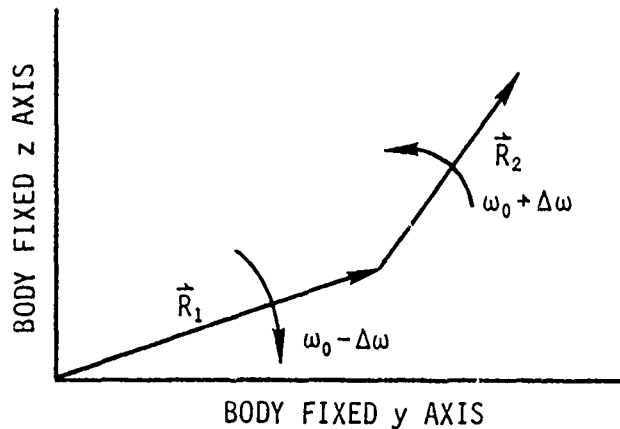
Other parameters, including mass properties, aerodynamic characteristics and roll rate were not included in the limited study but are known to have an important effect on the high altitude lift dispersion.

#### 3.4.2 High And Low Altitude Roll Resonance

The dynamic spin motion experienced during reentry becomes more complex as the aerodynamic forces modify the exoatmospheric coning motion. An excellent mathematical derivation of this motion is contained in Reference 4. The results are summarized in this section for the purpose of explaining the mechanics of roll resonance and determining where it is expected to occur.

The motion of the RV spin axis as viewed from a spinning coordinate system fixed to the RV may be thought of in terms of two vectors representing angle-of-attack components revolving in different directions at different rates as shown in the sketch below:

DYNAMIC SPIN MOTION DURING REENTRY



The basic vehicle motion is thus represented by the vector  $\vec{R}_1$  which rotates at a rate  $\omega_0 - \Delta\omega$  with an angular magnitude of  $R_1$  with a superimposed vector  $\vec{R}_2$  which rotates in an opposite direction from  $\vec{R}_1$  at a rate  $\omega_0 + \Delta\omega$  with an angular magnitude  $R_2$ . The rates  $\omega_0$  and  $\Delta\omega$  are given by the following relationships:

$$\omega_0 = \frac{1}{2I_x} \sqrt{ \left[ -\frac{4C_{m\dot{\alpha}}}{I'} + p^2 \frac{I_x^2}{I'^2} - \left( \frac{C_{N\dot{\alpha}}}{m'} + \frac{C_{m\ddot{\alpha}}}{I'} \right)^2 \right] + \sqrt{ \left[ -\frac{4C_{m\dot{\alpha}}}{I'} + p^2 \frac{I_x^2}{I'^2} - \left( \frac{C_{N\dot{\alpha}}}{m'} + \frac{C_{m\ddot{\alpha}}}{I'} \right)^2 \right]^2 + 4 \left[ p \frac{I_x}{I'} \left( \frac{C_{N\dot{\alpha}}}{m'} + \frac{C_{m\ddot{\alpha}}}{I'} \right) + 2p \frac{C_{m\ddot{\alpha}}}{I'} \right]^2 } }$$

where  $I = I_y = I_z$ .

and  $\Delta\omega = p(1 - I_x / 2I)$ .

Neglecting the comparatively small damping terms and  $C_{N\dot{\alpha}}/m$  the expression reduces to the more usual expression for  $\omega_0$ :

$$\omega_0 = \sqrt{ \frac{-C_{m\dot{\alpha}} dAq}{I} + \left( \frac{p I_x}{2 I} \right)^2 }$$

For exoatmospheric motion the dynamic pressure is nearly zero resulting in  $\omega_0 = pI_x / 2$ . If the two rotational rates are referenced to a non-spinning reference frame these frequencies become:

$$\begin{aligned} \omega_0 - \Delta\omega + p &= \omega_0 + \frac{pI_x}{2I} = \frac{pI_x}{I} \quad (\text{precession}) \\ \omega_0 + \Delta\omega + p &= \omega_0 - \frac{pI_x}{2I} + 2p = 2p \quad (\text{nutaton}) \end{aligned}$$

The above expressions are the familiar exoatmospheric precession or coning frequency ( $pI_x / I$ ), and nutation ( $2p$ ).

Prior to reentry the rate  $\omega_0 - \Delta\omega$  is negative and equal to  $-p(1 - I_x / I)$ . However, as reentry progresses the dynamic pressure and hence  $\omega_0$  increases, causing  $\omega_0 - \Delta\omega$  to increase in a positive sense until at some time the vector  $\vec{R}_1$  reverses direction relative to the vehicle. This is the condition referred to as roll resonance and results in a divergence of the resultant angle-of-attack,  $\vec{R}_1 + \vec{R}_2$ . The magnitude of this divergence is governed by the damping parameter  $\lambda_0 / \omega_0$  where

$$\lambda_0 = -\frac{1}{2} \left( \frac{C_{N\alpha}}{m'} - \frac{C_{m\dot{\theta}}}{I'} \right)$$

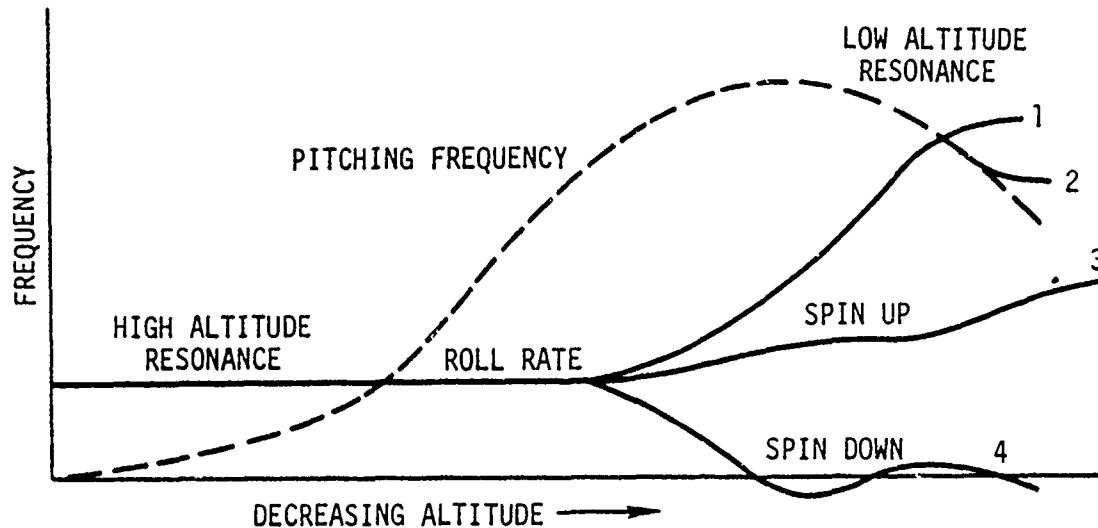
The condition for roll resonance is then  $\omega_0 = \Delta\omega$ . This is equivalent to the following after some manipulation.

$$\sqrt{\frac{-C_{m\alpha} dAq}{I}} = p \left( 1 - \frac{I_x}{I} \right)^{1/2}$$

The quantity on the left is the natural pitching frequency of the RV,  $f_N$ , in the absence of a spin rate. Furthermore, for slender high ballistic coefficient vehicles the roll moment of inertia is usually much less than the pitch and yaw moments ( $I_x \ll I$ ). The condition for roll resonance may then be approximated by  $p = f_N$ . Hence, whenever the vehicle natural pitch frequency approaches the vehicle spin rate, a resonance condition occurs and the vehicle angle-of-attack of the vehicle at that point will be amplified by the resonance condition, resulting in increased lift and drag. Typical roll rate and natural pitch frequency for a high ballistic coefficient vehicle are presented

below:

ROLL RATE AND PITCHING FREQUENCY BEHAVIOR DURING REENTRY



The sketch illustrates the typical behavior that roll rate and pitching frequency exhibit during reentry, and shows that roll resonance may occur at low as well as high altitude. High altitude roll resonance occurs when the vehicle's pitching frequency increases and passes through the roll rate frequency. This typically occurs above 100 KFT, and the resulting lift and drag effects are usually not severe due to the low dynamic pressure in this region.

If roll torques should develop during reentry which cause the vehicle spin rate to increase, the roll rate may again cross through the natural pitching frequency with a resonant condition. This typically occurs at low altitude in a region of decreasing dynamic pressure and natural pitching frequency as shown in the sketch for cases 1 and 2. If the vehicle center of gravity offset and trim angle-of-attack happen to be of sufficient magnitude and at the correct orientation a roll torque will be developed which will tend to decrease the roll rate to match the natural pitching frequency and result in "lock in" phenomenon as shown in

case 2.

The roll torques experienced during reentry may cause the vehicle spin rate to increase as in case 3 which avoids low altitude roll resonance. However, the roll trim phenomena, discussed in Section 3.4.4, is accentuated by a low spin rate and can result in even larger dispersions than for the low altitude roll resonance condition. Finally, the roll torques may cause the vehicle to roll down through zero roll rate, similar to case 4. Under this condition the lift vector is no longer rotating, resulting in dispersions of very large magnitude. This condition must be avoided for an accurate reentry system.

The two most important parameters determining the magnitude of roll resonance dispersions are (1) the magnitude of the roll resonance induced angle-of-attack divergence and (2) the altitude of the roll resonance phenomena. Both of these quantities are dependent upon the vehicle's aerodynamic and mass properties, the vehicle's roll rate, and the reentry conditions including dynamic pressure and reentry angle. The magnitude of the roll resonance divergence is dependent upon the damping characteristics which can vary significantly for different vehicles. The effect of the roll resonance on the trajectory is generally not very significant unless the angle-of-attack divergence is excessive or it occurs at a low altitude.

The altitude of the roll resonance phenomenon can be estimated from the resonance criteria given previously. Equating  $p^2 = f_H^2$  yields:

$$-\frac{C_{m\alpha} dA q_{Res}}{I} = p^2$$

or rearranging terms yield the desired expression:

$$q_{Res} = \frac{I p^2}{-C_{m\alpha} dA}$$

Thus given the vehicle's aerodynamic and mass properties and spin rate the dynamic pressure required for resonance may be determined. The dynamic pressure altitude correlation then provides the resonance altitude.

For altitudes above 100 KFT the dynamic pressure history, and hence roll resonance altitude, is nearly independent of reentry angle and ballistic coefficient. Figure 3.36 presents the parameter  $I/C_m dA$  as a function of the corresponding altitude of roll resonance for various roll rates. Typical values of  $I/C_m dA$  for high ballistic coefficient vehicles are above 10 slug/ft. In this region the altitude of roll resonance is observed to be determined primarily by its roll rate, with only a weak dependence on the aerodynamic and mass properties. For purposes of this error budget study it was assumed that high altitude roll resonance would occur at an altitude sufficiently high to preclude significant lift effects. This will probably require roll rates of 2 RPS or less. Once a vehicle configuration is chosen then studies need to be performed to determine the expected dispersions resulting from high altitude roll resonance.

#### 3.4.3 Boundary Layer Transition Instabilities

During reentry the aerodynamic boundary layer on the surface of the reentry vehicle transitions from a laminar to turbulent condition. The transition results in a marked change in boundary layer velocity profile, heat transfer rates and thickness. Transition depends on critical Reynolds number and typically begins in the region of 70 KFT to 100 KFT altitude. It has been observed that transition on high ballistic coefficient vehicles tends to occur fairly rapidly and often asymmetrically about the vehicle resulting in impulsive moments being applied to the vehicle. This, coupled with the vehicle dynamics, results in a divergence of the vehicle's oscillatory angle-of-attack history in the region of boundary layer transition. Typically, the angle-of-attack oscillations occur in a region where the dynamic pressure is beginning to increase to a significant level and the lateral loads on the vehicle reach moderate proportions. Since the phenomenon is asymmetric in nature and typically produces lateral loads which persist for less than a full revolution of the vehicle, there

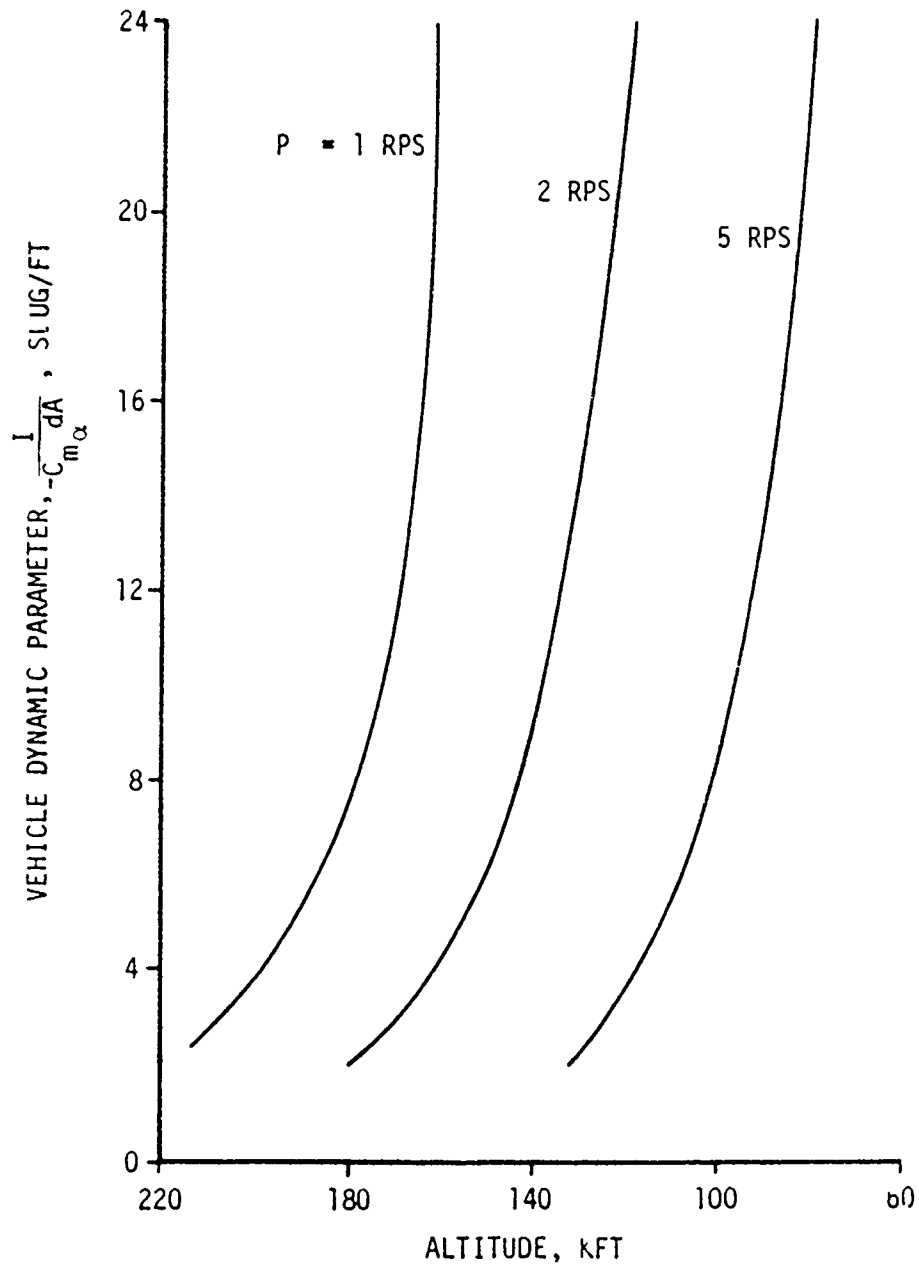


Figure 3.36 Roll Resonance Altitude for Various Roll Rates

is an opportunity for lift dispersion to develop during the boundary layer transition process. It is not uncommon to experience one to two degrees angle-of-attack divergence during this period.

A detailed analyses of transition effects was not performed, since like roll resonance, these effects are very vehicle dependent. However, some aspects of the roll trim discussion, discussed next, may be applied to transition induced dispersions.

#### 3.4.4 Roll Trim Dispersions

Roll trim dispersions result from lift forces being applied to the vehicle in such a manner that they are not cancelled by the vehicle spin rate. In general, this occurs when the lift direction or magnitude shifts at a rate significantly faster than the roll rate of the vehicle, so that an asymmetric lift force is present for only a portion of one revolution. It is the change in lift vector rather than the steady state value which is most critical in determining the magnitude of the roll trim dispersion. The mechanisms for developing a changing lift force on the vehicle include transition instability (Section 3.4.3), asymmetric ablation either on nose tips or antenna windows, spallation of heat shield or nosetip materials, etc.

Roll trim dispersions for high ballistic coefficient vehicles have been observed to occur at altitudes ranging up to 70 KFT, corresponding to the beginning of significant ablation effects. The resulting dispersion is often the largest contribution to reentry miss and has received extensive analysis during the past few years. Figure 3.37 presents a typical angle-of-attack history and the associated windward meridian for a high ballistic coefficient reentry vehicle. The figure clearly shows boundary layer transition occurring at 88 KFT with its associated angle-of-attack divergence and subsequent damping. Note that the windward meridian is constantly changing in this region. At 30 KFT the figure also shows an apparent trim angle developing with the characteristic constant windward

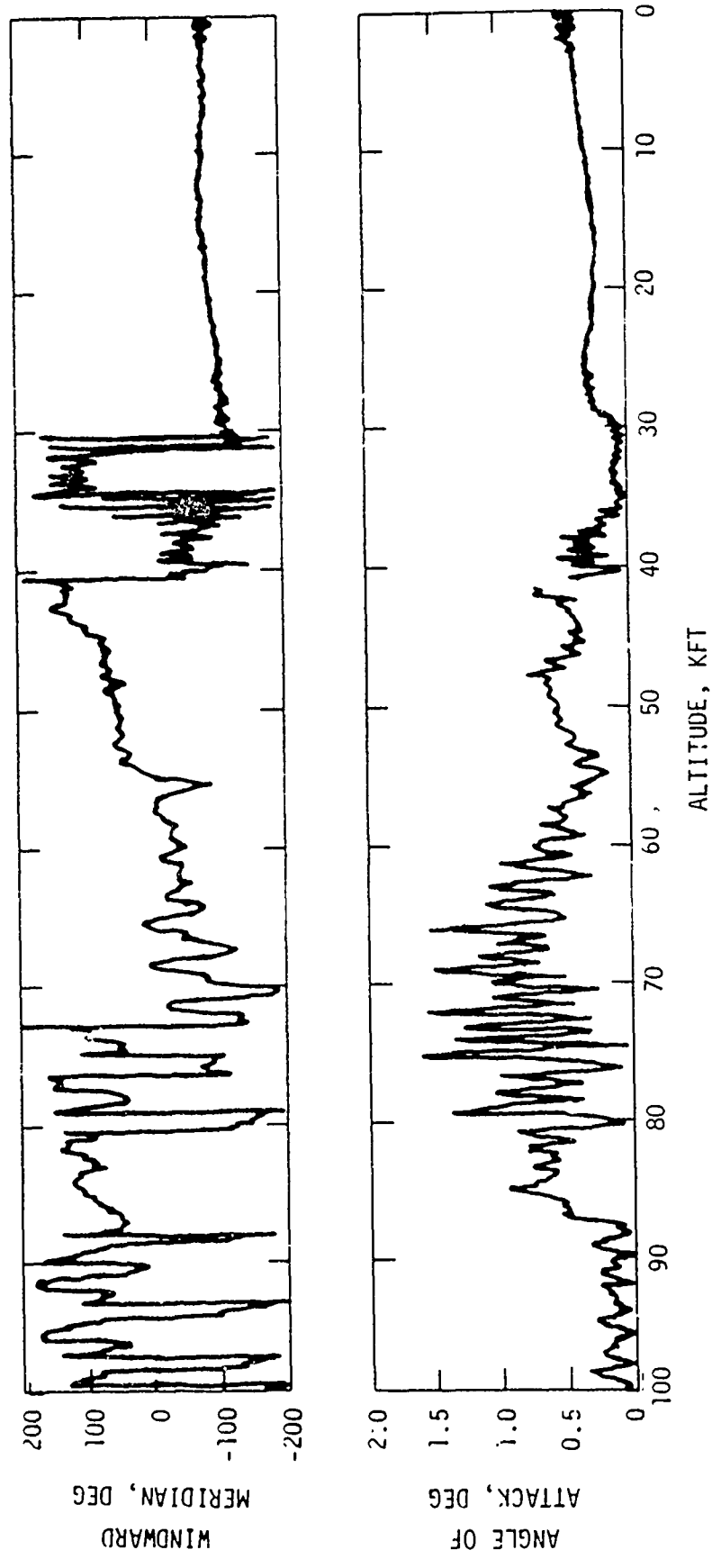


Figure 3.37 Typical Angle of Attack and Windward Meridian History During Reentry

meridian. This condition is what is commonly referred to as roll trim.

Roll trim effects are dependent upon many vehicle parameters, including roll rate, trim angle, static margin, lift coefficient, altitude and others. This dependency is evident from the following analytical relationship derived in Reference 5 for a high ballistic coefficient vehicle experiencing a step change in the trim angle-of-attack,  $\Delta\alpha_T$ :

$$R = 1/2 \left( C_{N_\alpha} A/m \right) \left( \rho v h / \sin \gamma \right)_h \left( \Delta\alpha_T / p \right) \quad (3.1)$$

where the quantity  $(\rho v h / \sin \gamma)_h$  is computed at the altitude,  $h$ , of the trim angle change. The displacement  $R$  is measured in a direction normal to the trajectory at impact and can be of an arbitrary orientation. The amount of roll trim deflection per degree of trim,  $R/\Delta\alpha_T$ , is then dependent on the vehicle parameter  $C_{N_\alpha} A/m$ , the trajectory parameter  $\rho v h / \sin \gamma$ , and roll rate  $p$ . Figure 3.38 parametrically presents  $R/\Delta\alpha_T$  as a function of the altitude at which the step change in trim occurs for reentry angles of 20 and 40 degrees and for ballistic coefficients of 2000 and 4000 psf with masses of 11 and 22 slugs respectively. These influence coefficients indicate that the vehicle is increasingly sensitive to trim angle changes down to about 40 KFT due to the rapid increase in density. Below this altitude, the velocity and altitude term  $(vh)$  decrease more rapidly than the increase in density resulting in a decreasing sensitivity. All calculations were performed assuming a 2 RPS roll rate.

The analytical relationship for roll trim assumes that a trim angle change occurs as a step function. In reality, the trim may develop in a different fashion. To study this problem, and to provide a check on the results on Figure 3.38, a series of six-degree of freedom trajectory simulations were made. Three different shapes of trim angle development were studied: a step function, a ramp function and a square wave function change.

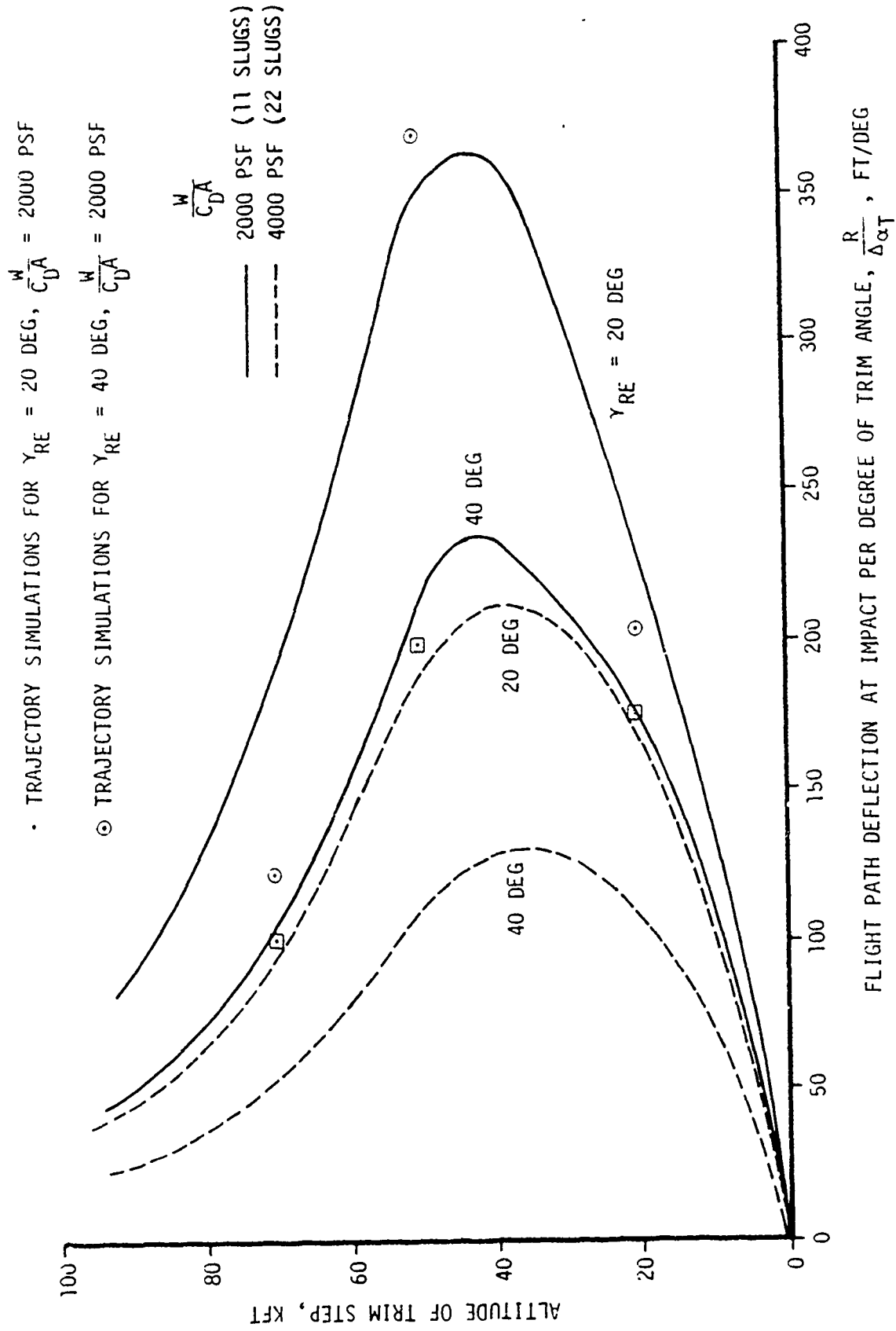
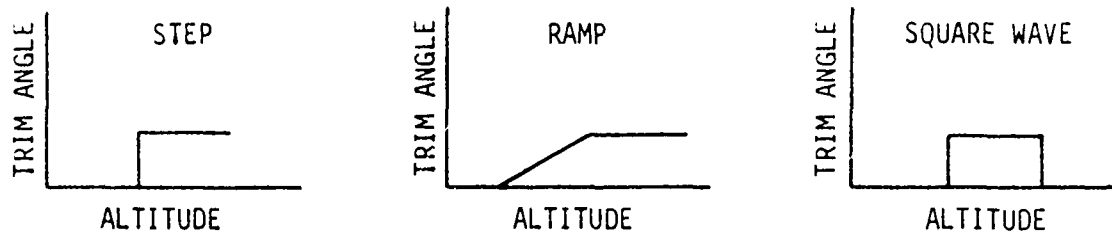


Figure 3.38 Effect of Step Change in Trim Angle on Impact Displacement for Two RPS Spin Rate

## DIFFERENT TRIM ANGLE DEVELOPMENT HISTORIES



In performing the six degree of freedom simulations the following parameters were held constant:

- Trim Angle Change ( $\Delta\alpha_T$ ) = 1 degree
- Ballistic Coefficient ( $W/C_D A$ ) = 2000 psf
- Vehicle Mass = 11 slugs
- Constant Roll Rate (P) = 2 RPS
- Constant Windward Meridian

Results of the simulations are presented on Figures 3.39 through 3.42 for a step function at 70 KFT, ramp functions from 70 KFT to 65 KFT (equivalent to about 1 roll revolution) and from 70 KFT to 50 KFT, and finally a square wave function. The displacement along the trajectory (x) is significant for all cases, reflecting angle-of-attack induced drag effects. Displacements in the crossrange (y) direction are exclusively due to lift effects, while lateral in plane displacements (z) are primarily due to lift effects with secondary effects caused by the difference in trajectory bending resulting from the difference in drag profiles. Drag effects on the velocity profile and subsequent z-displacements are evident at lower altitudes and appear as a curve in the z-displacement.

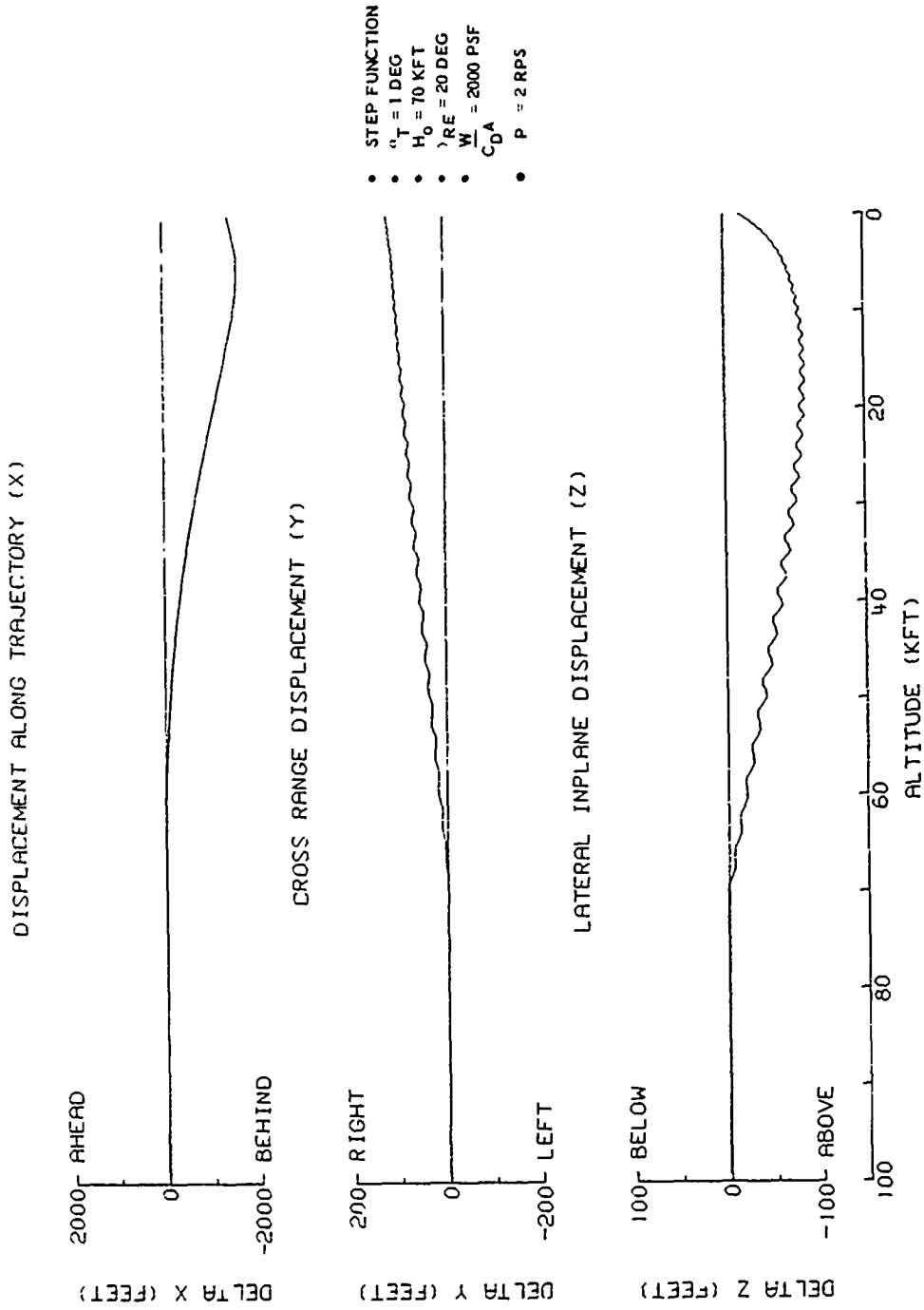


Figure 3.39 Trajectory Coordinate Comparison for Roll Trim Simulations

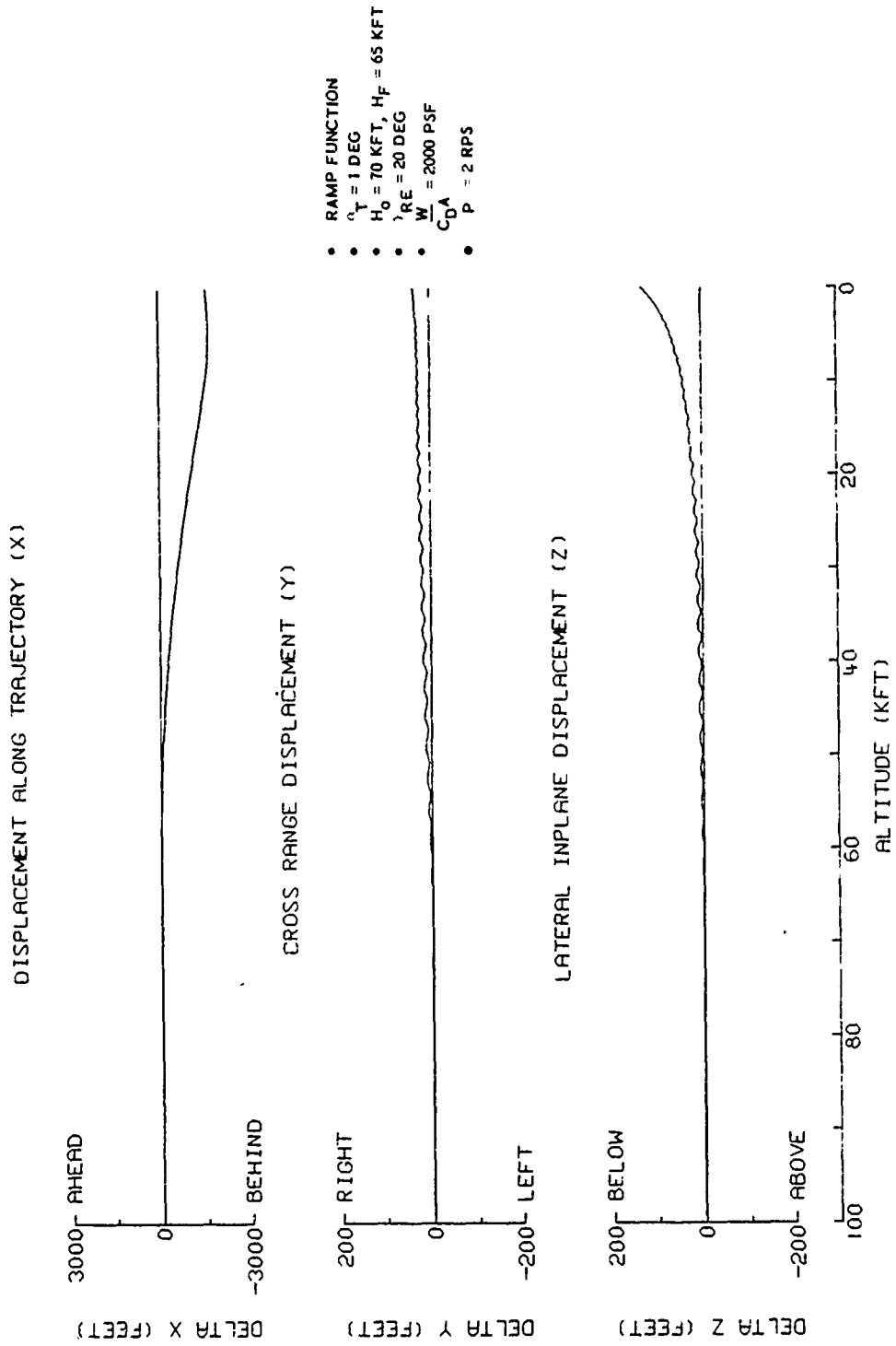


Figure 3.40 Trajectory Coordinate Comparison for Roll Trim Simulations

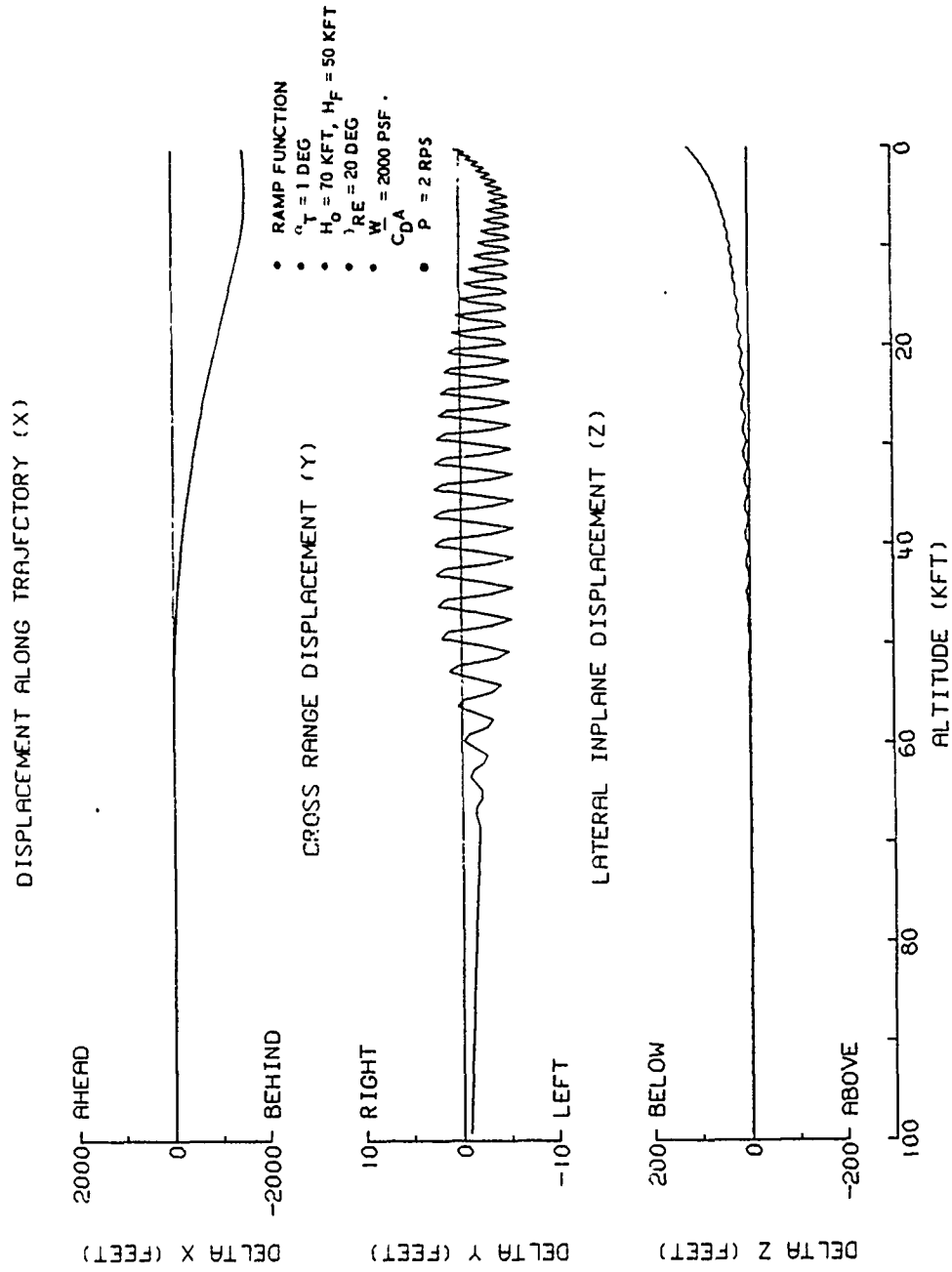


Figure 3.41 Trajectory Coordinate Comparison for Roll Trim Simulations

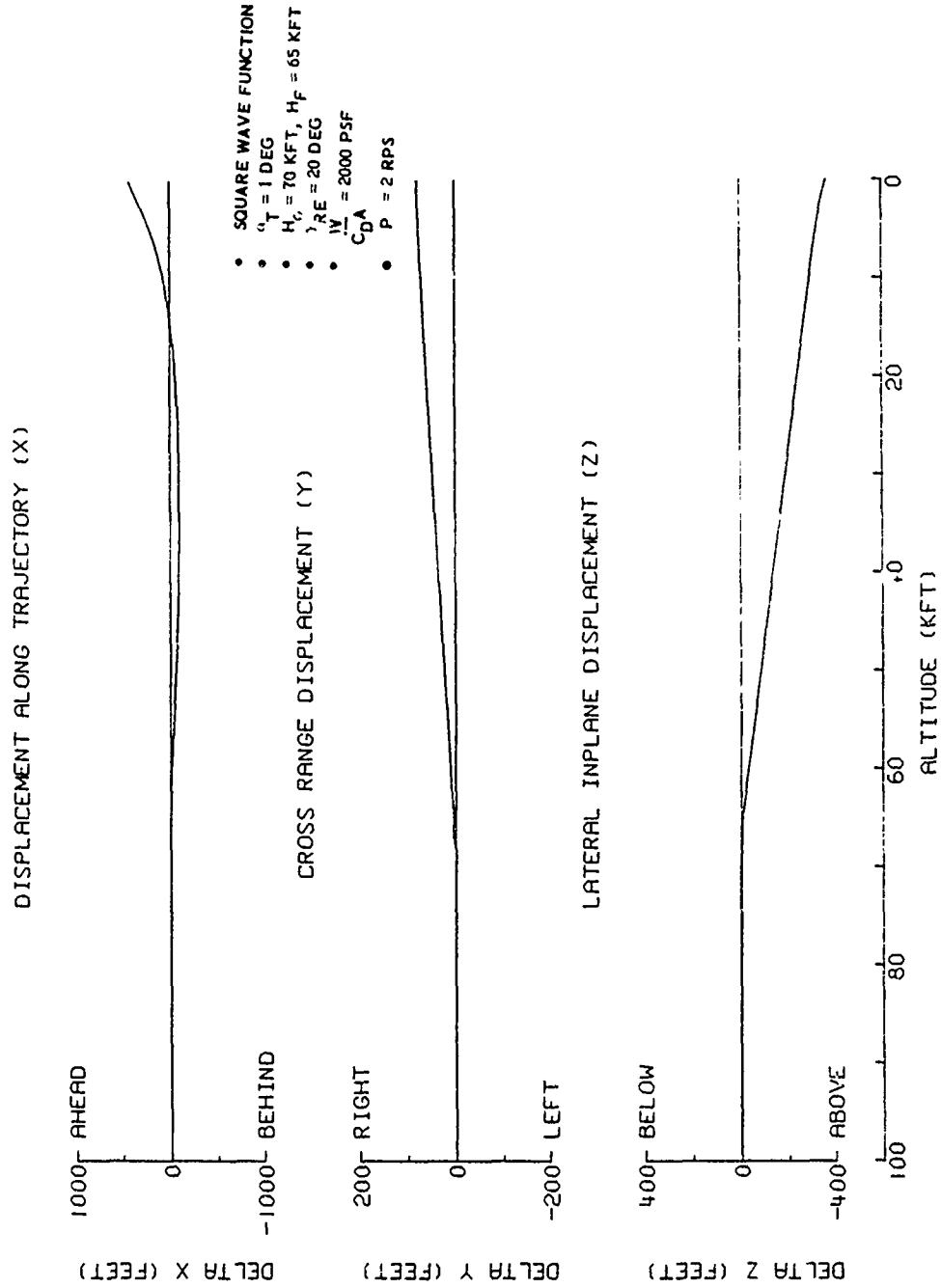


Figure 3.42 Trajectory Coordinate Comparison for Roll Trim Simulations

Several observations can be made from a comparison of these figures. First, application of any trim condition causes a sudden change in the vehicles flight path with a resulting linearly increasing trajectory displacement history (i.e.  $dY/dh = \text{constant}$ ) after application of the perturbation. Comparison of Figures 3.39 and 3.40 indicates that a ramp function can significantly modify the trajectory displacement magnitude relative to the step function results. If the ramp is very long in duration, as in Figure 3.41, almost no displacement occurs. Hence, the displacement resulting from a ramp function is dependent upon the length of the ramp. The square wave trim angle change of Figure 3.42 appears to increase the trajectory displacement, as evidenced by the larger Z displacement in Figure 3.42. This is expected since the square wave is equivalent to applying a step function twice. It may be concluded that the manner in which the trim angle develops is a major factor in determining the magnitude of the displacement. Gradually developing trim angles result in small displacements while abruptly developing trim angles result in large displacement.

An actual best estimate of trajectory derived from flight test data is presented on Figure 3.43, showing Y and Z displacements from the non-lifting reference trajectory. The lift induced displacements appear very similar to the displacements of Figures 3.39 through 3.42 derived from the six degree of freedom simulations. Transition or roll trim effects are observed to occur at or slightly above 60 KFT, followed by an apparent change in trim angle at 25 KFT as evidenced by the second slope change of the displacement.

The effect of other parameters on the trajectory, including roll rate, vehicle mass, altitude of trim onset, and trim angle were also studied by a series of six degree of freedom simulations, making a step function change in trim. The results agreed very well with the analytical relationship of Equation 3.1, lending confidence in that model. Some of the resulting impact displacements are presented on Figure 3.38 for comparison.

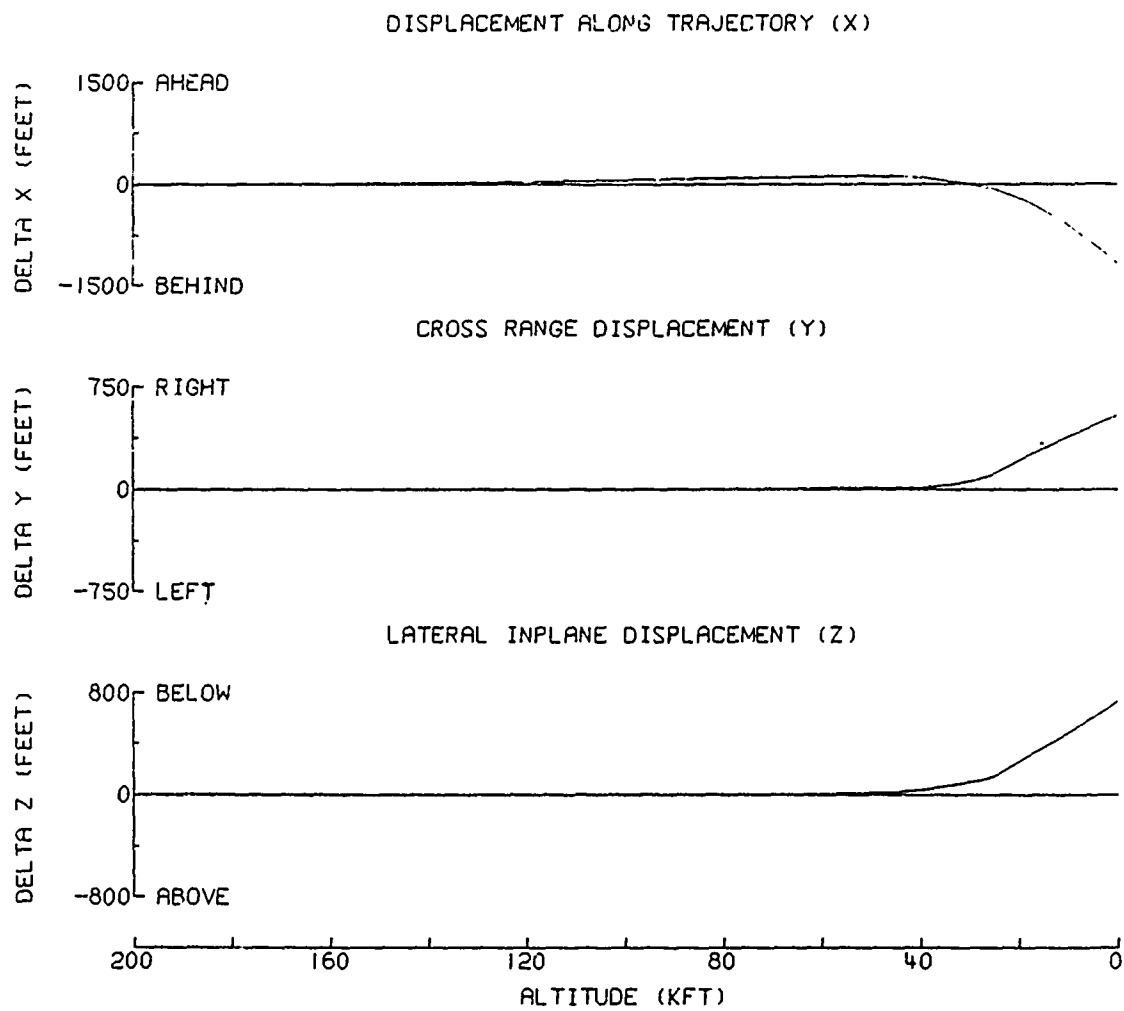


Figure 3.43 Trajectory Coordinate Comparison for Typical Flight Test

The deflection magnitude,  $R$ , for a degree of trim is observed from Figure 3.38 to be significant. Since the onset of trim and hence the orientation of this deflection is random, it can result in downrange or crossrange dispersions. While the crossrange miss will be identical to  $R$ , the downrange miss will be larger and equal to  $R/\sin\gamma$ . Furthermore, if several changes in trim angle develop in a random fashion, the impact dispersion will be an integrated composite of these changes in a statistical sense. Clearly, if one degree trim angles are experienced the potential dispersion is very large.

Methods of reducing the roll trim effect can be found by analyzing some of the terms in Equation 3.1. One obvious way is to increase the mass to area ratio of the vehicle,  $m/A$ . While this approach is a feasible consideration in designing a new vehicle, it would probably result in a higher ballistic coefficient. Associated with this would be a higher velocity at any altitude below 100 KFT, which would partially offset the gain in  $m/A$ . Furthermore, higher ballistic coefficient vehicles experience increased ablation rates, which could aggravate the asymmetric ablation, and hence increase the changes in trim angles.

Another method of minimizing the dispersions is to use a steep reentry angle. The difference between the dispersion for 20 and 40 degree trajectories is almost a factor of two. However, this too could aggravate the asymmetric ablation.

A third method, and the one currently receiving a great amount of attention, is to design a nosetip that will minimize the amount of trim angle that can develop. A step change in trim angle of 0.2 degree, for example, would reduce the values on Figure 3.38 by a factor of five.

A fourth method under consideration is to increase the spin rate. Several factors, however, must be considered as potentially adverse effects of this solution. First, if the higher spin rate is imparted at spin stabilization immediately after deployment, larger spin engine plume induced velocity uncertainties could result in large

impact dispersions. This could be avoided by first spinning the vehicle to a low spin rate at deployment and then increasing the spin rate just prior to reentry, thus reducing the potential impact dispersion. A second factor is the increased danger of roll resonance effects accompanying a higher roll rate. Figure 3.36 reveals that high altitude roll resonance will occur at a lower altitude for an increased roll rate, which in turn can result in larger dispersions due to the increased dynamic pressure. The real danger, however, lies in the potential for low altitude roll resonance to occur at a higher altitude, as evident from the sketch on page 3-56. Resulting dispersions of over 1000 feet have been observed for low altitude roll resonance. A method of overcoming this problem would be to spin the vehicle to a roll rate sufficiently high to preclude both high and low altitude roll resonance. An adverse effect of this solution, however, is that the increased centrifugal loads corresponding to a high roll rate may be sufficient to cause structural failure. It must be remembered that high ballistic coefficient vehicles are frequently observed to roll up to rates several times higher than the initial rate due to roll torques experienced during reentry.

### 3.5 TOTAL REENTRY ACCURACY

The intent of the dispersion studies of Sections 3.2 through 3.4 was to identify the potential dispersion mechanisms, and their relevant altitude regions and magnitudes, for the purpose of selecting sensor measurement requirements in subsequent sections. Since the objective of the study is to consider only improved accuracy reentry vehicles, it is useful to combine the results of the individual dispersion studies to determine if the lower limits of ballistic coefficient and reentry angle initially selected (1500 PSF and 15 degrees respectively) are reasonable for high accuracy.

Table 3.1 presents the reentry error categories including each of the subcategories, the significant parameters necessary to determine

Table 3.1 Summary of Reentry Error Categories, Significant Determining Parameters, and Applicable Figure Numbers

ERROR CATEGORY	REQUIRED PARAMETERS	ASSUMED VALUES OF REQUIRED PARAMETERS FOR ANALYSIS	APPLICABLE FIGURE NO.	
			DOWN	CROSS
Climatology				
1. Density	<ul style="list-style-type: none"> <li>● Dispersion about targeted profile</li> </ul>	Kwajalein annual	3.10	-
2. Winds	<ul style="list-style-type: none"> <li>● Dispersion about targeted profile</li> </ul>	Kwajalein annual	3.19	3.20
Ballistic Coefficient				
1. Mass Loss	<ul style="list-style-type: none"> <li>● Uncertainty</li> <li>● Final mass loss ratio</li> </ul>	10 Percent 0.05	3.23	-
2. Drag Coefficient (Zero angle-of-attack)	<ul style="list-style-type: none"> <li>● Uncertainty</li> </ul>	2.5 Percent	3.27	-
3. Initial angle-of-attack	<ul style="list-style-type: none"> <li>● Mean</li> <li>● Uncertainty</li> <li>● Aerodynamic/mass properties</li> </ul>	5.0 Degrees 3.0 Degrees See Appendix A	3.29	-
Lift				
1. Initial angle-of-attack	<ul style="list-style-type: none"> <li>● Uncertainty</li> <li>● Aerodynamic/mass properties</li> </ul>	Negligible	-	-
2. Roll Resonance	<ul style="list-style-type: none"> <li>● Altitude</li> <li>● Angle-of-attack divergence</li> <li>● Roll rate</li> <li>● Aerodynamic/mass properties</li> </ul>	Negligible	-	-
3. Transition	<ul style="list-style-type: none"> <li>● Altitude</li> <li>● Angle-of-attack divergence</li> <li>● Roll rate</li> <li>● Aerodynamic/mass properties</li> </ul>	Not considered	3.38	3.38
4. Roll Trim	<ul style="list-style-type: none"> <li>● Altitude of trim angle change</li> <li>● Trim angle-of-attack</li> <li>● Roll rate</li> <li>● Aerodynamic/mass properties</li> </ul>	40,000 Feet 0.2 Degree 2 RPS See Appendix A	3.38	3.38

the reentry dispersion, the assumptions made in this study and the appropriate Figure numbers where each of the dispersion values may be found. A sample calculation is presented in the following subsection to indicate how specific dispersions may be determined for a given vehicle using these figures. Subsection 3.5.2 extends these calculations to a range of ballistic coefficients and reentry angles.

### 3.5.1 Sample Dispersion Calculations

This section presents the specific assumptions and calculations necessary to determine the reentry dispersion for a particular reentry vehicle from the material presented earlier in this Section. The description of the specific vehicle and trajectory analyzed is as follows:

- Ballistic coefficient: 2000 PSF
- Reentry Angle: 30 Degrees
- Target Area: Kwajalein

### Climatology

As indicated on Table 3.1, the significant parameters for determining wind and density induced impact dispersions are the dispersions of the wind and density about the targeted profile. It was assumed for this study that the Kwajalein annual climatology would be used for targeting; therefore the dispersion of winds and density throughout the year about the annual (mean) profile was used. Figure 3.10 and Figures 3.19 and 3.20 give the resulting impact uncertainties. For the ballistic coefficient and reentry angle of interest, these figures indicate that the expected one sigma impact dispersions are as follows:

CLIMATOLOGY INDUCED DISPERSION		
SUBCATEGORY	DOWN (FT)	CROSS (FT)
Density	3	0
Winds	<u>39</u>	<u>30</u>
Total (RSS)	39	30

Ballistic Coefficient

Mass Loss: Impact dispersions resulting from mass loss uncertainties can be computed from Figure 3.23 if the mass loss uncertainty ( $\sigma_{m_a\%}$ ) and final mass loss ratio ( $m_a/m_0$ ) are known. It was assumed for this study that these values are 10% and .05 respectively. Figure 3.23 indicates that for the reentry angle and ballistic coefficient of interest, the impact dispersion per percent mass loss divided by the mass loss ratio is 6.0. The downrange dispersion is then:

$$\sigma_{DR} = (6.0)(10)(.05) = 3 \text{ feet}$$

Drag Coefficient (Zero Angle-of-Attack): The total drag coefficient uncertainty (excluding angle-of-attack) was assumed to be 2.5 percent. Figure 3.27 indicates that this magnitude of uncertainty results in an impact dispersion of 26 feet.

Initial Angle-of-Attack: It was assumed that a deployment system would be selected that could yield a mean initial angle-of-attack ( $\alpha_m$ ) of 5 degrees and an initial angle-of-attack uncertainty ( $\sigma_\alpha$ ) of 3 degrees. The impact dispersion can then be approximately determined from the expression:

$$\sigma_{DR} \approx \frac{1}{2} [\sigma_{DR} (\alpha_m + \sigma_\alpha) + \sigma_{DR} (\alpha_m - \sigma_\alpha)] = \frac{1}{2} [\sigma_{DR} (8^\circ) + \sigma_{DR} (2^\circ)]$$

Figure 3.29 then indicates that the resulting downrange dispersion due to induced drag effects is:

$$\sigma_{DR} = \frac{1}{2} [7.5 + 1] = 4 \text{ degrees}$$

Summary: A summary of the ballistic coefficient contributors is given below.

BALLISTIC COEFFICIENT INDUCED DISPERSION

SUBCATEGORY	DOWN (FT)
Mass Loss	3
Drag Coefficient	26
Initial Angle-of-Attack	<u>4</u>
Total (RSS)	26

### Lift

Lift induced uncertainties require the additional specification of the vehicle aerodynamic and mass properties before the resulting impact dispersion can be computed. Unlike climatology and ballistic coefficient effects, the governing parameters for lift can vary significantly and any specific parameters selected for this study would not be applicable to the generalized case, without making further assumptions on the vehicle design. This problem is partially solved by noting that for a reentry vehicle designed to achieve high accuracy roll trim effects would be much larger than the other lift categories. In this case it is assumed that to minimize the reentry dispersion the following design constraints would be applied:

- Initial angle-of-attack less than five degrees
- High altitude roll resonance occurs above 130 KFT  
(See Figure 3.36)
- Low altitude roll resonance is strictly prevented through design
- Transition begins above 100 KFT and induces less than 0.5 degree divergence

The consideration of just roll trim lift effects still impose a problem since the effects are dependent on the aerodynamic and mass properties, roll rate and on the changes in trim angle governed largely by various nosetip characteristics including material, bluntness, etc. Hence, a generalized treatment of roll trim effects with the same statistical rigor used for climatology and ballistic coefficient uncertainties is not possible and a more simplistic approach was adopted.

It has been observed that trim angle changes generally tend to occur between 30 KFT and 40 KFT, which unfortunately coincides with the region of maximum impact dispersion sensitivity. To achieve acceptably small reentry dispersion, a high accuracy vehicle will have to restrict trim angle changes to about 0.2 degree or less. The following parameters were assumed in determining roll trim effects:

$$\frac{C_{N\alpha} A}{m} = 0.0077 \text{ Ft}^2/\text{slug-degree}$$

$$h = 40,000 \text{ Ft}$$

$$\sigma_{\Delta\alpha_T} = 0.2 \text{ degree}$$

$$p = 2 \text{ RPS (12.6 radians/second)}$$

Equation 3.1 (or Figure 3.38) can then be used to determine the impact dispersion to replacing R by  $\sigma_R$  and  $\Delta\alpha_T$  by  $\sigma_{\Delta\alpha_T}$  since variations in the other paramters are small at 40 KFT. This results in a trajectory dispersion,  $\sigma_R$ , of 57 feet at impact. Since the orientation of the trim angle is arbitrary the impact dispersion can be either crossrange or downrange. The downrange dispersion is  $\sigma_R/\sin \gamma$  at impact.

ROLL TRIM IMPACT DISPERSION

Down            113 Ft  
Cross            57 Ft

Total Reentry Dispersion

The total reentry dispersion for this sample case is summarized below:

TOTAL REENTRY DISPERSION

$$\left(\frac{W}{C_{DA}}\right) = 2000 \text{ PSF, } \gamma_{RE} = 30 \text{ Degrees}$$

CONTRIBUTION	IMPACT DISPERSION ( $1\sigma$ )		CEP [.59( $\sigma_{DR} + \sigma_{CR}$ )]
	Down (Ft)	Cross (Ft)	
Density	3	0	
Wind	39	30	
Ballistic Coefficient	26	0	
Lift (Roll Trim)	<u>113</u>	<u>57</u>	
Total (Excluding Roll Trim)	47	30	45
Total (Including Roll Trim)	122	64	110

### 3.5.2 Reentry Error Budget Summary

Calculations similar to those performed in the sample calculation of Section 3.5.1 were performed for the other reentry angles and ballistic coefficients of interest. The tabular summary of Table 3.2 compares the relative dispersion magnitudes for each contributor and presents the total reentry CEP for the various ballistic coefficients and reentry angles considered in the study. This same data are pictorially presented on the bar charts in Figure 3.44 for selected reentry angles. Only ballistic coefficients of 2000, 3000, and 4000 psf and reentry angles of 20, 30, and 40 degrees are presented since lower values resulted in much degraded accuracies. Similar tables could, of course, have been constructed for air burst accuracies which would consider axial trajectory displacements as well. Figure 3.44 indicates that roll trim is potentially the most significant factor, followed by winds, ballistic coefficient, and density. At low reentry angles, ballistic coefficient effects are somewhat larger than wind effects.

The reentry CEP is also presented on Figure 3.45 as a function of reentry angle and illustrates the tradeoff between ballistic coefficient and reentry angle. Lower ballistic coefficient vehicles require higher minimum reentry angles if accurate reentry CEP requirements are to be achieved. Similarly, if low minimum reentry angles are desired, high ballistic coefficients are necessary.

The reentry CEP is observed to increase in a somewhat linear fashion with decreasing reentry angle until a reentry angle of approximately 25 degrees for the 2000 psf ballistic coefficient and 18 degrees for 4000 psf. Below this, the accuracy degrades very rapidly and should be avoided for an accurate reentry vehicle. Of course, these accuracies are valid for the Kwajalein target area only.

Based on the above conclusions, the measurement requirements study of the following Sections were restricted to ballistic coefficients of 2000 and greater, and reentry angles of 20 degrees and greater.

Table 3.2 Reentry Error Budget Summary

BALLISTIC COEFFICIENT (PSF)	REENTRY ANGLE (DEG)	1: CONTRIBUTORS (FT)							CEP (FT)	
		DENSITY DOWN	WINGS		$\frac{W}{C_D A}$ DOWN	LIFT (ROLL TRIM)		EXCLUDE LIFT (ROLL TRIM)	INCLUDE LIFT (ROLL TRIM)	
			DOWN	CROSS		DOWN	CROSS			
1500	15	163	464	369	1660	419	108	1239	1277	
	20	95	249	198	1065	245	88	765	792	
	25	28	124	95	285	188	80	240	288	
	30	8	69	53	72	141	71	90	155	
	40	2	36	28	14	93	60	40	99	
2000	15	105	215	162	1085	358	93	751	799	
	20	23	100	76	212	203	73	184	245	
	25	13	57	45	62	153	65	77	150	
	30	3	39	30	26	113	57	45	110	
	40	1	22	17	7	73	47	24	75	
3000	15	31	98	71	247	275	71	200	286	
	20	9	53	40	70	151	54	76	143	
	25	4	30	30	27	111	47	42	103	
	30	2	23	18	12	81	41	26	77	
	40	1	13	10	4	52	33	14	52	
4000	15	19	66	48	140	221	57	120	204	
	20	6	36	27	43	119	43	50	107	
	25	2	20	16	17	87	37	28	79	
	30	1	17	13	8	63	32	19	60	
	40	1	10	7	2	40	26	10	40	

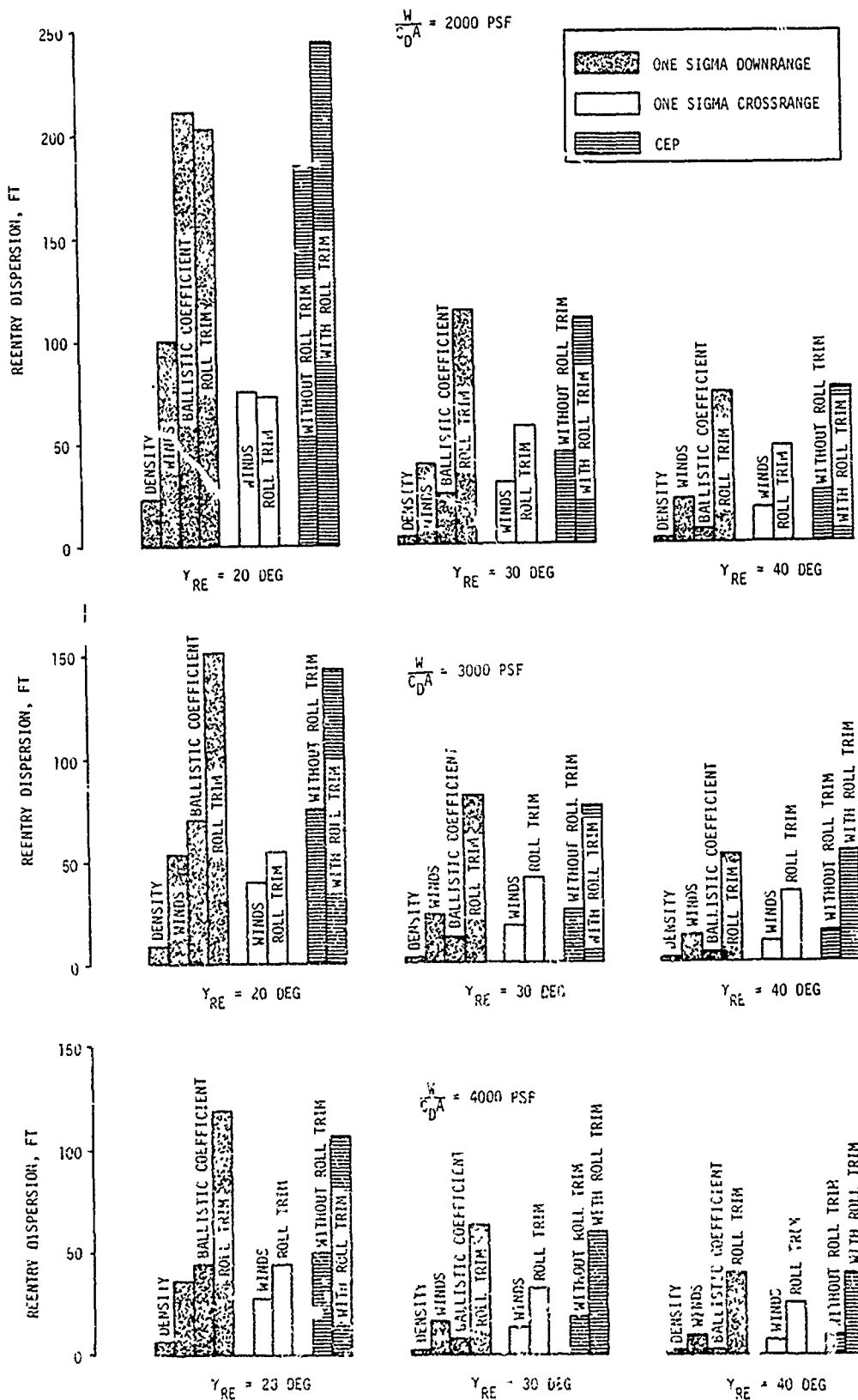


Figure 3.44 Reentry Error Budget for Kwajalein Target Area

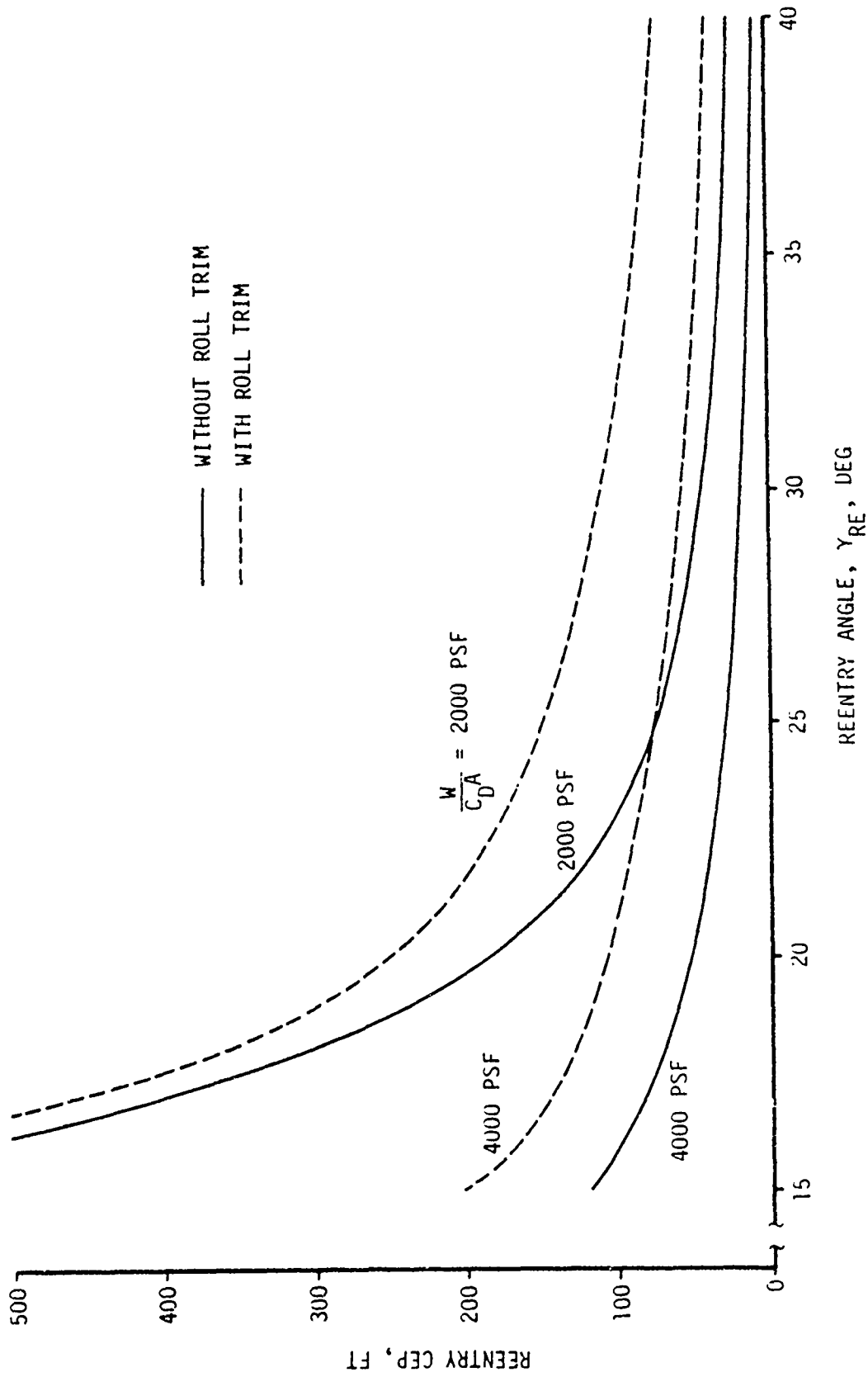


Figure 3.45 Variation of Reentry CEP with Ballistic Coefficient and Trim Angle

## 4.0 FLIGHT TEST MEASUREMENT REQUIREMENTS

### 4.1 INTRODUCTION

Analytical techniques used to predict the expected reentry accuracy performance during the design and development phase are subject to some variation. These uncertainties about the predicted performance result in the dispersions previously presented in Section 3.0. Flight test verification of the predicted accuracy performance is therefore necessary for establishing confidence in the reentry models and theoretical accuracy. The objective of this section is to determine the flight test measurement requirements which will allow identification of the mechanisms producing reentry dispersions. Results of the study will specifically address the following questions:

- What reentry measurements are necessary?
- What measurement accuracy is required?
- What altitude regions should be measured?
- What on-board and off-board instrumentation is available for measuring the reentry parameters?

Sections 5.0 and 6.0 subsequently compare measurement accuracies achievable using on-board and off-board instrumentation with the measurement requirements established in this section.

Flight test measurements are generally directed toward one of three measurement objectives:

- (1) Measurement of total reentry miss;
- (2) Separation and identification of the basic contributors to the reentry miss including climatology, ballistic coefficients, and lift effects;

- (3) Measurement of specific flight parameters indicative of reentry vehicle anomalies including heating rates, ablation rates, pressures, angle-of-attack, etc.

It is observed that the above measurement objectives proceed from the most general level to the most detailed. The first level enables the weapon system miss to be divided into that portion occurring prior to reentry and during reentry. The second level explains the reentry miss in terms of basic error contributors. If one of these contributors is excessive or a catastrophic failure occurs, the third level of analysis can be used to indicate the source of the anomaly and explain the difference between the predicted and actual performance. While each of these measurement objectives is useful and will be discussed, it is the second one which is of primary interest in this study, since it provides the necessary verification of a vehicle's predicted performance.

The study first addresses a general approach to establishing measurement requirements based on the reentry accuracy level and altitude regions of maximum sensitivity (Section 4.2). Next, the requirements for measuring total reentry miss are discussed (Section 4.3). Sections 4.4 through 4.6 then determine the in-flight measurement requirements necessary to separate ballistic coefficient, climatology and lift effects respectively. Finally, Section 4.8 derives the measurement requirements for a specific example for the purpose of showing how the results of the Section are to be applied.

#### 4.2 GENERAL MEASUREMENT REQUIREMENT

This section provides the rationale used to establish measurement accuracy requirements for each of the specific reentry contributors. The basic principles used in establishing these general measurement requirements were the following:

- (1) The measurement accuracy should be related and proportional to the reentry system accuracy requirement as impact;

- (2) The measurement accuracy should be a function of altitude, becoming more accurate in regions of higher sensitivity to perturbations in the parameter being measured;
- (3) The measurement should enable verification of the reentry models at reentry angles other than the one being tested.

These are equivalent to a functional statement of the following form once a particular ballistic coefficient has been specified:

$$\sigma_m = f(\text{CEP}, h, \gamma_{\min})$$

Each of these independent variables is discussed in the following subsections.

#### 4.2.1 Impact Accuracy

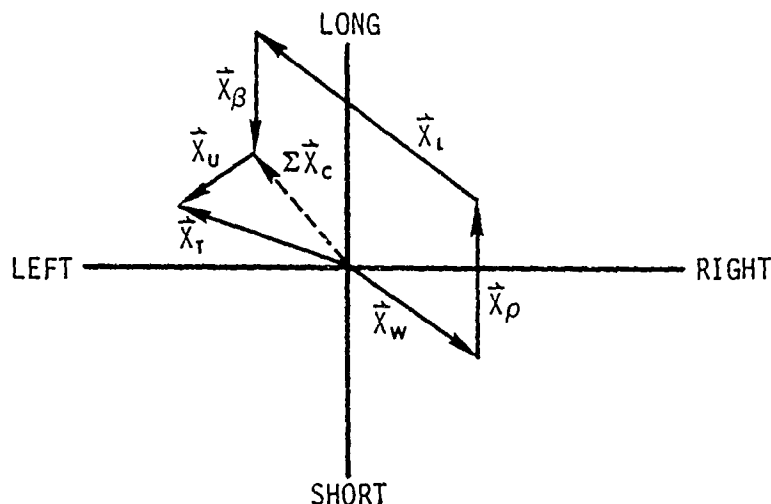
Verification of the performance of a highly accurate reentry vehicle logically requires more stringent measurement accuracies than for one designed for lesser accuracy. This includes measurement of both the total reentry system performance and separation of this performance into component parts. The reentry vehicle accuracy requirements are assumed in this study to be defined in terms of impact. The basic measurement requirements must then be similarly expressed in terms of impact uncertainties.

Closed loop reentry error analyses attempt to account for the observed miss by evaluating all known error contributors. Any residual errors between the sum of these contributors and the total miss must be attributable to unaccountable sources. This unaccountable miss can be expressed as:

$$\vec{X}_U = \vec{X}_T - \sum \vec{X}_C$$

where the component miss contributors are wind, density, ballistic coefficient and lift. This "closed loop" analysis is sketched below:

## CLOSED LOOP REENTRY ERROR ANALYSIS



An accurate verification of the total reentry accuracy performance can only be achieved if the unaccountable miss is small relative to the required RV accuracy. This can be accomplished by restricting the allowable uncertainty associated with the unaccountable miss. The nature of this restriction is somewhat arbitrary, but one approach is to specify that the 99% confidence interval associated with the unaccountable miss be no greater than the one sigma RV accuracy requirement in both the downrange and crossrange directions:

$$2.58 \sigma_{X_U} \leq \sigma_{ACC} \quad (4.1)$$

The unaccountable miss uncertainty is simply:

$$\sigma_{X_U} = \left[ \sigma_{X_T}^2 + \sigma_{\Sigma X_C}^2 + \sigma_{X_T \Sigma X_C} \right]^{1/2}$$

where  $\sigma_{X_T \Sigma X_C}$  is the covariance between the total reentry miss measurement and the sum of the component miss measurements.

An expression for  $\sigma_{ACC}$  can be found by noting from Table 3.1 that for vehicles with ballistic coefficients and reentry angles larger than 2000 psf and 20 degrees respectively, the total downrange dispersion and crossrange dispersion are approximately related by:

$$\frac{\sigma_{CR}}{\sigma_{DR}} = \begin{cases} .5 \text{ to } .7 \text{ neglecting lift effects} \\ S \sin \gamma_{RE} \text{ including lift effects} \end{cases}$$

The  $S \sin \gamma_{RE}$  relationship experienced when lift effects are present is due to the dominant influence of lift effects which approximately follow this relationship. Experience with current high ballistic vehicles indicates that lift is indeed the most significant contributor, and that the  $S \sin \gamma_{RE}$  relationship is valid.

Given a reentry CEP requirement, the allowable downrange and crossrange accuracies are then:

$$.59(\sigma_{DR} + \sigma_{DR} S \sin \gamma_{RE}) \leq CEP$$

or

$$\sigma_{DR} \leq \frac{CEP}{.59(1 + S \sin \gamma_{RE})}$$

Similarly

$$\sigma_{CR} \leq \frac{CEP S \sin \gamma_{RE}}{.59(1 + S \sin \gamma_{RE})}$$

Substituting  $\sigma_{DR}$  and  $\sigma_{CR}$  for  $\sigma_{ACC}$  in Equation 4.1 and assuming negligible covariance between the total reentry miss measurement and the component measurements, the measurement accuracy requirement becomes approximately:

$$\text{Downrange: } \left( \sigma_{X_T}^2 + \sigma_{\Sigma X_C}^2 \right)_{DR}^{1/2} \leq \frac{2}{3} \frac{\text{CEP}}{(1 + \sin \gamma_{RE})}$$

$$\text{Crossrange: } \left( \sigma_{X_T}^2 + \sigma_{\Sigma X_C}^2 \right)_{CR}^{1/2} \leq \frac{2}{3} \frac{\text{CEP} \sin \gamma_{RE}}{(1 + \sin \gamma_{RE})}$$

The above constraints represent the basic measurement requirements in terms of impact accuracy and reentry angle.

The miss contributors that must be considered include those that were addressed in the error budget study of Section 3.0: climatology, ballistic coefficient and lift. Measurement of these parameters is usually achieved through density, wind, drag deceleration and lateral acceleration measurements. Assuming that measurement errors in these parameters are independent, the total uncertainty may be expressed:

$$\sigma_{\Sigma X_C} = \left[ \sigma_{X_W}^2 + \sigma_{X_P}^2 + \sigma_{X_{A_D}}^2 + \sigma_{X_{A_T}}^2 \right]^{1/2}$$

The measurement accuracy criteria then becomes:

$$\text{Downrange: } \left( \sigma_{X_T}^2 + \sigma_{X_W}^2 + \sigma_{X_P}^2 + \sigma_{X_{A_D}}^2 + \sigma_{X_{A_T}}^2 \right)_{DR}^{1/2} \leq \frac{2}{3} \frac{\text{CEP}}{1 + \sin \gamma_{RE}} \quad (4.2)$$

$$\text{Crossrange: } \left( \sigma_{X_T}^2 + \sigma_{X_W}^2 + \sigma_{X_{A_T}}^2 \right)_{CR}^{1/2} \leq \frac{2}{3} \frac{\text{CEP} \sin \gamma_{RE}}{1 + \sin \gamma_{RE}} \quad (4.3)$$

The constraints of Equations 4.2 and 4.3 can be satisfied by an infinite number of measurement accuracy allocations. To define a unique set of requirements, it was conveniently assumed that each of the crossrange components would be measured to the same accuracy, i.e.

$$\frac{2}{3\sqrt{3}} \frac{\text{CEP Sin } \gamma_{RE}}{1 + \text{Sin } \gamma_{RE}} \bullet$$

To derive the downrange measurement requirements, each downrange component was related to its crossrange requirement in proportion to their approximate dispersion relationship in Table 3.1:

$$\left(\sigma_{X_T}\right)_{CR} = \left(\sigma_{X_T}\right)_{DR} \text{ Sin } \gamma_{RE} \tag{4.4}$$

$$\left(\sigma_{X_W}\right)_{CR} = \left(\sigma_{X_W}\right)_{DR}$$

$$\left(\sigma_{X_{A_T}}\right)_{CR} = \left(\sigma_{X_{A_T}}\right)_{DR} \text{ Sin } \gamma_{RE}$$

Under these conditions and equally allotting the downrange uncertainty, it can be shown that the following constraints satisfy the criteria stated in Equations 4.2 and 4.3:

$$\sigma_{X_D}, \sigma_{X_{A_D}} \leq \frac{2}{3\sqrt{6}} \frac{\text{CEP Cos } \gamma_{RE}}{1 + \text{Sin } \gamma_{RE}}$$

$$\left(\sigma_{X_T}, \sigma_{X_W}, \sigma_{X_{A_T}}\right)_{CR} \leq \frac{2}{3\sqrt{3}} \frac{\text{CEP Sin } \gamma_{RE}}{1 + \text{Sin } \gamma_{RE}} \tag{4.5}$$

$$\left(\sigma_{X_T}, \sigma_{X_{A_T}}\right)_{DR} \leq \frac{2}{3\sqrt{3}} \frac{\text{CEP}}{1 + \text{Sin } \gamma_{RE}}$$

$$\left(\sigma_{X_W}\right)_{DR} \leq \frac{2}{3\sqrt{3}} \frac{\text{CEP Sin } \gamma_{RE}}{1 + \text{Sin } \gamma_{RE}}$$

Constraints for  $\sigma_{X_T}$  and  $\sigma_{A_T}$  in the crossrange direction were converted to downrange using Equation 4.4. These constraints are presented on Figure 4.1 as functions of reentry angle, per foot of CEP. Multiplication of the parameters by the required CEP yields required measurement accuracies.

Other approaches could have been used for establishing these measurement requirements. One possible modification is to make the reentry CEP requirement reentry angle dependent. Since CEP requirements are generally established at a specific reentry angle, accuracies at other angles can be related to this CEP. This is alluded to in the discussion of Section 4.2.3.

#### 4.2.2 In-Flight Measurement Accuracy

The impact accuracy requirements previously established set a limit on the total integrated measurement error during reentry but do not specifically identify the measurement requirements at any particular point along the trajectory. Some method must therefore be found to determine point by point measurement requirements that will achieve the desired impact accuracy.

One of the primary objectives of flight testing is to verify the accuracy of the reentry targeting model. To minimize impact dispersions, it is necessary to maximize the accuracy of the model in altitude regions where the trajectory is most sensitive to variations in the modeled parameters. This can be accomplished by verifying the reentry parameters at each altitude to accuracies which will result in the same uncertainty at impact. For example, the measurement uncertainty for the drag deceleration at 90 KFT should result in an impact uncertainty equivalent to that associated with measuring the drag coefficient at 45 KFT, etc.

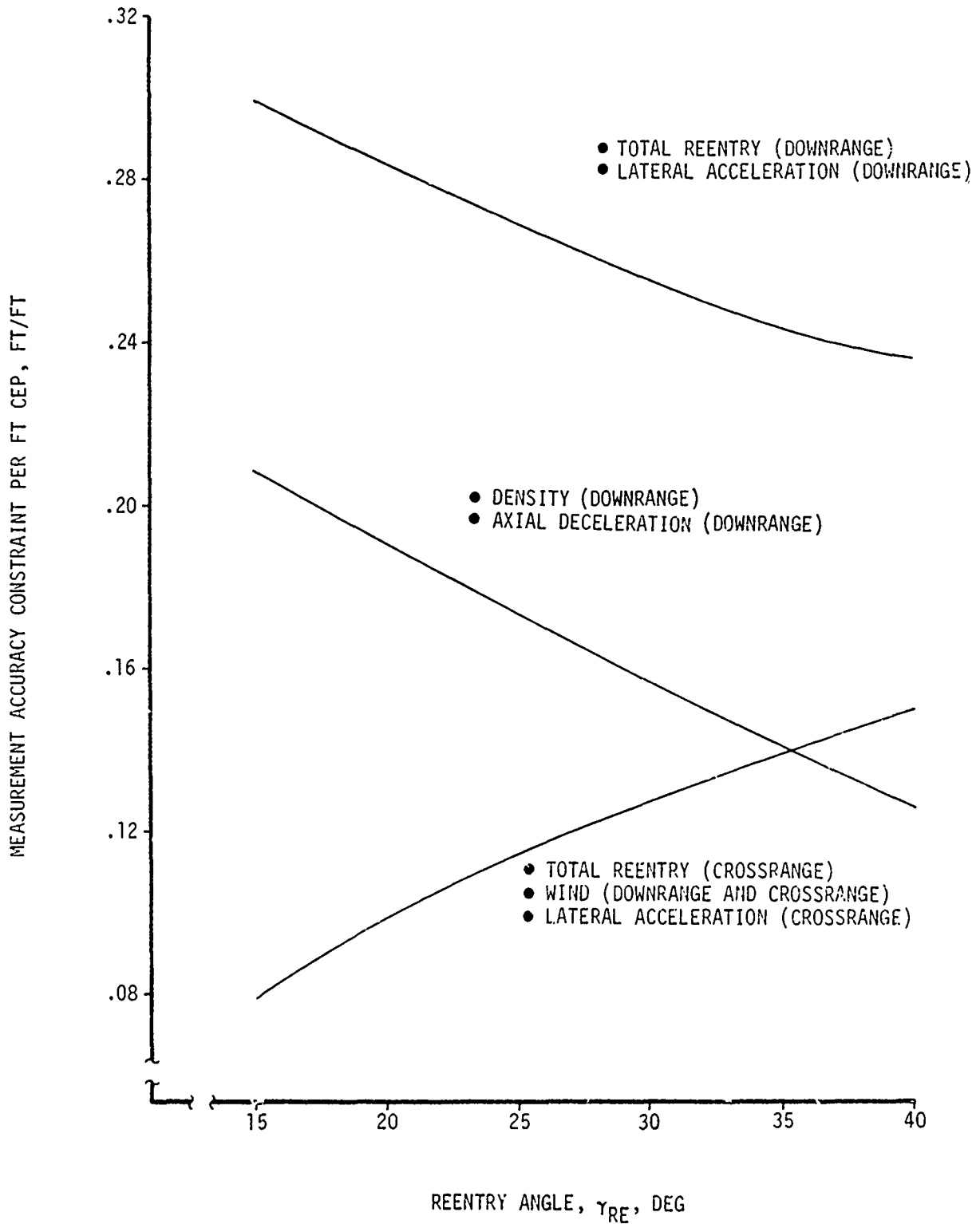


Figure 4.1 Impact Measurement Requirements for Reentry Contributors

The effect of measurement uncertainties during flight can be propagated to impact using influence coefficients in an analogous manner to the Section 3.0 studies. Expressed as an integral, the resulting impact variation becomes:

$$\sigma_X^2 = \int_0^{H_m} \int_0^{H_m} \sigma_m(h) I(h) R(h, h) \sigma_m(\bar{h}) I(\bar{h}) dh d\bar{h},$$

where  $R(h, \bar{h})$  represents the correlation coefficient between measurement errors at altitude  $h$  and  $\bar{h}$ . Inspection of the above integrand reveals that the quantity  $\sigma_m(h) I(h)$  is the propagated effect of a measurement error of magnitude  $\sigma_m(h)$ , acting over one foot of altitude, at impact. Equivalent impact uncertainties due to measurement errors can thus be achieved by maintaining  $\sigma(h) I(h)$  constant throughout reentry. This implies that in regions of high sensitivity where the influence coefficient becomes large, the measurement uncertainty must decrease. The impact uncertainty can then be expressed as:

$$\sigma_X^2 = \sigma_m^2(h) I^2(h) \int_0^{H_m} \int_0^{H_m} R(h, \bar{h}) dh d\bar{h}.$$

It is apparent that the correlation coefficient is a significant factor in determining the amount of impact dispersion. At one extreme, perfect correlation between errors implies that  $R(h, \bar{h}) = 1$  throughout the measurement region. This would result from systematic instrumentation errors. No correlation, however, implies that only random measurement errors exist and then  $R(h, \bar{h}) = 1$  only when  $h = \bar{h}$  with otherwise zero correlation. The difference in these assumptions has a significant effect, as much as two orders of magnitude or more on the impact uncertainty.

This study made the pessimistic assumption that perfect correlation exists between instrument errors throughout reentry, i.e.,  $R(h, h) = 1$ . Although this is admittedly conservative, it is believed to be more representative of actual instrumentation errors than an assumption of no correlation. Due to the general nature of this study, no attempt was made to determine more precise values for the correlation. Once particular instrumentation has been selected, however, such an analysis is strongly recommended because of its obvious effect on the measurement accuracy requirements. The impact variance corresponding to the perfect correlation assumption then becomes:

$$\sigma_x^2 = \sigma_m^2 (h) I^2 (h) H_m^2$$

This may be rearranged to determine the measurement uncertainty in terms of the allowable impact uncertainty:

$$\sigma_m (h) = \frac{\sigma_x}{I (h) H_m} \quad (4.6)$$

The allowable impact uncertainty for each contributor,  $\sigma_x$ , was previously specified in Equations 4.5. The influence coefficients,  $I(h)$ , are presented in Section 3.0 for the wind, density, and axial deceleration, while lateral acceleration influence coefficients are derived in Section 4.6.

#### 4.2.3 Reentry Model Verification At Other Reentry Angle Conditions

The limited number of ABRES flight tests prevents verification of the reentry model over the entire range of proposed flight path angles,

and it is necessary to infer the adequacy of the reentry model over the design range from data obtained at one or two reentry angle conditions. It is observed from the Section 3.0 studies that predicted dispersions are largest for the most shallow angles, decreasing as the reentry angle steepens. However, influence coefficient profiles are strongly dependent on the specific reentry angle, becoming significantly smaller as the angle increases. Hence, measurements for high reentry angle missions require much less measurement accuracy (larger uncertainties) than lower angles. However, to verify the accuracy of the reentry model to a level sufficient to maintain the desired CEP at a shallower reentry angle than being flight tested requires a more stringent measurement accuracy.

A solution to this problem is to establish measurement accuracies based on influence coefficients corresponding to the lowest design reentry angle intended for the RV. This, of course, is dependent on the lowest angle that will still meet the CEP requirements. Since this angle is critically dependent upon the amount of lift (Section 3.4), it cannot be anticipated in this study. Hence, measurement accuracies corresponding to 20 and 30 degrees are presented.

Throughout this section it was assumed that the basic RV accuracy requirement was in terms of an impact accuracy. A height and position of burst accuracy, however, could have been used in addition to impact. In this case, the time influence coefficients (reflecting axial displacements) would be used in addition to the downrange and crossrange impact influence coefficients.

Section 4.2 has developed a general rationale for establishing reentry measurement accuracy requirements as functions of reentry CEP, altitude, and the minimum intended flight path angle. The following four sections apply these criteria to the specific measurements needed to measure the total reentry miss and its components, including climatology, ballistic coefficient and lift effects.

#### 4.3 TOTAL REENTRY MISS MEASUREMENT

Knowledge of the total reentry miss is useful for two purposes. First, it separates errors occurring prior to reentry from reentry errors. This enables identification of system level errors and indicates the degree to which each system (G&C, deployment and reentry) achieves its required accuracy. The second purpose of the total reentry miss, and the one of primary interest in this study, is its use in verifying the accuracy of the measurement of individual reentry error contributors through a closed loop comparison.

The total reentry miss is derived by establishing: (1) the pierce point state vector of the RV just prior to reentry, and (2) the impact location. The pierce point is used to initialize a trajectory simulation which is then propagated to impact using targeted reentry parameters (climatology and ballistic coefficients). The position difference between this simulated impact point and the measured impact location is the total reentry miss.

Determination of the pierce point requires a trajectory derived from external sensors. The technique used to derive a trajectory from off-board sensor data typically involves the use of a least squares regression program to solve for the state vector, reentry parameters, and radar errors. The accuracy of the solution depends on many factors, including the quality of the metric data, survey accuracy of the sensor location, and knowledge of the forces acting on the reentry vehicle. Impact scoring consists of determining the location where the reentry vehicle penetrates the earth's surface. The accuracy associated with defining this location is dependent upon the characteristics of the scoring sensor and target dependent errors. The total accuracy with which the reentry miss can be defined, assuming independence of the two measurement errors, is then:

$$\sigma_{X_T} = [ \sigma_{X_{pp}}^2 + \sigma_{X_{sc}}^2 ]^{1/2}$$

The total reentry miss measurement criteria was established in Equation 4.5 and presented on Figure 4.1. At a 30 degree reentry angle for example, the requirement per 100 feet of allowable CEP is:

$$[\sigma_{X_{pp}}^2 + \sigma_{X_{sc}}^2]^{1/2} \leq \begin{array}{l} 13 \text{ Feet Downrange} \\ 26 \text{ Feet Crossrange} \end{array} \quad (4.7)$$

Hence, a tradeoff exists between the allowable pierce point and scoring accuracy. A detailed analysis of both metric tracking and scoring capabilities in the Kwajalein terminal area is contained in Section 5.0.

#### 4.4 DRAG DECELERATION MEASUREMENTS

The drag experienced by a reentry vehicle results in a deceleration which is related to the dynamic pressure, weight and drag coefficient by the expression:

$$A_D = \frac{\rho v^2 C_D A}{2 W} \quad (\text{g's})$$

Since the deceleration is a measureable parameter, the ballistic coefficient may be inferred from it if the density profile and velocity history are known:

$$\frac{W}{C_D A} = \frac{\rho v^2}{2 A_D}$$

The accuracy of the derived ballistic coefficient can be estimated if the density, velocity, and deceleration measurements are nearly independent. This uncertainty is then:

$$\sigma_{B\%} = \left[ \sigma_{m_{\rho\%}}^2 + 4\sigma_{m_{v\%}}^2 + \sigma_{m_{A_D\%}}^2 \right]^{1/2}$$

It will be shown in Section 5.0 that velocity can be determined from metric data to less than .02% uncertainty, which is negligible compared with deceleration or density uncertainties. In-flight deceleration measurement uncertainties are addressed in this section, while density is the subject of the next.

The measurement accuracy requirement for drag deceleration may be determined from Equations 4.5 and 4.6:

$$\sigma_{mAD}(h) \leq \frac{2}{3\sqrt{6}} \frac{CEP \cos \gamma_{RE}}{(1 + \sin \gamma_{RE}) I_{DR}^{\beta}(h) H_m}$$

where  $I_{DR}^{\beta}(h)$  is the influence coefficient for ballistic coefficient variations, as shown on Figures 3.1 through 3.4. Once the maximum measurement altitude  $H_m$  is specified, a measurement accuracy profile can be constructed from this constraint.

Measurement of the deceleration is necessary only over the altitude region where variations from the targeting model could significantly degrade the impact accuracy. The error budget study of Section 3.0 found that, if the vehicle maintained a near zero angle of attack during reentry, ballistic coefficient dispersions above 100 KFT to 120 KFT induced small impact errors. However, more typically a flight reenters with some non-zero angle of attack and experiences angle of attack divergence at roll resonance, inducing a random drag component which is difficult to model. It is therefore desirable to measure the deceleration up to the maximum altitude where roll resonance can occur. This altitude can be estimated once the vehicle's roll rate and aerodynamic properties are known. A maximum altitude of  $H_m = 180$  KFT was chosen for this study and should encompass most feasible vehicle designs.

Figure 4.2 presents the deceleration measurement accuracy requirement per 100 feet of a reentry CEP expressed as a percent of the instantaneous deceleration for ballistic coefficients of 2000, 3000, and 4000 psf at reentry angles of 20 and 30 degrees. Higher ballistic coefficients and minimum reentry angles are observed to result in less stringent requirements. The figure also shows the need for more accurate measurements in the region of maximum sensitivity to drag perturbations, with highest accuracy requirements between 20 KFT and 60 KFT altitude.

Two methods of measuring a vehicle's deceleration are: (1) indirect measurements using off-board metric tracking data, and (2) direct on-board measurements using axial accelerometers. Deriving aerodynamic deceleration from metric tracking data requires smoothing and differentiation of position and rate data or fitting of the data to a reentry model in which drag and lift coefficients are regressed for. Section 5.0 examines the accuracies of this later method in detail. An analytical study of on-board instrumentation and its ability to meet the requirements is presented in Section 6.0.

#### 4.5 CLIMATOLOGY MEASUREMENTS

Climatology measurements near the time of the test are essential if the portion of the reentry miss resulting from variations in wind and density from the targeting model are to be separated from lift and ballistic coefficient effects. This section establishes the accuracy requirements for such measurements using the general constraints previously established and compares these specific requirements with current climatology measurement accuracies.

##### 4.5.1 Density

Density measurements must be made if variations in the vehicle's deceleration are to be properly distributed between density and ballistic coefficient effects. The altitude extent of density measure-

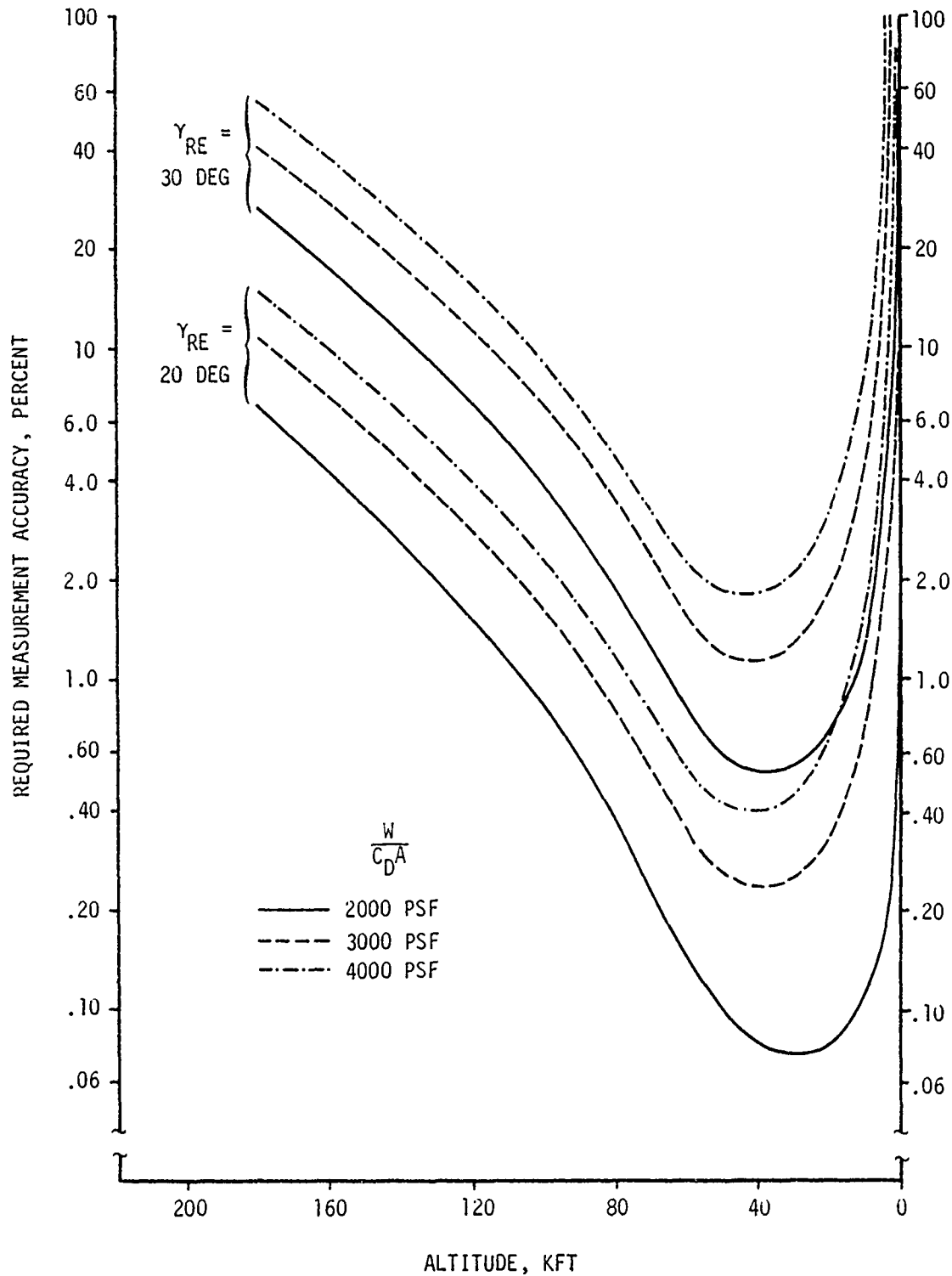


Figure 4.2 Deceleration Measurement Accuracy Requirements Per 100 Feet of Allowable Reentry CEP

ments should then be approximately the same as deceleration measurements: hence the same value of 180 KFT was used for the maximum measurement altitude,  $H_m$ . Since density influence coefficients are nearly identical to those used for drag deceleration, the density measurement accuracy criteria are the same as those shown in Figure 4.2. These are duplicated in Figure 4.3.

Instrumentation typically used to obtain density profiles consists of Rawinsonde and Rocketsonde observations which may be used to measure density profiles to over 200 KFT with the following accuracies:

DENSITY MEASUREMENT RELIABILITIES

Instrument Type	Altitude Range (KFT)	Data Reliability
Rawinsonde	0-30	0.4%
	30-100	1. %
Rocketsonde	80-160	3 %
	160-230	5 %

The data reliabilities are statements of precision representing RMS deviations about a mean value. In the present study these reliabilities were chosen as statements of accuracy, i.e., the degree to which the measured value agrees with the "true" value. In actual calibrations, the "true" value is never known and instrument uncertainties must be inferred from the scatter of repeated measurements about some mean.

A comparison of the data reliabilities with the required accuracy is presented on Figure 4.3. This comparison indicates that current density measurements are not sufficiently accurate over much of the trajectory, particularly for reentry angles of 20 degrees. One method that could enhance this accuracy is the use of multiple Rawinsonde and Rocketsonde measurements on the day of the test. A second method of enhancing the accuracy would be, of course, through improved sensor accuracy. If such

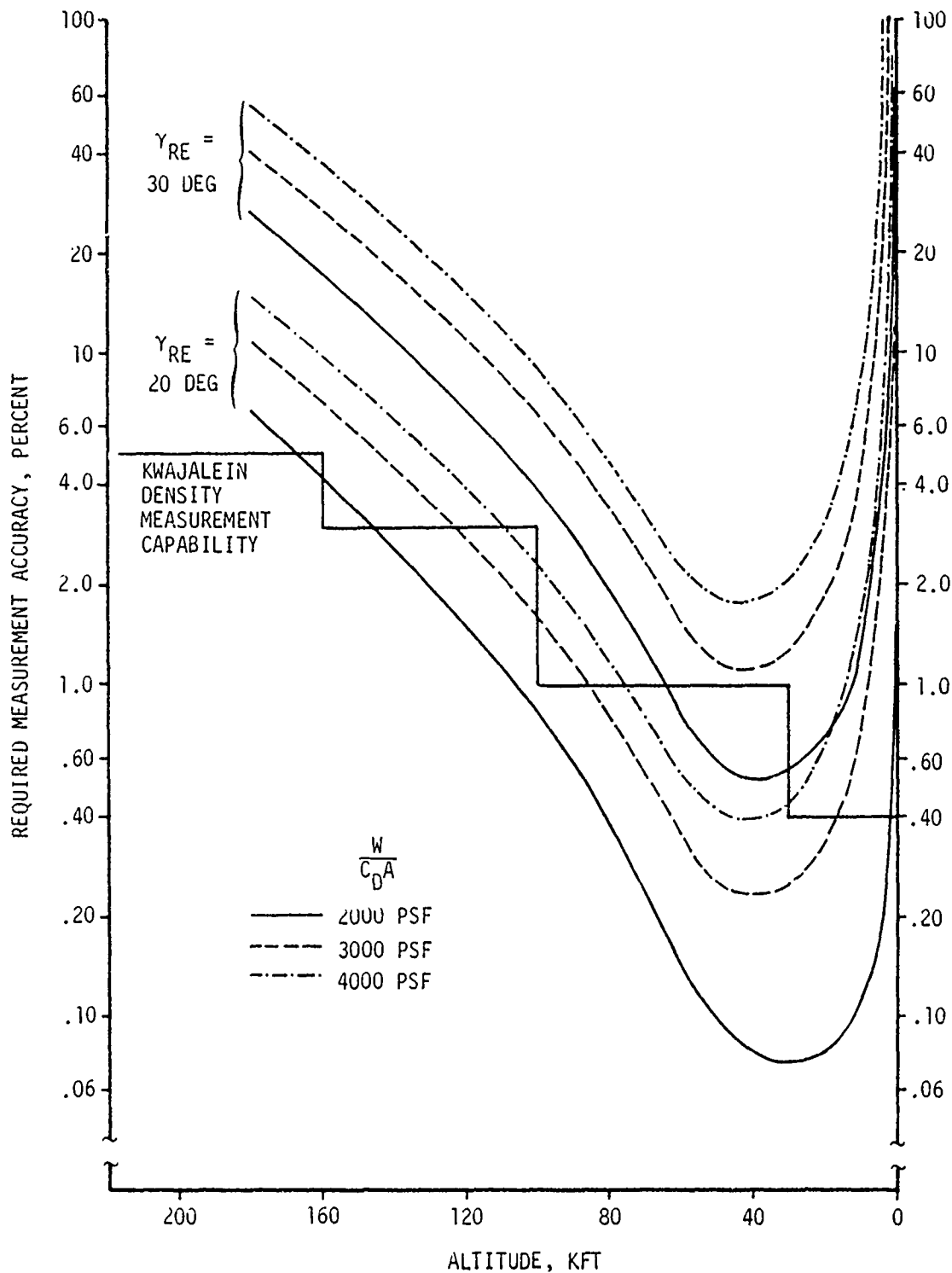


Figure 4.3 Density Measurement Accuracy Requirements Per 100 Feet of Allowable Reentry CEP, and Current Capabilities

improvements are contemplated, it is recommended that they first be directed at the lower altitude Rawinsonde measurements.

#### 4.5.2 Wind

Wind effects tend to displace a vehicle from its otherwise ballistic trajectory, a result similar to lift effects. Accurate separation of lateral displacements between wind and lift effects requires an accurate measurement of winds experienced along the reentry trajectory.

The measurement criteria for winds was previously established by Equations 4.5 and 4.6:

$$\sigma_{m_w}(h) \leq \frac{2}{3\sqrt{3}} \frac{\text{CEP} \sin \gamma_{RE}}{(1 + \sin \gamma_{RE}) I_{DR}^w(h) H_m}$$

where  $I_{DR}^w(h)$  is the influence coefficient for wind variations as shown in Figures 3.13 through 3.16. This requirement is the same for both downrange and crossrange. The altitude region recommended for wind measurements should include those regions of the trajectory where lift induced dispersions are expected to dominate. The error budget study of Section 3.0, however, showed that wind effects above 80 KFT or 90 KFT usually contribute much less than one foot at impact. Hence, a value of 90 KFT was chosen for  $H_m$ .

The wind measurement requirements are presented in Figure 4.4 in feet per second wind velocity for 2000, 3000 and 4000 psf ballistic coefficients at 20 and 30 degrees reentry angle, per 100 feet of a reentry CEP. The resulting criteria are observed to be most stringent in the 10 KFT to 20 KFT region where the trajectory is most sensitive to wind effects.

Many methods are available for measuring wind velocity. These are summarized in Reference 6. Measurements from the surface to 80 KFT to 90 KFT can generally be achieved with accuracies of three to four knots or ten percent of the vector wind, whichever is greater. The four knot (6.8 ft/sec)

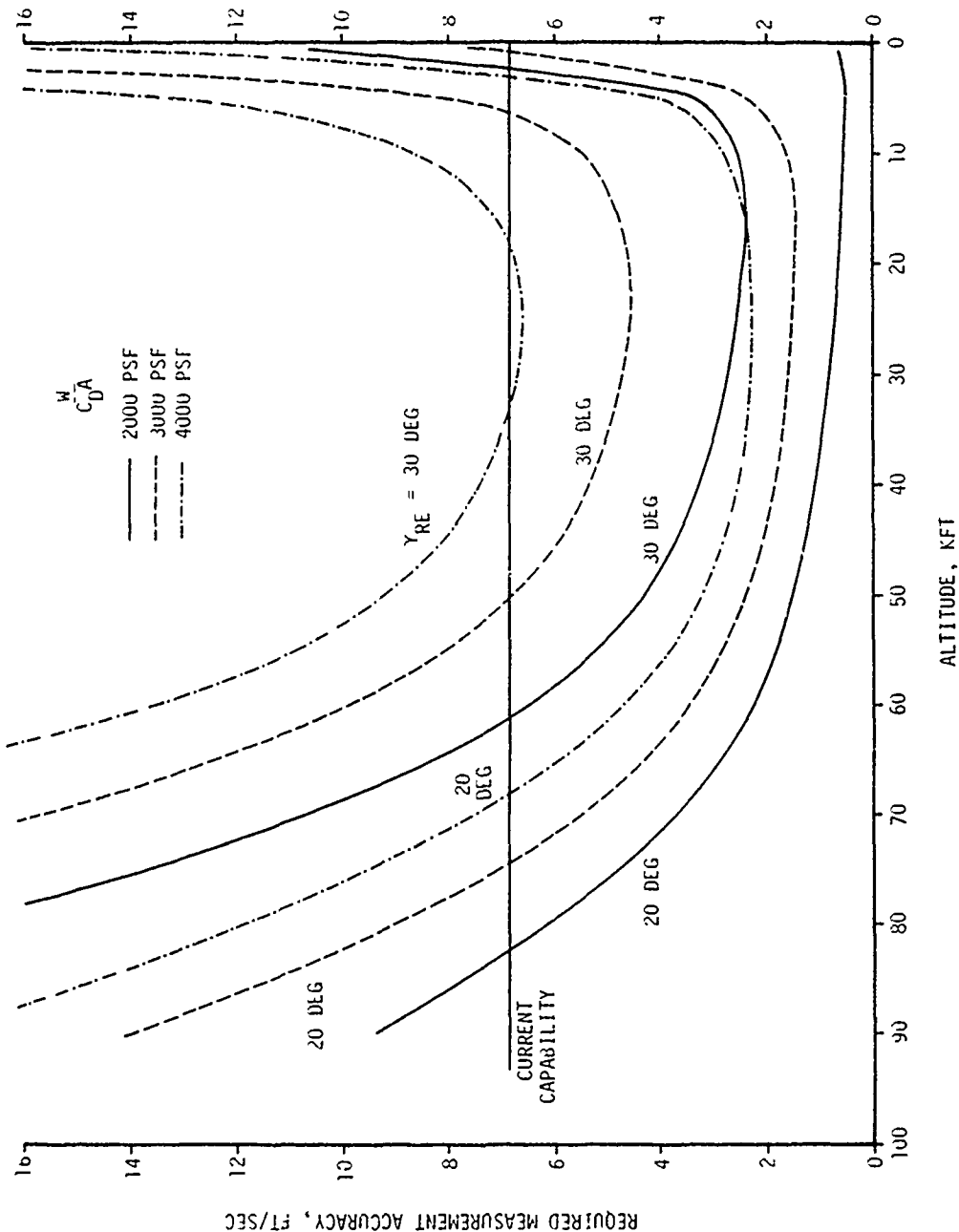


Figure 4.4 Wind Measurement Accuracy Requirements Per 100 Feet of Allowable Reentry CEP, and Current Capabilities

reliability is presented on Figure 4.4 for comparison with the measurement criteria and reveals that better measurements are required for 20 and 30 degree reentry angle flights throughout much of the altitude region of interest. Again, this improved accuracy may be achieved either by multiple measurements or improved sensor accuracy. Comparisons between climatology measurement requirements and current capabilities have indicated that better measurements are needed. However, it should be recalled that the measurement requirements established in Section 4.2 assumed perfect correlation between errors at different altitudes. Since this assumption is admittedly pessimistic, comparisons between current capabilities and the requirements are probably more favorable than shown. However, more analysis is required to establish the exact nature of this correlation.

In addition to data reliability, two other factors are significant in obtaining accurate measurements of the climatology environment experienced by the reentry vehicle. First, measurements should be made close to the time of the test, perhaps just after impact, since wind and density are very dynamic. Kwajalein density profiles, for example, have been observed to change as much as 2 percent over a 24-hour period. A second factor is the proximity of the climatology measurements to the trajectory. The Kwajalein weather station, for example, is up to 30 nautical miles away from the target location. Although the effect of this distance on the climatology is not known, it is believed to be of less significance than the time factor.

#### 4.6 LIFT MEASUREMENTS

Lateral position displacements (Y and Z) of a vehicle from its ballistic trajectory due to asymmetric lift forces are usually measured in one of two manners: (1) comparison of the vehicle's position with respect to its otherwise ballistic trajectory, or (2) direct measurements of the vehicle's lateral accelerations. The choice of measurement

technique involves a tradeoff between measurement of the cause (angle-of-attack) or effect (displacement). While the first method yields lateral displacements directly, it does not quantitatively indicate why such behavior occurred (i.e., angle-of-attack). The second method, however, does enable the angle-of-attack history to be derived but requires double integration of these accelerations before the displacements are known. This section addresses the measurement accuracy requirements of each technique.

#### 4.6.1 Acceleration Measurements

The measurement constraints developed in Section 4.2 indicate that lift induced lateral acceleration effects at impact must be known to the following accuracy if satisfactory verification of the reentry miss is to be achieved:

$$\sigma_Y, \sigma_Z \leq \frac{2}{3\sqrt{3}} \frac{\text{CEP} \sin \gamma_{RE}}{1 + \sin \gamma_{RE}}$$

The use of lateral accelerometers to determine lift effects requires a double integration of these accelerations to determine lateral displacements:

$$Y = \iint A_{TY} \, dt \, dt$$

$$Z = \iint A_{TZ} \, dt \, dt$$

where  $A_{TY}$  and  $A_{TZ}$  are given in the trajectory fixed coordinate system.

To relate impact accuracy constraints to the in-flight acceleration measurements requirements, influence coefficients were again used as described in Section 4.2.2.

$$\sigma_{A_T} \leq \frac{2}{3\sqrt{3}} \frac{\text{CEP} \sin \gamma_{RE}}{(1 + \sin \gamma_{RE})} \frac{1}{H_m I_T^A}$$

Since lift influence coefficients have not yet been developed in this study, their derivation was necessary before this method could be applied.

The influence coefficient for lift may be defined in the usual manner:

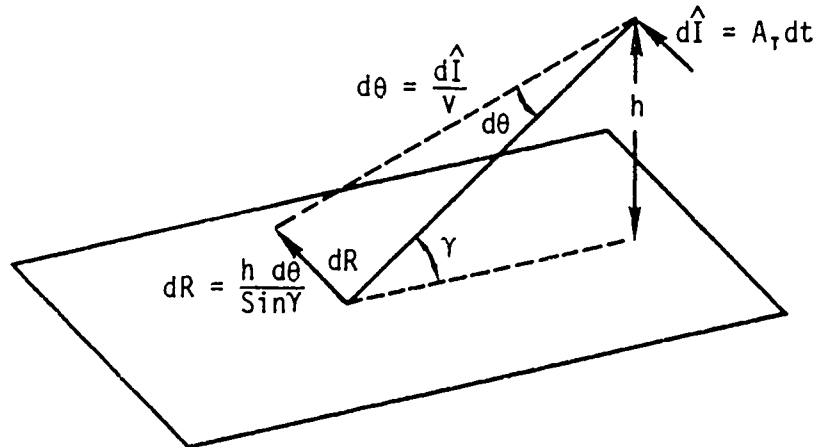
$$I_{A_T} = \frac{1}{A_T} \frac{dR}{dh}$$

where  $dR$  is the trajectory deflection at impact caused by an acceleration  $A_T$  acting throughout an altitude interval  $dh$ . Noting that altitude and time are instantaneously related by  $dh = v \sin \gamma dt$ , the influence coefficient becomes:

$$I_{A_T} = \frac{1}{v A_T \sin \gamma} \frac{dR}{dt}$$

The acceleration component,  $A_T$ , applied over an interval of time,  $dt$ , may be considered as an impulse acting on the vehicle. The effect of such an impulse is to cause a bend in the trajectory,  $d\theta$ . Assuming negligible bending of the trajectory in the absence of lift, the effect of the change is to cause a rotation of the entire trajectory, resulting in a deflection of  $dR$  at impact. This is shown in the sketch below:

TRAJECTORY DEFLECTION DUE TO LIFT IMPULSE



The deflection  $dR$  is then related to the lateral acceleration impulse by:

$$dR = \frac{h A_T dt}{v \sin \gamma}$$

It is apparent that the influence coefficient is then given by:

$$I_{A_T} = \frac{h}{v^2 \sin^2 \gamma_{RE}} \quad (4.8)$$

This is the relationship that will be used in deriving acceleration measurement accuracies. It should be noted that while the crossrange influence coefficient is identical to  $I_{A_T}$ , the downrange coefficient must be divided by  $\sin \gamma_{RE}$ . Assuming negligible bending of the trajectory, then:

$$I_{A_{TZ}}^{DR} = \frac{h}{v^2 \sin^3 \gamma_{RE}}$$

Combining Equations (4.3), (4.6) and (4.8) yields the following criteria for  $A_{TY}$  and  $A_{TZ}$ :

$$\sigma_{m A_T} \leq \frac{2}{3 \sqrt{3}} \frac{v^2 \text{CEP} \sin^3 \gamma_{RE}}{(1 + \sin \gamma_{RE}) h H_m}$$

The choice of  $H_m$  should correspond to the highest altitude where significant lift forces can occur. The error budget study of Section 3.0 discusses four independent sources of lift effects. The following table summarizes these contributors and the relevant altitude regions.

LIFT CONTRIBUTORS DURING REENTRY

Lift Contributors	Affected Altitude Region (KFT)	Dispersion Mechanism
Initial Angle-of attack	100 - 250	Momentum vector offset from velocity vector
High Altitude Roll Resonance	100 - 180	Angle-of-attack divergence at crossing of roll resonance frequency
Boundary Layer Transition	55 - 100	Boundary layer transition causes angle-of-attack to diverge
Roll Trim	20 - 70	Asymmetric nosetip ablation causes angle-of attack divergence and preferred orientation

It is evident that if an initial angle-of-attack is expected, measurements should be acquired to 250 KFT. Substitution of 250 KFT into the previous expression yields:

$$\sigma_{m_{AT}} \leq 1.540 \times 10^{-6} \frac{v^2 \text{ CEP } \sin^3 \gamma_{RE}}{h(1 + \sin \gamma_{RE})} \quad (4.9)$$

The quantity  $v^2/h$  is ballistic coefficient and reentry angle dependent. Figure 4.5 presents the measurement requirements per 100 feet of allowable CEP for ballistic coefficients of 2000, 3000, and 4000 psf at 20 and 30 degree reentry angles. It should be remembered that these criteria assume perfectly correlated instrumentation errors throughout reentry. If the initial angle-of-attack, including the momentum vectory orientation and

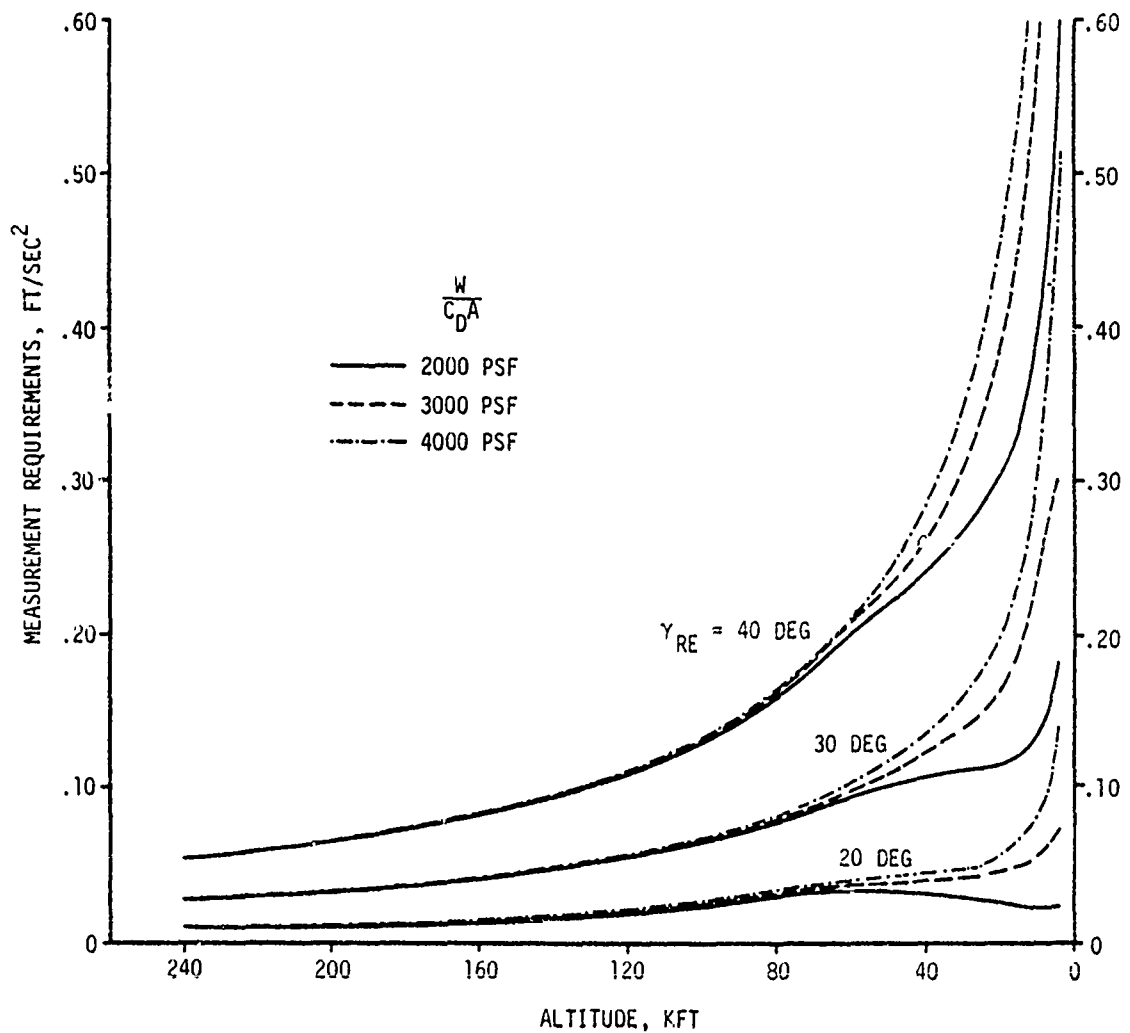


Figure 4.5 Lateral Acceleration Measurement Requirements in Trajectory Coordinates Per 100 Feet of Allowable Reentry CEP

half coning angle, is known or is very small it may be possible to decrease  $H_m$  to an altitude just above high altitude roll resonance. This would somewhat relax the measurement criteria.

#### 4.6.2 Position Measurements

A second method commonly used to evaluate lift effects is through a comparison of the vehicle's observed position with a non-lifting ballistic trajectory simulation. This method of evaluating reentry dispersions resulting from lift offers several advantages over measurements of lateral acceleration. One advantage is that lift induced displacements are measured directly, without the necessity of integrating the accelerations and attitude rates in order to reconstruct the displacement history. Another advantage is that it avoids the use of expensive on-board instrumentation and the associated weight penalty. Offsetting these advantages, however, are some significant drawbacks. First, while position measurements sense the effect of lift, they usually are not accurate enough to allow derivation of the instantaneous angle-of-attack history of the vehicle. Furthermore, lateral displacements can also result from other trajectory dispersion sources, especially wind effects, which must be differentiated from lift effects. This section addresses the position measurement accuracy requirements necessary for evaluating lift effects based on an analysis of displacements from a non-lifting trajectory, and the problems of separating correlated errors.

If position measurements are to be used to evaluate lift effects, they must provide an accurate means of separating the lift contribution to reentry miss from other dispersion mechanisms appearing as lift effects along the trajectory. The total lift effect contribution can be evaluated based on the vehicle's position both prior to reentry (pierce point), and at impact. The portion of reentry miss attributable to lift is then the difference between total reentry dispersion and that attributed to ballistic coefficient and climatology effects. This can be derived based on a

trajectory calculation in which the measured pierce point, the derived ballistic coefficient history and test day climatology are used in the simulation. The lift contribution to the total reentry error is then the difference between the impact location of this simulated ballistic trajectory and the actual impact location:

$$\vec{X}_L = \vec{X}_A - \vec{X}_S$$

The uncertainty associated with the lift contribution is then:

$$\sigma_{X_L} = \left[ \sigma_{X_A}^2 + \sigma_{X_S}^2 \right]^{1/2}$$

The actual impact uncertainty,  $\sigma_{X_A}$  is equivalent to the scoring uncertainty, while the simulated impact uncertainty,  $\sigma_{X_S}$ , may be expressed as the following summations of uncertainties:

$$\text{Downrange: } \sigma_{X_S} = \left[ \sigma_{X_{pp}}^2 + \sigma_{X_{AD}}^2 + \sigma_{X_p}^2 + \sigma_{X_w}^2 \right]^{1/2}$$

$$\text{Crossrange: } \sigma_{X_S} = \left[ \sigma_{X_{pp}}^2 + \sigma_{X_w}^2 \right]^{1/2}$$

The accuracy of the lift contribution to reentry error is then given by:

$$\text{Downrange: } \sigma_{X_L} = \left[ \sigma_{X_{sc}}^2 + \sigma_{X_{pp}}^2 + \sigma_{X_{AD}}^2 + \sigma_{X_p}^2 + \sigma_{X_w}^2 \right]^{1/2}$$

$$\text{Crossrange: } \sigma_{X_L} = \left[ \sigma_{X_A}^2 + \sigma_{X_{pp}}^2 + \sigma_{X_w}^2 \right]^{1/2} \quad (4.10)$$

If the measurement accuracies for the quantities on the right side of the above relationships are known, the accuracy,  $\sigma_{X_L}$ , achievable using lateral position measurements can be estimated. Noting that the sum of the pierce point and scoring variances is the total reentry miss variance,  $\sigma_{X_T}^2$ ,

Equations 4.4 and 4.5 can be used to determine the potential downrange and

crossrange lift measurement accuracies from Equation (4.10).

$$\begin{aligned} \text{Downrange: } \sigma_{X_L} &\leq \frac{4}{3\sqrt{6}} \frac{\text{CEP}}{1 + \sin \gamma_{RE}} \\ \text{Crossrange: } \sigma_{X_L} &\leq \frac{4}{3\sqrt{6}} \frac{\text{CEP} \sin \gamma_{RE}}{1 + \sin \gamma_{RE}} \end{aligned}$$

A comparison of the above potential accuracies with those achievable by measuring lateral accelerations to the accuracies required by Equation 4.5 indicates that this method is nearly fifty percent less accurate. Hence, some degradation in measuring the total lift contribution at impact would be experienced by this method unless the total miss or other contributors were measured more accurately.

In addition to measuring total lift effects, it is also desirable to measure the lateral displacement history throughout reentry to determine the characteristics of the lift induced dispersion. This requires that position measurements be acquired through reentry with sufficient accuracy to discern the development of lift induced dispersions. It also requires decorrelation of lift effects from other reentry errors. The Section 3.0 error budget study identified four lift dispersion mechanisms which have been summarized in the table on page 4-26. Figure 4.6 presents typical lateral dispersions resulting from various lift effects during reentry and identifies the expected magnitude of the lift effects as a function of altitude. The predicted dispersions are representative of a 2000 PSF ballistic coefficient vehicle at 20 and 30 degree reentry angles.

Lateral position measurement accuracy criteria per 100 feet of reentry CEP are also presented on Figure 4.6. These were derived based on the constraint that lift induced dispersions be evaluated with an equal accuracy throughout reentry. The accuracy with which lift effects can be determined depends on two factors: (1) the position measurement accuracy, and (2) the accuracy with which other reentry errors can be decoupled from lift:

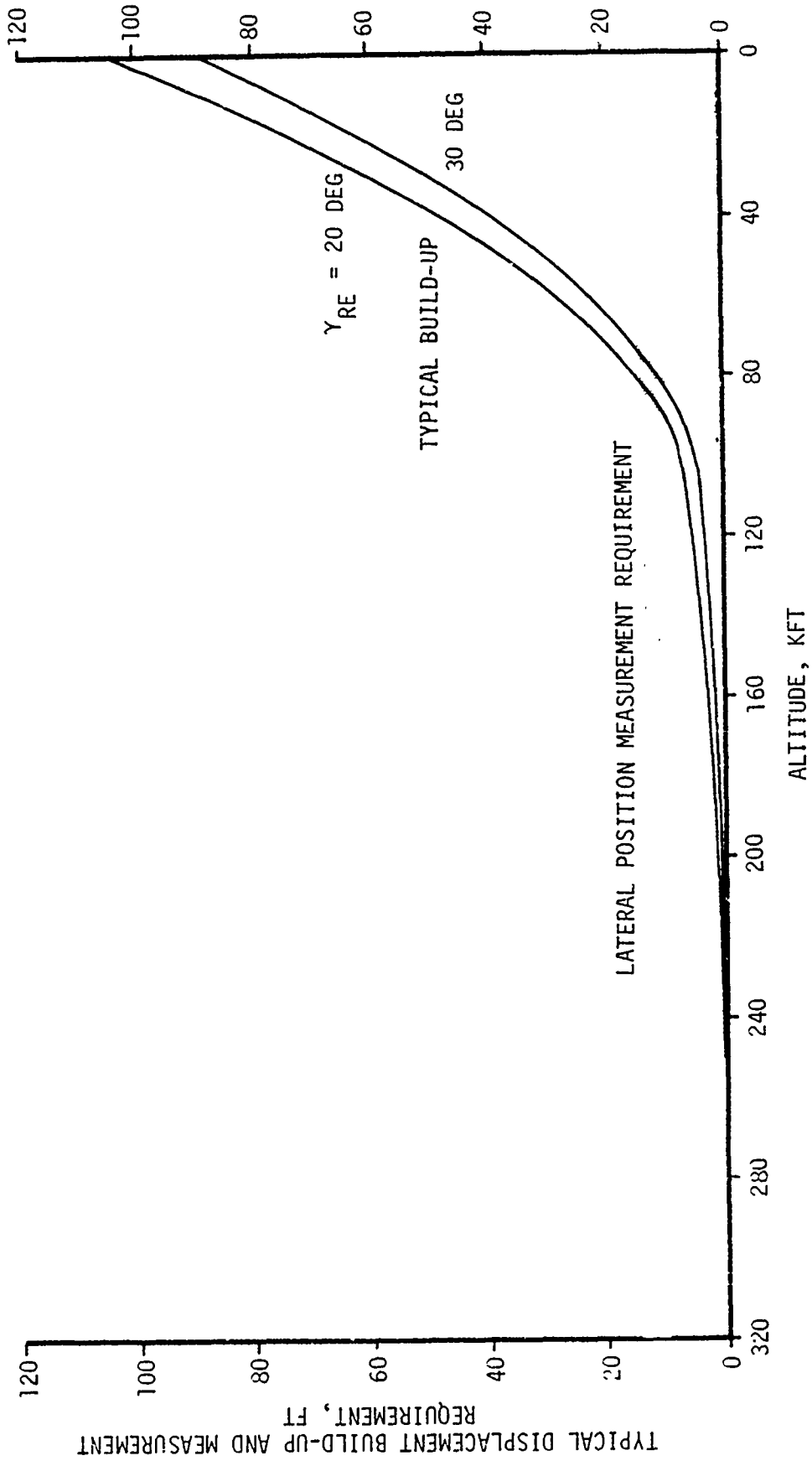


Figure 4.6 Position Measurement Requirements For Lift Effects Per 100 Feet of Required Reentry CEP Accuracy

$$\sigma_L = \left[ \sigma_{\text{pos}}^2 + \sigma_w^2 + \sigma_\rho^2 + \sigma_{A_D}^2 \right]^{1/2}$$

If the measurement of lift induced errors,  $\sigma_L$ , are to remain constant, it is obvious that the position measurement accuracy must increase if other reentry errors cannot be completely separated from lift effects.

The position measurement requirement at high altitude reflects the pierce point accuracy criteria previously established in Section 4.3 assuming negligible impact measurement uncertainty. This accuracy constraint would be expected to remain constant until that region of the trajectory where other reentry errors could contribute to the lateral position dispersions. During the course of the Section 3.0 error budget study it was found that wind effects were negligible above 80 to 90 KFT and ballistic coefficient and density variations caused very small lateral displacements above this altitude region (less than one foot in Z). In fact, the climatology and ballistic coefficient effects on the lateral position were found to be quite small down to 60 KFT. It can be safely assumed that observed lateral position displacements from the targeted trajectory down to 60 KFT must be attributable to lift, and the accuracies achievable in this manner are only limited by the position measurement uncertainty. This is reflected by the constant accuracy requirement shown on Figure 4.6, down to 60 KFT. However, below this altitude climatology and deceleration measurement uncertainties also affect lateral dispersions and, hence position measurements must be made more accurately if the resultant lift induced dispersion is to be measured to the same accuracy. Somewhere in the vicinity of 10 KFT the accuracy of these other measurements totals the initial position measurement uncertainty, requiring a theoretical zero position uncertainty at this altitude. This is reflected by the continuously decreasing measurement accuracy criteria below 60 KFT.

Several interesting observations may be made from Figure 4.6. First, "typical" lift induced lateral displacements may not be discernable above 100 KFT even if the required position measurement accuracies are met, since lift induced dispersions above this altitude are expected to be significantly less than the required measurement accuracies. Second, below 60 KFT roll trim is the only significant lift contributor present and should be easily discernable if the required measurement accuracies are met, since it is potentially the largest contributor. Finally, it should be noted that the upper altitude extent of the measurement criteria should correspond to the highest altitude at which lift dispersions can occur. If the reentry angle-of-attack can be reduced to near zero or known very accurately the upper altitude extent could be reduced to the region of roll resonance.

#### 4.7 SPECIAL INSTRUMENTATION REQUIREMENTS

If flight test data indicate a major departure from the predicted performance it is then necessary to perform a detailed study of the reason for the unexpected behavior. This would require special measurements of specific parameters affecting lift and drag. This section summarizes several common measurements used for this purpose including: (a) ablation rate measurements, (b) transition detection measurements and (c) angle-of-attack measurements. The study of Reference 7 was used for much of this analysis.

##### 4.7.1 Ablation Measurements

Accurate separation of the ballistic coefficient history into its weight and drag components requires validation of the predicted vehicle shape change and mass loss resulting from ablation. This requires measurements of recession rates on both the vehicle nosetip and fustrum. Nosetip recession and shape change are difficult to predict and are most reliably determined from flight test measurements. While these changes have little effect on drag variation because of the small nosetip area involved, they

band of  $\pm 1000$  feet. However, if transition occurs while the vehicle is at an angle-of-attack of one degree or more, considerably larger disagreement may be observed. This reflects the asymmetry in the transition front that can accompany small angles-of-attack.

#### 4.7.3 Angle-of-Attack Measurements

Section 3.0 studies have indicated the importance of the vehicle's angle-of-attack on both lift and drag. If lift and drag effects on the reentry miss are to be correctly evaluated, it is necessary to determine the magnitude and altitude regions of angle-of-attack divergence and correlate the occurrence of roll resonance, transition and roll trim effects with increases in drag and asymmetric lift dispersions.

Evaluation of induced drag requires only the magnitude of the angle-of-attack divergence. Measurement of lift effects requires, in addition, the orientation measurement of the lift vector relative to an earth fixed coordinate system. The need for accurate angle-of-attack and orientation measurements was implied by the lateral acceleration requirements established in Section 4.6. Section 6.0 subsequently provides a study of on-board lateral acceleration instrumentation that will achieve these requirements.

#### 4.8 SUMMARY

The purpose of the measurement requirement study of Sections 4.2 through 4.6 was to answer the questions: (1) What reentry measurements are necessary? (2) What measurement accuracy is required? and (3) What altitude regions should be measured?. The following table summarizes the significant results of the study which answer these questions.

REENTRY MEASUREMENT REQUIREMENTS

REENTRY PARAMETER	AVAILABLE MEASUREMENT METHOD	REQUIRED ACCURACY (FIG NO.)	MAXIMUM MEASUREMENT ALTITUDE	
			CONSTRAINT	THIS STUDY
Total Reentry Miss	1) Metric Trackers 2) Scoring Sensors	4.1	-	-
Drag Deceleration	1) Metric Trackers 2) Axial Accelerometers	4.2	Roll Resonance	180 KFT
Climatology				
Density	Rawinsonde/ Rocketsonde	4.3	Roll Resonance	180 KFT
Winds	Rawinsonde/ Rocketsonde	4.4	Trajectory Sensitivity	90 KFT
Lift Acceleration	1) Lateral Accelerometers 2) Metric Trackers	4.5,4.6	Initial Angle-of-attack	240 KFT

Sample Calculation: As an example of the use of the requirements established in this section, consider a vehicle with the following characteristics:

- $\frac{W}{C_D A}$  : 2000 PSF
- $\gamma_{RE}$  : 30 Degrees
- Target Area: Kwajalein
- Roll Resonance Altitude: 180 KFT
- Reentry CEP: 100 Feet

1. Total Reentry Miss

Figure 4.1 and Equation 4.7 indicate that to evaluate a reentry vehicle designed to achieve a 100 foot reentry CEP and flown at 30 degrees reentry angle, the pierce point and scoring uncertainties combined

must be less than 13 feet. If a scoring accuracy of five feet can be achieved, the pierce point accuracy must be 12 feet or less. For a design CEP of 200 feet the values would be twice as large.

## 2. Drag Deceleration

Figure 4.2 presents the deceleration accuracy requirements as a function of altitude assuming that measurements are required to 180 KFT. If roll resonance occurs at a lower altitude and initial angle-of-attack uncertainties are minimized, the required measurement uncertainties can be increased by the ratio of  $180 \text{ KFT}/H_m$  where  $H_m$  is the altitude of roll resonance.

## 3. Climatology

- a. Density measurements are given in Figure 4.3, again assuming that roll resonance occurs at 180 KFT and hence the deceleration measurements need to be made to this altitude. Again, if roll resonance occurs at a lower altitude, these measurement requirements can be relaxed by the ratio of  $180 \text{ KFT}/H_m$ .
- b. Wind measurement requirements are presented on Figure 4.4, which assumes that measurements will be made to 90 KFT. Measurements should be made near the time of reentry and in close proximity of the trajectory. Multiple measurements should be considered.

## 4. Lift Acceleration

Figure 4.5 presents the lateral acceleration requirements as a function of altitude, assuming measurements will be made to 240 KFT, correspondent to the altitude at which initial angle-of-attack effects result in discernable lateral displacements. If the initial angle-of-attack can be well defined or minimized, the measurements can be relaxed by the ratio of  $240 \text{ KFT}/H_m$  where  $H_m$  is the altitude of roll resonance.

## 5.0 REENTRY METRIC TRACKING ANALYSIS

### 5.1 INTRODUCTION

This section examines the current and future capability of metric trackers in the Kwajalein terminal area to measure trajectory dispersions using trajectory error estimation techniques. Specifically, the study analyzes the uncertainty associated with estimating position, velocity, and accelerations (axial drag decelerations and lateral accelerations) through reentry. The uncertainties are then compared with the requirements established in Section 4.0.

The metric sensors used in this error analysis include the following:

- Radar - MPS-36, ALCOR, TRADEX, Instrumentation Ship
- Optical - RADOT, Ballistic Camera
- Doppler - KREMS

The tracker errors considered in the analysis include random errors, systematic bias errors and relative survey uncertainties. This excludes several tracker errors which are known, and sometimes observed to occur, including timing errors (both constant and time varying), nonconstant biases, data dropouts, etc. The exclusion of these error sources results in somewhat optimistic accuracy estimates which must be considered as lower bounds on the achievable accuracy.

A significant portion of the study was devoted to determining the sensitivities of the derived position, velocity, and acceleration to several parameters. The parameters specifically examined in this study were:

1. Tracker error magnitudes (random and systematic bias)
2. Tracker combinations

3. Survey uncertainties
4. High altitude lift uncertainties
5. Ballistic coefficient and reentry angles
6. Target location

## 5.2 ERROR ANALYSIS TECHNIQUE

An understanding of the technique used in the error analysis is necessary if the results are to properly interpreted. A brief description of the general approach used by TRW in the error analysis follows.

### 5.2.1 Mathematical Description of Error Analysis\*

The development of the mathematical model assumes some prior knowledge of the least squares approach to estimating a trajectory from a large set of measurements. The intent is to indicate the treatment of random versus systematic (modeled and unmodeled) errors in estimating the trajectory accuracy and the propagation of a least squares estimate of uncertainty from one time point to another.

Consider first the simple case where the measured data contains only random errors with no systematic error content. Let  $X$  be the vehicle state vector of position and velocity, and  $Y=f(X)$  be the equation relating the measurements to the state vector. If this equation is expanded in a first order Taylor series about a reference trajectory, the familiar relationship is:

$$\delta Y = A\delta X + n,$$

where

$$A = \frac{\partial f}{\partial X},$$

$\delta Y$  is the difference between the observed and computed measurements (residuals),  $\delta X$  is a small deviation from the reference state vector, and  $n$

\* Much of this section is drawn from the mathematical portion of Reference 8.

is the vector of unbiased Gaussian random noise on the measurements  $Y$ .  
The weighted least squares estimate of  $\delta X$  is then:

$$\delta X_e = (A^T W A)^{-1} A^T W \delta Y$$

with a covariance matrix

$$\Sigma_e = (A^T W A)^{-1}$$

where  $W^{-1}$  is the covariance of the noise  $n$ .

The case just treated rarely exists in practice since:

1. Measurement errors seldom have a zero mean;
2. Errors exist in modeling the forces acting on the body (aerodynamic and gravitational forces);
3. Random errors are unlikely to be purely Gaussian.

For these reasons it is frequently desirable to estimate systematic errors, including model errors in the force field, along with the state vector parameters. The residuals are then expressed as:

$$\delta Y = A \begin{bmatrix} \delta X \\ \delta Z \end{bmatrix} + n$$

where  $\delta Z$  is the vector of systematic errors and  $A$  is partial matrix including systematic error effects:

$$A = \begin{bmatrix} \frac{\partial Y}{\partial X} & \frac{\partial Y}{\partial Z} \end{bmatrix}$$

The estimates  $\delta X_e$  and  $\delta Z_e$  can be determined in a fashion similar to before:

$$\begin{bmatrix} \delta X_e \\ \delta Z_e \end{bmatrix} = (A^T W A)^{-1} A^T W \delta Y$$

where  $\delta Z_e$  is the estimate of systematic errors. The covariance matrix is given by:

$$\Sigma_e = (A^T W A)^{-1} A^T W M W A (A^T W A)^{-1}$$

which now includes X and Z, and M is the covariance of the random noise,  $M = E (nn^T)$ . If the noise is again random, and  $W^{-1}$  is chosen equal to M, the covariance reduces to  $(A^TWA)^{-1}$ .

The third case to be examined considers known systematic errors in the least squares estimates but neglects them in the actual forming of this estimate. Survey uncertainties, for example, while not solved for, should be considered and are frequently treated in this manner. The residuals for this case are given by:

$$\delta Y = A\delta X + B\delta Z + n$$

where  $\delta Z$  is the vector of "considered" systematic errors, and  $B = \partial Y / \partial Z$ . The A matrix in this case includes only the partials for the state variables, X. The estimate  $\delta X_e$  is given by:

$$\delta X_e = (A^TWA)^{-1} A^TW \delta Y$$

since no systematic errors are being estimated. However, the covariance matrix is now:

$$\Sigma_e = (A^TWA)^{-1} + (A^TWA)^{-1} A^TWB \Sigma_Z B^TWA (A^TWA)^{-1}$$

The first term,  $(A^TWA)^{-1}$ , represents the contribution from random noise while the second term represents the contribution from the "considered" parameters, where  $\Sigma_Z$  is the covariance of these parameters. It is observed that the covariance matrix,  $\Sigma_e$ , is always larger when considered parameters are included.

The last case assumed that all systematic errors are included in the "consider" portion of the analysis. Sometimes, however, it is desirable to "solve" for some systematic errors and "consider" others. Under this condition the expressions appear similar to those just presented, with the partial derivative matrix A now including both X and the Z terms for systematic errors being solved for. The matrix B excludes these

solved-for parameters.

The least squares estimates of this state vector and covariance are computed at some initial time  $t_0$ . However, it is desirable to propagate the estimates to some other time  $t_1$ . It can be shown that the estimates  $\delta X_1$  and  $\delta Z_1$  are related to  $\delta X_0$   $\delta Z_0$  by:

$$\begin{bmatrix} \delta X_{e_1} \\ \delta Z_{e_1} \end{bmatrix} = \begin{bmatrix} \frac{\partial X_1}{\partial X_0} & \frac{\partial X_1}{\partial Z_0} \\ 0 & I \end{bmatrix} \begin{bmatrix} \delta X_{e_0} \\ \delta Z_{e_0} \end{bmatrix}$$

where  $I$  is the identity matrix. The propagated covariance matrix is given by:

$$\Sigma_{e_1} = \begin{bmatrix} \frac{\partial X_1}{\partial X_0} & \frac{\partial X_1}{\partial Z_0} \\ 0 & I \end{bmatrix} \Sigma_{e_0} \begin{bmatrix} \frac{\partial X_1}{\partial X_0} & \frac{\partial X_1}{\partial Z_0} \\ 0 & I \end{bmatrix}^T$$

### 5.2.2 Tracking Error Analysis Programs

Estimates of trajectory accuracies achievable with various combinations of trackers were derived using two TRW programs, RETAP (REEntry Trajectory Analysis Program), and SMAP (Statistical Matrix Analysis Program). Together these programs can be used to compute the covariance matrix of the state variables. The variables that can be solved for include:

- State vector
- Lift and drag coefficients
- Sensor Biases
- Sensor locations

The last three can also be used as "consider" parameters.

The relationship between the two programs, including their input and output requirements, is shown on Figure 5.1. The RETAP program generates the normal matrix of partials,  $A^{TWA}$ , and the partial derivatives

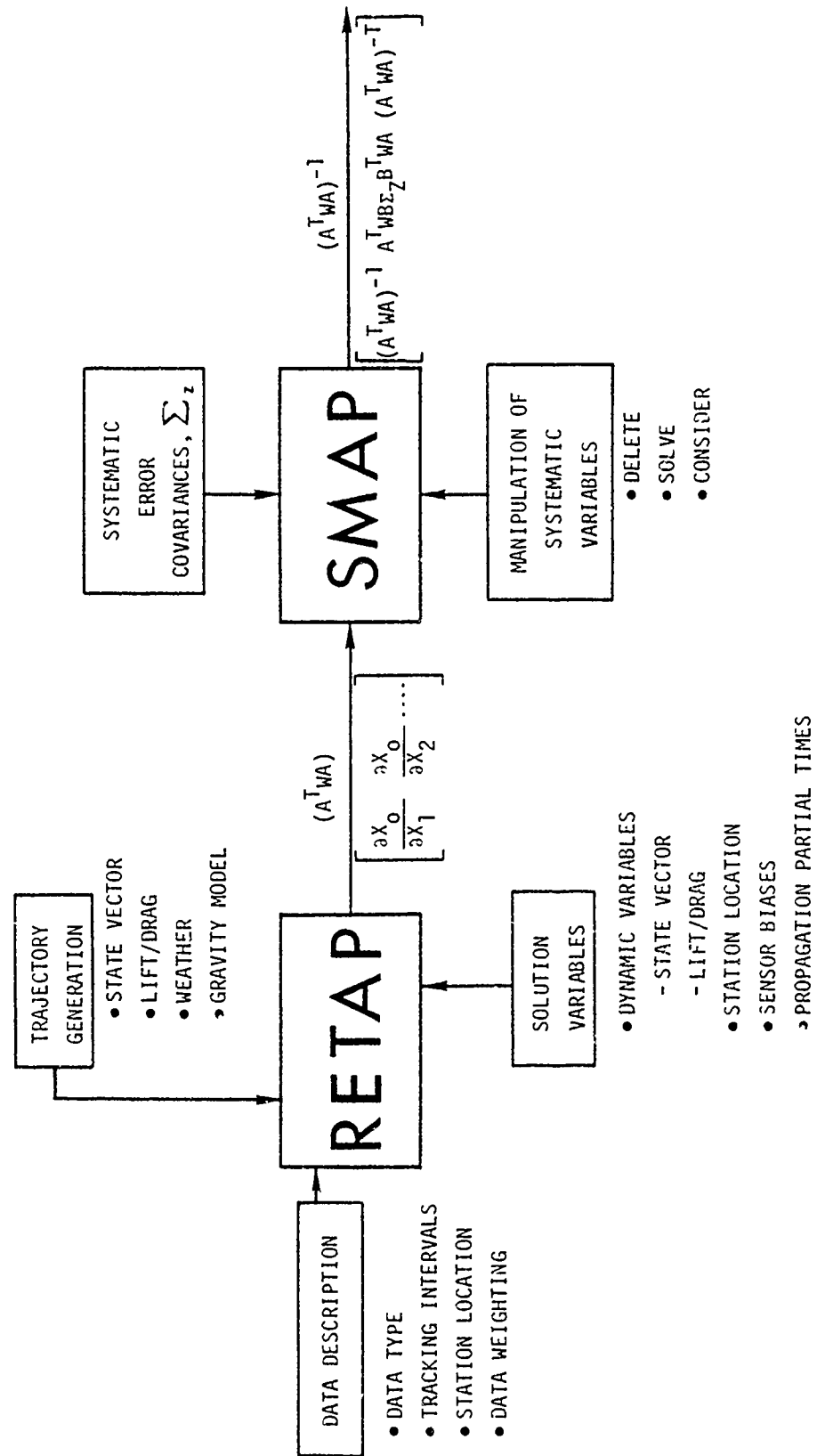


Figure 5.1 Input/Output for RETAP and SMAP Programs

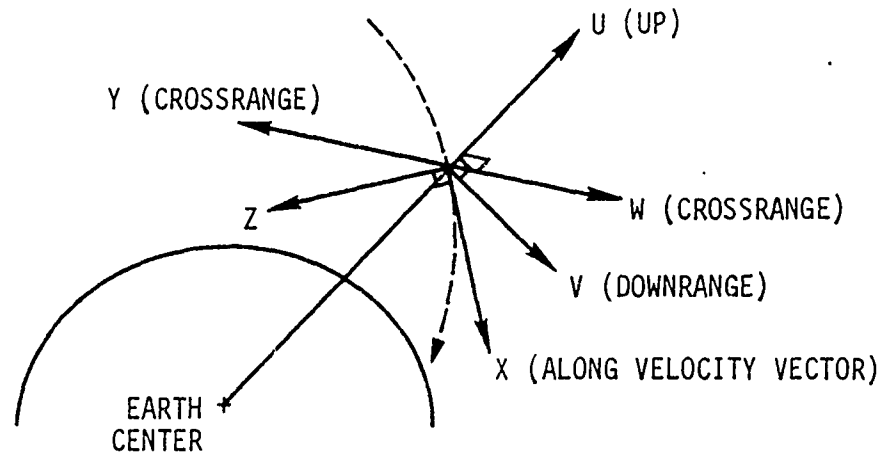
for propagating the covariance matrix from time  $t_0$  to other desired time points. Required inputs for RETAP can be grouped into the three categories shown. Trajectory generation inputs include those parameters necessary to create a reference trajectory from the initial state vector to a specified end time. The data description input specifies the type, tracking interval, reference location of the data, and the weighting,  $W$ , to be assigned to each data type. Finally, the variables to be included in the solution are specified, although no distinction is made between solved or considered systematic errors. In addition, the times for which propagation partials are to be computed are also specified.

The output of RETAP serves as the primary input to SMAP. The input variables allow manipulation of the specific systematic error parameters of the normal matrix including the deletion or inclusion of a "solved for" or "considered" variable. After the matrix manipulation has been performed, the program inverts the proper matrices, and combines them to yield the "solved for" portion of the covariance matrix,  $(A^TWA)^{-1}$  and the "solve plus consider" portion,  $(A^TWA)^{-1} + (A^TWA)^{-1} A^T W B \Sigma_z B^T W A (A^TWA)^{-1}$ . These covariance matrices are then propagated to the desired times using the propagation partials.

### 5.2.3 Error Analysis Coordinate Systems

The two coordinate systems most useful in interpreting the results of the error analyses are the UVW and XYZ coordinate systems. Both trajectory coordinate systems move but do not rotate with the vehicle as shown in the sketch on the following page:

### TRAJECTORY COORDINATE SYSTEMS



In the UVW system, U is a geocentric vector passing through the center of the earth and the vehicle, V is in the trajectory plane and perpendicular to U, and W points crossrange. These coordinates may also be considered as pointing in the vertical (up), downrange and crossrange directions respectively. In the XYZ system, X lies in the trajectory plane and is coincidental with the velocity vector, Z is perpendicular to X and is in the trajectory plane, and Y is normal to the trajectory, completing the orthogonal set.

The UVW system is most useful in defining downrange and cross-range position uncertainties, since impact miss distances are calculated in this system. The XYZ system is most useful in estimating the uncertainties in measuring aerodynamic parameters since X is oriented along the velocity vector (drag direction) and Y - Z displacements are related to lift effects. The magnitude of the XYZ uncertainties indicates regions during reentry

where lift and drag can be accurately measured and regions where improvements are desirable.

### 5.3 TRAJECTORY PARAMETERS

The estimate of trajectory measurement uncertainties depends on the trajectory geometry and equations of motion parameters and estimate of tracker uncertainties. This section specifies the trajectory geometry and equations of motion parameters used in the analysis. Section 5.4 addresses the tracker characteristics and error models used in the analysis.

The reference trajectory is defined by the following parameters:

- Initial state vector
- Aerodynamic coefficients (Lift/Drag)
- Climatology (Winds/Density)

Several factors must be considered in selecting the values for each of the trajectory parameters.

#### 5.3.1 Initial State Vector

The initial state vectors used in the study were selected based on the vehicle ballistic coefficient, reentry angle, reentry azimuth and impact location desired. Of these parameters only the reentry azimuth for a Vandenberg to Kwajalein flight is relatively fixed. A representative value of 238 degrees was chosen for the analyses. Parametric studies were performed at the various conditions shown in the matrix on the following page. Velocities corresponding to the different reentry angles are given in Appendix A.

TRAJECTORY PARAMETERS USED IN DEFINING  
INITIAL STATE OF ACCURACY ANALYSIS

Ballistic Coefficient (PSF)	Flight Path Angle (DEG)	Target Number
2000*	20	39
3000	30*	41
		54*

\* Nominal values

The large number of trajectory and sensor parameters considered in the error analyses precluded analysis of all possible permutations of the trajectory parameters. The nominal values indicated were chosen for the majority of the runs with the effects of the other combination of parameters being investigated by changing each of the parameters individually and comparing the results with the nominal conditions.

A planar illustration of the Kwajalein complex is shown on Figure 5.2. It includes the locations of the various targets, and a ground trace of a trajectory into one of these targets. Figure 5.3 presents trajectory traces on an altitude range scale and indicates the effect that reentry angle has on the vehicle range altitude relationship. Since the tracker locations are fixed, the target location and reentry angle affect the sensor-trajectory geometry and are significant parameters in the error analyses.

### 5.3.2 Aerodynamic Coefficients

Definition of the aerodynamics for the RETAP program requires specification of the following parameters:

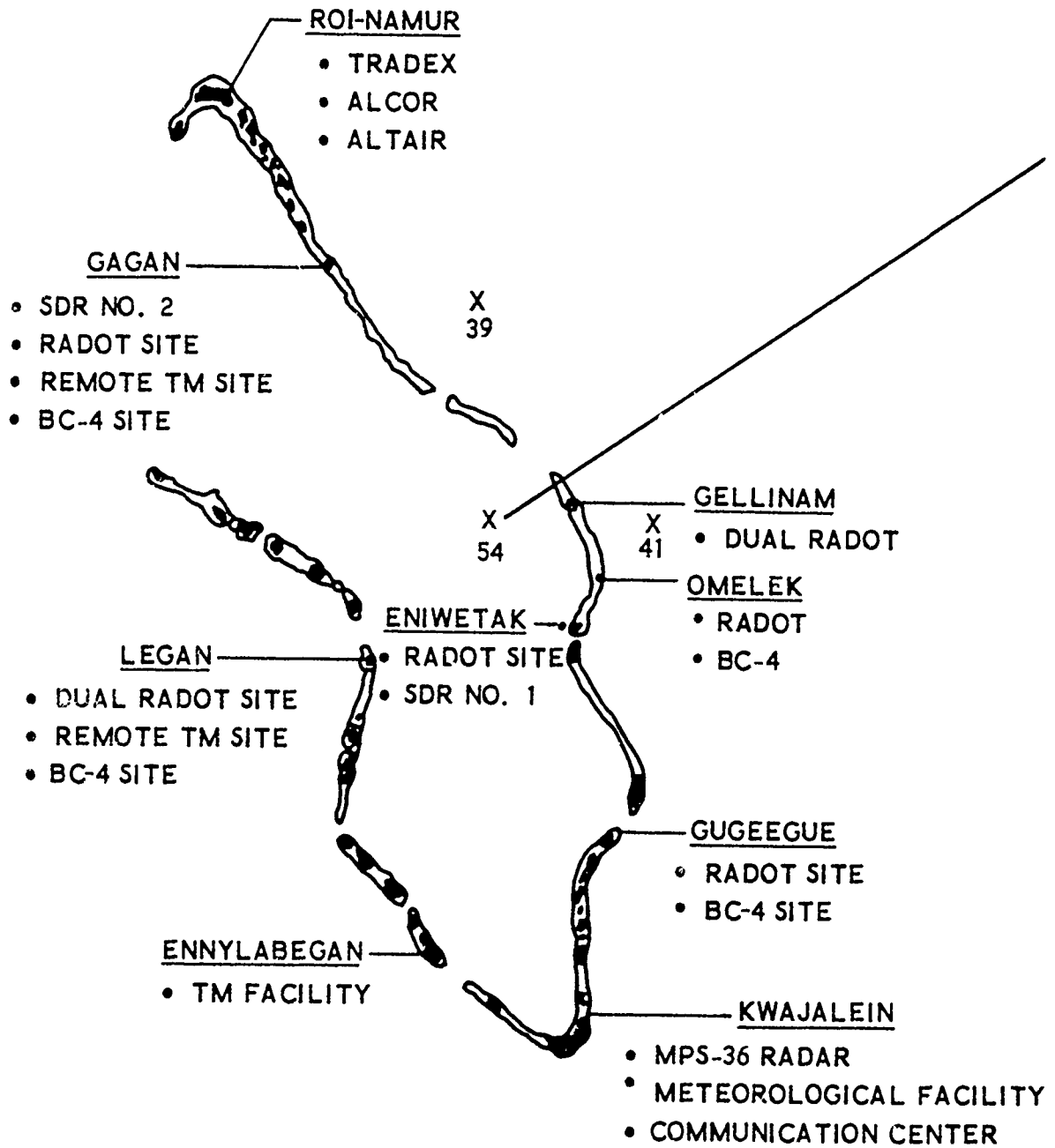


Figure 5.2 KMR Primary Targets and Instrumentation Sites

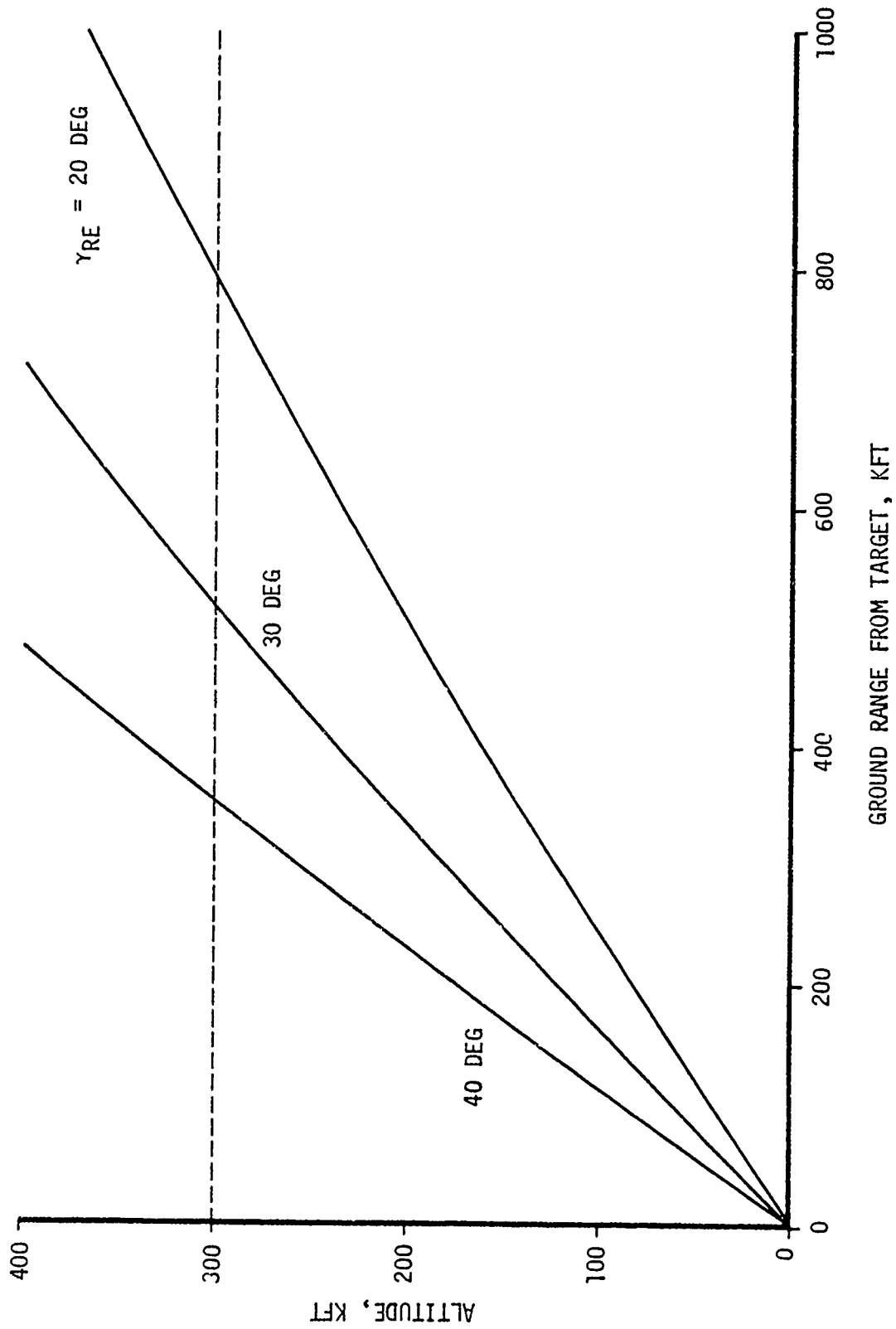


Figure 5.3 Effect of Reentry Angle on Range - Altitude Relationship

- $C_D A/2m$  (Drag)
- $C_L A/2m$  (Lift)

The  $C_D A/2m$  parameter is simply a variation of the ballistic coefficient parameter ( $W/C_D A$ ). Ballistic coefficient histories for the various vehicles are presented in Appendix A. Although a zero lift was input for the reference trajectory it was assumed in most of the analyses that lift up to 220 KFT did exist and hence this parameter was included in the state variables.

### 5.3.3 Climatology

Climatology (winds and density) has a minimum influence on the tracking error analysis if a reasonable model is used for the density profile. Since climatology uncertainties are not included in this error analysis the results of this section study must be added to the density uncertainty to determine the total ballistic coefficient and angle-of-attack uncertainty. The specific model chosen for the input was an annual density profile and zero winds.

## 5.4 TRACKER CHARACTERISTICS

The metric trackers in the Kwajalein area were used to provide a baseline on the expected metric tracker accuracy performance in the near future. The sensors for which a considerable data base exists from past operational experience include the following:

- Radars - ALCOR, TRADEX, ALTAIR, MPS-36, Ship
- Optics - RADOT System, Ballistic Cameras (BC-4)
- Scoring - SDR's, RADOT

Figure 5.2 shows the site locations of these sensors throughout the Kwajalein complex. Most of these sensors have been used extensively in the past and are well known to range users. It is assumed that the reader has

some prior knowledge of these trackers and only a brief description of their capabilities, and current and predicted measurement uncertainties is included. Additional information may be obtained from References 9 and 10.

#### 5.4.1 Metric Radars

Exoatmospheric and reentry metric tracking data can be acquired by several Kwajalein radars including: ALCOR, ALTAIR, TRADEX, MPS-36, and the ship (mobile terminal radar). The ALCOR, ALTAIR, and TRADEX radars are located on Roi Namur Island at the north end of the Kwajalein complex and are operated under the direction of Lincoln Laboratory. Two MPS-36 radars are located on Kwajalein Island on the south end of the Kwajalein complex and are operated by Kentron Hawaii Ltd. Of the five radars, the MPS-36's, ALCOR and TRADEX radars have provided the most accurate metric radar data because of their narrower beam width, higher frequency, and other characteristics which make them more suitable for acquisition of metric as compared with observables data. It was assumed in the analysis that these radars were operated in the C-band beacon mode except TRADEX, which is a skin tracker.

The measurement characteristics of the five radars, current and predicted, are given on Table 5.1. ALCOR is currently the most accurate radar in both random and systematic error levels. However, it is envisioned by the range that within a year the MPS-36 will have an equivalent systematic accuracy. The range expects to realize the predicted system accuracy levels by the fall of 1974. Both current and predicted performance characteristics were used in the error analysis.

In addition to random and systematic tracking errors, the ship has a survey error associated with its determined position relative to the Kwajalein datum. Standard errors of 30 feet and less have been achieved in both latitude and longitude using the SAMTEC ASPS/SRN-9 survey package.



This and a value of zero were used in the error analysis.

#### 5.4.2 Metric Optics

Two additional sources of metric tracking data are the RADOT cinesextant system and ballistic cameras. The responsible contractor for operating these camera systems is Kentron Hawaii Ltd.

The RADOT system (Recording Automatic Digital Optical Tracker) has demonstrated the capability to acquire highly accurate metric track on the RV from approximately 125 KFT altitude to impact on both daylight and night operations, provided cloud cover does not obscure the vehicle. This system basically consists of cameras mounted on a cinesextant tracking mount used to record the azimuth and elevation of the line-of-sight to a target. The time of exposure is also encoded onto the film. The metric data acquired with the RADOT consist of angular measurements without range information. While data provided by two RADOT stations are sufficient to determine the position of a target in space, three or more independent RADOT stations are usually employed to improve the accuracy through an over determined solution.

BC-4 ballistic cameras are also available, and offer potential accuracies of at least that of RADOT. The still camera system, mounted on Theodolite mounts, records the image on optically flat photographic plates. Like RADOT, ballistic cameras record only angle data. Precise orientation of the system is obtained by recording the star field background without moving the camera from its mission orientation. This enables extremely accurate angular data measurements.

The measurement accuracy characteristics of the two optical systems are presented on Table 5.1 and indicate that currently the ballistic camera system yields the more accurate angular measurements. However, the

Range is upgrading the RADOT systems to yield comparable accuracy in the near future.

#### 5.4.3 Scoring Systems

A review of the several methods available for measuring impact location and time resulted in the selection of a set of scoring systems which are believed to be suitable for the current study. Two candidates for determining impact location are the Splash Detection Radar (SDR) and optical triangulation using RADOTs. Other systems were studied but discarded, either because of insufficient measurement accuracy or because their accuracy potential has not yet been demonstrated. The most accurate method of determining impact time was found to be the use of telemetry loss of signal (LOS).

Splash Detection Radars - Splash Detection Radars (SDR's) are search radars which transmit a narrow beam along the horizon in a continuous circular sweep. When the RV impacts, it produces a water plume which for high ballistic coefficient vehicles reaches several hundred feet in height and is approximately 100 to 200 feet across. The water plume is observed by the SDR and the range and azimuth to the plume are measured. These data are then used to determine the latitude and longitude of impact based on the known location of the SDR site. The accuracy of the score therefore depends on how accurately the range and azimuth can be measured and how well the plume location represents the true impact point of the vehicle. The estimated uncertainty of the SDR score based on the system level and target dependent error uncertainties, but excluding geodetic errors, will range between 35 to 45 feet for optimally located targets and considerably larger for targets at extended range. These uncertainties are considered excessive for verifying an accurate reentry system.

RADOT Scoring - The RADOT optical tracking system can be used in two different modes for obtaining impact location. If the target area

surface is chosen such as to be above the optical horizon for two or more RADOT sites, then RADOT cameras can be pointed to cover the expected position of impact. During the time of impact, the cameras are fixed and observe the vehicle as it enters the field of view and impacts the water surface. A computer program is used to assure that the camera is being pointed at the actual vehicle impact location based on updated trajectory data gathered during reentry.

The other method of obtaining RADOT scoring information is to use the RADOT system in its tracking mode and derive a best estimate of trajectory which intersects the surface. This dynamic mode of operation is particularly well suited for targets below the optical horizon which cannot be scored in the static mode. Considerable experience has been obtained on the Minuteman III program using the RADOT system in this mode of operation and has resulted in obtaining more accurate impact scoring than can be achieved using the SDR system. However, the RADOT system does have limitations in that the weather must be somewhat better than is required for SDR operation, and good pointing information is required from a radar track file to assure a high probability of track.

A comparison of the two methods of RADOT scoring was obtained on a target dependent error test where both methods of scoring were used. The system level uncertainty for the static method, including target dependent errors resulting from vehicle motion smearing of the film image, was quoted as 2 to 4 feet on all tests. The quoted uncertainty for the dynamic RADOT measurements for the same target area were 4 to 7 feet. For target areas beyond the optical horizon, the quoted uncertainty is larger since the range to the target is greater and the trajectory has to be propagated a greater distance to the surface. Typical one sigma uncertainties for this latter case range between 6 to 15 feet. These scoring accuracies are sufficiently accurate for verifying reentry system accuracies being addressed in this study.

5.5 ERROR ANALYSIS: CURRENT VERSUS PREDICTED SENSOR ERRORS

This section presents the estimated uncertainties associated with the derived position, velocity and deceleration errors based on a set of "nominal" trackers and a "typical" trajectory. Both current and predicted uncertainties were used for the sensor random and systematic errors. The results may therefore be viewed as best estimates of the current and predicted metric capabilities, and will be used throughout the remainder of the metric tracker study as the baseline case.

5.5.1 Analysis Baseline and Variable Parameters

The specific trajectory parameters assumed for this baseline case are as follows:

$$\frac{W}{C_D A} = 2000 \text{ psf}$$

$$\gamma_{RE} = 30 \text{ Degrees}$$

Target Number 54

The effects of changes in each of these parameters will be considered later. The nominal sensor coverage used in the study is shown below:

NOMINAL TRACKER COVERAGE

Sensor	Altitude Regions (KFT)	
	Start	Stop
ALCOR	500	0
MPS-36	500	0
RADOT (LEGAN)	125	0
RADOT (GAGAN)	125	0
RADOT (ENIWETAK)	125	0

The above reentry coverage and combination of trackers have been obtained on many past Minuteman missions with the exception of ALCOR. ALCOR has usually been switched to the skin mode during reentry to satisfy other objectives. Skin track, however, has degraded the quality of ALCOR data and is not recommended.

The "solve" and "consider" parameters used in the baseline analysis included radar errors, lift and drag. Solve parameters included in the covariance matrix consist of both the vehicle state vector at 500 KFT, and lift and drag forces. Lift forces were solved for below 160 KFT, while drag was solved for below 220 KFT. The state vector covariance matrix was subsequently propagated to impact using propagation partials. Consider parameters included all radar systematic errors with the associated uncertainties listed on Table 5.1, and lift uncertainties above 160 KFT, representative of the region affected by initial angle-of-attack uncertainties. The baseline analysis assumed approximately a one degree angle-of-attack uncertainty at high altitudes.

#### 5.5.2 Results

Results of this analysis are presented on Figures 5.4 through 5.7. Position uncertainties, presented on Figures 5.4 and 5.5 for XYZ trajectory coordinates and for downrange, crossrange respectively, show the following:

1. Lateral position uncertainties (Y and Z) are relatively large at high altitudes, decreasing as the RV reenters. This reflects the relatively poor radar as compared with good RADOT angle accuracy and the greater acquisition range for radar;

2. The position uncertainty along the trajectory (X) remains fairly constant throughout reentry until 75 KFT. This is attributed to measurements in the radar range direction which have relatively high

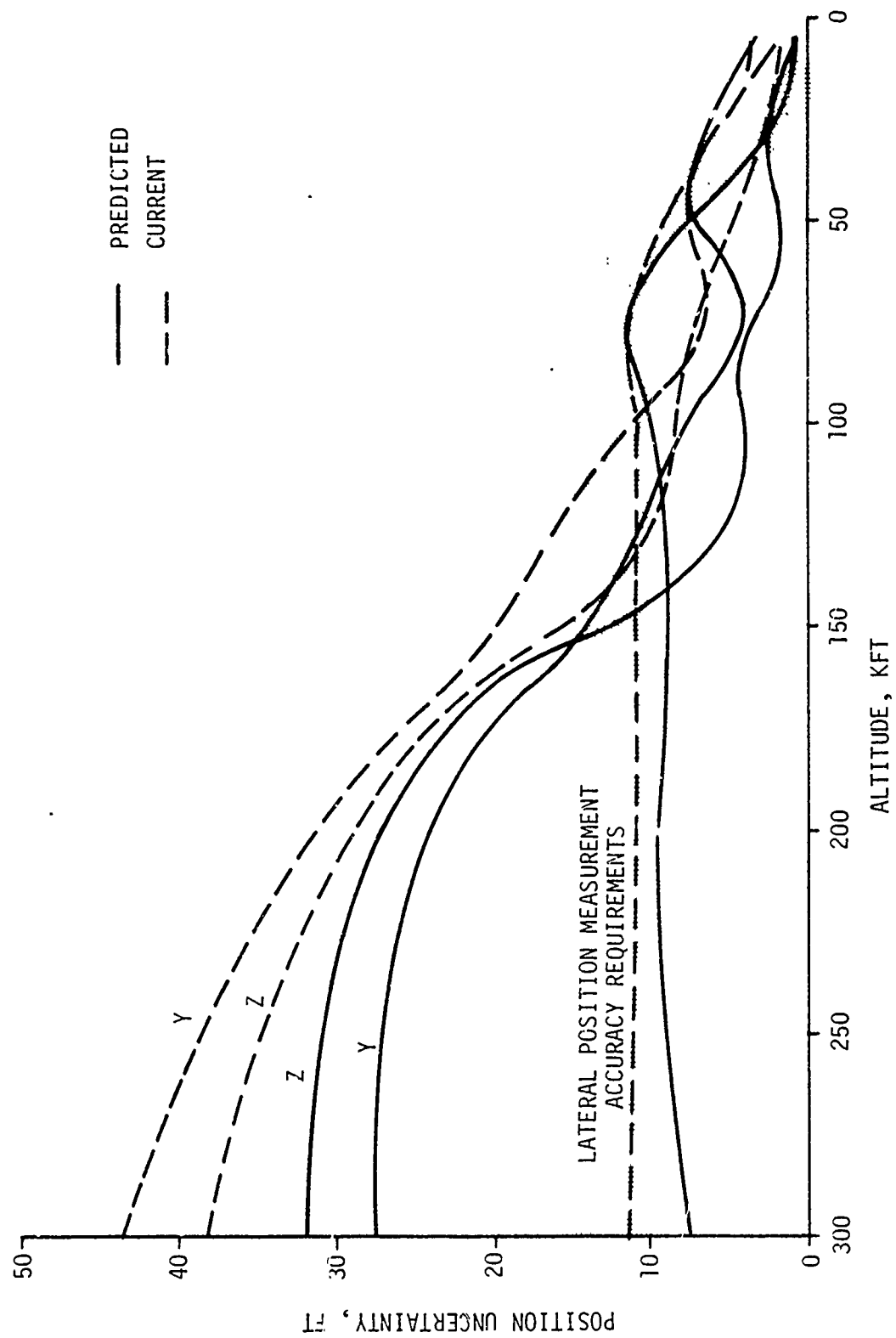


Figure 5.4 Trajectory Position Uncertainties (XYZ) for Nominal Error Analysis

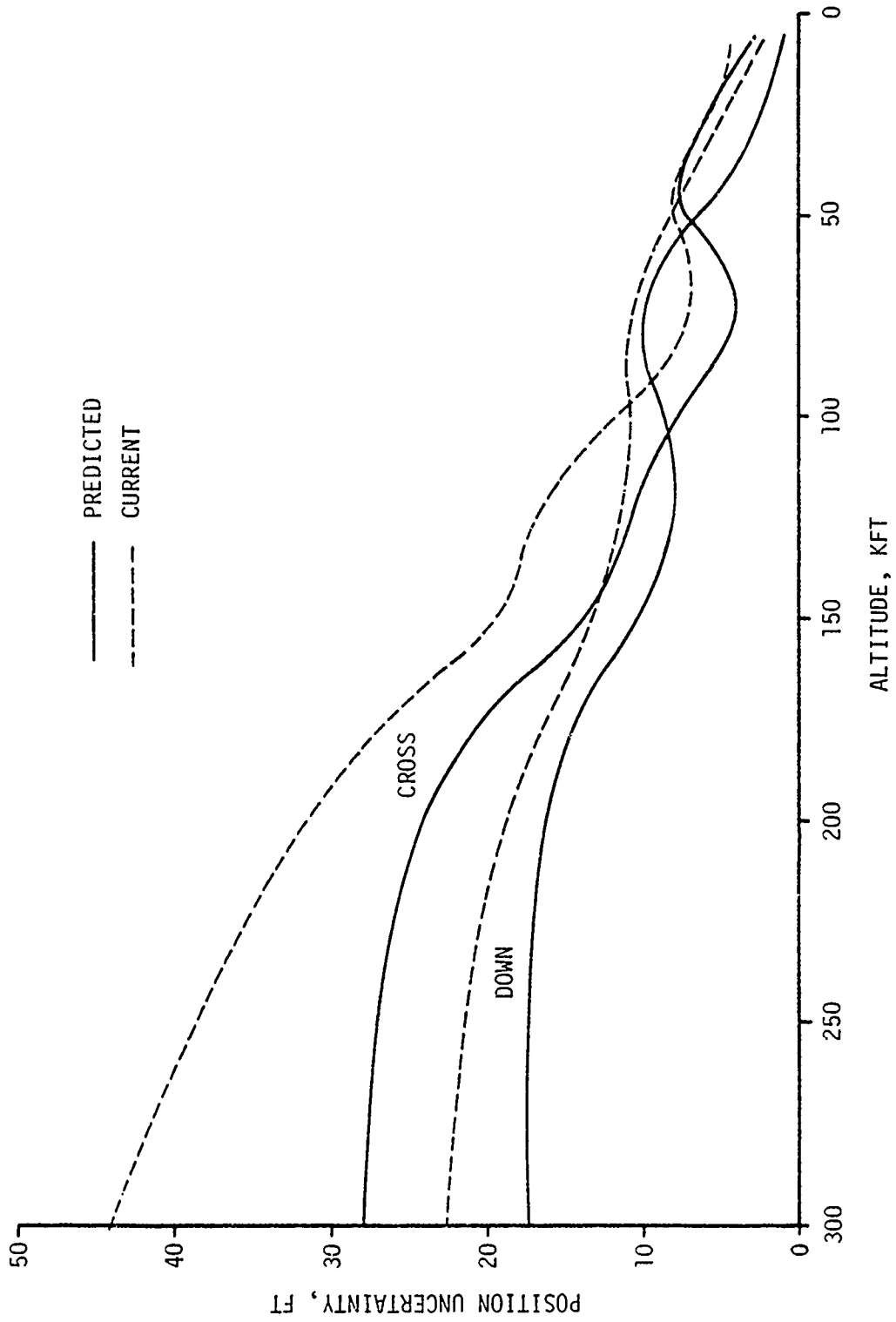


Figure 5.5 Trajectory Position Uncertainties (Downrange and Crossrange) for Nominal Error Analysis

accuracy over the entire useful measurement range. It should be noted that the RADOT angle solution is weakest along this direction and hence contributes little to the radar solution along X when it first acquires track;

3. The trajectory coordinate position accuracy below 100 KFT is very good, generally less than 15 feet in each direction. The decreasing-increasing - decreasing behavior results from the variation in the ability to correlate successive measurement points through the equations of motion as the uncertainty in the motion parameters varies through reentry (particularly the lift effects);

4. Lateral position accuracies are insufficient to measure lift effects above 100 to 150 KFT, but do achieve the ten to fifteen foot accuracy requirements established in Section 4.6 below this altitude. Since the majority of lift effects occur below 100 KFT, this may be satisfactory if high altitude lift effects are very small. Lift effects on position accuracies are discussed in some detail in Section 5.8;

5. Predicted improvements in the sensor errors will result in significant improvements in the lateral position accuracy, but only slight improvement in the axial trajectory position (X) throughout reentry. This reflects the large predicted improvement for angle accuracies;

6. Pierce point accuracies at 200 KFT are observed from Figure 5.5 to be 15 to 25 feet downrange and 25 to 45 feet crossrange. This compares with requirements of 30 to 40 feet and 15 to 20 feet respectively.

The percent velocity uncertainty,  $\sigma_{\dot{X}}\%$ , presented on Figure 5.6 is observed to increase during most of reentry due to the corresponding increase in drag deceleration. The small uncertainties constitute a negligible contribution to the total dynamic pressure uncertainty. Analyses of subsequent sections, therefore, do not present velocity uncertainties.

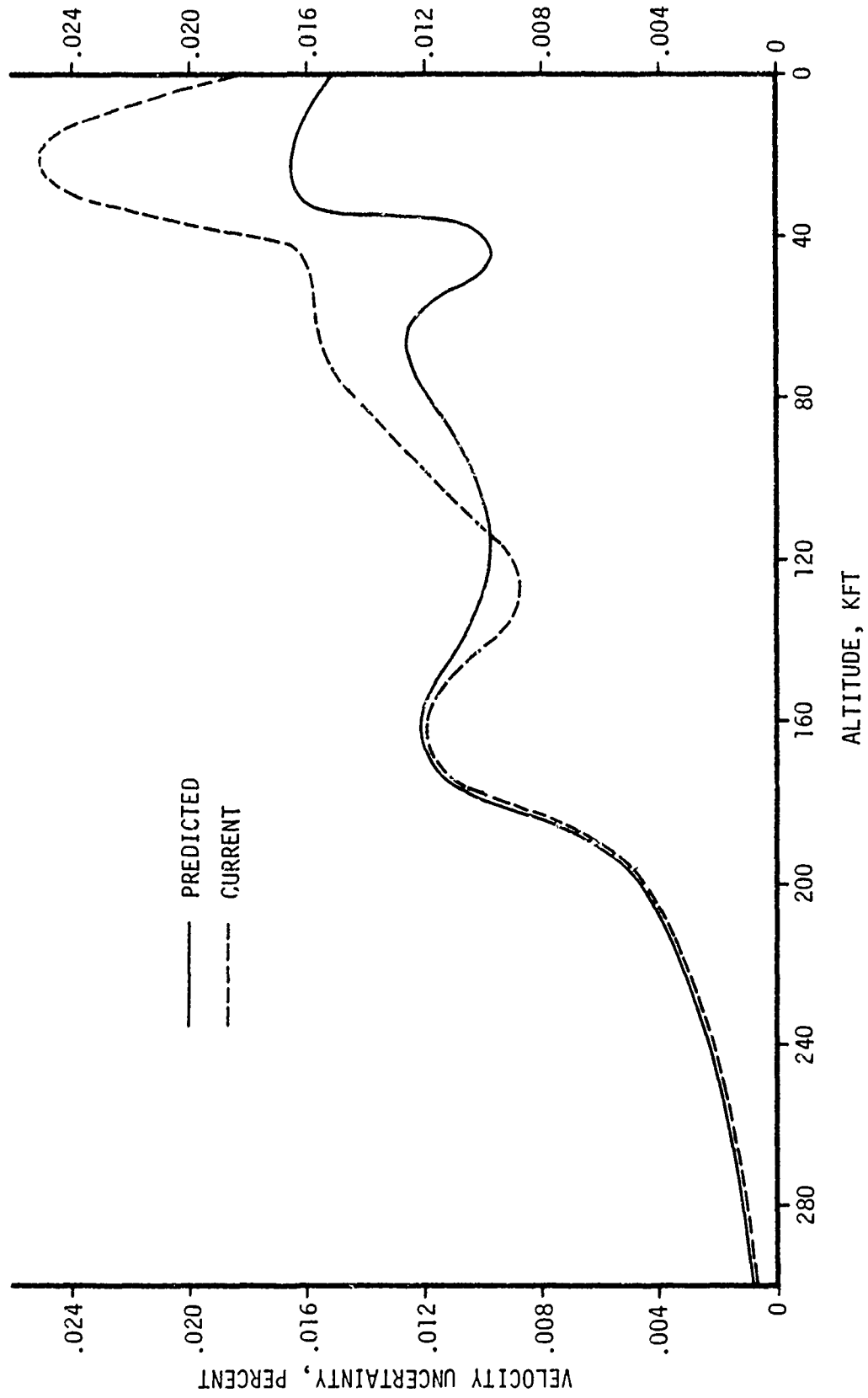


Figure 5.6 Trajectory Velocity Uncertainties for Nominal Error Analysis

The percent deceleration accuracies,  $\sigma_{AD\%}$ , achievable using metric sensors are presented on Figure 5.7 and compared with the decelerations measurement requirements derived in Section 4.4. The significant observations are as follows:

1. The derived deceleration uncertainty decreases markedly with decreasing altitude, increasing only slightly during the region of boundary layer transition where the drag coefficient is very small;
2. Predicted sensor error models will not result in a significant improvement in the deceleration measurement capability. This is attributed to the strong dependence of accurate deceleration measurements on the range measurement capability, which will not be significantly improved, except at low altitude reflecting increased optical accuracy.
3. The capability of external metric sensors to meet deceleration measurement requirements is dependent on the minimum design reentry angle. Figure 5.7 presents the design requirements per 100 feet CEP and indicates that the measurement accuracies are not sufficient to achieve a desired accuracy objective of 100 feet for a 20 degree design trajectory but can meet the same CEP requirements for a 30 degree reentry trajectory design. It should be noted that the baseline trajectory for the measurement accuracies shown has a 30 degree reentry angle.

The final set of solved for parameters was lift. The accuracies associated with the derived lateral accelerations ranged from two to three feet per second per second in the trajectory Y direction and 0.5 to three feet per second per second in Z. This is significantly larger than the measurement requirements established in Section 4.6 and it must be concluded that metric measurements do not yield sufficiently accurate lateral accelerations to integrate through reentry to provide lift effects.

This section has presented detailed results for "nominal" trajectory and tracking parameters into the Kwajalein terminal area. Subsequent sections consider the effects of variations in these parameters on the

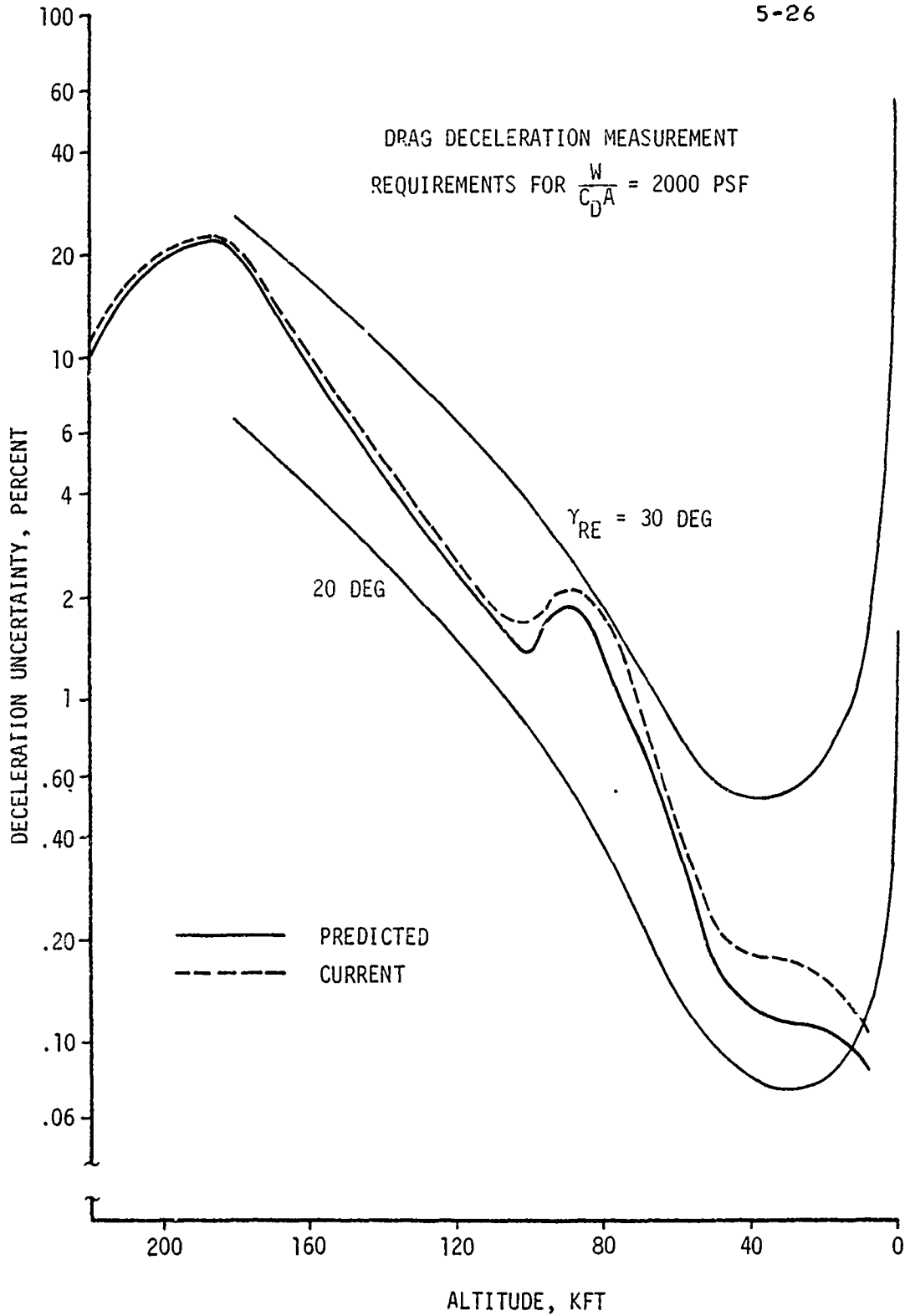


Figure 5.7 Trajectory Deceleration Uncertainties for Nominal Error Analysis

derived position and deceleration histories.

#### 5.6 ERROR ANALYSIS: EFFECT OF DIFFERENT TRACKERS

The sensor combination used in the "nominal" error analysis of Section 5.5, while representative of the metric tracking net, is only one of many possible combinations that could be employed in the Kwajalein complex. This section studies the effects of different sensors on the position and deceleration measurement capabilities. The sensors considered in this study included:

- RADOT
- MPS-36/ALCOR
- Ballistic Camera
- TRADEX
- Instrumentation Ship
- Doppler

Predicted error models for the sensors were used throughout this portion of the study.

##### 5.6.1 RADOT

The effect of including and excluding RADOT sensors in the trajectory solution was examined. The effects on position and deceleration results are shown in Figures 5.8 and 5.9. The case without RADOT sensors shows the accuracy achievable with only the ALCOR and MPS-36 radar data. When Gagan RADOT is added to the solution the accuracy of the trajectory estimate is significantly improved in the Y and Z position below the RADOT acquisition altitude. Improvement is also noted in the axial deceleration measurement. It can be concluded that optical data are mandatory for a high accuracy trajectory reconstruction requirement.

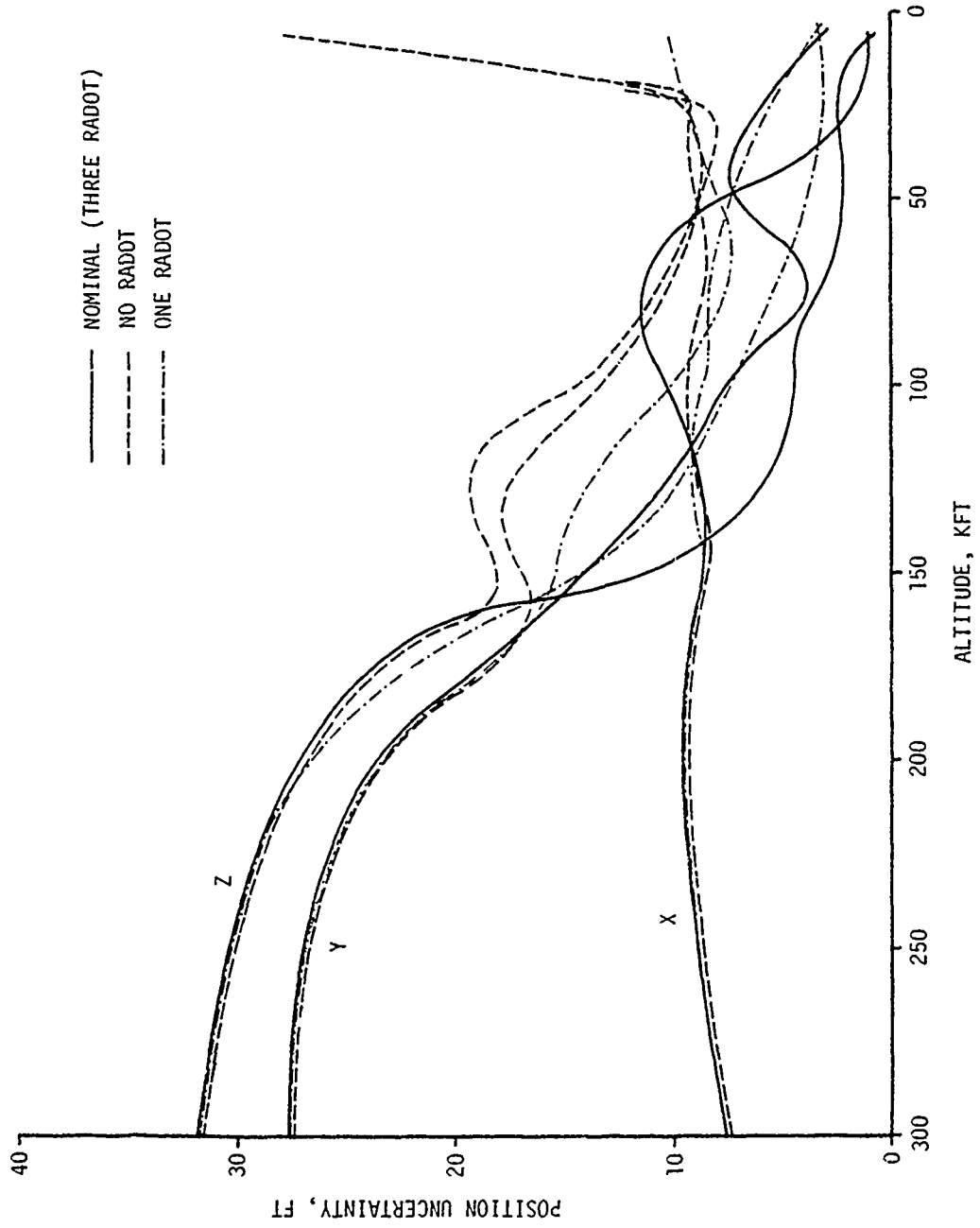


Figure 5.8 Trajectory Position Uncertainties using Different RADOT Combinations

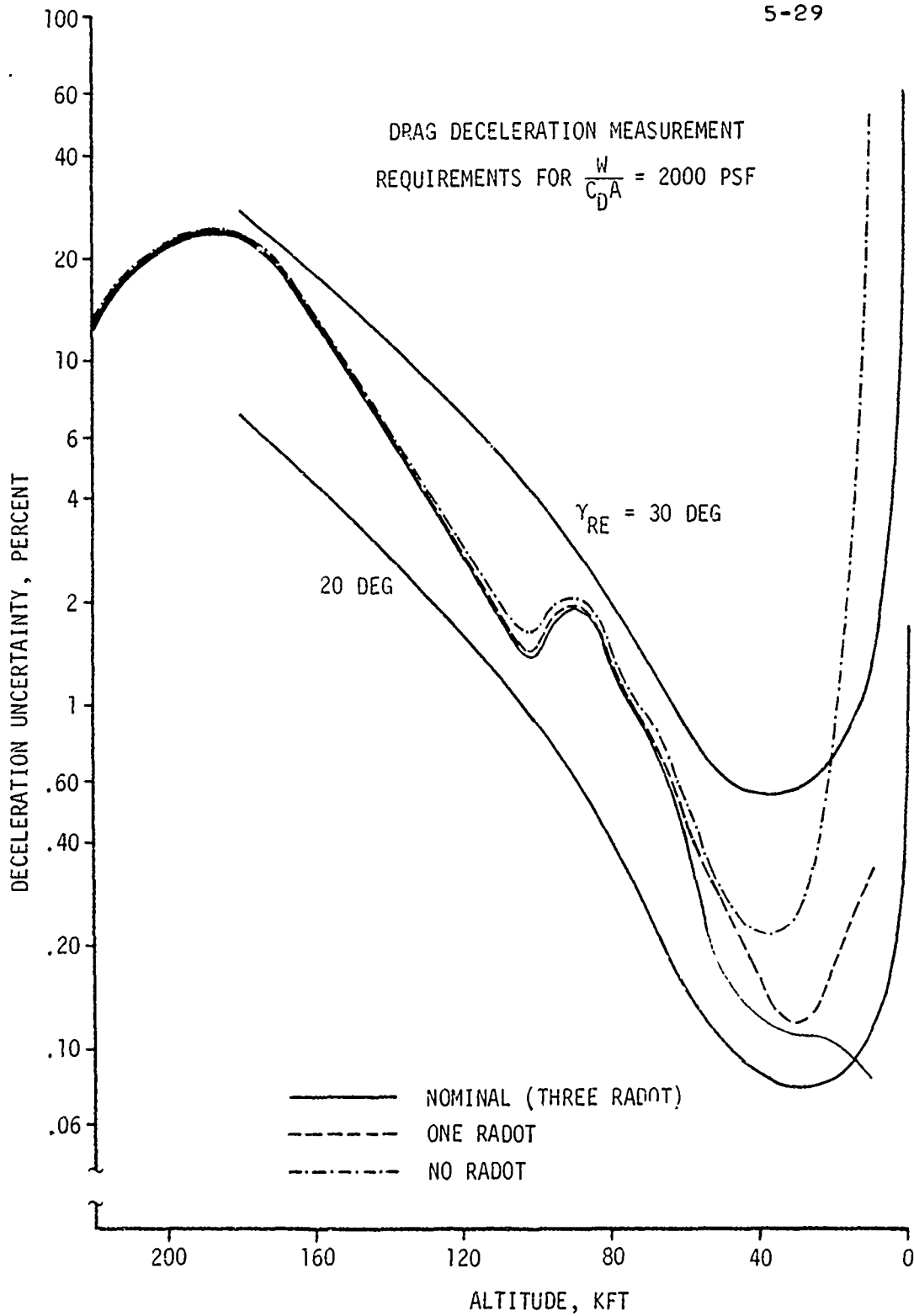


Figure 5.9 Trajectory Deceleration Uncertainties Using Different RADOT Combinations

#### 5.6.2 Ballistic Camera

The primary difference in accuracy between RADOT and BC-4 optical sensors is in the systematic error as indicated on Table 5.1. However, the difference in the derived position and deceleration accuracies between a solution with RADOT sensors and BC-4 sensors was insignificant and a comparison is not presented.

#### 5.6.3 MPS-36/ALCOR

The trajectory accuracy for a MPS-36/ALCOR only solution was previously presented in Figures 5.8 and 5.9 (no RADOT case), and was observed to be significantly less accurate at lower altitudes than when optical trackers are used in the solution. The degradation in trajectory accuracy resulting from using only one metric tracker is shown in Figure 5.10. This figure compares trajectory accuracies achievable using only the MPS-36 and using both the MPS-36 and ALCOR radars with the nominal case which includes optical trackers. The addition of the second radar, ALCOR, enhances the high altitude accuracy above 30 KFT due to the favorable geometry of the two radars, one on each side of the trajectory. It is recommended that both radars be used for an accurate trajectory reconstruction.

#### 5.6.4 TRADEX

The use of TRADEX in lieu of ALCOR at the KREMS site results in the degradation of the lateral (Y) position accuracy as shown in Figure 11. This results from the significant difference between the random noise levels of the two sensors, Table 5.1. It should be noted, however, that the use of ALCOR in the "nominal" analysis assumed beacon track throughout reentry. If ALCOR skin track was used instead, accuracies similar to TRADEX would result. It is recommended that ALCOR beacon track be used throughout reentry.

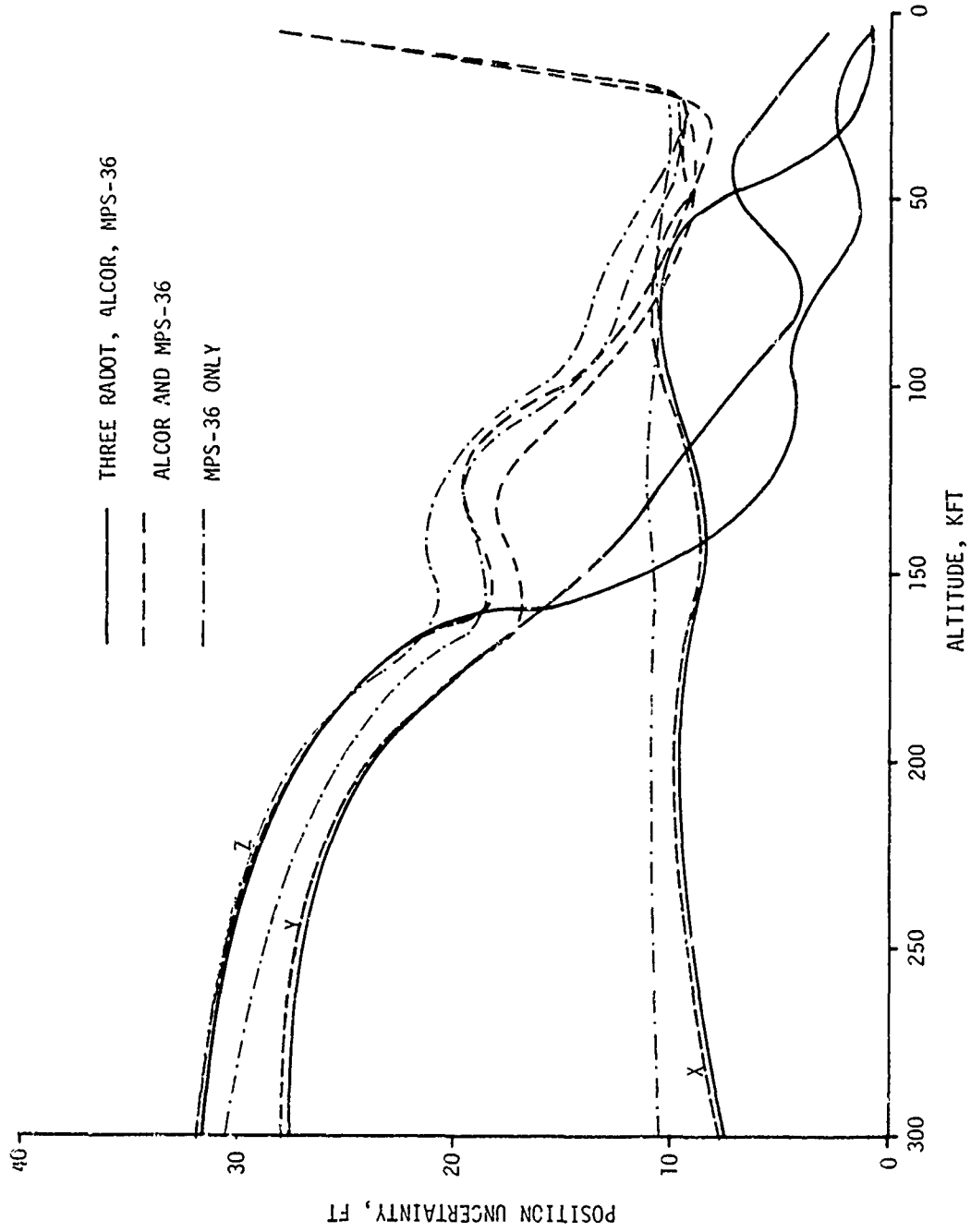


Figure 5.10 Trajectory Position Uncertainties using Different Radar and RADOT Combinations

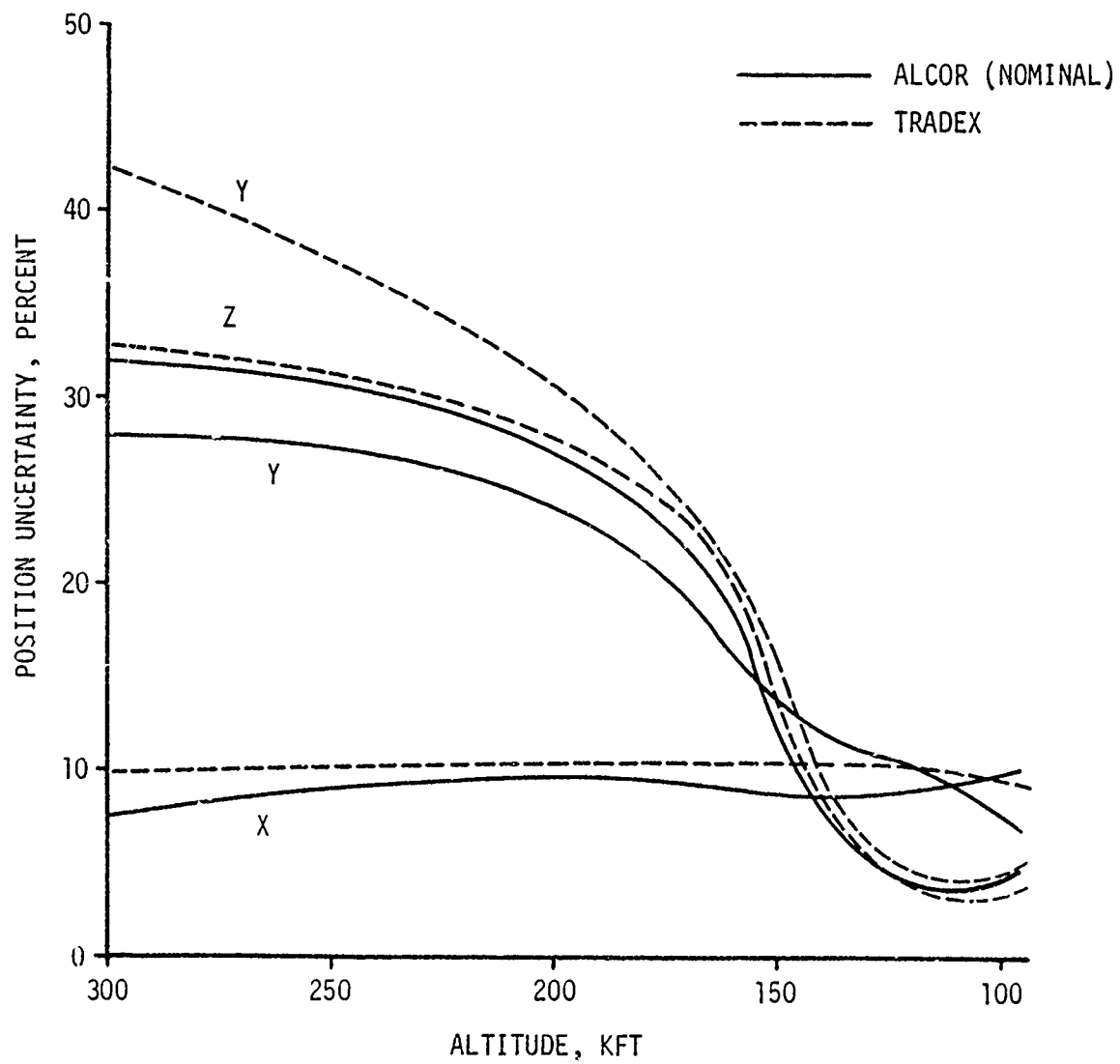


Figure 5.11 Trajectory Position Uncertainties using TRADEX  
in Lieu of ALCOR

#### 5.6.5 Instrumentation Ship

The ship, being a mobile tracker, offers the user an opportunity to place this sensor in a location where it can most benefit the solution. From the "nominal" position uncertainties presented on Figure 5.4 it is evident that such a sensor would be beneficial if it could improve the lateral position accuracy (Y - Z) above 150 KFT. To determine representative accuracy improvements to be obtained with a ship, a radar sensor was included in the solution at a location of 60 miles uprange and 5 miles crossrange of the trajectory. In this position the point of closest approach corresponds to an altitude of 200 KFT. The radar error model representative of that for the ship is presented in Table 5.1.

A significant factor in using any mobile sensor is the survey uncertainty associated with establishing its reference location. Survey capabilities of 30 feet in longitude and latitude have been demonstrated using an Acoustic Ship Positioning System. To bound the effects of ship survey uncertainty on the accuracy of the trajectory estimate, values of both 30 feet and zero were used in the analysis.

Results of the study are presented on Figure 5.12, which compares the position uncertainty of the "nominal" land based tracking array with that derived using the same array but including a mobile sensor with its associated measurement and survey uncertainties. The results indicate only slight improvement in the solution accuracy above 100 KFT even for a ship with zero foot survey uncertainty. Based on these simulations it is concluded that if the predicted range and angle accuracies of the ALCOR and MPS-36 are realized, little benefit is to be gained by utilizing a mobile sensor in the reentry area.

#### 5.6.6 Doppler

The use of doppler data to enhance the velocity and hence X-position and deceleration measurement accuracies was considered in the

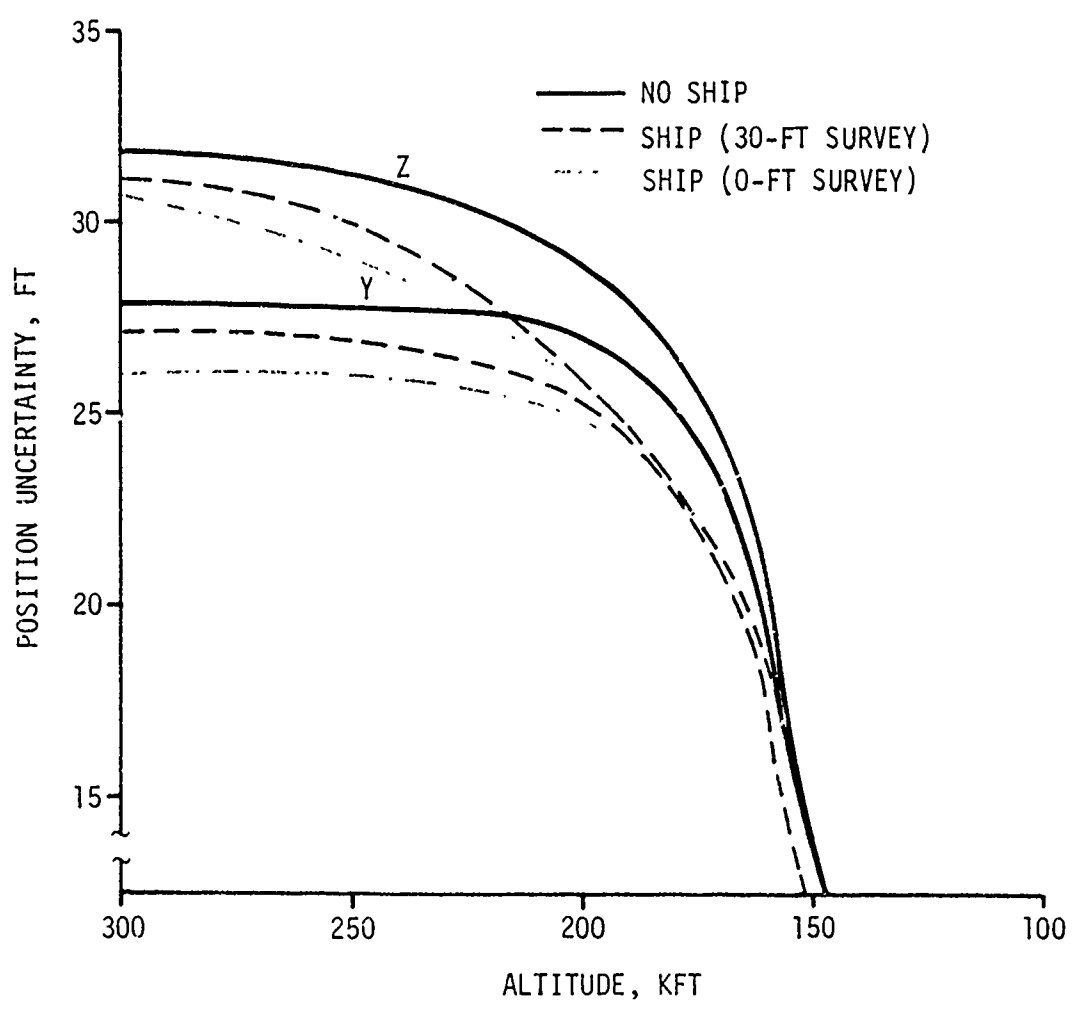


Figure 5.12 Trajectory Position Uncertainties Using Shipboard Radar

analysis by adding such data to the "nominal" solution. Figure 5.7 indicated that deceleration measurement capabilities using external sensors are only marginal using the "nominal" set of external metric trackers. Therefore, the use of doppler measurements as a means of improving the solution accuracy was investigated. Currently, the KREMS site has the capability to make doppler measurements; hence, an error analysis was performed adding doppler measurements to the "nominal" case.

Figure 5.13 presents the improvement to the derived deceleration for two values of measurement noise. These values, 0.1 and 1.0 FPS, are believed to bound the doppler velocity measurement capability of the KREMS radars. The results indicate that doppler measurements can benefit the deceleration measurement accuracy below 100 KFT, and the use of accurate doppler data should be considered.

#### 5.7 ERROR ANALYSIS: EFFECT OF SURVEY ACCURACY

The accuracy of the multiple sensor trajectory solution depends not only on the measurement accuracy of each sensor but also the accuracy with which the true location of each sensor is known with respect to other sensors in the solution. For a reentry trajectory solution in which all the sensor locations are referenced to the Kwajalein local datum it is not necessary to include the World Geodetic Survey uncertainties relative to the earth center. Since the reentry analysis is performed using Kwajalein sensors exclusively the WGS uncertainties do not affect the trajectory accuracies relative to the terminal area. However, within the Kwajalein area, the relative position of the different sensors is not known with complete accuracy. Although information regarding the relative survey uncertainties is not readily available, it is believed that accuracies of at least 1 part in 100,000 to 50,000 feet are being achieved, which is equivalent to an average of two to four feet uncertainty.

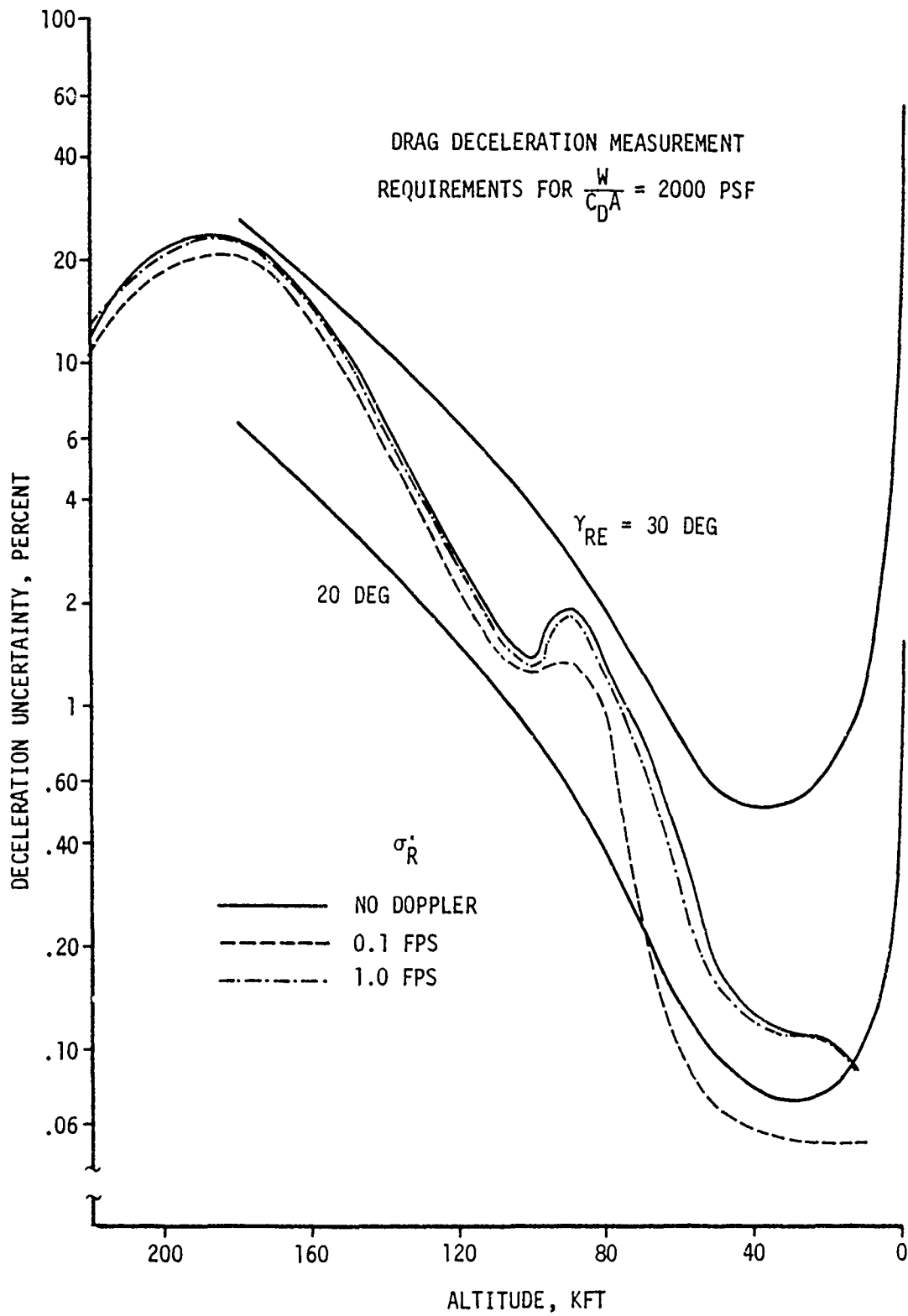


Figure 5.13 Trajectory Deceleration Uncertainties Using Doppler Measurement

Figure 5.14 compares position accuracies achieved using the "nominal" sensor configuration with relative survey uncertainties of zero and five feet. The results indicate that survey uncertainties of this magnitude do not significantly degrade the accuracy of the solution.

#### 5.8 ERROR ANALYSIS: EFFECT OF HIGH ALTITUDE LIFT

The high altitude lift model and its associated uncertainty directly affect the accuracy of the trajectory regression solution in which the successive sensor measurements are correlated through the equations of motion. The nominal analysis assumed a random uncertainty of one degree above 160 KFT, and a "solved" for value below this altitude. To determine the effects of different high altitude angle-of-attack uncertainties on trajectory accuracies, two additional simulations were made. In the first case it was assumed that the vehicle reenters with a five degree angle-of-attack uncertainty and decreases to one degree by 160 KFT. The second case assumed the vehicle either is known to reenter with a negligible angle or that on-board instrumentation is used to accurately determine the angle-of-attack and momentum vector orientation.

The results presented on Figure 5.15 reflect the high correlation between the lateral position accuracy and the high altitude angle-of-attack uncertainty. It is of particular interest to note the appreciable increase in solution accuracy that results when the angle-of-attack is accurately known. If on-board instrumentation is used to determine the lateral acceleration to the accuracies established in Section 4.0, the minimum trajectory accuracies shown in Figure 5.15 should be achievable.

#### 5.9 ERROR ANALYSIS: EFFECT OF BALLISTIC COEFFICIENT AND REENTRY ANGLE

The baseline conditions for the error analyses performed thus far have used a 2000 ballistic coefficient and a 30 degree reentry angle.

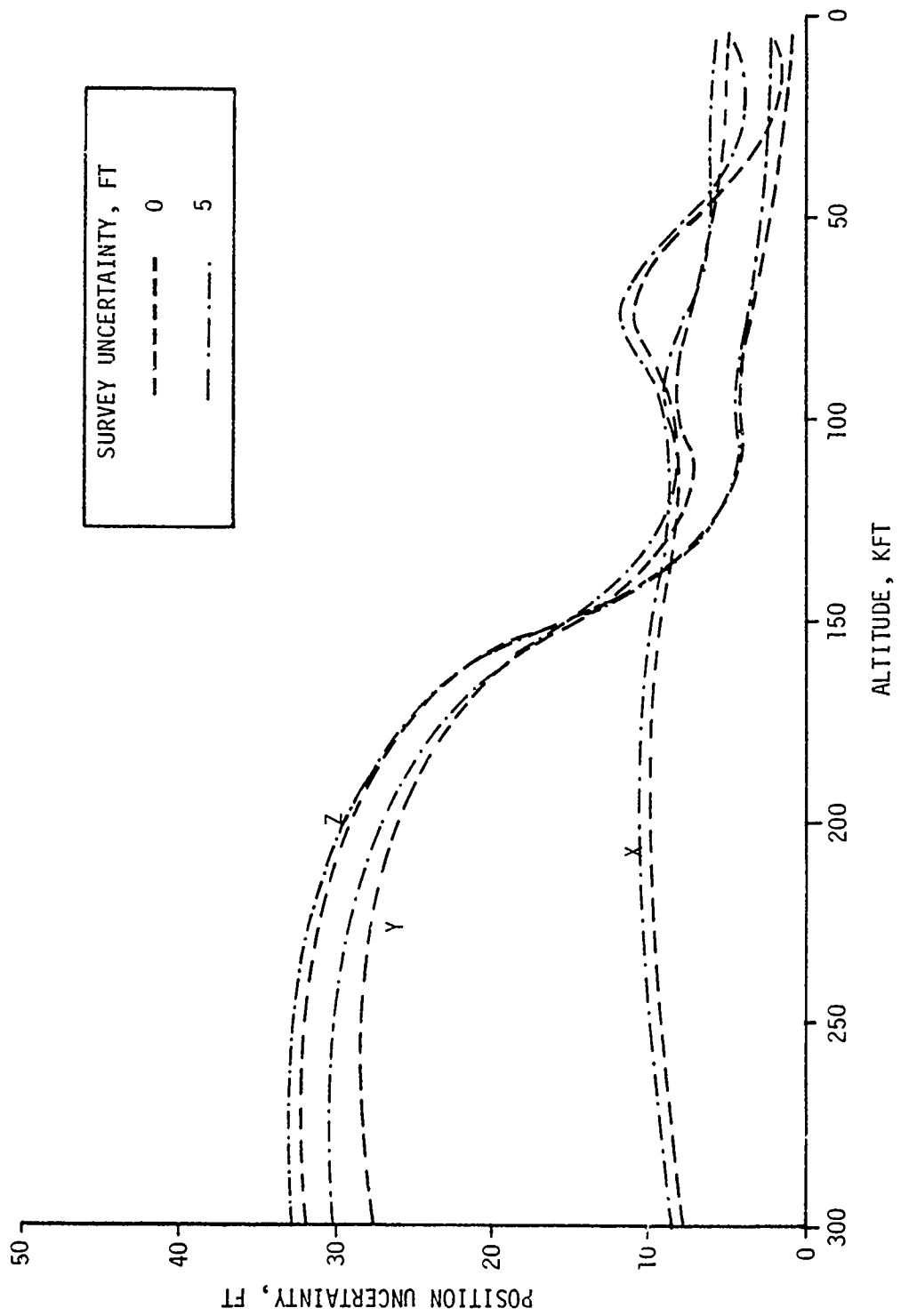


Figure 5.14 Effect of Relative Survey Accuracy on Position Accuracy

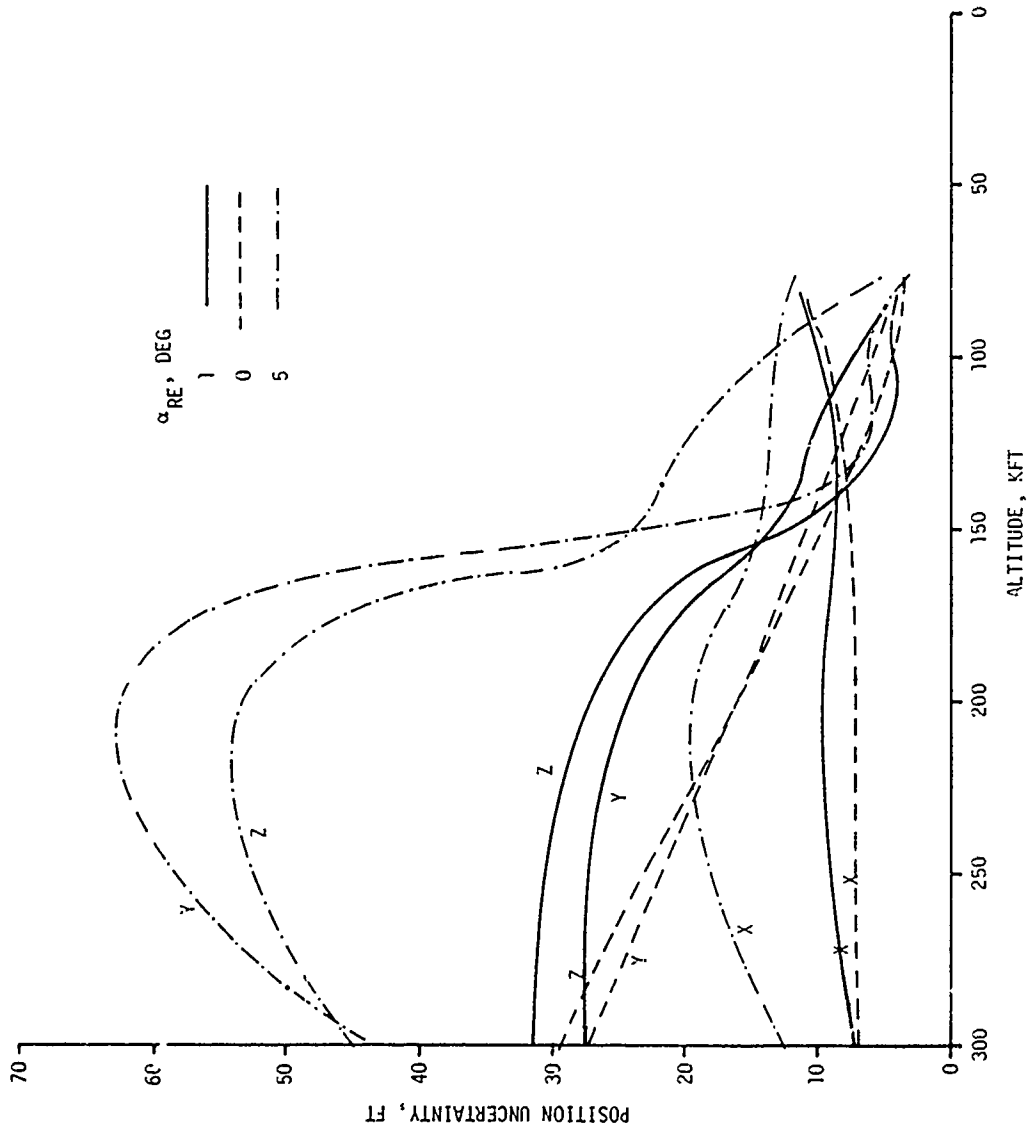


Figure 5.15 Effect of High Altitude Lift on Position Accuracy

To determine the effect of varying the ballistic coefficient and reentry angle on the position and deceleration accuracies, additional simulations were made in which these parameters were varied. The trajectories were all chosen such that they terminate at Target 54. The tracker coverage, in terms of altitude extent, is identical to the "nominal" case, although different reentry angles result in different length tracking spans in terms of time and geometry, as evident from Figures 5.3 and A.2.

#### 5.9.1 Ballistic Coefficient

A vehicle with a ballistic coefficient of 3000 psf was substituted in place of the 2000 psf and flown at the same 30 degree angle as "nominal". A comparison of the position and deceleration accuracies for the two vehicles, shown on Figures 5.16 and 5.17, reveals a negligible difference. This is an expected result since the two trajectories are nearly coincidental in position although displaced in time, a characteristic of high ballistic coefficient vehicles whose trajectories experience little change in flight path angle during reentry. It is concluded that the metric tracking measurement accuracy is nearly invariant with the ballistic coefficient for all high ballistic coefficient (above 2000 psf) vehicles.

#### 5.9.2 Reentry Angle

The same 2000 psf ballistic coefficient vehicle used in the "nominal" trajectory was flown at a 20 degree instead of a 30 degree reentry angle to determine the effects path angle has on trajectory estimation accuracy. All other parameters, including the sensor configuration, were the same as that used in the "nominal" analysis. Figures 5.16 and 5.17 present comparisons of these two trajectories and indicate that, unlike ballistic coefficient, reentry angle is an important parameter in the accuracy of deriving position and deceleration. The effect of lower reentry angles is to decrease the position accuracy but increase the deceleration accuracy. The degraded position accuracies result from the larger ranges from

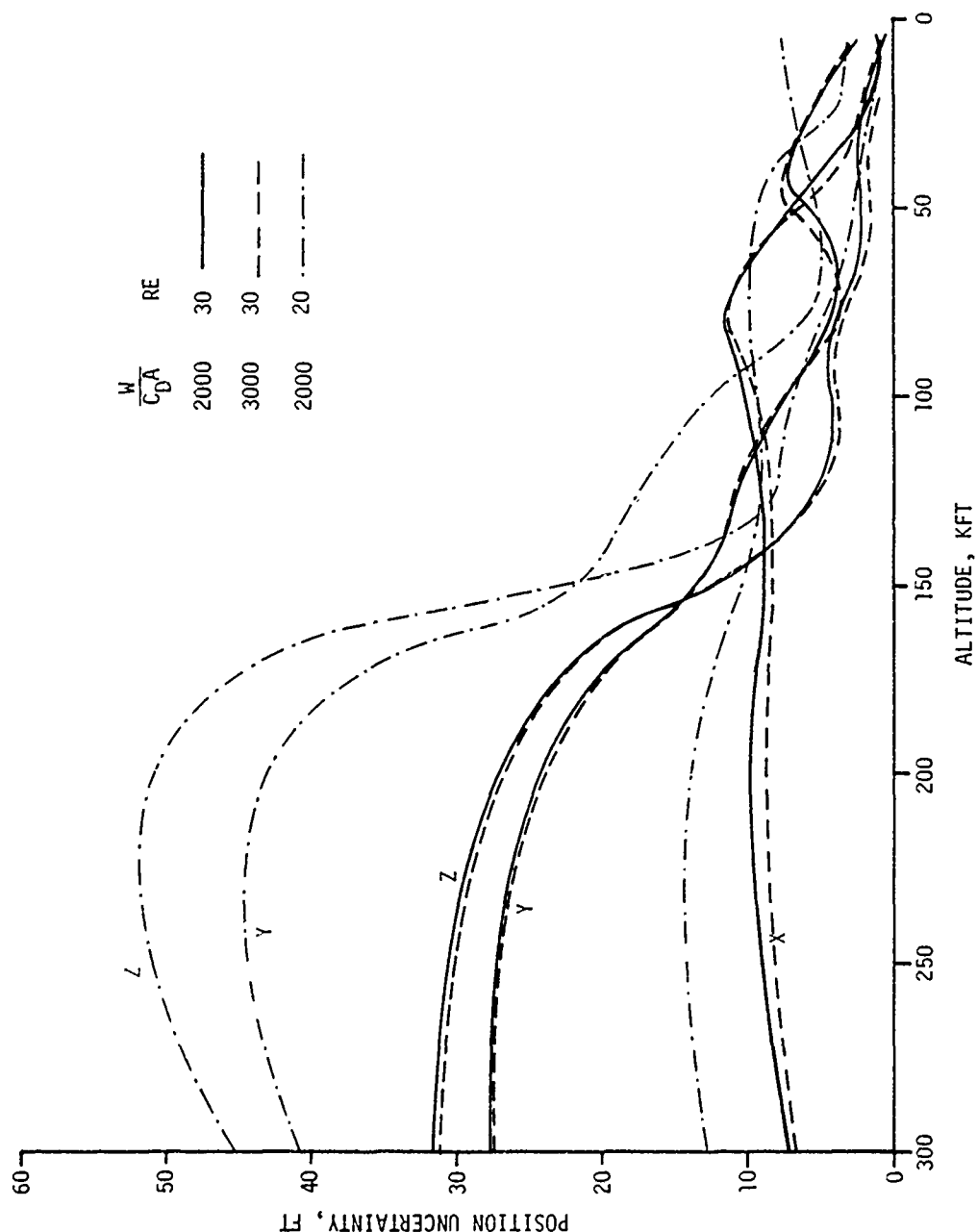


Figure 5.16 Effect of Ballistic Coefficient and Reentry Angle on Position Accuracy

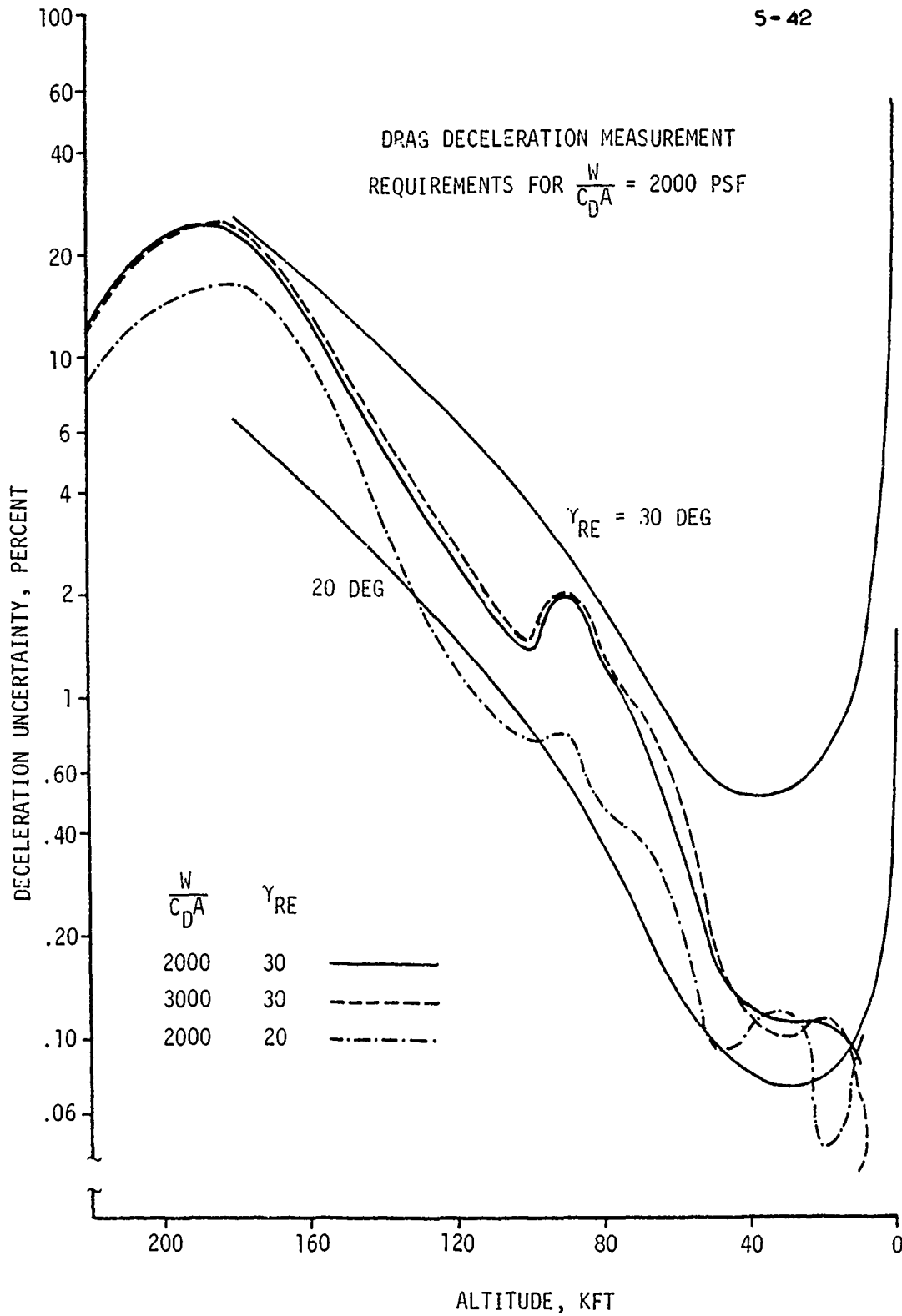


Figure 5.17 Effect of Ballistic Coefficient and Reentry Angle on Deceleration Accuracy

the sensors to the vehicle, resulting in magnified angle errors, while the improved deceleration accuracy results from the longer tracking span. Due to the very high sensitivity of position errors, steeper reentry angles are recommended.

#### 5.10 ERROR ANALYSIS: EFFECT OF TARGET LOCATION

The effect of the target location on the measurement accuracy was examined by performing the "nominal" error analysis using Targets 39 and 41 in lieu of Target 54. These targets are shown on Figure 5.2. Target 54 was originally chosen for the analysis since it is inside the lagoon approximately midway between the MPS-36 and ALCOR, representing an approximate geometric center of the various optical sensors. However, this may not result in the optimum trajectory for a reentry analysis. Although this study does not yield the precise target location of the optimum trajectory, it does give an indication of the sensitivity of the measurement accuracy to changes in the target, and indicates the approximate area where an optimum should exist.

Figures 5.18 and 5.19 present comparisons of the position and deceleration measurement accuracies for the three target locations. All other parameters are the same as "nominal". Position measurement accuracies are observed to be fairly insensitive to the target location, particularly in the lateral directions (Y - Z). However, deceleration measurement accuracy is very sensitive to target location, although the nature of this sensitivity is altitude dependent. Deceleration measurements for the Target 39 trajectory are the most accurate above 40 KFT, reflecting the improved ALCOR range tracking geometry. Below this altitude, Target 54 results in the best accuracy, reflecting the improved RADOT tracking geometry. The measurement accuracy requirements established in Section 4.3 are presented for comparison and indicate that the capability of metric trackers is still marginal for any of these targets.

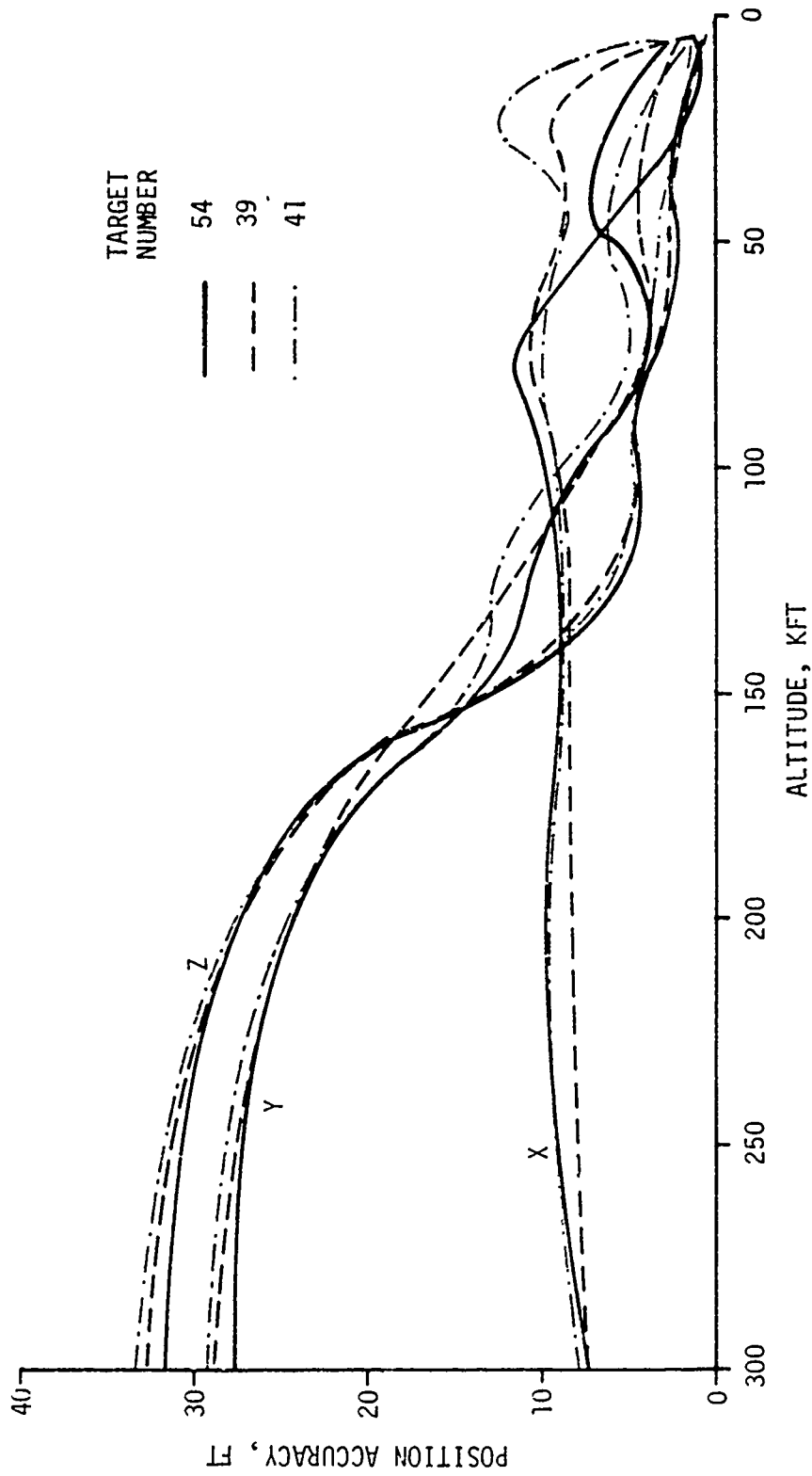


Figure 5.18 Effect of Target Location on Position Accuracy

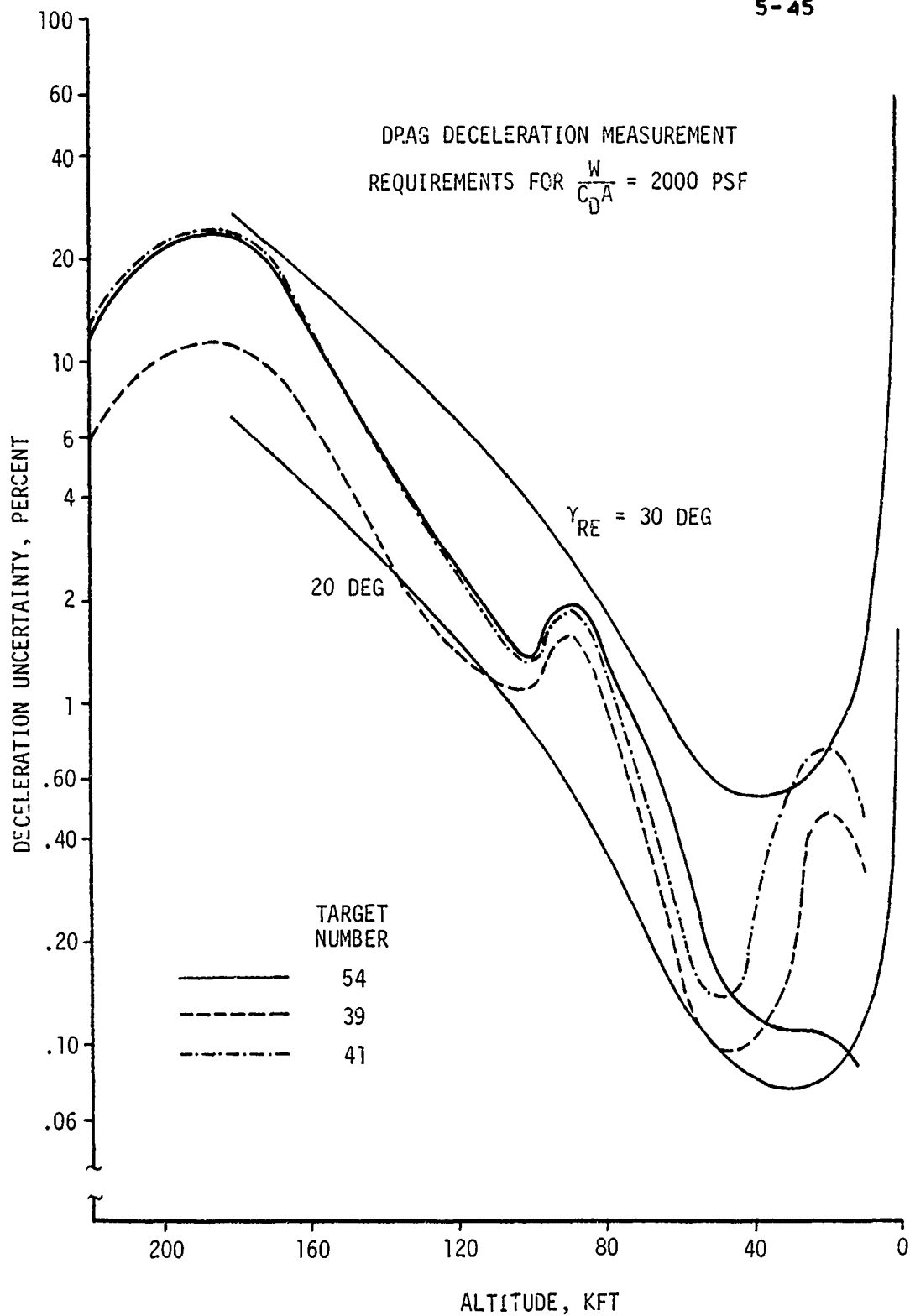


Figure 5.19 Effect of Target Location on Deceleration Accuracy

Based on this study it appears that target location is not of material significance in determining the accuracy of the trajectory solution, and, in fact, the region of Target 39 may be more desirable than inside the lagoon. However, if scoring considerations are included, targets inside the lagoon may be preferable since more accurate RADOT and SDR scoring can then be achieved.

## 6.0 ON-BOARD INSTRUMENTATION STUDIES

### 6.1 INTRODUCTION

The metric sensor error analysis of Section 5.0 indicates off-board data provide an accurate means of deriving the RV position and velocity during reentry but may not provide an adequate evaluation of drag and lateral accelerations to satisfy the measurement constraints established in Section 4.0. This section examines the capability of on-board instrumentation to measure drag and lift accelerations. Specifically, the objectives of this study are the following:

1. Determine the required on-board instrumentation accuracies based on the Section 4.0 study;
2. Survey the available instrumentation that could be used to meet these accuracy criteria.

### 6.2 AXIAL ACCELERATION MEASUREMENTS

The measurement requirements established in Section 4.0 were specified in terms of trajectory coordinates and must be transformed to a form compatible with quoted instrumentation accuracies. This section performs that transformation for axial decelerations to derive allowable error budgets for the on-board instrumentation.

#### 6.2.1 Required Accuracies

On-board longitudinally mounted accelerometers provide an excellent means of measuring a vehicle's drag deceleration. Selection of an accelerometer suitable for such measurements requires specification of the anticipated acceleration range and the allowable acceleration error. Accelerometer error models generally include terms for bias, scale factor error, nonlinearity errors, and cross axis sensitivities. If the cross axis

sensitivity terms are assumed negligible, the acceleration error can be expressed as:

$$\Delta A = K_0 + K_1 A_i + K_2 A_i^2 + K_3 A_i^3$$

where  $A_i$  is the input axis acceleration and

$\Delta A$  = accelerometer error

$K_0$  = accelerometer bias

$K_1$  = scale factor error

$\left. \begin{array}{l} K_2 \\ K_3 \end{array} \right\}$  = nonlinearity errors

It is evident that the accelerometer accuracy is dependent on the acceleration history throughout reentry. If values of  $K_0$ ,  $K_1$ ,  $K_2$  and  $K_3$  are known for any particular accelerometer, the acceleration error can be determined and applied to determine the true acceleration.

Each of the above terms, however, is subject to some uncertainty. This uncertainty will limit the accuracy to which the acceleration can be determined during reentry. If the acceleration accuracy criteria established in Section 4.0 are to be satisfied, accuracy levels must be determined for the accelerometer error coefficients.

The accuracy to which the accelerometer error can be determined may be expressed as:

$$\sigma_{\Delta A} = \left[ \sigma_{K_0}^2 + (A_i \sigma_{K_1})^2 + (A_i^2 \sigma_{K_2})^2 + (A_i^3 \sigma_{K_3})^2 \right]^{1/2}$$

$$\text{or, } \sigma_{\Delta A\%} = 10^2 \left[ \left( \frac{\sigma_{K_0}}{A_i} \right)^2 + \sigma_{K_1}^2 + (A_i \sigma_{K_2})^2 + (A_i^2 \sigma_{K_3})^2 \right]^{1/2}$$

The maximum value of  $\sigma_{\Delta A\%}$  has been previously established as a function of altitude. Hence, given  $A_i$ , constraints for the error coefficient uncertainties may be established.

The most severe constraints for the error coefficient uncertainties during reentry were determined for one ballistic coefficient, 2000 psf, and are presented below for reentry angles of 20 and 30 degrees. Higher ballistic coefficients have less stringent requirements.

#### ALLOWABLE ACCELEROMETER ERROR COEFFICIENT UNCERTAINTIES

Error Coefficient	Allowable Uncertainty	
	$\gamma_{RE} = 20 \text{ Deg}$	$\gamma_{RE} = 30 \text{ Deg}$
$K_0 \text{ (g)}$	$5 \times 10^{-3}$	$5 \times 10^{-3}$
$K_1 \text{ (g/g)}$	$8 \times 10^{-4}$	$7 \times 10^{-4}$
$K_2 \text{ (g/g}^2\text{)}$	$2 \times 10^{-5}$	$1 \times 10^{-5}$
$K_3 \text{ (g/g}^3\text{)}$	$3 \times 10^{-7}$	$2 \times 10^{-7}$

#### 6.2.2 Available Instrumentation

A survey was conducted to determine if accelerometers with the above accuracies are available. The survey was limited to digital accelerometers, since analog accelerometer accuracies are limited by the analog telemetry scale factor stability, which ranges up to 5%. The survey yielded one accelerometer, the Bell Aerospace Model VII, which has been successfully used on previous Minuteman missions. The digital unit has a range of  $10^{-6}$  to 200 g's with the following error coefficients and accuracies:

BELL AEROSPACE MODEL DAS VII ACCELEROMETER SPECIFICATIONS

	Scale Factor	Bias
Long Term Stability.....	$\pm$ 100 ppm	$\pm$ 100 $\mu$ g
Repeatability.....	$\pm$ 50 ppm	$\pm$ 50 $\mu$ g
Temperature Sensitivity*.....	$\pm$ 3 ppm/ $^{\circ}$ F	$\pm$ 1 $\mu$ g/ $^{\circ}$ F

Non-Linearities

$K_2$ .....  $3 \times 10^{-6} \text{g/g}^2$

$K_3$ .....  $3 \times 10^{-8} \text{g/g}^3$

\* Internally compensated, no temperature control.

The Bell Aerospace error model accuracies are observed to satisfy the accelerometer accuracy requirements. Figure 6.1 presents a comparison of the measurement criteria established in Section 4.0 for a 2000 psf ballistic coefficient vehicle and the corresponding capabilities of the Bell Aerospace accelerometer, ignoring temperature sensitivity effects.

It must be concluded that accelerometers are available for measuring decelerations to the required accuracies. Since such measurements offer an improvement over metric capabilities and are readily available they should be considered for any flight testing of an accurate reentry vehicle.

6.3 LIFT MEASUREMENTS

On-board measurements of lift effects require instrumentation to measure both the lateral accelerations experienced by the vehicle, and the vehicle's orientation relative to an earth fixed coordinate frame so that these accelerations can be transformed to trajectory coordinates.

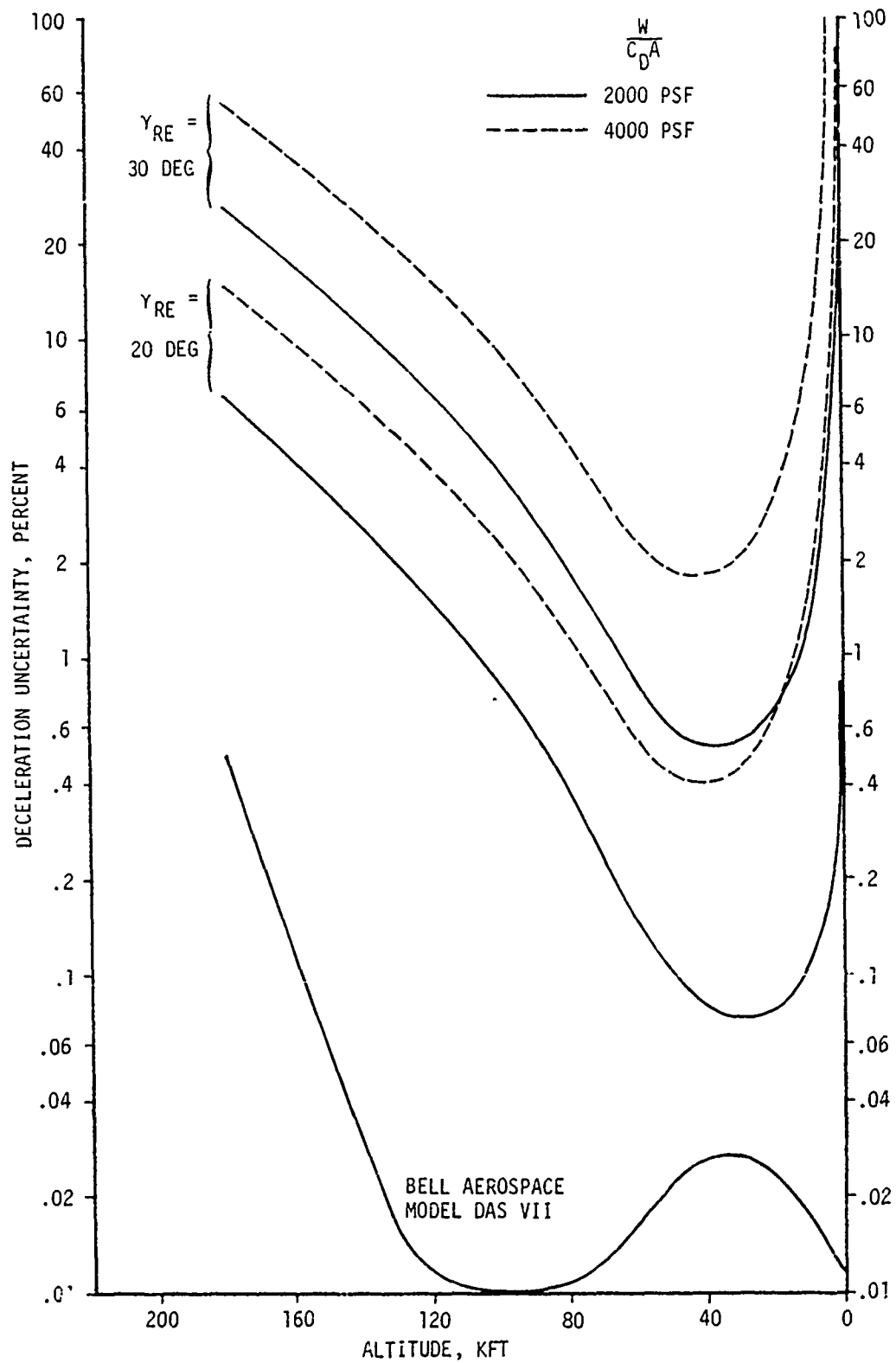
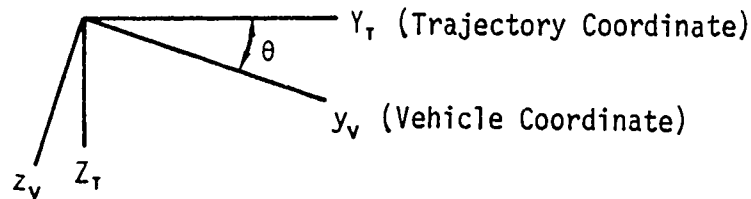


Figure 6.1 Comparison of Drag Deceleration Measurement Requirements Per 100 Feet of Allowable CEP With Bell Aerospace Accelerometer

Once such measurements have been made, lift effects can be integrated throughout reentry to determine the effect on the trajectory. This section establishes accuracy criteria for lateral acceleration and orientation measurements, and reviews instrumentation that can be used for such measurements.

### 6.3.1 Required Accuracies

The required lift measurement accuracies of Section 4.0 were derived in terms of a non-rotating trajectory fixed coordinate system. Before measurement accuracies can be established for on-board instrumentation a transformation matrix must be derived which relates the body fixed coordinates to the trajectory system. Assuming the vehicle's roll axis ( $x$ ) and velocity vector are nearly coincidental (small angle-of-attack) we can view the transformation as a single rotation;  $\theta$ :



AFT VIEW LOOKING FORWARD  
ALONG VELOCITY VECTOR

This transformation is expressed by:

$$\begin{bmatrix} A_Y \\ A_Z \end{bmatrix}_{\text{Traj}} = \begin{bmatrix} C \end{bmatrix} \begin{bmatrix} a_y \\ a_z \end{bmatrix}_{\text{RV}}$$

where:

$$\begin{bmatrix} C \end{bmatrix} = \begin{bmatrix} \cos \theta & -\sin \theta \\ \sin \theta & \cos \theta \end{bmatrix}$$

The vehicle fixed acceleration uncertainties may be now expressed in terms of trajectory fixed coordinates through the transformation matrix. This relationship, after some manipulation, is given by:

$$\begin{aligned}\sigma_{A_Y} &= \left[ A_Z^2 \sigma_\theta^2 + \sigma_{m_a}^2 \right]^{1/2} \\ \sigma_{A_Z} &= \left[ A_Y^2 \sigma_\theta^2 + \sigma_{m_a}^2 \right]^{1/2}\end{aligned}\tag{6.1}$$

where the measurement uncertainties,  $\sigma_{m_{a_y}}$  and  $\sigma_{m_{a_z}}$ , are assumed equal and expressed by  $\sigma_{m_a}$ . These expressions quantitatively reveal the intuitive fact that the relative orientation,  $\theta$ , and the acceleration components must be accurately measured if the acceleration components in trajectory coordinates are to be accurately determined.

Measurement constraints for  $\sigma_{A_Y}$  and  $\sigma_{A_Z}$  are identical and were previously expressed in Equation 4.9 and presented in Figure 4.5. When Equation 4.9 is used to constrain  $\sigma_A$  in Equation 6.1 the on-board measurement accuracy requirement is:

$$\left[ \sigma_{m_a}^2 + A_Z^2 \sigma_{m_\theta}^2 \right]^{1/2} \leq \frac{1.540 \times 10^{-6} v^2 \sin^3 \gamma_{RE} CEP}{h (1 + \sin \gamma_{RE})}\tag{6.2}$$

If each term on the left of Equation 6.2 is allotted an equal portion of the available error, the accuracy constraints become:

$$\sigma_{m_a}, |A_Z| \sigma_{m_\theta} \leq \frac{1.089 \times 10^{-6} v^2 \sin^3 \gamma_{RE} CEP}{h (1 + \sin \gamma_{RE})}\tag{6.3}$$

The acceleration accuracy constraint is straight-forward and is presented in Figure 6.2 per 100 feet of allowable CEP. The constraint for the orientation measurement, however, is dependent on the lateral acceleration.

A constraint for  $\sigma_{m_\theta}$  can be established if an average value for  $|A_z|$  is used. If it is assumed that the angle-of-attack and dynamic pressure remain constant over one revolution of RV's windward meridian about the mean trajectory, the average value of  $|A_z|$  is:

$$\overline{|A_z|} = \frac{C_N A \rho v^2}{\pi m}$$

Substituting the expression into Equation 6.3 yields the following constraint for  $\sigma_{m_\theta}$  in degrees:

$$\sigma_{m_\theta} \leq \frac{1.96 \times 10^{-4} m \sin^3 \gamma_{RE} CEP}{C_N A \rho h (1 + \sin \gamma_{RE})}$$

This constraint was evaluated for a typical 2000 psf ballistic coefficient vehicle at 20, 30 and 40 degree reentry angles assuming the following vehicle parameters:

$$m/A = 4 \text{ slugs/ft}^2$$

$$C_{N_\alpha} = .034/\text{degree}$$

$$\alpha = 0.1 \text{ degree up to 100 Kft}$$

$$1.0 \text{ degree above 200 Kft}$$

The angle-of-attack was assumed to vary quadratically between 100 KFT and 200 KFT. The resulting measurement criterion,  $\sigma_{m_\theta}$ , is presented on Figure 6.3 and observed to require very accurate angular measurements.

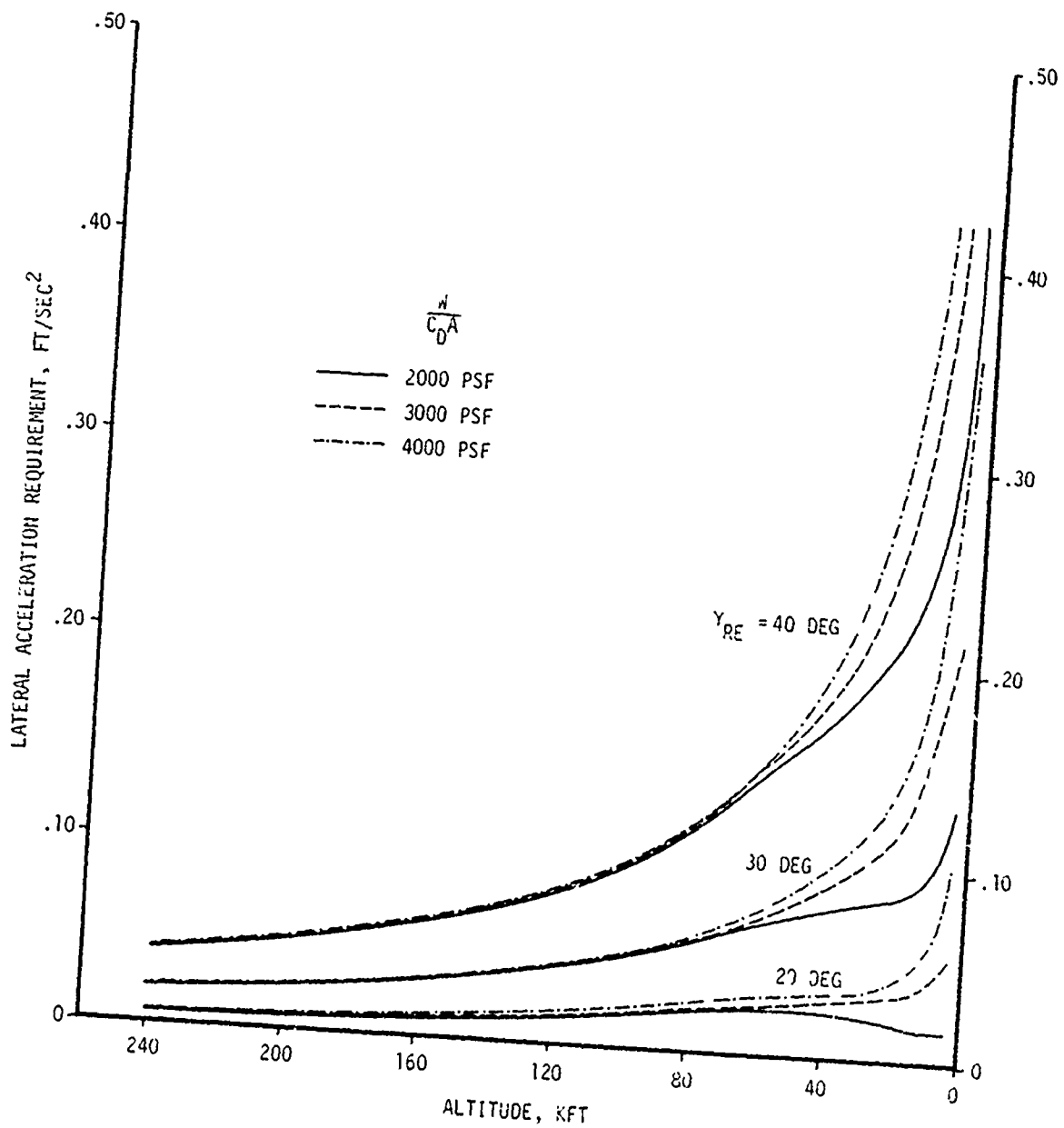


Figure 6.2 Vehicle Fixed Lateral Acceleration Measurement Requirements Per 100 Feet of Allowable CEP

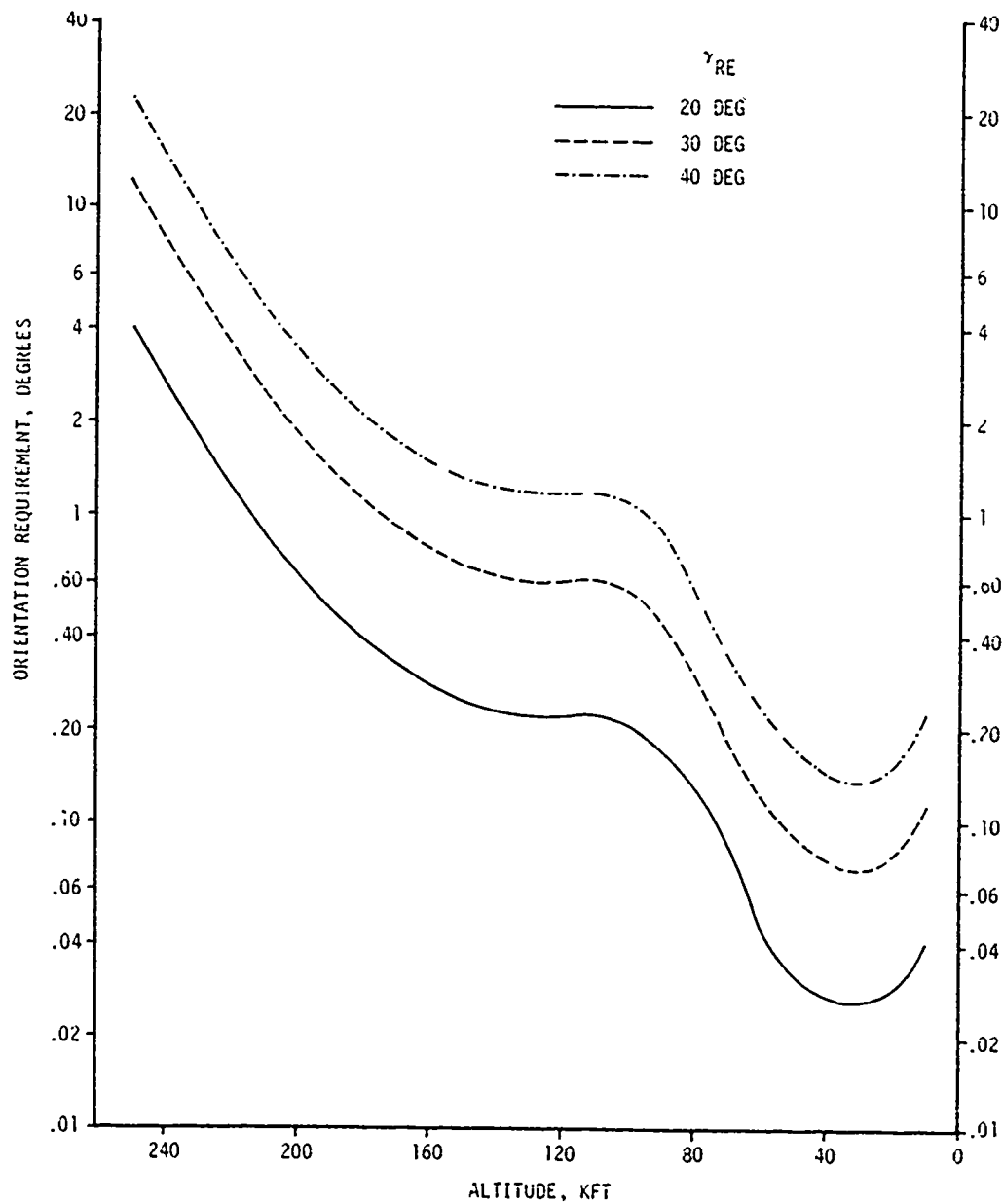


Figure 6.3 Vehicle Orientation Measurement Requirements Per 100 Feet of Allowable CEP

### 6.3.2 Available Instrumentation

A survey was conducted to determine if the lateral acceleration requirements of Section 6.3.1 can currently be achieved with state of the art instrumentation, including both strap down and inertial sensors. Although an inertial platform offers more accurate measurements, it is also more expensive. Of course a combination of the two types may be found satisfactory.

### 6.3.3 Strap Down

Exclusive use of strap down instrumentation is very desirable because of their simple application. These measurements are generally accomplished in one of two manners:

- 1) Body Rate Integration - three orthogonally mounted rate gyros are used to measure body angular rates. The rates are transmitted to the ground and integrated in post flight analysis to find the body angular position. Knowledge of the velocity vector enables computation of the angle-of-attack and hence lateral accelerations;
- 2) Acceleration Measurement - Orthogonally mounted accelerometers are used to measure acceleration. Lateral and roll rate gyros are required to measure the RV orientation and compensate for centripetal accelerations.

The first method relies on the integration of rate data, which is one of the major sources of error. Occurrence of data dropouts during reentry can preclude continuous integration unless a complicated on-board recorder is used which stores data for transmission late in the flight. Furthermore, an initial orientation must be provided at the time integration is started. This point is usually given at high altitudes where the vehicle is assumed to be coning about a zero angle of attack. Hence, the integration process is subject to serious errors. Because of these difficulties this method was not considered further.

The second strap down method has the advantage of measuring accelerations directly, but suffers the same problem with determining an initial orientation at the start of integration. One method of overcoming this difficulty is to integrate from RV deployment, where the guidance system can be used to accurately determine the vehicle's orientation. However, this requires very accurate measurements of the vehicle's lateral rates and roll rates from deployment to reentry. Assuming for simplicity that no coning exists, the vehicle orientation at reentry would be given by:

$$\theta_{RE} = \int_0^t p \, dt + \theta_0$$

where  $p$  is the roll rate,  $t$  is the time from deployment to reentry and  $\theta_0$  is the initial orientation at deployment. Since the roll rate is nearly constant over the exoatmospheric portion of flight to time  $t$ , the orientation becomes  $pt + \theta_0$  with an associated uncertainty of:

$$\sigma_{\theta_{RE}} = [t^2 \sigma_p^2 + \sigma_{\theta_0}^2]^{1/2}$$

Advanced guidance systems are expected to yield orientation uncertainties of under .01 degree. The quantity  $\sigma_{\theta_{RE}}$  can range up to 0.1 degree and still satisfy the constraint previously established. Hence,  $\sigma_{\theta_0}$  was ignored. The time from deployment to reentry is typically 1500<sup>0</sup>seconds. This implies that roll rate measurement accuracies are constrained by:

$$\sigma_{m_p} \leq \frac{.1}{1500}$$

or

$$\sigma_{m_p} \leq 6.7 \times 10^{-5} \text{ deg/sec}$$

Rate gyros of this accuracy are not currently known to exist. Hence, some other technique will have to be found if orientation requirements are to be satisfied.

Inertial platforms have been successfully demonstrated on guided RV's where accurate orientation measurement requirements have been met. Hence, some effort has been expended in this field resulting in a few inertial systems oriented toward RV use. A review with Aerospace indicated that in general these inertial measurement systems were designed for accuracies considerably less than required to measure orientation from deployment through reentry. Only a few systems exist which could be considered.

One such system is the SHIP (Small Hardened Inertial Platform) system designed for use on the Trident Program. The gyro error budget, while not quite sufficient to achieve the orientation requirements, could be considered if some degradation in measurement accuracy was allowed.

A second system currently being developed is the AIRS (Advanced Inertial Reference Sphere). The high accuracy being predicted for this system would meet the measurement requirements; however, its high cost would certainly be a deterrent.

## 7.0 REENTRY DATA ANALYSIS TECHNIQUES

### 7.1 INTRODUCTION

There exists within the reentry data processing community a variety of different techniques for analyzing on-board and off-board reentry data. The literature written on the subject is voluminous. No attempt can be made in this study to review each of the techniques. The purpose of this section is to provide a review of the most popular of these techniques and to comment on their application.

The techniques examined in this section are limited to those which are used to provide information regarding the trajectory, including the position history and vehicle dynamics based on both off-board and on-board data. The most common techniques can be generalized into three types:

- (1) Single point in time analysis of off-board data;
- (2) Multiple point in time analysis of off-board data;
- (3) Multiple point in time analysis of off-board data and on-board data.

The above techniques are ordered from the least to most complex. All three techniques use minimum variance theory for achieving a best fit to the data, but they differ in the extent to which they use the reentry equations of motion to correlate successive time points. The choice of technique depends on the desired degree of complexity and accuracy, and on the type and quality of available data.

### 7.2 SINGLE POINT IN TIME ANALYSIS OF OFF-BOARD DATA

Although many variations of this method are in use, the basic characteristic of this technique is that multiple sensor data are all

analyzed at single points in time along the trajectory to arrive at a best estimate of trajectory. No consideration is given to the equations of motion which relate successive time points, except to the extent to which a polynomial filter tends to preclude sharp discontinuities in the derivatives. The degree of sophistication of this technique can vary from a simple least squares solution of raw data at common time points to one which filters the data, differentiates the resulting polynomial for velocity and deceleration, and solves for systematic error sources. The altitude history and velocity profile from this latter method can then be used in conjunction with acclerometer data (derived or on-board) to determine the ballistic coefficient. The advantage of this method lies in its simplicity and resulting lower computing costs. Two principle drawbacks, however, offset this advantage. First, it does not make use of the reentry equations of motion to relate data at different times. Second, on-board data are not directly used in deriving the best estimate of trajectory. The application of this technique can often prevent the detection of inaccurate data, resulting in a derived trajectory that displays unreasonable RV behavior. In summary, a single point in time solution with or without polynomial filtering is not recommended if an accurate reconstruction of the trajectory and analysis of the vehicle dynamics are desired.

### 7.3 MULTIPLE POINT IN TIME ANALYSIS OF OFF-BOARD DATA

The principle feature of this technique is its use of the equations of motion to relate an entire time span of multiple sensor data. Since a vehicle's motion can be characterized by lift, drag and gravitational forces, knowledge of these forces enables successive data points in time to be correlated through the equations of motion. Through this correlation, data at one altitude aids in determining the RV position at any other altitude, thus reducing the position uncertainty over a point by point solution. The degree of correlation, however, is dependent on the accuracy

associated with defining the aerodynamic forces.

Many varied applications of this technique are currently in existence. The differences generally relate to the various types of error models that are considered and the extent to which they model the vehicle's and sensor's true behavior. These coefficients can include radar systematic errors (dynamic lag, biases, etc.) and aerodynamic coefficients (lift and drag). The ability to regress on lift and drag is, of course, essential for reconstructing a reentry trajectory.

One such program, the TRW RETAP program, has been previously described in Section 3.2, where it was used in the metric data error analysis. The input sensor data is a tape of time sequentially merged data from all sensors precompensated for known sensor errors. Weighting factors are selected for each type of data based on the analyst's evaluation of the sensor's random noise content and the confidence he has that the data are free of unmodeled systematic errors.

The actual trajectory solution is highly dependent on the manner in which the analyst chooses to solve for the initial state vector, sensor systematic errors and aerodynamic coefficients. Historically, the initial state vector and sensor biases have been solved for by regressing on exoatmospheric data to the reentry portion of the trajectory. This effectively isolates radar biases from uncertainties in defining aerodynamic coefficients. The resulting biases are then applied to the data and assumed constant throughout reentry. The reentry trajectory analysis is then performed by fixing the initial, exoatmospheric state vector and solving for aerodynamic coefficients throughout reentry until a best fit to the data is achieved and a reentry trajectory is derived. With the advent of highly accurate optical data, however, modifications to the application of this technique have been utilized.

The historical technique does not make use of optical data in solving for systematic errors since optical data are typically not

acquired until 100 KFT to 130 KFT, well into reentry. The exclusion of optical data in this portion of the analysis, however, precludes achieving the indicated accuracies of Section 5.0. Recent attempts to include optical data in the derivation of the initial state vector and radar systematic errors for Minuteman flights have been very successful. The application of this method to a highly accurate ABRES vehicle should be addressed in a future study which includes an actual application to a RV trajectory analysis.

Once a state vector has been determined and systematic error corrections have been applied to the data, aerodynamic coefficients must be solved for throughout reentry. The results of Section 5.0 raise several questions regarding the approach that should be used in this phase. The altitude to which aerodynamic coefficients are actually solved for in the regression analysis will obviously influence the results. The Section 5.0 error budget study indicates that above the region of accurate optical data angle-of-attack uncertainties have a significant effect on derived position uncertainties. In addition, the uncertainties of derived lift and drag coefficients were observed to increase with increasing altitude. This suggests that an altitude may exist at which the uncertainties associated with the derived and estimated aerodynamic coefficients are equal, and above which lift and drag values are known with more accuracy than they can be derived from regression. Preliminary studies have indicated that this altitude is significantly lower for lift than for drag. This suggests one obvious advantage of using on-board accelerometers to estimate the coefficients at high altitudes. Further study of this area is suggested if this technique is to be optimized to achieve the greatest accuracy.

A second question that has been addressed is the inherently different nature of high altitude lift effects, which tend to persist over some time, and low altitude asymmetric lift effects, especially roll trim, which tend to act over small time intervals and appear as an impulse to the vehicle. These different effects are inherent in the TRW RETAP program, which includes the capability to regress on either a steady state lift coefficient or an impulsive lift coefficient or both. The trajectory comparison of Figure 3.39, for example, used the impulse coefficient at lower altitudes. This approach is recommended in any reentry regression solution where roll trim effects are expected to occur.

The only shortcoming of this multiple point in time analysis of off-board data is that on-board data are not directly used in the solution. However, on-board data may be used in an iterative fashion to modify the lift and drag coefficients to correspond to those observed in the on-board data. This requires the derivation of a trajectory dynamic pressure history which can then be used to reduce on-board data. It should be noted that this approach has been used very successfully on many Minuteman flights.

#### 7.4 MULTIPLE POINT IN TIME ANALYSIS OF OFF-BOARD AND ON-BOARD DATA

The basic principles used in this technique are similar to those previously described in Section 7.3, except that on-board data are included with off-board sensor data. The advantages of such a method include:

- (1) It utilizes the reentry equations of motion to correlate data;
- (2) All datasources can be analyzed simultaneously;
- (3) Data sources with serially correlated errors can be accurately modeled and analyzed with minimum error.

Several applications of this technique are currently being used with varying degrees of sophistication and success. One of the best known of these techniques is the Kalman filter method. The literature abounds with descriptions and applications of this technique to data analysis problems

in general. However, its application and success for reentry trajectory analysis has been limited, particularly when data from fully instrumented vehicles, including rate gyro data, have been used. This method potentially, however, offers an improved method of trajectory analysis, and continued effort in this field is recommended.

This section has attempted to provide a summary description of the major data analysis techniques currently in use. It is recommended that further studies be initiated in this area, particularly in the area of off-board data analysis techniques and the combined use of off-board and on-board data.

## 8.0 REFERENCES

1. Density/Pressure Correlations and Associated Statistics, United States Air Force Environmental Technical Applications Center, Data Processing Division, Report CL10696, Part I, 1971. (Unclassified)
2. Means, Standard Deviations and Extremes of Rocketsonde Data, United States Air Force Environmental Technical Applications Center, Data Processing Division, Report CL10696, Part II, 1972. (Unclassified)
3. Inter and Intra Level Wind Correlations, United States Air Force Environmental Technical Applications Center, Data Processing Division, Report CL10696, Part II, 1971. (Unclassified)
4. Nelson, R. L., The Motions of Rolling Symmetrical Missiles Referred to a Body Axis System, NACA Technical Note 3737, Langley Aeronautical Laboratory, Langley Field, Va, November 1956. (Unclassified)
5. Crenshaw, J. P., Effect of Lift Variation on the Impact of a Rolling Reentry Vehicle, Journal of Spacecraft and Rockets, Vol 9, No. 4, 1972, pp 284-286. (Unclassified)
6. Reliability of Meteorological Data, White Sands Missile Range Document 110-71, Range Commanders Council, New Mexico, March 1971. (Unclassified)
7. Martellucci, A., and E. J. Studerus, Ballistic Vehicle Drag for Offensive Weapons Systems (U), General Electric Company Document, General Electric Company, Philadelphia, Pennsylvania, 30 March 1970. (Secret)
8. Kemp, M. J., The Statistical Matrix Analysis Program, Vol I, TRW Report 6613.10-14, TRW Systems, Redondo Beach, California, October 1973. (Unclassified)
9. Range Instrumentation and Support Facilities Manual, United States Army Safeguard System Command, Kwajalein Range Directorate, 15 December 1972. (Unclassified)
10. Systems Performance and Accuracy Report, Space and Missile Test Center Technical Report TR73-1, Air Force Systems Command, Vandenberg Air Force Base, California, May 1973. (Unclassified)

## APPENDIX A

DESCRIPTION OF THE VEHICLE'S AERODYNAMIC  
COEFFICIENTS AND TRAJECTORIES

## A.1 AERODYNAMIC COEFFICIENTS

This section presents the aerodynamic coefficients that were used to define the vehicle's reentry behavior. The class of vehicles considered were 200 to 600 pound slender sphere-cone vehicles. The most important of the aerodynamic parameters, ballistic coefficient, dictates the axial deceleration profile experienced by the vehicle. Ballistic coefficient histories for the various vehicles considered in this study were derived using a simplified aerothermodynamic reentry program that computes the various drag components including reference drag, skin friction, base drag, nose drag, surface roughness and angle-of-attack effects, and also performs a simplified ablation rate calculation. The ballistic coefficient histories derived for 1500 psf, 2000 psf, 3000 psf and 4000 psf ballistic coefficient vehicles are presented on Figure A.1.

The other aerodynamic parameters that were assumed throughout the study as representative values were the following:

$$C_{N_{\alpha}} = .034/\text{degree}$$

$$I_x = 2 \text{ slug} - \text{ft}^2$$

$$I_y = I_z = 20 \text{ slug} - \text{ft}^2$$

## A.2 VEHICLE TRAJECTORY

This section presents the initial trajectory conditions at pierce point used to initialize all simulations, and the reentry environment experienced by the vehicle throughout reentry. The relevant initial conditions at 300 Kft are reentry angle and velocity. The conditions are shown on page A-3 for flights into Kwajalein.

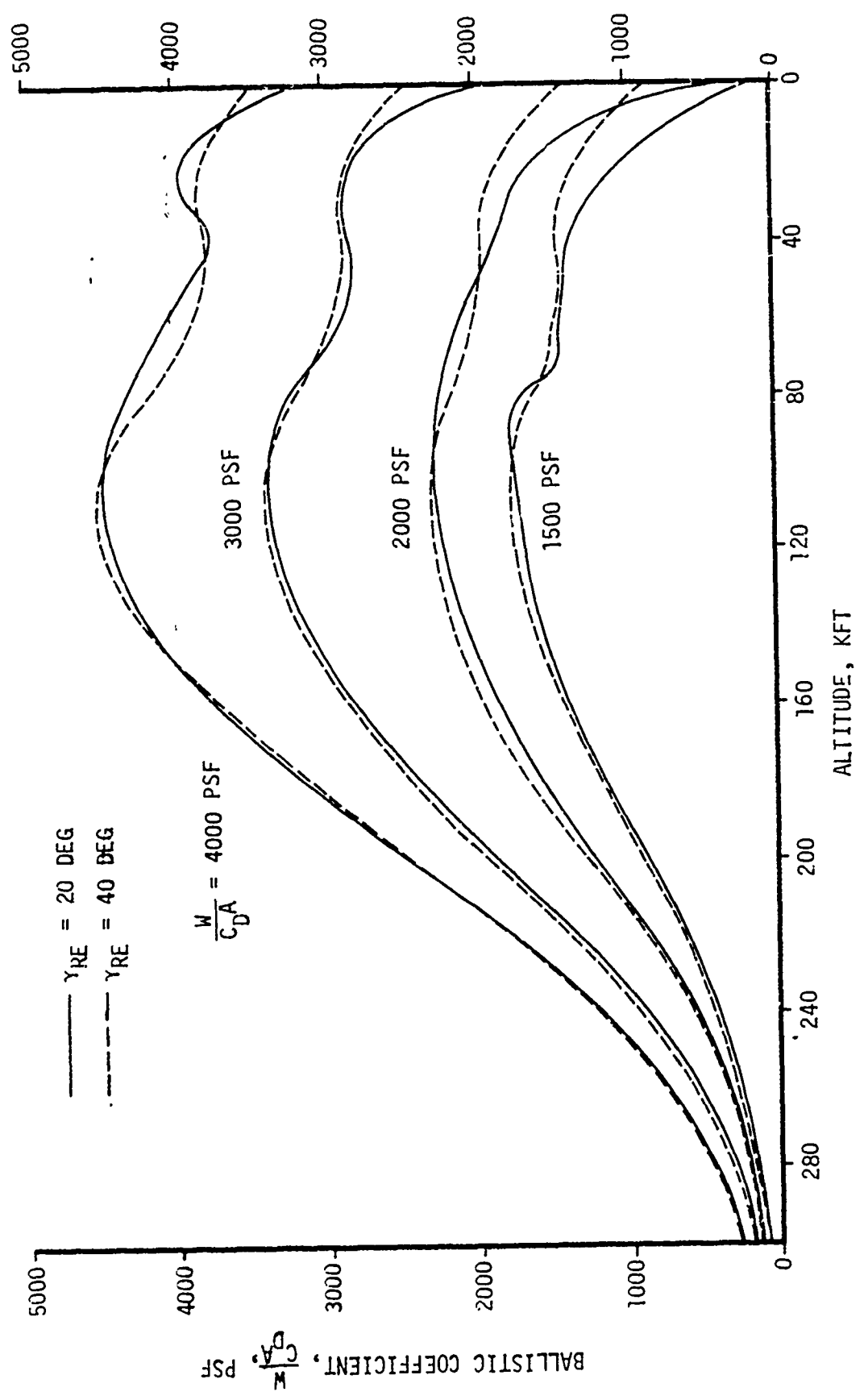


Figure A.1 Ballistic Coefficient Histories

<u>Reentry Angle (Deg)</u>	<u>Reentry Velocity (Ft/Sec)</u>
15	23100
20	22715
25	22430
30	22355
40	22800

The resulting reentry environment for each of the vehicles is dependent on both the ballistic coefficient and reentry angle. Figures A.2 through A.6 present the most significant parameters as functions of altitude for several ballistic coefficients. Figure A.2 presents the altitude history, which is observed to have a constant slope until near the end of the trajectory. Velocity histories are shown on Figure A.3, which indicate that the velocity does not appreciably change until after 80 KFT. This is due to the small drag deceleration above this altitude, as evidenced in Figure A.4. The dynamic pressure history is presented on Figure A.5 and reflects both the velocity and density profiles. Finally, Mach number histories are presented on Figure A.6 and indicate that with the exception of the low ballistic coefficient and reentry angle configurations, the vehicle impacts in the supersonic to hypersonic regime.

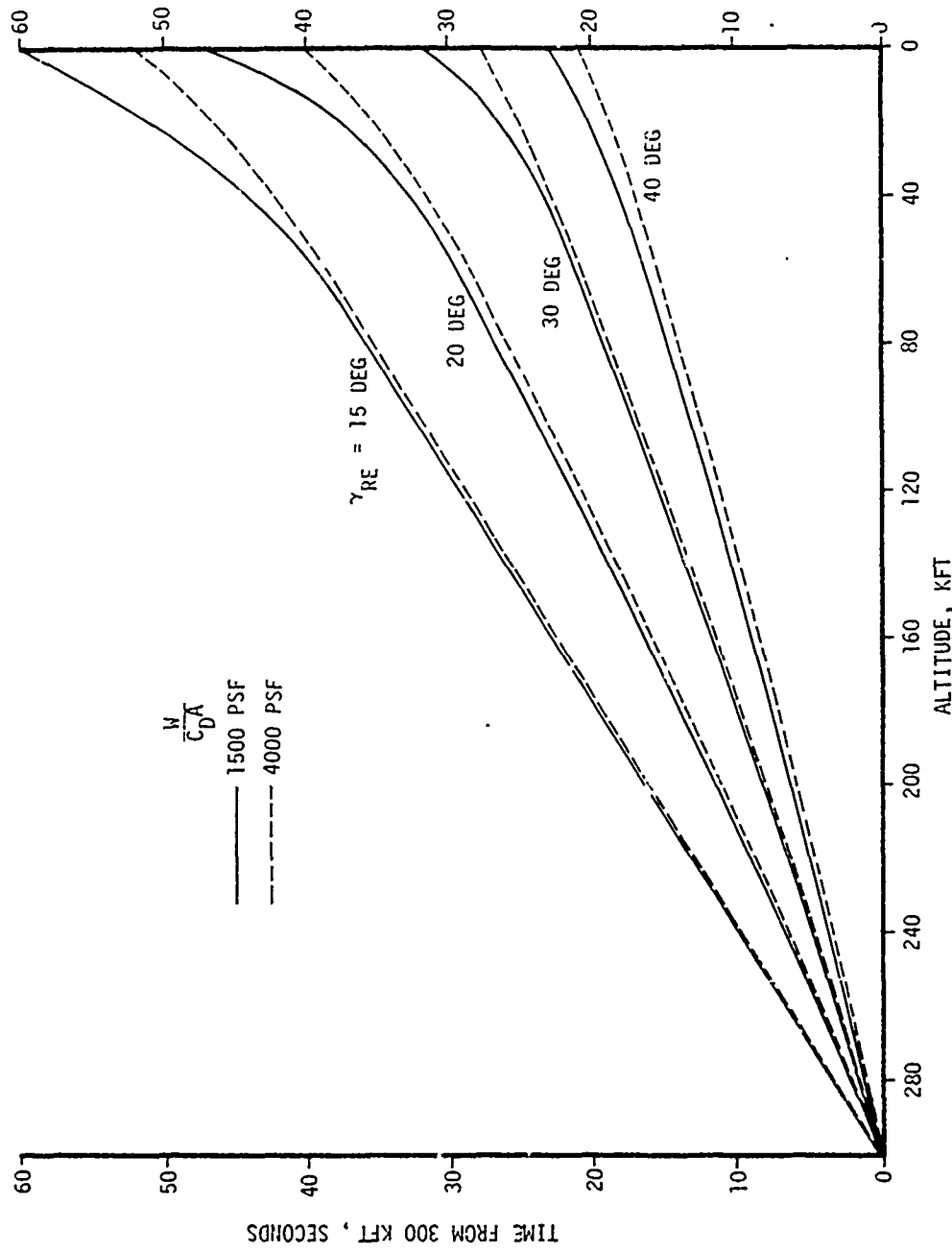


Figure A.2 Altitude Histories

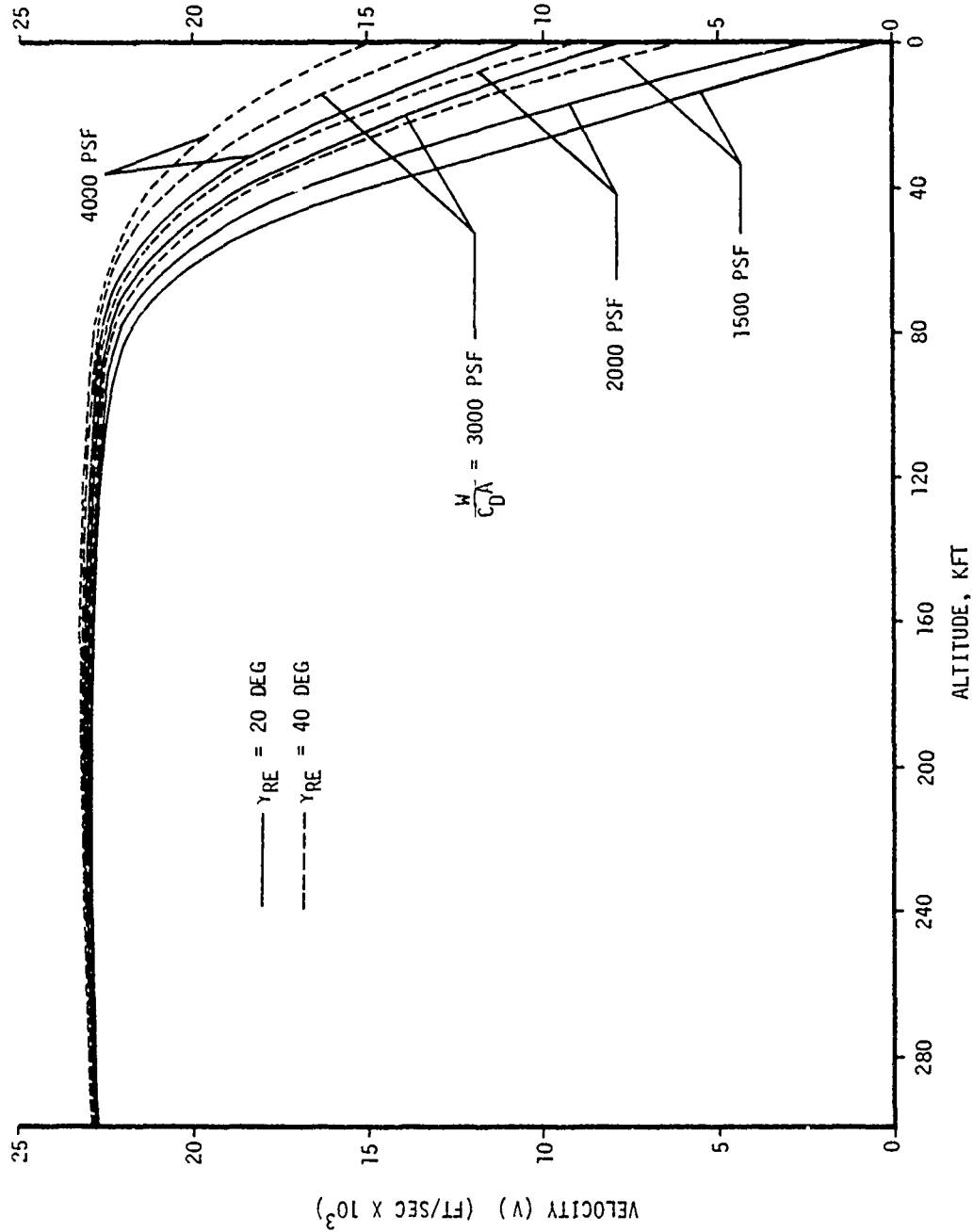


Figure A.3 Velocity Histories

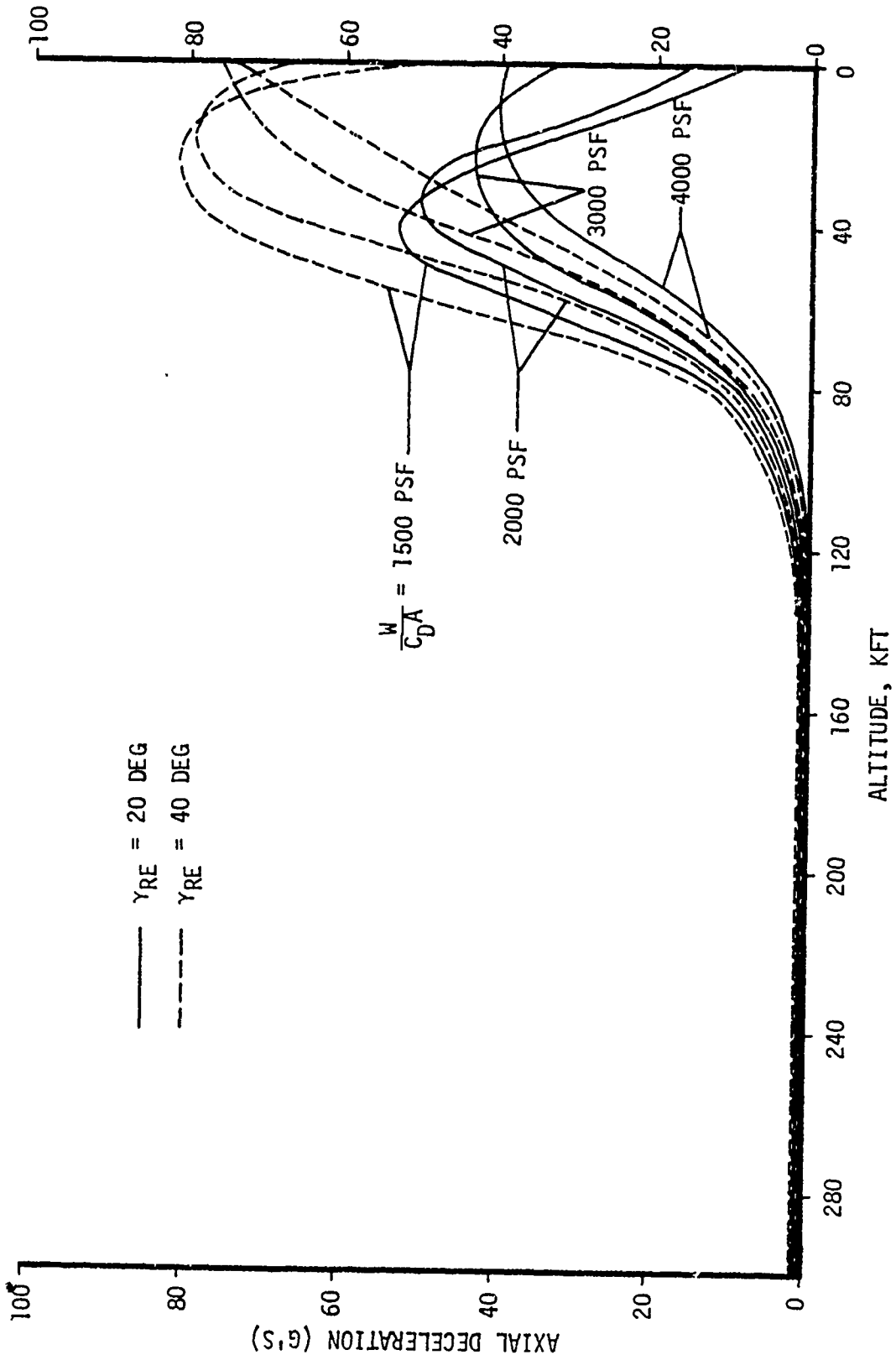


Figure A.4 Deceleration Histories

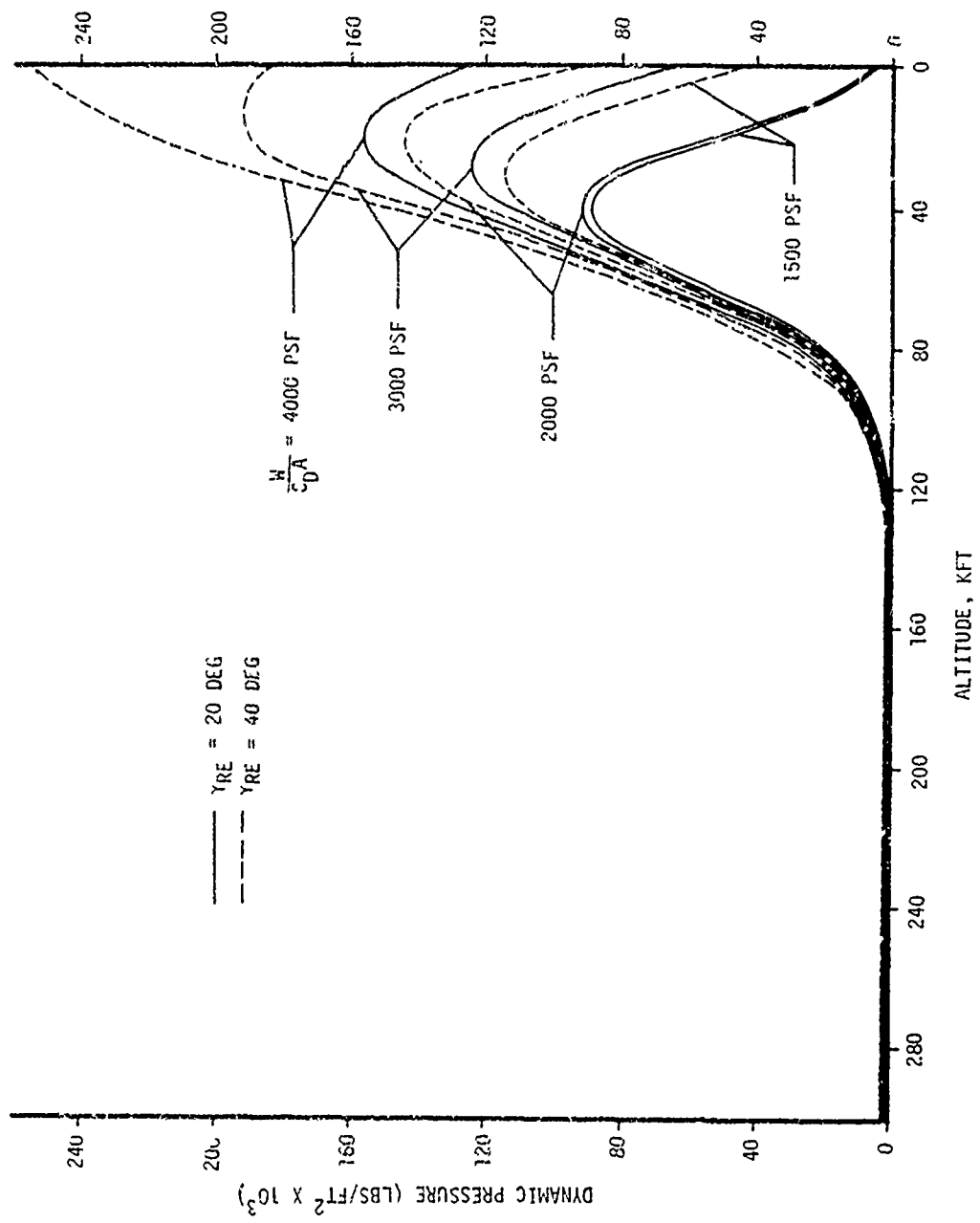


Figure A.5 Dynamic Pressure Histories

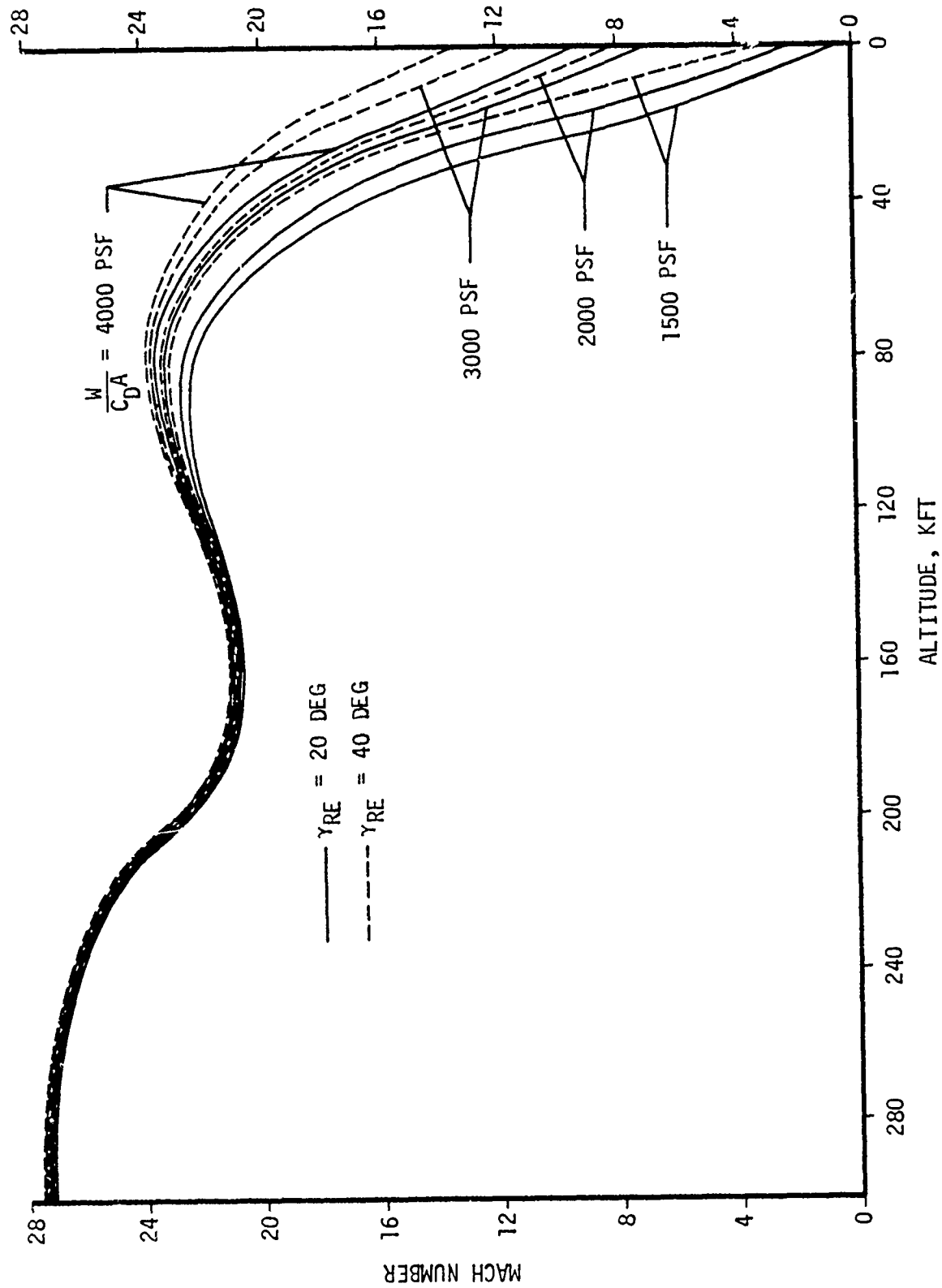


Figure A.6 Mach Number Histories

## APPENDIX B

## INFLUENCE COEFFICIENTS

The reentry error budget and measurement requirement studies make extensive use of influence coefficients. These coefficients are computed as functions of altitude to determine the sensitivity of the RV position at some event, usually impact, to altitude dependent dispersions in winds, density, or ballistic coefficient. The influence coefficients and perturbations can then be integrated over any given altitude region to determine the effects of variations in that region on the dispersion at some other point in the trajectory (normally impact).

## B.1 WIND INFLUENCE COEFFICIENT

The wind influence coefficient,  $I^W$ , for a particular altitude is defined as

$$I^W = \lim_{\Delta h \rightarrow 0} \frac{\Delta R_W}{v_W \Delta h} \quad (B.1)$$

where  $R_W$  is the change in range, in feet, caused by a wind of  $v_W$  feet per second throughout an altitude interval of  $\Delta h$  feet with its midpoint at the specified altitude. Thus, the wind influence coefficient for any altitude may be considered as the change in range caused by a one foot per second velocity over a one foot altitude interval centered at the specified altitude. This coefficient (in seconds per foot) is defined for both downrange and crossrange winds. The wind influence coefficient,  $I^W$ , is useful because  $\Delta R_W = I^W v_W \Delta h$  where  $v_W$  is the speed of the wind blowing throughout the specified interval. The wind influence coefficient depends upon RV characteristics and reentry trajectory parameters.

The total reentry wind induced change in range can be obtained by integrating the product of the wind speed and the influence coefficient as a function of altitude:

$$\Delta R_{W_T} = \int I^W(h) \Delta v_W(h) dh \quad (B.2)$$

where  $\Delta R_{W_T}$  is the total reentry wind induced range change. Although the influence coefficient is a continuous function of altitude, the computation is simplified by using a series of altitude intervals with an influence coefficient that is constant in each interval. Computations are thus reduced to summing products instead of integrating. The total reentry wind induced change in range can be obtained by summing the  $\Delta R$  values from the altitude of reentry into the atmosphere to impact.

$$\Delta R_{W_T} = \sum_i \Delta R_{W_i} = \sum_i I_i^W \Delta v_{W_i} \Delta h_i \quad (B.3)$$

where the subscript  $i$  indicates evaluation over the  $i^{\text{th}}$  altitude interval from reentry to impact.

To evaluate Equation (B.3), the wind speed must be known for each  $i^{\text{th}}$  altitude interval. These values can be obtained from average wind profiles (graphical or tabular forms of average wind speed, in a specified direction, as a function of altitude). Such profiles, constructed from large samples of meteorological data, are for a specified month or season at a particular location. Wind data are available to approximately 90,000 feet; therefore, direct evaluation of wind effects above this altitude cannot be made. However, the wind influence coefficient function decreases very rapidly with altitude above 40,000 feet; above 90,000 feet, the function is less than one tenth of its low altitude peak value. The coefficient is so small in this upper zone that the range change from winds in this zone can be neglected without introducing significant error.

## B.2 DENSITY INFLUENCE COEFFICIENTS

The density influence coefficient,  $I^D$ , for a particular altitude is

$$I^D = \lim_{\Delta h \rightarrow 0} \frac{\Delta R_\rho}{\left( \frac{\rho - \rho_{STD}}{\rho_{STD}} 10^2 \right) \Delta h} \quad (B.4)$$

where  $\Delta R_{\rho}$  is the change in range (in feet) caused by a change in density from standard density of  $\left[ \frac{\rho - \rho_{STD}}{\rho_{STD}} \right] 10^2$  (percent) through an altitude interval  $\Delta h$  (feet) which has its midpoint at the specified altitude. Instead of using an absolute value of the variable, as was done with wind, the density effect is measured in terms of the percentage variation of the density,  $\rho$ , at a particular altitude from the standard density,  $\rho_{STD}$ , for that same altitude. Since the density variation is expressed as a percentage of standard density, mutually consistent units must be used for  $\rho$  and  $\rho_{STD}$ . As with the wind influence coefficient, the density influence coefficient for any altitude may be considered as the change in range caused by a 1 percent variation from standard density that occurs throughout a 1 foot altitude interval centered at the specified altitude. The density influence coefficient which has the dimensions of ft/ft-% or  $\%^{-1}$  is unlike the wind influence coefficient in that it is defined only in the downrange direction (i.e., density variations have no crossrange effects). As with the wind coefficient, the advantage of the density coefficient is that the density induced change in range for a particular altitude interval is the product of the density influence coefficient, the height of the altitude interval, and the percentage variation of density from standard throughout that interval, i.e.,

$$\Delta R_{\rho} = I_{\rho} \Delta h \frac{\rho - \rho_{STD}}{\rho_{STD}} 10^2 \quad (B.5)$$

### B.3 STANDARD DEVIATIONS

The standard deviations of a set, such as range change values, are the scatter of the individual values about the set mean and can be computed directly from the set values. However, it is faster and less laborious to use influence coefficients and arrays of weather statistics to compute the standard deviations of the wind induced and density induced range changes.

The influence coefficients have been defined in previous sections. The weather statistics required for computation of standard deviations comprise the means and standard deviations of the particular weather variable at a selection of altitude levels, with the interlevel correlation coefficients. (The latter identify the degrees of relationship between the values of the variable at the different altitude levels.) In terms of influence coefficients and weather statistics, the standard deviations are:

$$\sigma_{R_W}^2 = \iint I^W(h) \sigma_W(h) R_W(h, \bar{h}) \sigma_W(\bar{h}) I^W(\bar{h}) dh d\bar{h} \quad (B.6)$$

$$\sigma_{R_\rho}^2 = \iint I^\rho(h) \sigma_{\rho\%}(h) R_\rho(h, \bar{h}) \sigma_{\rho\%}(\bar{h}) I^\rho(\bar{h}) dh d\bar{h} \quad (B.7)$$

where

$\sigma_{R_W}$  = standard deviation of reentry wind induced range change, ft

$\sigma_{R_\rho}$  = standard deviation of reentry density induced range change, ft

$I^W(h)$  = wind influence coefficient at altitude  $h$ , sec/ft

$I^W(\bar{h})$  = wind influence coefficient at altitude  $\bar{h}$ , sec/ft

$I^\rho(h)$  = density influence coefficient at altitude  $h$ , %<sup>-1</sup>

$I^\rho(\bar{h})$  = density influence coefficient at altitude  $\bar{h}$ , %<sup>-1</sup>

$\sigma_W(h)$  = standard deviation of wind speed at altitude  $h$ , ft/sec

$\sigma_W(\bar{h})$  = standard deviation of wind speed at altitude  $\bar{h}$ , ft/sec

$\sigma^\rho(h)$  = percent standard deviation of density at altitude  $h$ , %

$\sigma^\rho(\bar{h})$  = percent standard deviation of density at altitude  $\bar{h}$ , %

$R_\rho(h, \bar{h})$  = correlation coefficient between values of density at altitude  $h$  and altitude  $\bar{h}$ , dimensionless

$R_W(h, \bar{h})$  = correlation coefficient between values of wind speed at altitude  $h$  and altitude  $\bar{h}$ , dimensionless

Numerical computations of standard deviations are also reduced to summing products instead of integrating. Standard deviations for density and wind induced range changes are:

$$\sigma_{R_W}^2 = \sum_{i=1}^n \sum_{j=1}^n I_i^W \sigma_{W_i} \Delta h_i R_{ij} \Delta h_j \sigma_{W_j} I_j^W$$

$$\sigma_{R_\rho}^2 = \sum_{i=1}^n \sum_{j=1}^n I_i^\rho \sigma_{\rho\%i} \Delta h_i R_{ij} \Delta h_j \sigma_{\rho\%j} I_j^\rho$$

where subscripts  $i$  and  $j$  indicate evaluation over the  $i^{\text{th}}$  and  $j^{\text{th}}$  altitude regions from reentry to impact.

This description of influence coefficients has considered down-range coefficients exclusively. Time and crossrange influence coefficients are used in an identical manner.

DISTRIBUTION

SAMSO/RSPP  
P.O. Box 92960  
Worldway Postal Center  
Los Angeles, California 90009  
Attention: Col. R. L. Stone (5)

Aerospace Corporation  
P.O. Box 92957  
El Segundo, California 90009  
Attention: J. Bailey (4)

SAMTEC  
Vandenberg Air Force Base, California 93437  
Attention: E. E. Clary (1)

SAMSO/MNNC  
Norton Air Force Base, California 92409  
Attention: Maj. T. Thomason (2)